Michael Pachler

Synergistic Activity of Antimicrobial Peptides

Doctoral Thesis

For obtaining the academic degree of

Doktor der technischen Wissenschaften

Doctoral Programme of Technical Sciences
Technical Physics

Graz University of Technology

Supervisor:
Assoc.-Prof. Dr. Georg Pabst

Institute of Materials Physics
in cooperation with: Institute of Molecular Biosciences, University of Graz

Graz, July 2019

EIDESSTATTLICHE ERKLÄRUNG

AFFIDAVIT

Ich erkläre an Eides statt, dass ich die vorliegende Arbeit selbstständig verfasst, andere als die angegebenen Quellen/Hilfsmittel nicht benutzt, und die den benutzten Quellen wörtlich und inhaltlich entnommenen Stellen als solche kenntlich gemacht habe. Das in TUGRAZonline hochgeladene Textdokument ist mit der vorliegenden Dissertation identisch.

I declare that I have authored this thesis independently, that I have not used other than the declared sources/resources, and that I have explicitly indicated all material which has been quoted either literally or by content from the sources used. The text document uploaded to TUGRAZonline is identical to the present doctoral dissertation.

Datum / Date	Unterschrift / Signature

Acknowledgment

The last couple of years were challenging, exciting and occasionally frustrating. Looking back makes me feel grateful for the opportunity to study in such a unique environment. The combination of an interdisciplinary working field and friendly, kind and helpful colleagues made me enjoy work most days. Of course there were always those other days...
I would like to thank Georg and Charlie for all their help and guidance provided over the years. Their efforts made my task significantly more doable. Also i would like to thank Robert Vácha and Ivo Kabelka for the fruitful cooperation. Our combined working groups are quiet the synergistic duo. A big thank you to my thesis readers Lisa Marx and Anton Orthacker. Your input was highly appreciated. Office wise, I am going to miss the occasional coffee breaks and countless discussions with everyone talking about literally anything imaginable. Also I would like to thank my family, Gertraud, Fritz and Andreas Pachler for their constant support and comforting words as long as I can think back. You were and are still a rock I can lean against. Last but not least Angelina, you have been there for me during the last 10 years. You always stood by my side and found the right words to lighten my mood. For that I am eternally grateful. For my personal future, as a wise man once said "Urlaub, is wonn I nix vua hob".

Abstract

Multiresitant bacterial strains pose a serious threat to our health. They are resistant against first and second order antibiotics and infections therewith cause severe damage or death. Main problems are the careless use of antibiotics, their mode of action and the high degree of adaptability of bacteria. A promising approach is offered by antimicrobial peptides (AMPs). They exhibit a fast non receptor based killing of bacteria, with the cytoplasmatic membrane as their main target. Prime candidates are the magainins PGLa and MG2a, which exhibit a tenfold increase in killing efficacy when applied as cocktail. Currently there is a wide range of information on the enhanced killing ability of magainins (synergistic activity) in literature available. Unfortunately much of it stands in contradiction with observations and only little quantitative information on the membranes structural response is available. A large part of this thesis was spent on the creation of an analysis for scattering data to retrieve precisely those quantities in a statistical approach. In general, fundamental studies on systems with living bacteria and AMPs are a highly complex task. Therefore we aimed to establish an simple as possible lipid only mimic, which still captures the essential response of Gram-negative bacterial membranes to the peptides.
We observed that the leakage induced in 100 nm large unilamellar vesicles (LUV) composed of POPE/POPG (3/1) by L18W-PGLa, MG2a, their equimolar mixture and the chemically linked hybrid peptide correlates remarkably with growth inhibitation (MIC) experiments performed on live bacteria. In particular we found that key characteristics for the occurrence of synergistic activity are a tight polar-apolar interface of the membrane (negative J_0) and the presence of negatively charged lipids. This clearly states how crucial the proper choice of lipids for a mimic is. Those insights prompted us to perform an in-depth small angle scattering study in a low (before synergism) and high (synergism) peptide concentration regime. To access quantitative information in diffusive scattering data at a molecular level

the during this thesis developed analysis was employed for a peptide/lipid (P/L) ratio $\leqslant$ 1:200, which allowed global data fitting including scattering contributions from the peptide. A joint analysis of neutron and X-ray data provided information on the peptides transbilayer position, also showing that when applied as a mixture both peptides were relocated. Further we showed that the relocation process most likely originates in the formation of parallel heterodimers. At synergistic conditions (P/L $\geqslant$ 1:50) we were able to correlate the observed dye-release with the occurrence of a sponge and cubic Pn3m phase. Together with a variety of complementary molecular dynamics (MD) simulations performed by our collaboration partners, we proposed a possible way for L18W-PGLa and MG2a synergistic mode of action against Gram-negative bacterial mimics. Their enhanced killing efficacy starts with the early formation of heterodimers, before synergism is even observed. Those dimers insert shallow into the membrane with their cationic residues exposed to the aqueous solution. The charged amino acids lead to adhesion and aggregation of multiple vesicles via electrostatic interactions. Dimers, as well as the fibre-like peptide structures, formed at higher peptide concentration both induce a strong membrane curvature. Additionally fusion stalk formation between bilayers in close proximity in the presence of heterodimers and larger aggregates was observed. Those stalks eventually transformed the system in a leaky sponge like structure that accounts for the increased amount of fluorescence. Contributions to the observed leakage from defect enriched zones might also be of relevance.

Kurzfassung

Mehrfach resistente Bakterienstämme erweisen sich als ernstes Problem für unsere Gesundheit. Sie sind resistent gegen Antibiotika ersten und zweiten Grades und Infektionen enden oftmals in schwerwiegenden Gesundheitlichen Schäden oder Tod. Hauptprobleme sind der sorglose Umgang mit Antibiotika, sowie deren Wirkungsweise und die enorme Anpassungsfähigkeit von Bakterien. Einen vielversprechenden Ansatz stellen antimikrobielle Peptide (AMPs) dar. Sie greifen die cytoplasmatische Membran an und töten Bakterien schnell und effizient. Anwärter für ein Antibiotikum dieser Art sind die Peptide PGLa und MG2a, beide zugehörig zur Familie der Magainins. Bei kombinierter Anwendung wird eine zehnfach höhere Wirksamkeit erzielt (Synergismus). Gegenwärtig ist eine Vielzahl an Informationen über Synergismus von den zuvor genannten Peptiden in der Literatur auffindbar. Ein beachtlicher Teil dieser Schriften steht jedoch in Widerspruch zueinander. Zusätzlich gibt es kaum quantitative Information über die strukturelle Reaktion der Membran auf angreifende Peptide. Deswegen wurde ein großer Teil dieser Doktorarbeit damit verbracht eine Analyse zu entwickeln, welche genau dieses Wissen zugänglich macht. Untersuchungen an lebenden Systemen wie Bakterien sind wegen ihrer enormen Komplexität für fundamentale Aussagen über die Wirkungsweise von Peptiden nicht der beste Startpunkt. Im ersten Teil dieser Arbeit wurde nach einem "Minimalsystem" gesucht, welches zugleich die für diese Arbeit essentielle biophysikalische Reaktion des Bakteriums auf angreifende Peptide wiederspiegelt. Im Speziellen beobachteten wir, dass die induzierte "Leakage" von L18W-PGLa, MG2a, ihrer äquimolaren Mischung und dem chemisch gelinkten Hybridpeptid in 100 nm großen unilamellaren Vesikeln (LUV) mit den Ergebnissen von Wachstumsinhibitationsmessungen an lebenden Bakterien in hervorragender Übereinstimmung sind. Das Auftreten von Synergismus konnte auf zwei Schlüsselkomponenten zurückgeführt werden, nämlich, eine dicht gepackte Schnittstelle polarer und apolarer Komponenten der

Membran und das Vorhandensein von negativ geladenen Lipiden. Dies zeigt bereits wie wichtig die Wahl der Lipide des Testsystem ist. Obige Erkenntnisse motivierten uns zu einer systematischen Studie mittels Kleinwinkelstreuexperimenten als Funktion der Peptidkonzentration, vor und bei synergistischen Bedingungen. Für ein Peptid/Lipid Verhältnis (P/L) $\leqslant$ 1:200 wurde mittels Einsatz der entwickelten Analyse die Eindringtiefe der Peptide in die Membrane bestimmt. Im speziellen wurden Röntgen- und mehrere Neutronendatensätze gleichzeitig mit einem Model ausgewertet. Des Weiteren wurde gefunden, dass wenn L18W-PGLa und MG2a als Mischung eingesetzt wurden eine Umpositionierung der Peptide in der Membran stattfand. Bei synergistischen Bedingungen wurden Fluoreszenzmessungen mit dem Auftreten einer lamellaren Struktur in Röntgendaten korreliert. Cryo-Transmissionselektronenmikroskopische (cryo-TEM) Messungen identifizierten diese als multilamellare Vesikel. Zusammen mit zahlreichen Molekulardynamiksimulationen (MD), ausgeführt von unserem Kooperationspartner konnte eine mechanistische Beschreibung für die synergistische Wirkung von L18W-PGLa und MG2a gefunden werden.
Der Nukleus ihrer erhöhten Wirksamkeit ist mit der Ausbildung von parallelen Heterodimeren bevor synergistische Bedingungen erreicht sind gegeben. Diese Dimere dringen nur oberflächlich in die Membran ein, mit ihrer kationischen Seite der Bufferlösung zugewandt. Attraktive Interaktionen mit Peptiden auf benachbarten Vesikeln führen zu Adhäsion, gefolgt von der Aggregation von mehreren Vesikeln. Bei einer erhöhten Peptid Konzentration wurde die Ausbildung von Peptid-Fasern festgestellt. Diese Fasern, sowie auch die Dimere induzieren eine starke Membran Krümmung, welche zusammen mit den beobachteten Fusionhälsen das System im Verlauf der Zeit in eine schwammartige Struktur transformiert. Diese Struktur ist stark Porös und beschreibt somit den beobachteten Anstieg in Fluoreszenz.

Contents

List of Figures

1. Introduction

This thesis is split into five parts, providing the reader with a motivation and the necessary background in the first chapter, followed by the description of the employed methods in the second chapter. Core results from attached publications are presented and discussed in chapter three. A short conclusion with a brief subsequent discussion of the derived mechanism with focus on the comparison to proposed models for synergism in literature is given in chapter four. Last but not least technical suggestions to improve the analysis can be found in the last part.

Motivation

The increase of antibiotic resistance is rising to dangerously high levels. The World Health Organization (WHO) published in February 2017 a list of antibiotic-resistant pathogens to guide medical development towards high priority targets. This list highlighted in its most critical group the "ESKAPE" pathogens which are multidrug resistant bacteria that pose a severe threat in hospitals, nursing homes and community settings [6]. The ESKAPE pathogens consist of *Enterococcus faecium*, *Staphylococcus aureus*, *Klebsiella pneumoniae*, *Acinetobacter baumannii*, *Pseudomonas aeruginosa* and *Enterobacter*. Infections with any of them leads to severe damage and worst case death. Key problems of antibiotic resistance are the mode of action of conventional antibiotics (receptor/target), the bacteria's adaptability towards such attacks and their immense number. Nearly all commercially available antibiotics target specific parts of a bacterium, e.g a specific protein. Unfortunately bacteria's response to such an attack is a prime example of evolution. Its various ways of defense reach from mutational adaption towards horizontal gene transfer, ultimately leading to resistance against the employed drug

(for more detail see [6]). This inauspicious development is further aided by the steady decrease in yearly approved antibiotics by the Federal Drug Association (FDA) thus severely limiting treatment options. In the last three decades most "new" introduced drugs were only structural derivatives of already existing antibiotics. Their similarity caused extremely high vulnerability towards resistance development and generally led to a low life span. Hence there is an urgent need of compounds which are less likely to encounter bacterial resistance. Prime candidates are host defense peptides. In particular the class of antimicrobial peptides (AMPs) which offer new and "novel" multifaceted ways of killing bacteria within minutes. Most AMPs do not bind to a specific protein target. Their site of action is the lipid bilayer of the cell membrane. Further electrostatic interactions between cationic AMPs and negatively charged lipids in the exofacial leaflet of the plasma membrane lead to a strong discrimination between mammalian (zwitterionic lipids) and bacterial (enriched in anionic lipids) cells. Considering the full architecture of live bacteria, AMPs have to bypass all outer layers of the cell [7] (Figure S1.3) until their final target the cytoplasmic membrane is reached. There they insert depending on their amphipathicity and kill bacteria due to membrane rupture. Their precise interaction with target membranes strongly depends on the present lipid composition. The latter influences the peptides due to different molecular shapes (intrinsic lipid curvature), charge and chemistry. It is imperative to posses a detailed level of understanding on the architecture and lipid composition of the bacteria for faithful studies on AMP-bacteria interactions [8, 9].

This thesis focuses on the interactions of L18W-PGLa and MG2a with first order lipid only mimics for Gram-negative bacteria. Both peptides are part of innate immune system of the African clawed frog *Xenopis Laevis* [10, 11] and are classified as magainins. Of particular interest is their enhanced killing ability observed in bacteria and lipid only mimics thereof [12–17]. Originally (1998) synergism was attributed to a transmembrane pore formation with a 1:1 stoichiometry between L18W-PGLa and MG2a [12–14]. In 2016 Bechinger introduced the idea of lipid-mesophase like structures for peptides where they are aligned side-by-side with their helices parallel to the membrane surface [2]. This was followed again by a pore, stabilized via a tetrameric heterocomplex of transmembrane aligned PGLa in combination with a surface state for MG2a [3]. Interestingly, nuclear magnetic resonance

(NMR) spectroscopy experiments clearly state that MG2a and PGLa both never adopt a transmembrane position for the main constituent lipids of a Gram-negative bacterium's cytoplasmatic membrane, not even when applied as a cocktail [18, 19]. This fact clearly stands in contradiction to any pore based model for synergism in Gram-negative bacterial mimics. Currently there is a lack of understanding in how both peptides remain surface bound and at the same time synergistically disrupt bacterial membranes. This motivated us to perform a comprehensive study utilizing molecular dynamics (MD) simulations paired with a wide range of experimental techniques, breaching dimension from nanoscopic to macroscopic length scales in order to elucidate the interactions of L18W-PGLa and MG2a with first order lipid only mimics and to unravel the mystery of their synergistic killing efficacy.

1.1. Lipid Curvature - Lipid Bilayer Model - Gram-Negative Bacterial Cell Membrane

The core of every biological cell is shielded by a barrier, the so called plasma membrane. This barrier is a highly dynamic fluid structure and consists of a double layer composed of various lipids. Lipids are small amphiphile molecules with a hydrophilic headgroup (polar, water loving) and hydrophobic tails (non polar, water hating). Their structure, hydrophilic and hydrophobic regions of two major constituents in a Gram-negative bacterium's plasma membrane are given in Figure 1.1.

Lipids can be classified in terms of their intrinsic curvature J_0, which is defined as the negative inverse radius of the neutral plane of a stress less monolayer [20, 21]. It is a geometrical parameter providing information about the shape a lipid wants to adopt at a certain temperature. Figure 1.2 shows cylindrical $J_0 \approx 0$, conical $J_0 > 0$ and inverse conical $J_0 < 0$ shaped lipids. Directly below is the preferred membrane of each species, highlighting that cylindrical lipids prefer bilayers whereas curved lipids favor bend monolayers. Dissolved in aqueous solution, lipids self assemble, driven by the need to minimize hydrophobic exposure of the hydrocarbon core and their molecular shape. For example, cylindrical shaped lipids tend

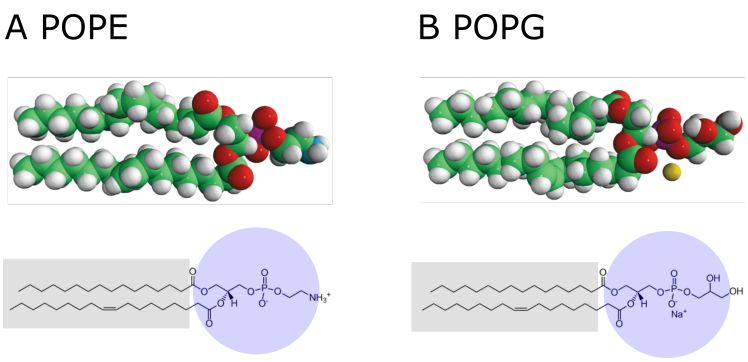

Figure 1.1.: Spatial structure of the phospholipids (A) POPE and (B) POPG. Grey shaded areas mark hydrophilic fatty acids and blue shaded circles highlight the lipid headgroups.

to form multilamellar (onion) or unilamellar vesicles (onion shell, panel D) whereas a negative overall geometry can lead to inverted hexagonal phases (panel E). By mixing of differently shaped lipids, depending on their molar ratios and temperature bi-continuous cubic phases can be observed. E.g. the cubic Pn3m phase is build up by a complex network of water channels encapsulated by one continuous lipid bilayer (Figure 1.2 panel E) exhibiting zero overall gaussian curvature.

To tune artificial model systems towards the present topic of interest the architecture and lipid composition of Gram-negative bacteria (target) with focus on *Escherichia coli (E. coli)* has to be briefly reviewed.

In terms of architecture the bacterial cell wall is a complex structure (Figure 1.3) consisting of the inner membrane (cytoplasmatic membrane), a rigid peptidoglycan (PGN) layer and the outer membrane. The purpose of this barrier is to provide stability to the cell interior, to protect it from harm originating in the environment and simultaneously provide material transport and information exchange with the outside. Studying peptide/bacteria interactions at a quantitative level is a highly sophisticated task and requires due to the large amount of unknown factors a simplification of the bacterial cell wall. AMPs in general will have different affinities to different parts of the cell wall. For example lipopolysaccharides (LPS) are the main constituents of the outer leaflet of the outer membrane. It is anionic and therefore could potentially trap AMPs until all LPS is saturated. Consequently reducing the peptides concentration at the cytoplasmatic membrane

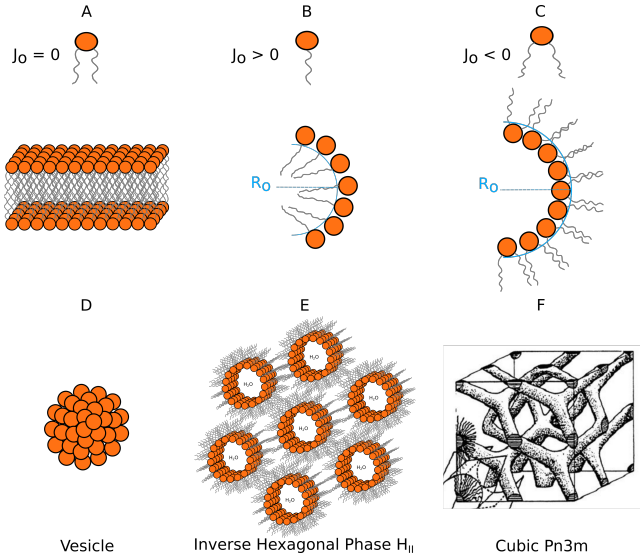

Figure 1.2.: The top row shows cylindrical (A), conical (B) and inverse spherical shaped lipids (C). Below are the corresponding membranes and formed aggregates (D), (E) and (F). Panel F was adapted from Tresset 2009 [1].

(attack site of the peptide) but not changing the peptides mode of action. Literature suggests that the PGN layer which is located between the IM and the OM possibly guides the AMPs through its sponge like network towards the inner membrane [22]. Thus it is a valid approach to discard all outer layers completely and solely focus on the inner membrane. It is well known that most AMPs do not have a specific protein target and to further simplify it is possible to mimic the cytoplasmatic membrane with a lipid only system representative for the bacterium's lipid composition. A previous publication [23] demonstrated that the cytoplasmatic membrane of *E. coli* is reasonably represented by 82% phosphatidylethanolonamine (POPE), 6% phosphatidylglycerol (POPG) and 12 % diphosphatidylglycerol (DPG). This is further substantiated by the fatty acid chain profiles of *E. coli PE* and *E. coli PG* extracts, which are enriched in palmitic (16:0) and elaidic (18:1) acids. Also, DPG's intrinsic curvature heavily depends on the ionic composition of the aqueous buffer [24]. To avoid any ambiguities from this issue we substituted each DPG molecule with two POPG lipids, leading to a final membrane composition of 75% POPE and 25% POPG as a first order mimic for the inner membrane of *E. coli* in terms of lipid constituents and

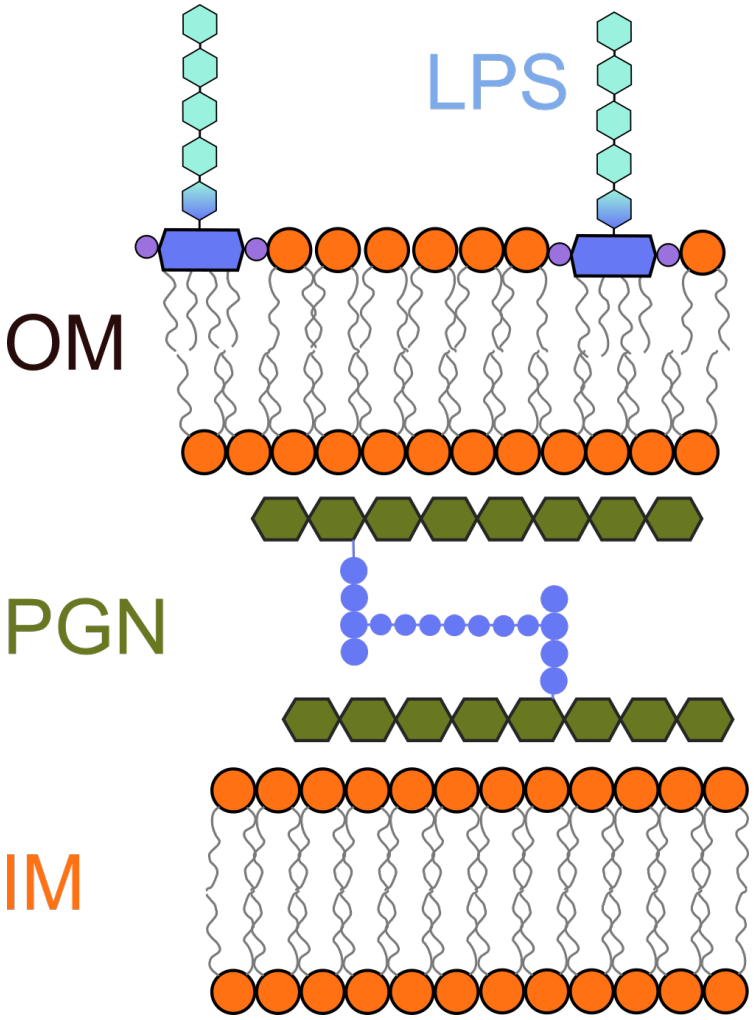

Figure 1.3.: Cell envelope of a Gram-negative Bacterium. Lipopolysaccharide LPS, outer membrane OM, peptidoglycan layer PGN and the cytoplasmatic (inner) membrane of *E. coli*.

stored intrinsic curvature strain. To mimic the scenario of bacteria getting attacked from the outside 100 nm large unilamellar vesicles were prepared and peptides added externally. Findings from such model systems have to be viewed critically and should not be taken directly to describe living cells however they are imperative to unravel the fundamental biophysics behind it. Their biggest advantage is the possibility of biophysical studies in highly controlled chemical and experimental environments [25].

1.2. Antimicrobial Peptides AMPs

Antimicrobial peptides are part of the innate immune system and act as natures very own antibiotics [26, 27]. They exhibit a broad spectrum of activity against various strains of Gram-negative and Gram-positive bacteria. In contrast to conventional antibiotics most AMPs interactions with bacterial membranes do not involve specific protein targets [28, 29]. They primarily attack the cytoplasmatic membrane and therefore reduce the risk of bacterial resistance. For those reasons AMPs have been extensively studied over the last three decades and data of over 3000 AMPs have been collected in databases [30, 31]. Yet compelling structure-function relationships are still lacking. AMPs in general are constructed of a short sequence (8 - 35) of amino acids. Their secondary structures may embrace an α-helical conformation, β-sheets, or may be looped or extended structures (Figure 1.5). Despite all their variety AMPs share two common features, amphipathicity and a positive charge. Electrostatic interactions between negatively charged lipids and cationic peptides lead due to the compositional differences in mammalian (zwitterionic) and bacterial (anionic) membranes to favored interactions with the latter. Upon adsorption to the membrane many AMPs adopt conformations where the spatial distribution of amino acid residues results in amphipaticity. Their ability to insert into the membrane is driven by hydrophobic interactions. Overall a delicate balancing of electrostatic and hydrophobic forces between peptides, lipids and the aqueous environment is required.

Researchers discovered in the past various modes of action for AMP activity. Figure 1.4 provides a brief overview over the most commonly used mecha-

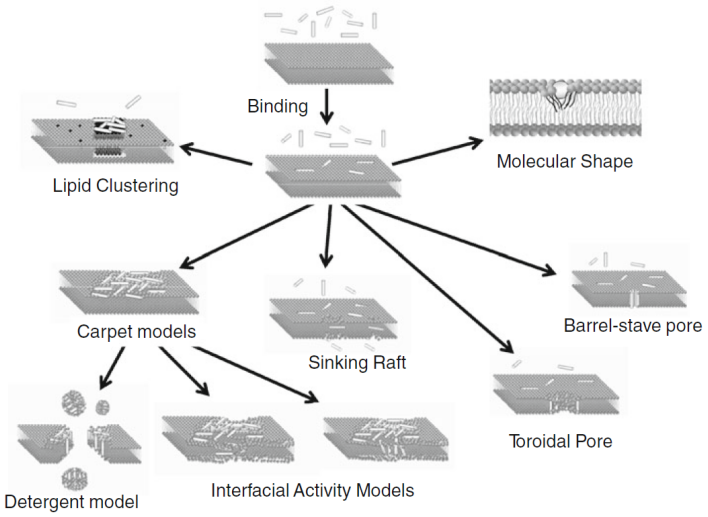

Figure 1.4.: Overview of popular models for AMP activity proposed in literature. Figure taken from Wimley 2011.

nisms in literature. In any case the AMPs action starts with initial binding at the target membrane. From there it is strongly dependent on the specific peptide, its concentration and system of interest which process will act. The models shown in Figure 1.4 can be classified in two categories, transmembrane pore formers and non-pore models. The barrel-strave [32] and torodoidal pore [33] both create a water filled channel across the membrane. Main differences are their geometry and the way the pore is stabilized and constructed. The barrel-strave pore perturbs only the surrounding lipid matrix to a small degree whereas the toroidal pore affects the membrane by inducing curvature with phospholipids intercalated between the long peptide axis. In addition, peptide activity has been shown with plenty different non pore models. The carpet model [34] describes the lysis of membranes at high peptide concentrations. Peptides accumulate at the membrane and once a critical concentration is reached permeabilization occurs via global membrane disruption/destabilization. Closely related is the detergent model where upon a critical peptide concentration a collapse of membrane integrity starts until it is completely destroyed in detergent like fashion [35–38]. The molecular shape concept [37, 38] is based on permeabilization due to a disturbance of lipid packing. Once a peptide inserts into the membrane in a

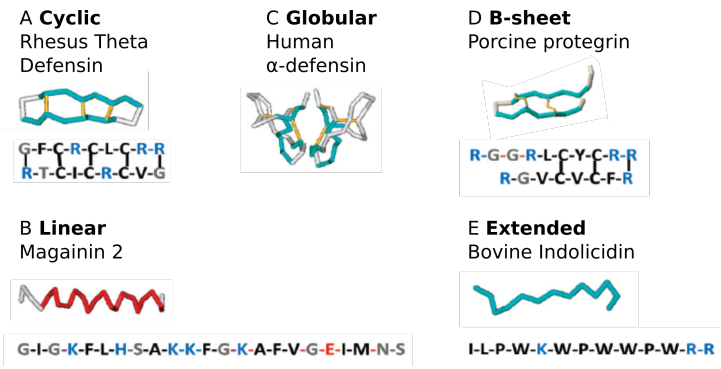

Figure 1.5.: Various antimicrobial peptides and their versatile primary/secondary structures, reaching from cyclic (A), linear (B), globular (C), β-sheets (D) to extended (E) conformations.

surface state, a void in the hydrocarbon region is created. Such a situation is energetically extremely unfavorable and the surrounding lipids close the gap with their hydrocarbon chains. Depending on the degree of mismatch dimple formation (membrane thinning) or interdigitated bilayers can be observed. Next Epand proposed that AMPs induce lipid phase separations or induce lipid clustering and that the resulting permeabilization originates from defects at the boundary region [39, 40]. Almeida and coworkers have proposed the sinking raft model where a transient pore is induced due to peptide translocation through the bilayer [41, 42]. Last but not least Wimley and Rathainakumar proposed the interfacial activity model [43, 44]. It is driven by imperfect amphipathicity. Peptides insert into the interface region and due to polar/apolar mismatches of lipid and peptides lipids become vertically rearranged, resulting in a perturbation of the membranes permeability barrier. Note that in literature there are far more non pore forming models proposed. Yet in many publications pores are used to describe the observed. Interestingly, experiments are often well described by one or more of those models. However no model describes all observations.

Of particular interest is the enhanced killing ability (synergism) of PGLa and MG2a when applied as equimolar mixture to live bacteria and lipid only mimics thereof [12–16]. Their enhanced killing efficacy is much larger than the sum of the individual effects. This manifold increase in activity has been studied for the last 30 years with a wide array of biophysical techniques and its molecular mechanism is still a matter of debate. A summary of

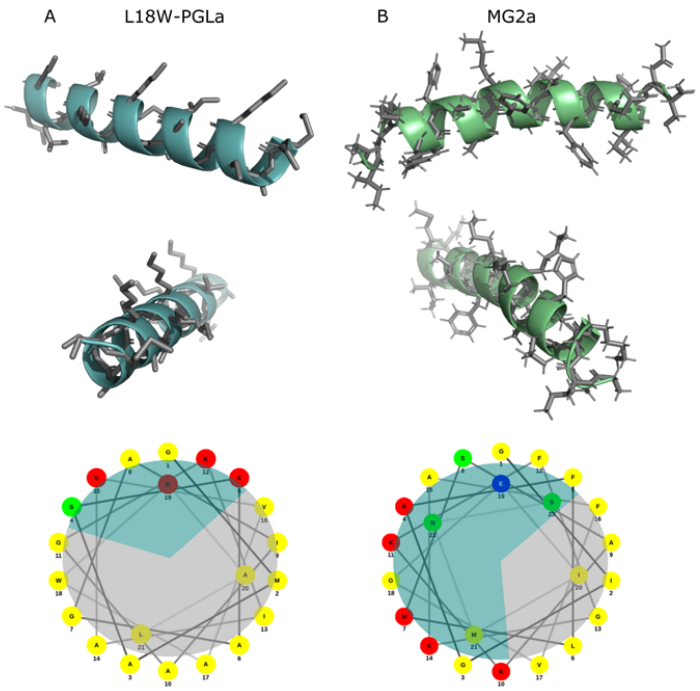

Figure 1.6.: Different views of the secondary structure of L18W-PGLa (A) and MG2a (B) including their side chains. Below are the corresponding hydrophobic wheel schematics. The hydrophob section is shaded in grey and the hydrophil section is shown in dark cyan. Polar/basic residues are shown in red, whereas polar/acid, polar/uncharged and nonpolar residues are colored in blue, green and yellow respectively.

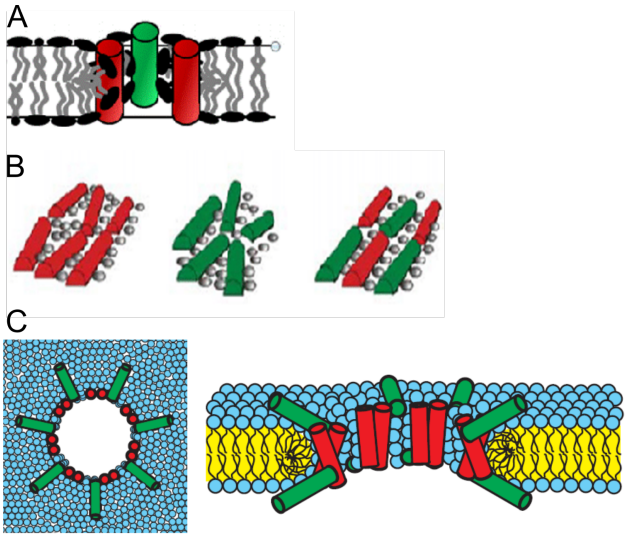

Figure 1.7.: Currently proposed models for synergism in literature. Panel (A) shows a toroidal pore, formed by parallel heterodimers. (B) Illustrates lipid-mesophase like peptide arrangements and (C) displays a tetrameric pore. Schematics are taken from [2, 3].

the proposed mechanism for synergism is given in Figure 1.7. In brief, Matsuzaki and coworkers proposed that heterodimers of PGLa and MG2a together form in 1:1 stoichiometry a peptide-lipid supramolecular complex pore (toroidal pore) [12–14]. This was followed in 2016 by Bechinger with the suggestion of mesophase-like peptide arrangements that creates patches on the membrane at elevated peptide concentration inducing membrane perturbations [2]. Last but not least the Ulrich group (2017) postulated pore formation based on a tetrameric heterocomplex. This particular pore is constructed from antiparallel transmembrane PGLa dimers and surface state aligned MG2a and is stabilized via Gly-Gly contacts (GxxxG motif) between the PGLa dimers and C-terminal interactions between MG2a and PGLa.

In the present work we used L18W-PGLa instead of native PGLa to stay comparable with the work performed by Matsuzaki [13]. There they exchanged leucine at position 18 with tryptophan for fluorescence experiments and demonstrated in the same paper that L18W-PGLa has a similar activity than native PGLa.
L18W-PGLa and MG2a are short (21 and 23 residues) linear cationic peptides

which are unfolded in solution and adopt an amphipathic α-helical conformation next to membranes. Their primary structure (sequence) is given in Figure 2.1 panel B. Once in α-helical conformation they exhibit hydrophobic (grey shaded) and hydrophilic (green shaded) sectors (Figure 1.6). This simple view already indicates that L18W-PGLa inserts due to its larger hydrophobic section deeper into lipid membranes compared to MG2a. We previously found that their synergistic activity against lipid only model system composed of POPE and POPG (3/1 molar ratio) correlates closely with their growth inhibition efficacy for *E. coli* [17]. NMR studies of PGLa, MG2a individually and mixtures thereof on our lipid only system have shown that at any investigated peptide concentration only surface state aligned topologies were observed [18, 19]. These facts stand in direct contradiction with currently the widest spread mechanism used to describe synergism in the community, namely transmembrane pore formation [3, 13].

The goal of this thesis was to identify new aspects of the synergistic acting magainins L18W-PGLa and MG2a. Particular focus was on the membrane's structural response towards attacks by AMPs. Ultimately a mechanistic description of the enhanced killing efficacy was desired.

2. Materials and Methods

This chapter focuses on the employed materials, sample preparation and the description of the methods for data analysis which were not fully given in publications.

2.1. Materials

All studied materials except DOPC and the sterol cholesterol are represented in Figure 2.1. Panel A provides an overview of the used phospholipids chemical structure, chain composition and headgroup variation and panel B shows the primary sequence of each investigated peptide. Residues are color coded with light blue and red for positive and negative charged amino acids at present pH conditions. Lipids were purchased from Avanti Polar Lipids, Alabaster, AL (purity>99%) as a powder. Cholesterol was ordered from Sigma-Aldrich, Vienna, Austria and L18W-PGLa, MG2a, as well as their GGC linked derivatives and the L18W-PGLa-MG2a heterodimer was obtained in lyophilized form (purity >95%) from PolyPeptide Laboratories (San Diego, CA). For further details see the publications appendix [4, 17, 45].

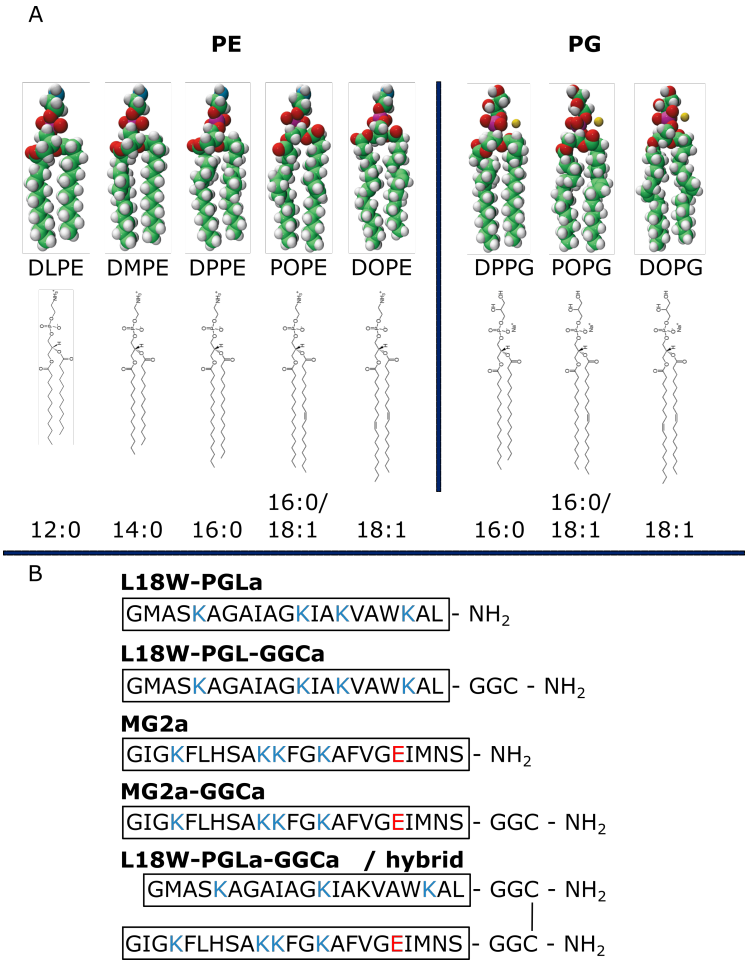

Figure 2.1.: Panel (A) shows the used phospholipids and panel (B) provides a color coded overview of the peptides primary sequences. Light blue/red corresponds to positive/negative charged residues respectively.

2.2. Sample Preparation

2.2.1. Samples for Intrinsic Lipid Curvature Determination

Samples for intrinsic lipid curvature determination were prepared via a modified version [46] of the rapid solvent exchange technique [47, 48]. Lyophilized lipids were brought to room temperature before opening, weighting and mixing with organic solvent. As standard organic solvent chloroform/methanol 9/1 v/v was used for any lipid except lyso-PE. Here we had solubility issues which were addressed by a solvent mixture of chloroform/methanol/H_2O 65/35/8 v/v/v. In a second step glass tubes (Pyrex) were filled with appropriate amounts of Sodium-Phosphate (NaPi) buffer (20 mM NaPi, 130 mM NaCL, pH 7.4) and equilibrated at the temperature used during the RSE experiment for 15 minutes. Once at temperature, adequate amounts of lipid stock solutions and tricosene were injected with hamilton syringes into test tubes succeeded by immediate mounting at the RSE system. The vortexer was turned on at pre-defined settings followed by rapid solvent exchange induced by an opening of the pressure valve between pump and sample environment. The pressure was set between the vapor pressure of water and organic solvent. That way after five minutes only NaPi buffer was present and the lipids were forced due to their amphipathicity and molecular shape into inverse hexagonal phases. Sample preparation was stopped after five minutes. During the evaporation process the system was constantly under a gentle stream of argon with 60 ml/min to speed up the removal of organic solvent. The temperature of each individual sample was set 15°C above reported H_{II} transition temperatures for the constituent lipids. To reduce the packing frustration of the H_{II} phase 12% wt of tricosene were added to all samples [49]. All experimental parameters can be seen in Table 2.1. In general when using the RSE it is advantageous to lower the pressure slowly in order to avoid foaming/bubbling of some samples and to apply lower vortex speeds of 600-800 rpm in the beginning. This helps to avoid material loss due to sticking at the boundaries of glass test tubes. Depending on the type of sample, from zero up to three days of equilibration times were needed to observe scattering from pure hexagonal

phases. For storage purposes samples were covered with argon to avoid oxidation of the hydrocarbon chains.

Table 2.1.: Experimental settings used during the rapid solvent exchange process.

Lipids	Temperature [°C]	Pressure [mbar]	Vortex speed [U/min]
DLPE/DOPE	50	300	800
DMPE/DOPE	70	450	600
DPPE/DOPE	65	350	1200
POPE	55	360	1000
DOPE	45	200	1200
POPG/DOPE	60	300	1000
DOPG/DOPE	45	200	1800
lyso-PE/DOPE	70	900	1000

2.2.2. Samples for Mechanistic Investigations of Peptide-LUV Interactions

Large unilamellar vesicles (LUVs, 100 nm) were prepared with standard thin film hydration followed by eight cycles of freeze and thaw in aqueous 10 mM HEPES 140 mM NaCL pH 7.4 buffer solution. First lipid stock solutions were made and for precise quantification of lipid concentration phosphate assayed [50]. Appropriate amounts of stock solution were mixed together with hamilton syringes. Next, organic solvent was evaporated under a gentle stream of nitrogen at 35°C succeeded by overnight storage in a vacuum chamber. Dry lipid films were hydrated in buffer and equilibrated at 55°C for one hour with eight subsequent cycles of freeze-and-thaw using liquid nitrogen. Large unilamellar vesicles were obtained by 31 cycles of extrusion with a hand held avanti mini extruder using a 100 nm pore diameter polycarbonate filter. Vesicle size and polydispersity were verified with dynamic light scattering. The final lipid concentration was determined again by phosphate assay. According to this adequate amounts of peptide stock solution (dissolved in the buffer used in the corresponding experiment) were added externally to LUVs. In the case of the equimolar mixture peptides were already premixed in the stock solution. All prepared lipid base systems can

be seen in Table 2.2 with the corresponding D_2O/H_2O [v/v] ratio of the buffer and the equilibration time before experiments.

Table 2.2.: Prepared lipid systems together with the corresponding D_2O/H_2O [v/v] ratios of 10 mM HEPES 140 mM NaCL pH 7.4 buffer solution and the used equilibration times before experiments.

Lipid System [molar ratio]	D_2O/H_2O [v/v]	equilibration [days]
POPE/POPG [3:1]	0	4
POPE/POPG [3:1]	100	4
POPE/POPG [3:1]	75	4
POPE/POPG [3:1]	50	4
POPE-d31/POPG/POPGd31 [75/22/3]	43.7	$\geqslant 3$
POPE/POPE-d31/POPG/POPGd31 [16.5/58.5/5.5/19.5]	43.7	$\geqslant 3$

2.3. Small-Angle Neutron and X-ray Scattering

Small-angle scattering (SAS) is a non-invasive tool to study e.g. proteins, liposomes and colloids with respect to their structure and overall shape. Depending on the experimental setup (wavelength, scattering angles) length scales from $\approx 1 - 1000$ Å are accessible. SAS provides an ideal platform for the interrogation of lipid bilayers which are in general about 50 Å thick.

In this thesis we mainly focus on scattering from dilute systems considering only Thomson scattering (elastic scattering). The corresponding experimentally detectable intensity is given by

$$I(q) = n|F(q)|^2, \tag{2.1}$$

where n is the number density of suspended particles and F(q) is the scattering amplitude with it's general form

$$F(q) = \int_V \rho(\mathbf{r}) e^{i\mathbf{qr}} \mathrm{d}r. \tag{2.2}$$

F(q) is the fourier transform of the electron density $\rho(\mathbf{r})$, q and r are coordinates in reciprocal and real space respectively. Here we deal with spherical suspended particles in a solvent and consequently $\rho(\mathbf{r})$ has to be substituted with the electron density of the solvent, leading to the observable contrast $\Delta\rho(\mathbf{r}) = \rho(\mathbf{r}) - \rho_{Solvent}(\mathbf{r})$. Considering unilamellar vesicles with a polydispersity P(q) the detectable intensity can be described as

$$I(q) = nP(q)|F(q)|^2. \tag{2.3}$$

Taking advantage of the particles spherical symmetry and size (100 nm) and the fact that the membrane thickness ($\approx$ 50 Å) is much smaller compared to the vesicles radius ($\approx$ 1000 Å) equation 2.3 simplifies by employment of the separated form factor approach [51, 52] to

$$I(q) = nP(q)|F_{TS}(q)|^2|F_M(q)|^2, \tag{2.4}$$

where F_{TS} is the thin shell scattering amplitude and F_M corresponds to scattering from a flat bilayer. In the present case F_{TS} is constant for data evaluation above $q = 0.025\frac{1}{\text{Å}}$ and will be neglected (scaling constants do not influence the retrieved structural parameters). The final Lorentz corrected intensity can be fully described with a flat bilayer form factor and a constant I_{inc} accounting for the incoherent scattering background by

$$I(q) \approx \left(\frac{1}{q^2}|F_M(q)|^2\right) + I_{inc}. \tag{2.5}$$

$\frac{1}{q^2}$ is the Lorentz correction and the scattering amplitude of a symmetric flat membrane F_M is given by

$$F_M = 2\int_0^D \Delta\rho(z)cos(qz)\mathrm{d}z. \tag{2.6}$$

The integration limit D corresponds to a position in real space where $\Delta\rho(z) = 0$ applies.

2.3.1. Modeling of Diffusive Scattering Signals

Currently the most elegant way of describing a lipid bilayer is the scattering length density profile (SDP) model proposed by Kučerka [53]. It characterizes the scattering contrast ρ in terms of a composition dependent lipid parsing by utilization of volume probability distribution functions (equation 2.12). A lipid bilayer (Figure 2.3 A) is parsed into several quasimolecular fragments/groups and their spatial distribution along the bilayer normal (z direction) is described with either a Gaussian-type function (eq 2.7) or error functions (eq 2.8).

$$P_i(z) = \frac{V_i}{A_U \sigma_i \sqrt{2\pi}} e^{\frac{(z-zi)^2}{2\sigma_i^2}} \tag{2.7}$$

$$P_{plat}(z) = \frac{1}{\sqrt{\pi}} \left(\int_0^{\frac{z-z_i}{\sqrt{2\sigma}}} e^{-x^2} \mathrm{d}x \right) \tag{2.8}$$

The pre-factors of those distributions are scaled with group specific neutron or X-ray scattering length densities. Single lipids were parsed according to previous reports on POPE [54] and POPG [55] into CH_3, CH_2, CH, carbonyl-glycerol CG, PO_4, ethanolamine ENX and glycerol PG2 groups. A schematic of the lipid parsing can be seen in Figure 2.2. To account for lipid mixtures similar to Belička [56] a hybrid lipid was introduced which combined the individual groups of POPE and POPG by molecular averaging.

In detail, we merged the CH_3, CH_2, CH, carbonyl-glycerol CG and the PO_4 groups under the assumption that they align at the same transbilayer position. This is reasonable since both lipids are chemically identical except for ethanolamine and gylcerol. That left the ENX and PG2 as two independent groups. Figure 2.3 shows in panel A the lipid membrane and the corresponding volume probability distributions.

By assuming spatial conservation in the hydrocarbon core ($P_{plat}(z <= z_{HC}) = 1$) we obtained the volume probability distribution of the methylene group P_{CH_2} by subtraction of the methyl and methin group from the

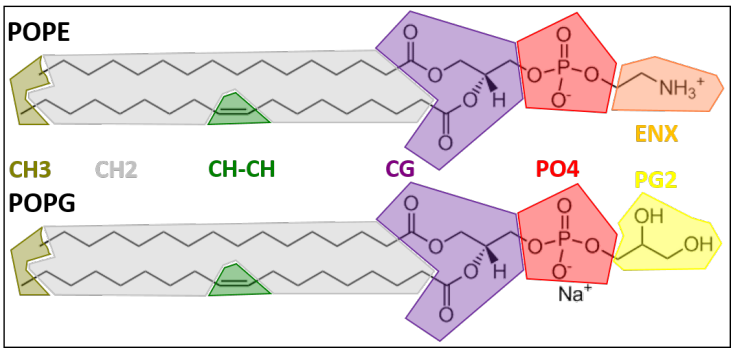

Figure 2.2.: The phospholipids POPE and POPG were parsed into six quasimolecular fragments. Due to their chemical similarities both have the CH_3, CH_2, CH, CG and the PO_4 group in common, while they differ in the last group, namely ENX and $PG2$.

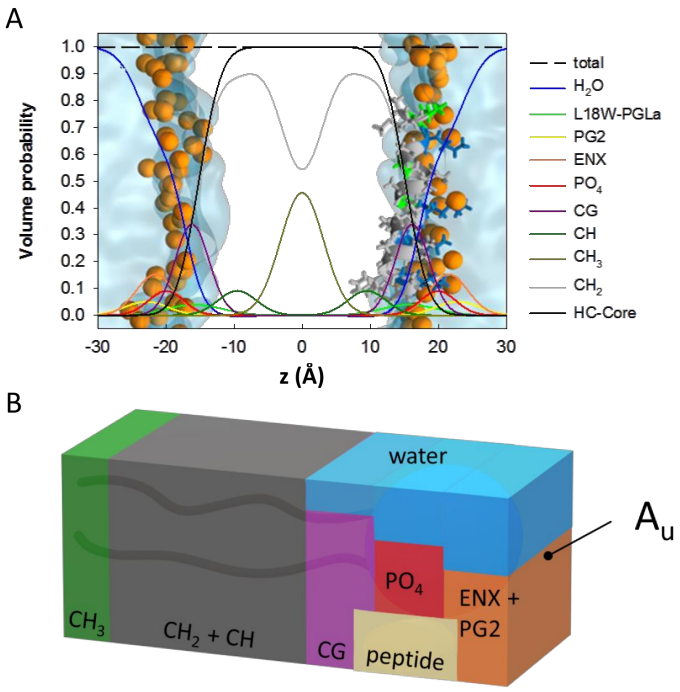

Figure 2.3.: Schematic of the applied SDP model. Top panel (A) shows the spatial distribution functions of the quasi molecular fragments which were overlayed with an MD simulation of a membrane. Orange spheres correspond to phosphor atoms. Panel (B) shows the employed unit cell/hybrid particle for data fitting together with its cross-section A_U.

hydrocarbon core function.

$$P_{CH_2}(z) = P_{plat}(z) - 2P_{CH_3} - 2P_{CH}(z) \tag{2.9}$$

Further, we acquired values of the water distribution function P_W by applying the requirement of ideal volume filling and defining water as the final group. It can be retrieved as

$$P_W(z) = 1 - \sum_{i}^{allgroups} P_i(z). \tag{2.10}$$

The current model is valid for pure lipid mixtures. Since we intend to study peptides interacting with membranes we included an analytical term for the scattering contribution of magainins. Previous NMR measurements of PGLa and MG2a in membranes composed of POPE/POPG at a molecular ratio of 3:1 showed that both peptides individually or applied together always stay in a surface aligned topology at any investigated peptide concentration [18, 19]. Therefore we were able to describe the peptide scattering with one additional Gaussian term. The volume of the new unit cell is defined as

$$V_{\mathrm{LP}} = \frac{n_{\mathrm{POPE}}}{n_{\mathrm{POPE}} + n_{\mathrm{POPG}}} V_{\mathrm{POPE}} + \frac{n_{\mathrm{POPG}}}{n_{\mathrm{POPE}} + n_{\mathrm{POPG}}} V_{\mathrm{POPG}} + \frac{n_{\mathrm{P}}}{n_{\mathrm{POPE}} + n_{\mathrm{POPG}}} V_{\mathrm{P}} + n_w V_{\mathrm{W}} \tag{2.11}$$

where V_{LP} is the volume of the unit cell, V_{X} is either the volume of a peptide, the individual lipids or water (x =POPE, POPG, P or W) and n_x stands for the total numbers of POPE, POPG and peptide in the sample or in the case of n_W for the total number of water molecules in the unit cell. The mathematical expressions in front of the volume terms are molecular weighting factors (e.g. $\frac{n_{\mathrm{POPE}}}{n_{\mathrm{POPE}}+n_{\mathrm{POPG}}}$). They are used during the creation of the hybrid lipid and later also for proper weighting of the peptides scattering contribution. Meaning that every volume V_i inserted in the equations used to evaluate the intensity (2.12, 2.16, 2.13, 2.14 and 2.15) was multiplied with the corresponding weighting factor. A schematic of the parsing for the unit cell can be seen in Figure 2.3 panel B.

The final scattering length density profile of the bilayer including the peptide in surface state conformation can be retrieved as

$$\Delta\rho(z) = \sum_{i}^{groups} (\rho_i - \rho_{Solvent}) P_n(z). \tag{2.12}$$

Since data fitting of the recorded intensity is performed in reciprocal space the model needs to be Fourier transformed. This led to eq. 2.13 for Gaussians F_i^g, equation 2.14 for error functions F_i^{erf} and to eq. 2.15 for the hydrocarbon core function F_{ij}^{plat}. Note that only the real parts of the Fourier transformations are used. The imaginary part (sinus) adds precisely to zero for symmetrical membranes.

$$F_i^g = \frac{V_i}{A} e^{-0.5q^2\sigma_i^2} \cos(z_i q) \tag{2.13}$$

$$F_i^{erf} = \frac{\sin(z_i q)}{q} e^{-0.5q^2\sigma^2} \tag{2.14}$$

$$F_{ij}^{plat} = (F_j^{erf}(q, z_j, \sigma_j) - F_i^{erf}(q, z_i, \sigma_i)) \tag{2.15}$$

The scattering amplitude of a flat membrane is then given by

$$\begin{aligned} F_M(q) \;=\; & 2\Delta\rho_{CH_2}(z) F^{erf}(q, z_{CH_2}, \sigma_{CH_2}) \\ & +2 \sum_{k}^{CH_3,CH,CG,PO_4,ENX,PG2} F_k^g(V_k, z_k, \sigma_k) \\ & -2\Delta\rho_{CH_2} F_{CH_3}^g(V_{CH_3}, z_{CH_3}, \sigma_{CH}) \\ & -2\Delta\rho_{CH_2} F_{CH}^g(V_{CH}, z_{CH}, \sigma_{CH}) \\ & +2\Delta\rho_{Pep} F_{Pep}^g(V_{Pep}, z_{Pep}, \sigma_{Pep}). \end{aligned} \tag{2.16}$$

To retrieve structural information at highest fidelity SAXS/SANS data were fitted simultaneously with a combined cost function

$$\chi^2 = \sum_{i,j} \left(\frac{I_i^j - I_{fit_i}^j}{w_i^j \sigma_i^j} \right)^2 \tag{2.17}$$

where I_i^j is the recorded intensity I_i of contrast j and the calculated intensity from fitting parameters is given by $I_{fit_i}^j$. σ_i^j are the experimental errors and w_i^j are weighting parameters accounting for the difference in data points between SAXS and SANS and they are also used to highlight specific regions in q space. In general SANS data is affected by instrumental smearing and the wavelength spread. To evaluate neutron data properly a Gaussian-type resolution function $G_{smear}(q, \sigma)$ was introduced. The theoretically calculated intensity $I_{fit_i}^j$ was smeared by performing a convolution with equation 2.18. Each (q,I) tuple was corrected with the provided σ from the beamline. For X-ray data no correction had to be performed. Data was convoluted over larger q ranges as used during the fitting procedure to avoid boundary effects.

$$I_i^j(q) = \int_{-\inf}^{\inf} I_{fit_i}^j(k) G_{smear}(q - k, \sigma_i^j) \mathrm{d}k \tag{2.18}$$

In general data fitting of model functions with many adjustable parameters is a highly delicate task often leading to an entrapment of the cost function in a local minimum. To counteract this issue we implemented four measures. First, based on the lipids geometry the number of adjustable parameters was reduced by connecting the CG group with the hydrocarbon core ($z_{CG} = D_C + 1$ [56]) and by a fixation of the intra headgroup distances between the ENX/PG2 with respect to the phosphate group to 1.57 Å and 2.92 Å respectively. Those values where obtained after molecular averaging from literature data [54, 55]. Second, a genetic algorithm was chosen as fitting routine. It excels at minimizing nonlinear cost functions with many fitting parameters and offers a high possibility to escape a local minimum. Third, to gather statistical information on the retrieved structural parameters every data set was fitted 400 times with random starting parameters. In any case

a normal distribution for each fitting parameter was observed encouraging a description of scattering in terms of averaged parameters with standard deviations for each of them. Additionally, Matlab code to explore possible correlations between parameters visually and quantitatively was developed. Last but not least energetic penalties for the cost function were introduced and various quadratic terms were tested and are listed below. Occasionally an overfilling of the unit cell at high peptide concentrations at certain transmembrane positions occurred. This effect was observed in negative values for the water probability function. We counteracted it with a quadratic penalty based on the amount of negative transmembrane positions (eq. 2.19).

$$w_{pw} = \left(\sum^{P_w(z)<0} P_w(z) \right)^2 \tag{2.19}$$

To help localize the peptides transmembrane position without sufficient sample contrasts (i.e. for SAXS data only) a second penalty was introduced. It located the peptides within ± 2.5 Å of the carbonyl glycerol group. Next, at rare events (2-5 times in 400 fits) a width of a Gaussian or even rarer a z position of a lipid group assumed non physical values. Those trends were stopped by penalizing deviations of $\sigma > 25\%$ and transmembrane position $\Delta z > 15\%$ per iteration via equation 2.20 and 2.21. Further, based on the maximal physical achievable distance between the carbonyl-glycerol and the phosphate group connectivity was assured by equation 2.23 which adds a small penalty upon separations above 4.5 Å. Last but not least the area per unit cell was penalized by eq. 2.24 if it changed more than 10% per iteration.

No penalties were needed for the joint simultaneous analysis of X-ray and neutron contrasts.

$$w_{\sigma} = \left(\sum^{\frac{\sigma_f}{\sigma_0}<0.75|>1.25} \left| \frac{\sigma_f(\sigma_l) - \sigma_0(\sigma_l)}{\sigma_0(\sigma_l)} \right| \right)^2 \tag{2.20}$$

$$w_z = \left(\sum^{\frac{z_f}{z_0}<0.85|>1.15} \left| \frac{z_f(z_l) - z_0(z_l)}{z_0(z_l)} \right| \right)^2 \tag{2.21}$$

$$w_{Peptide} = \left(\frac{|\Delta(z_{GC} - z_{Peptide})| - 2.5}{2.5} \right)^2 \tag{2.22}$$

$$w_{GP} = \left(\frac{|\Delta(z_{GC} - z_{PO_4})| - 4.5}{4.5} \right)^2 \tag{2.23}$$

$$\begin{aligned} if \qquad & \frac{A_f}{A_0} < 0.9| > 1.1 \\ w_A = & \left(\frac{|A_f - A_0|}{A_0} \right)^2 \end{aligned} \tag{2.24}$$

The final residual for the optimization routine was calculated via

$$\begin{aligned} \chi^2 = & \chi^2(S_{P_W} \cdot w_{PW} + S_\sigma \cdot w_\sigma + S_z \cdot w_z + S_A \cdot w_A \\ & + S_{GP} \cdot w_{GP} + S_{peptide} \cdot w_{peptide}) \end{aligned} \tag{2.25}$$

where w_{XX} (XX = σ, z, Peptide, GP, A) are the weighted cost contributions depending on the strength of disturbance for penalty XX and S_{XX} are scaling factors which were tested carefully to ensure that only the minimal amount of penalty was added to ensure the escape from a local minimum and at the same time not to trap the cost function due to its energetic contribution.

Structural parameters like the hydrocarbon chain thickness D_C and the bilayer thickness D_B where calculated similar to Tristram-Nagle et al. [57].

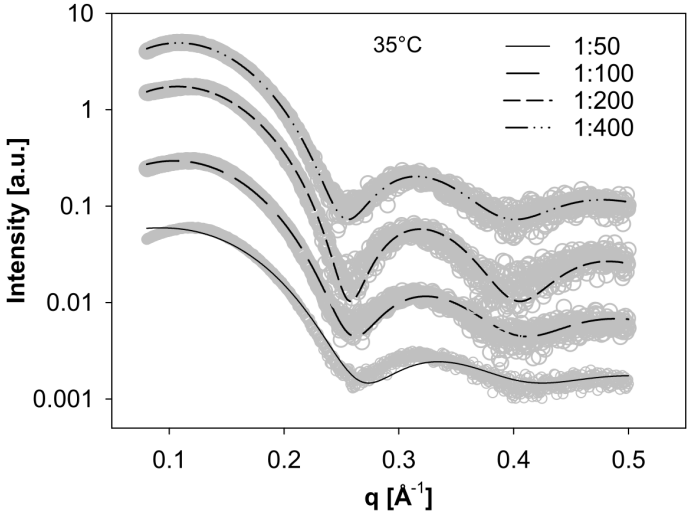

Figure 2.4.: X-ray data (circles) of 100 nm large unilamellar vesicles in the presence of MG2a at 35 °C at various molar ratios. Lines represent fits.

However, in this thesis the bilayer thickness contains a fraction of peptide volume.

$$D_C = \frac{V_{Chains}}{A} \tag{2.26}$$

$$D_B = \frac{2V_{LP}}{A} \tag{2.27}$$

Validation of the model for an X-ray standalone analysis
Figure 2.4 shows fits for POPE/POPG (3/1) in the presence of MG2a with molar P/L ratios of $1:50, 1:100, 1:200, 1:400$ at 35°C. This data set was taken from publication [45] for illustrative purposes only. The model shows excellent agreement at low and intermediate peptide concentrations. Slight offsets occur at $P/L = 1:50$ which in this case are dominated by contributions from the methyl and methylene groups as shown in the form factors in Figure 2.5. Advancement of the model towards asymmetry would improve those results.

Further a tool to compute histograms for any parameter of interest was coded. For example Figure 2.6 shows the obtained Gaussian distributions for

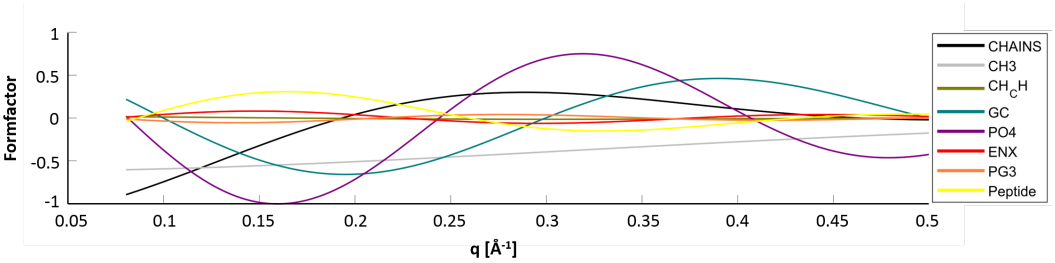

Figure 2.5.: Form factors of the individual groups for the unit cell as function of reciprocal vector q.

every fitted parameter of the POPE/POPG (3/1) system in the presence of MG2a at a P/L of 1:50. The Gaussian shape profile enables the description of scattering data in terms of averaged parameters and increases the statistical relevance of the retrieved results significantly. Also note that z_{PO_4}, z_{ENX} and z_{PG2} behave identical. This might cast doubt on the model at first but is reconciled with the fixation of the intra headgroup distances. To eludicate parameter dependencies 2D correlation maps between parameter pairs of interest were calculated. E.g. the 2D correlation map between the area per unit cell and the peptide position for dummy data is illustrated in Figure 2.7. It shows a negative linear dependency of the peptides transbilayer position with the area per unit cell. Consequently both parameters are not independent and this correlation could be used to simplify the model. No such simplifications were done in this work.

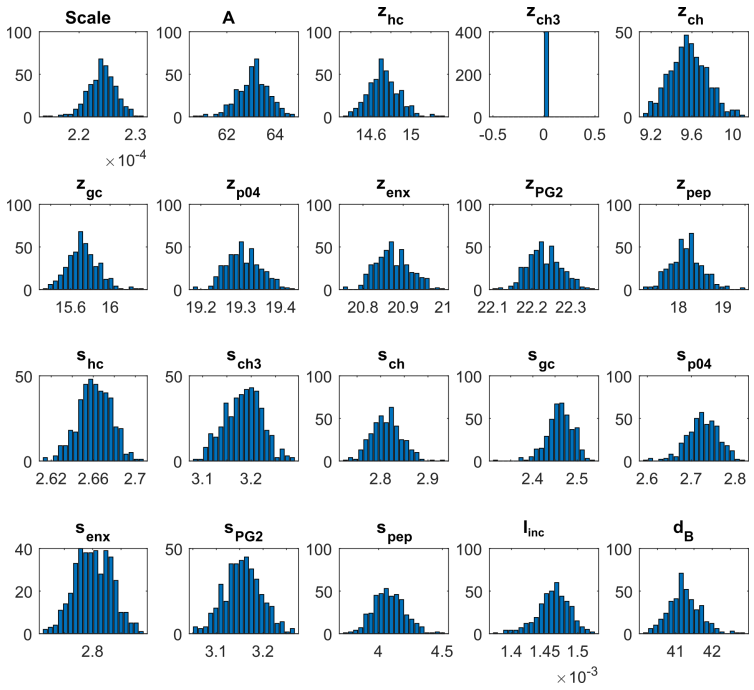

Figure 2.6.: Histogram of the retrieved parameters from a global statistical analysis.

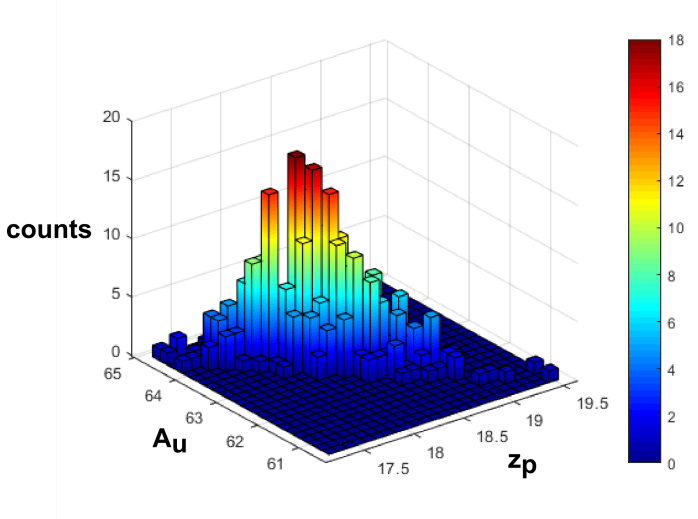

Figure 2.7.: Example of a correlation map for the area per unit cell A_u and the transbilayer position of the peptide z_p.

2.3.2. Interpretation of SANS Data for Zero Contrast Experiments

The intensity in a scattering experiment as described above is proportional to the observed contrast $\Delta\rho$ divided by q^2

$$I(q) \propto \frac{\Delta\rho}{q^2} = \frac{\sum_i (\rho_W - \rho_i)}{q^2}. \tag{2.28}$$

This means that any slight contrast mismatch will become dominant in the low q regime. In the case of neutrons the electrons density ρ has to be exchanged with the corresponding neutron scattering length density (NSLD), which for a certain molecule is defined as:

$$\rho = \frac{\sum_i bi}{V_m}. \tag{2.29}$$

The coherent neutron scattering factor of atom i is given by b_i and V_m represents the volume of the whole molecule. To identify the zero contrast condition of the present lipid mixture, deuteration degree depended theoretical calculations of the scattering from lipids using a 2 slab model were performed (HC-core and headgroup, ρ_i). The evaluation of this data is straight forward. Due to the presence of incoherent scattering zero signal will never be observed in experiments. Correspondingly a completely flat signal which increases in intensity at low q equals zero contrast scattering. If any peak arises at a certain q value in the plateau regime then zero contrast is broken and something is happening for realspace distances $d = \frac{2\pi}{q}$.

2.3.3. Model-free Analysis of MLV and H_{II} SAXS Data

To obtain real space information on any system from scattering electron density maps can be created. This was done via Fourier synthesis for data with Bragg peaks.

To do so, first the present lipid mesophase and its unit cell parameters had to be determined. Next the diffraction peaks were fitted with Lorentzian peak shape functions in combination with a linear background. To obtain

the form factors F_{hkl} the retrieved intensities I_{hkl} were Lorentz and peak multiplicity corrected. In diffraction experiments information about the phase α_{hkl} is lost but for simple geometries as discussed below it can be obtained by trial and error. The final electron density for a centrosymmetric system is given by [58–60]

$$\rho(\mathbf{r}) = \sum_{hkl}^{max} \alpha_{hkl} |F_{hkl}| \cos(\mathbf{q_{hkl}} \mathbf{r}) \tag{2.30}$$

where the phase α_{hkl} is restricted to ± 1. The reciprocal lattice vector is denoted as $\mathbf{q_{hkl}}$, hkl are the Miller indices and $\mathbf{r}$ corresponds to the real space vector.

For **lamellar systems** $\rho(\mathbf{r})$ was calculated by insertion of the lamellar lattice relationship $d_h = 2\pi/q_h$ into equation 2.30. Note that $\frac{F_h}{F_1}$ was used instead of F_h. The final electron density is then given by

$$\rho^*(z) = \sum_{h=1}^{h_{max}} \alpha_h \frac{F_h}{F_1} \cos\left(\frac{2\pi h z}{d}\right) \tag{2.31}$$

where F_h is the form factor of the h' reflection and α_h is the phase with values of [-1,-1,1,-1] for the four observed diffraction peaks. d denotes to the lamellar repeat distance. Electron density maps for **nonlamellar inverse hexagonal phases** were calculated according to Kollmitzer [49]. The final electron densities were derived in a similar way, as described above. The main goal was the extraction of intrinsic lipid curvature values for arbitrary lipids. In brief, J_0 was determined with its relation to the neutral plane R_0 by using $J_0 = -\frac{1}{R_0}$. R_0 itself was obtained from the phosphate position +0.44 Å ($R_0 = z_{PO_4} + 0.44$ Å) [20, 49].

The intrinsic curvature for non H_{II} forming lipids was retrieved under the assumption of linear additivity and the use of a host (DOPE) guest (lipid of interest) sample system via

$$J_0 = \frac{J_0^{mix} - (1-\chi) J_0^{DOPE}}{\chi}, \tag{2.32}$$

where J_0 serves as an estimate for the intrinsic curvature of the guest lipid and χ denotes to its molar fraction in the sample. Sometimes form factors F_{hkl} were corrected by manual fitting with a separate script followed by the routine developed by Kollmitzer.

For **cubic lipid mesophases** only structure and lattice parameter determinations were done with

$$\mathbf{q_{hkl}} = 2\pi \frac{\sqrt{h^2 + k^2 + l^2}}{a}, \tag{2.33}$$

where h, k, l are the Miller indices and a is the lattice parameter. Tables for the Miller indices were taken from [58] and tested against diffraction peak positions present in the scattering patterns. Lattice parameters were retrieved by indexation plots (f(hkl) vs $\mathbf{q_{hkl}}$) and subsequent fitting with a straight line where the slope is given by $\frac{2\pi}{a}$.

3. Results and Discussion

This chapter summarizes and discusses the core results from the attached publications and includes extended parts on the intrinsic lipid curvature section and the analysis of scattering data at low peptide concentrations. For more detail please see the attached manuscripts [4, 17, 45].

3.1. Intrinsic Lipid Curvature

All samples for intrinsic lipid curvature determination were measured using the SAXSpace System (Anton Paar, Austria). It is equipped with a Pilatus 100K-S detector (Dectris, Swiss), covering a q-range in the small angle configuration (SDD position 308mm) from $0.6nm^{-1}$ up to $10.9nm^{-1}$. Cu-Kα (1.54 Å) radiation was supplied by a Genix 3D microfocus tube (Xenocs, France). The sample temperature was controlled by the TC Stage 150. All samples were transferred into a paste cell holder (Anton Paar, Austria) and equilibrated for 10 minutes at each temperature before an exposure of 1 hour. Image integration was performed with the Software SAXStreat (Anton Paar, Austria).

To estimate the curvature stress in relevant lipid compositions we had to determine J_0 of the individual components first. Spontaneous curvatures of H_{II} forming lipids like POPE and DOPE could be determined directly. For non H_{II} formers a host guest lipid matrix with DOPE as template for the formation of the inverse hexagonal phase was used. Lipids were mixed at various molar ratios and values for the spontaneous curvature were extracted under the assumption of ideal mixing and linear additivity. We performed a systematic variation of chain length and hydrocarbon saturation (12:0 to 18:1) for PE lipids. Not surprisingly all PE lipids exhibited

significant negative intrinsic curvature at 35°C. J_0 decreased from $-0.22 \pm 0.02\,\mathrm{nm}^{-1}$ at a chain length of 12:0 to $-0.38 \pm 0.19\,\mathrm{nm}^{-1}$ for 16:0. The highest negative spontaneous curvature was observed for the twofold unsaturated hydrocarbon chains containing DOPE $-0.44\,\mathrm{nm}^{-1}$. In addition, we were able to show that J_0 of lyso-PE is strongly positive with $0.18 \pm 0.12\,\mathrm{nm}^{-1}$. Next we exchanged the headgroups from PE to PG for DO (18:1), PO (16:0/18:1) and DP (16:0) tails. Here we observed that J_0 changed to approximately zero for POPG and DOPG. The exchange of PE with PG headgroups showed the expected trend, since the PG headgroup is significantly larger. Further by exchanging NaPi with H_2O for POPE and POPG (Table 3.1 bottom 2 lines) a slight decrease in J_0 was observed. This suggested that the presence of ions in the NaPi buffer led to a more upwards orientation of the PE headgroup. All values mentioned before together with the temperature at which the analysis was performed, their error and the present buffer system are collected in Table 3.1.

Table 3.1.: Intrinsic/spontaneous curvature J_0 of relevant lipids for this thesis.

Lipids	Temperature [°C]	J_0 [nm^{-1}]	error [nm^{-1}]	Buffer
DLPE	35	-0.22	0.02	NaPi
DMPE	60	-0.32	0.03	NaPi
DPPE	35	-0.38	0.19	NaPi
POPE	35	-0.35	-	NaPi
DOPE	35	-0.44	-	NaPi
POPG	35	-0.02	0.03	NaPi
DOPG	35	0.025	0.06	NaPi
lyso-PE	35	0.18	0.12	NaPi
POPE	35	-0.33	-	H_2O
DOPE	37	-0.4	-	$H_2O^{\dagger}$

† Value taken from [49].

3.2. First Results Towards Synergism and a Proper First Order Lipid only Mimic for *E. Coli*

In a next step we performed a systematic study of the permeabilizing efficiencies (leakage experiments) of MG2a, L18W-PGLa and their equimolar mixture against mammalian and bacterial membrane mimics as function of charge and stored intrinsic curvature stress by a methodical variation of the lipid composition. As described in section 1.1 POPE/POPG 3/1 was chosen as prime mimic for the cytoplasmatic membrane of Gram-negative bacteria. Additionally, we interrogated POPC/POPG as frequently employed alternative mimic [19, 61]. Both model systems hold an equal amount of negatively charged lipids but differ strongly in the polar/apolar interface tightness. POPE/POPG exhibits with $J_0^{mix} = -0.258\ \mathrm{nm}^{-1}$ a strong negative intrinsic lipid curvature whereas POPC/POPG has approximately zero spontaneous lipid curvature. To elucidate the influence of lipid shape (intrinsic/spontaneous curvature) in more detail a third mimic composed of lyso-PE/POPE/POPG (1.6:1.4:1, molar ratios) with the same amount of charge and J_0 but now identical lipid headgroups was employed. Further POPC and POPC/Chol (3:1) were used as a simple first order mammalian mimic. Note that both systems contain no charge and exhibit close to zero intrinsic lipid curvature. A summary of all employed systems together with the corresponding J_0^{mix} values is given in Table 3.2.

We found that in order to observe synergism the target system has to feature a sufficiently dense packed polar/apolar interface, while for a high peptide retention time on the lipid membrane negatively charged lipids are required. All monomers, L18W-PGLa, MG2a and their equimolar mixture induced strong leakage in POPC/POPG and lyso-PE/POPE/POPG (Figure 3.1 panel A and C). Both systems have negligible J_0^{Mix}. This allowed the peptides to penetrate and disrupt the membrane easily. Leakage induced by the equimolar mixture was roughly the same as single L18W-PGLa application. These observations clearly show that no synergistic action occurs in POPC/POPG and lyso-PE/POPE/POPG. Switching to POPE/POPG with its densely packed polar/apolar interface we found weak leakage <10% at all investigated lipid/peptide ratios for both peptides individually (Figure

3.1 panel B). Interestingly, L18W-PGLa, MG2a and their equimolar mixture behaved identical until 0.2 μM peptide concentration. At 0.2 μM the observed dye release from the equimolar mixture started to level off until it reached an approximately five times higher leakage at 1 μM concentration compared to individual application. Thus providing strong evidence that lipid curvature is a key parameter in the development of synergistic activity. Next by interrogation of dye release from POPC and POPC/Chol model systems (Figure 3.1 panel D and E) the effect of charge on the peptides activity was studied. In any case low leakage was observed. This is directly related to the lack of electrostatic attraction from the membrane towards the cationic peptides. The difference in detected fluorescence between POPC and POPC/Chol originates in their individual values of J_0^{mix}. POPC exhibits roughly zero intrinsic lipid curvature whereas POPC/Chol has a considerably denser packed interface. The already low dye-release observed in POPC decreased further towards 2% in POPC/Chol. To correlate our results with bacteria the peptides antimicrobial activity of monomers and dimers were tested against live *E. coli* and compared with respect to our leakage data. Notably, the POPE/POPG mimic captured many of the observed experimental features and therefore strengthened its position as a proper mimic for synergistic studies. Our findings led to the suggestion of an activation barrier and to a preliminary hypothesis that for L18W-PGLa and MG2a synergism L18W-PGLa acts as the helper "molecule", preconditioning the membrane and assisting the more disruptive MG2a. A schematic of the proposed mechanism is shown in Figure 3.2. Further we emphasized the proper choice of lipids for bacterial mimics and identified that charge and interface packing are key parameters for the development of synergistic activity. More details can be seen in the attached publication [17].

Table 3.2.: Intrinsic curvature J_0^{mix} for various membrane mimetics and corresponding peptide synergy parameter $\sum$ ($\sum < 0.5$ synergistic activity).

Mimic	J_0^{mix} $[nm^{-1}]$	$\sum$
POPE/POPG(3:1)	-0.258 ± 0.013	0.4 ± 0.1
POPC/POPG(3:1)	-0.012 ± 0.015	0.8 ± 0.2
Lyso-PE/POPE/POPG (1.6:1.4:1)	-0.044 ± 0.059	1.3 ± 0.3
POPC	-0.022 ± 0.010	2.2 ± 0.4
POPC/Chol (3:1)	-0.14 ± 0.011	1.2 ± 0.3

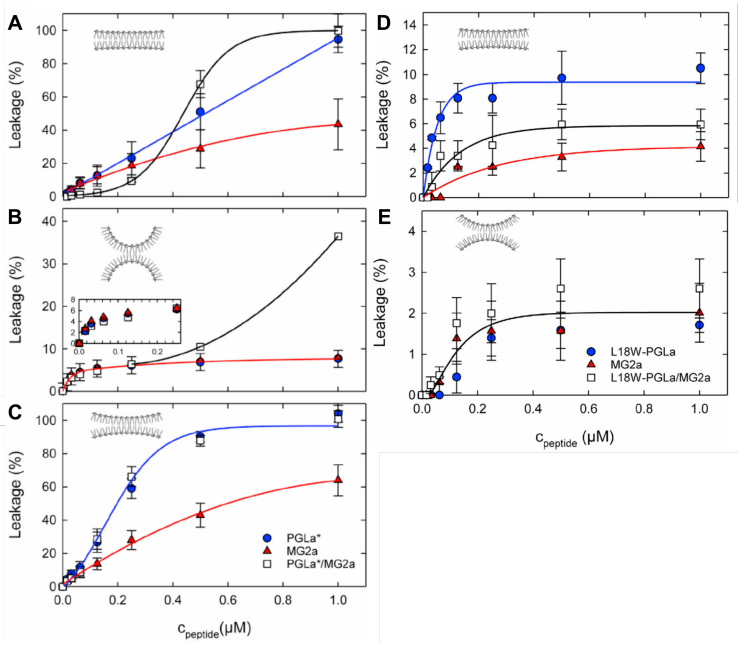

Figure 3.1.: Leakage of POPC/POPG (3:1 mol/mol, A), POPE/POPG (3:1 mol/mol, B), lyso-PE/POPE/POPG (1.6:1.4:1 mol/mol, C), POPC (D) and POPC/Chol (3:1 mol/mol, E) LUVs (50 μM). Solid lines represent guides to the eye and insets show corresponding monolayer curvatures.

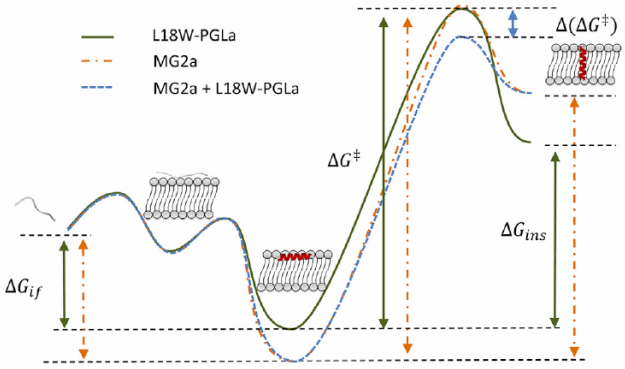

Figure 3.2.: Schematic of the energy landscape with various states during peptide insertion into a lipid bilayer. Adsorption and peptide folding at the membrane surface ΔG_{if}, insertion into the hydrophobic core ΔG_{ins}, activation barrier $\Delta G\ddagger$. Synergistic action decreases $\Delta(\Delta G\ddagger)$.

3.3. The Lipid Membranes Structural Response towards an AMP Attack

The remarkable correlation between dye release experiments and antimicrobial assays for POPE/POPG mimics and *E. coli* reported in [17] motivated us to perform a comprehensive study using a combination of experimental (we) and computational tools (Robert Vácha group, ceitec BRNO) to reveal the effects of L18W-PGLa and MG2a on free floating fully hydrated unilamellar vesicles (100 nm) from nanoscopic to macroscopic length scales. In experiments, attacks by peptides were always simulated by external addition of appropriate amounts of peptide stock solution to LUVs.

3.3.1. Low Peptide Concentration - Before Synergistic Conditions

We analyzed the membranes structural response to an attack by magainins at low peptide concentrations (P/L $\leqslant$ 1:200) via elastic X-ray and neutron scattering. The recorded 1D-patterns were of diffusive nature and required a model based analysis. For this purpose a statistical global joint analysis of X-ray and neutron data was custom tailored, including an explicit term for the scattering contributions originating from peptides (section 2.3.1 or publication [45]).

Joint examinations of four different contrasts per sample showed that all peptides at $P/L = 1:200$ individually or applied as mixture induced significant hydrocarbon core (HC) thinning (Table 3.3). Figure 3.3 illustrates this effect for one leaflet. The thinning can be easily seen by a shift in z position of the curves. Slopes (σ_s) varried only marginally. It was weakest for L18W-PGLa, followed by MG2a and the equimolar mixture L18W-PGLa/MG2a. To gain further insights we correlated the thinning induced by the peptides with their transbilayer positions. Analysis showed that L18W-PGLa inserted deepest in the membrane whereas MG2a was located more towards the aqueos phase. Note that both of these observations match perfectly with the peptides hydrophobic sections (see Figure 1.6). Figure 3.4 displays a histogram of the peptides position and the area per unit cell (which is

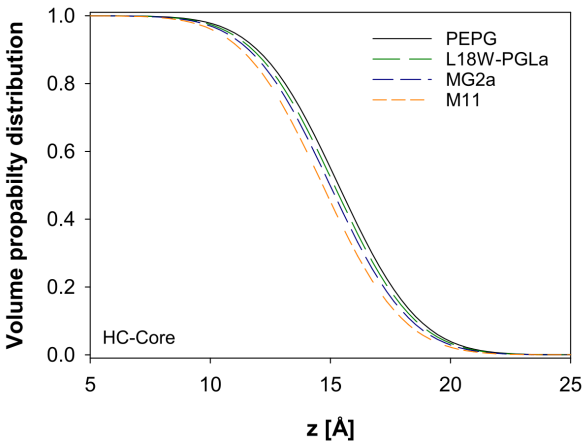

Figure 3.3.: Volume probability distribution of the hydrocarbon core (HC-core) function of POPE/POPG(3/1, mol/mol) at 35°C in the presence of L18W-PGLa, MG2a and the equimolar mixture M11 with a peptide/lipid ratio of 1:200.

directly related to the HC-core thickness) over 400 independent fits and their corresponding correlograms. z_p and A_u exhibit weak correlations, most pronounced for the equimolar mixture. Interpreting a physical effect in the observed correlations is beyond the resolution of the model but it still should be mentioned that it shows a clear difference between combined and individual magainin application for the retained fit parameters. According to the molecular shape model from Lohner and Bechinger [62] both peptides create a "void" under them. This gap has to be filled with lipid hydrocarbon chains. Since MG2a is the larger peptide and was located further towards the aqueous phase the resulting HC thinning was more pronounced. Interestingly the equimolar mixture was located between L18W-PGLa and MG2a in terms of position but resulted in the strongest overall HC thinning. This indicated that there has to be an additional interaction when both peptide species are present. The HC thinning, redistribution of hydrocarbon chains, as well as the peptides positioning was verified by MD simulations [45]. Our cooperation partners also tested the influence of peptide dimerization (homo and hetero) on the positioning within the bilayer. The general result was that any dimer positioned further towards the aqueous phase with the MG2a homodimer furthest outward, followed

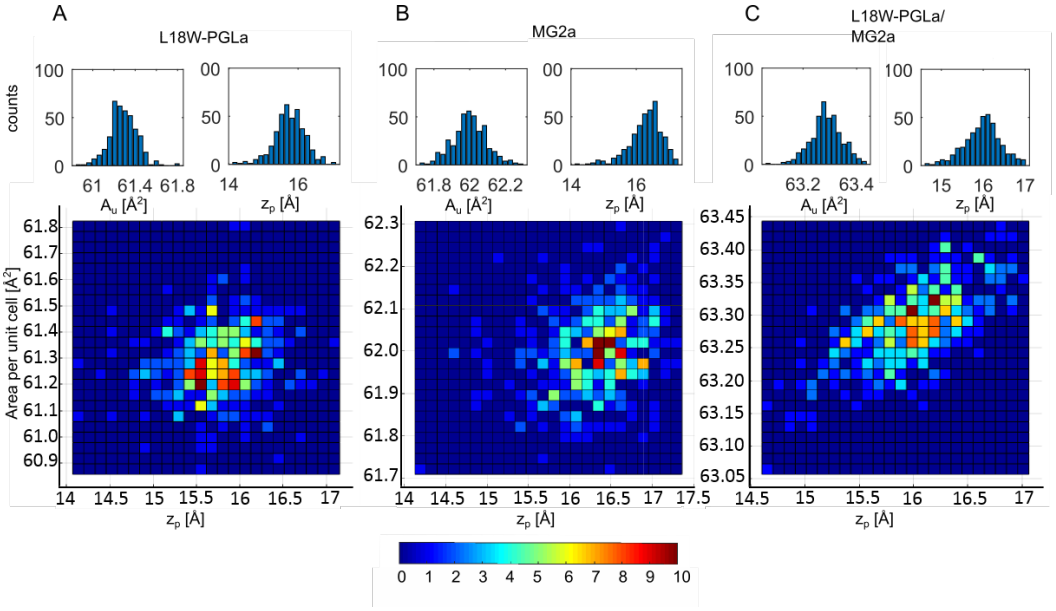

Figure 3.4.: Panel (A), (B) and (C) show histograms for the area per unit cell and the peptide's transbilayer position for L18W-PGLa, MG2a and the equimolar mixture at 35°C and $P/L = 1:200$ from 400 independent fits. Corresponding correlation maps are shown below. The color coding represents the amount of counted pairs.

by the L18W-PGLA/MG2a heterodimer and the L18W-PGLa homodimer. Further, they were able to show that the heterodimer created the strongest HC-core perturbation which is consistent with the results obtained from fitting. In a next step the peptides tendency to spontaneously form dimers was addressed, with the outcome that parallel heterodimers are more likely to be encountered especially at higher peptide concentrations. Combining all observations led to the new hypothesis that synergism, which occurs at higher peptide concentrations, could potentially originate in the early on-set of heterodimer formation. For more details see paper [45].

Last but not least the peptides influence on the lipid bilayers hydration was examined by a detailed interrogation of the water probability difference function. Since each membrane had different dimensions, the transmembrane direction was normalized by the phosphate position for all water probability functions before computation of $\Delta P_W = P_W^{Peptide} - P_W^{Membrane}$. Probability values themselves were left untouched and integrals thereof are

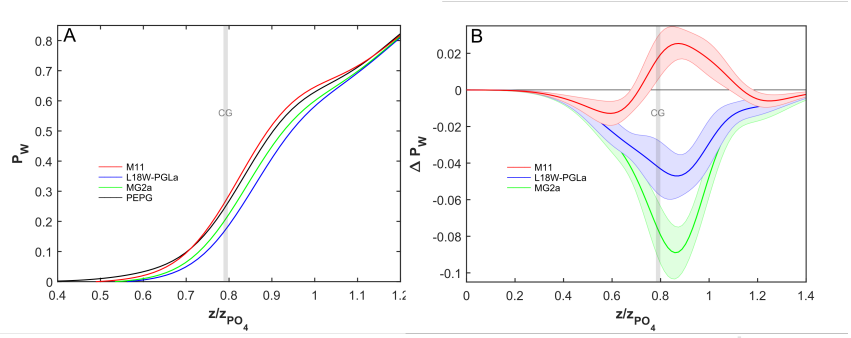

Figure 3.5.: Water probability distribution (A) and difference (B) function with and without magainins across one leaflet.

directly related to the amount of present water molecules. Figure 3.5 panel A shows a closeup of the water probability distributions for POPE/POPG in the absence and presence of L18W-PGLa, MG2a and their equimolar mixture. P_W of L18W-PGLa and MG2a was always below P_W of the pure membrane, showing that there was less water present at any transmembrane position for the individual magainins. L18W-PGLa/MG2a crossed P_W of the reference at 0.7 and 1.1, thus exhibiting regions where more water was present and regions where it dehydrated the membrane (water redistribution). Integration from the bilayer center (CH_3 position) towards the furthest outward positioned lipid group + twice its sigma led to 20.5, 19.1, 19.7, and 21 water molecules (n_W) per unit cell of the membrane in the absence and in the presence of L18W-PGLa, MG2a and the equimolar mixture respectively. The retrieved values are in good qualitative agreement with [63]. A complete depth dependency including a close-up of the transition regime of the cumulative amount of present water molecules as a function of transmembrane position is given in figure 3.6 panel A and B. The total number of water molecules per slice with the volume $A_U \cdot dz$ at any leaflet position is displayed in Panel C.

To further clarify we computed the water probability difference functions (Figure 3.5 panel B) together with their integrals across one leaflet towards z/z_P values where only water was present. The integral of the equimolar mixture was of particular importance, since positive and negative areas could potentially cancel each other. We obtained zero for the reference,

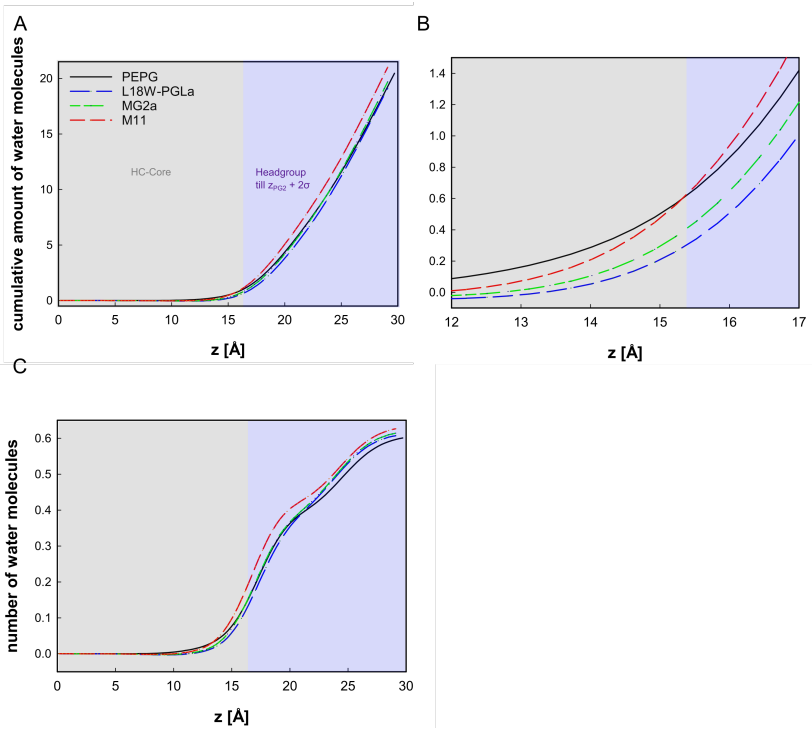

Figure 3.6.: Panel (A) shows the cumulative number of water molecules as a function of transmembrane position across one leaflet for POPE/POPG (3/1) in the absence (black) and presence of L18W-PGLa (blue), MG2a (green) and their equimolar mixture (red). A close-up of the transition regime is given in panel (B). The total amount of water molecules at any leaflet position (in any slice with the volume $A_U \cdot dz$) is displayed in panel (C). The grey area marks the hydrocarbon core of the lipid only membrane in the absence of peptides with its maximum at z_{CH_2} and the blue area extends from there towards the furthest outward lipid group + twice its standard deviation.

-0.0711 for L18W-PGLa, -0.0453 for MG2a and 0.0042 for M11. Therefore individual magainin application led to an overall dehydration of the membrane with a more pronounced effect for L18W-PGLa. The equimolar mixture induced a redistribution of water molecules and a slight increase of bilayer hydration. Those results should be viewed critically, since no other supporting data for that effect currently exists. A short summary of the most important structural results obtained from the SDP analysis in this chapter is given in Table 3.3.

Table 3.3.: Structural parameters of lipid membranes composed of POPE/POPG (3:1 mol/mol) with and without magainins.

Parameter	POPE/POPG	+ L18W-PGLa	+ MG2a	+ L18W-PGLa/MG2a
A_U [Å^2]	60.56±0.10	61.26±0.13	62.00±0.09	63.29±0.06
D_B [Å]	39.15±0.06	39.49±0.08	39.17±0.06	38.31±0.03
D_C [Å]	15.34±0.02 (15.10)[a]	15.16±0.03 (15.06)[a]	14.98±0.02 (15.01)[a]	14.68±0.01 (14.93)[a]
z_P [Å]		15.75±0.44	16.29±0.50	15.98±0.43
D_{HD} [Å]	4.19±0.05	4.07±0.06	3.80±0.06	4.45±0.04
n_W	20.5	19.1	19.7	21

[a] values in brackets are derived from all-atom MD simulations.

3.3.2. High Peptide Concentration - At Synergistic Conditions

Previous results suggested that the enhanced activity of L18W-PGLa/MG2a mixtures might be driven by an early formation of parallel peptide heterodimers [45]. To expand our current knowledge into the synergistic ($P/L \geqslant 1:50$) regime we investigated the thermotropic behavior as well as the structure and aggregate shape from nanoscopic to macroscopic length scales via DSC, SAXS, SANS and cryo-TEM experiments. Note that here we also used a chemically linked heterodimer of PGLa and MG2a. Its sequence is given in Figure 2.1 (material section) and will be referred to as hybrid.

First the peptides effect on the lipids chain melting behaviour (cooperativity and main transition temperature) was investigated. L18W-PGLa and MG2a caused a distinct splitting of the melting transition into multiple peaks,

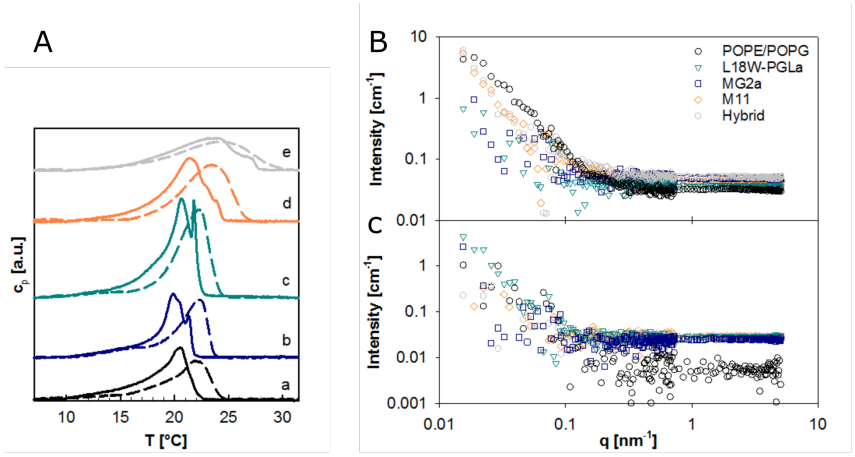

Figure 3.7.: Thermograms of large unilamellar vesicles (A) in the absence of peptides a and the presence of MG2a b, L18W-PGLa c, the equimolar mixture d and the hybrid e. Panel (B) shows zero contrast scattering for Matrix A and B at 35°C at $P/L = 1:50$.

which was most pronounced in cooling scans (Figure 3.7 panel A curves b and c). The equimolar mixture (M11) and the hybrid peptide also induced a splitting into multiple peaks but over a much larger temperature range (Figure 3.7 panel A curves d and e). Next to a hysteresis between heating and coolings scans a shift in main transition temperature and a loss of cooperativity was only observed for the peptide cocktail and the hybrid. Both effects were more pronounced for the latter. Those observations guided us to the hypothesis that cationic peptides induce lipid separation by forming regions enriched in peptide and anionic POPG and regions depleted of POPG which melt at different temperatures. To test this, zero contrast neutron scattering experiments on two differently deuterated versions of our *E. coli* lipid only mimic (Table 2.2 last two lines) at $P/L = 1:50$ and $1:25$ for each peptide application were carried out. Any sample was measured above and directly inside the lipid chain melting regime. Surprisingly no signal was observed in any case. Figure 3.7 panel B shows scattering data for both systems at 35°C. Accordingly the observed peak splitting in thermotropic experiments does not originate in lipid domains with different composition and had to be related to a non-homogenous distribution of AMPs on vesicles.

With lipid demixing ruled out as possible part of synergism we focused on structural aspects. Scattering from single peptide applications (L18W-

Table 3.4.: Structural parameters of peptide induced lamellar phases at P/L = 1:25 and 35°C.

POPE/POPG +	D [Å]	D_{HH}[Å]	D'_B[Å]	D_W[Å]
L18W-PGLa	52.1			
MG2a	53.3			
M11	50.3	37.6	43.4	6.9
Hybrid	50.3	37.6	43.4	6.9

PGLa and MG2a) at $P/L = 1:50$ showed purely diffusive signals whereas lamellar correlation peaks with similar repeat distance were observed for the equimolar mixture and the hybrid (Figure 3.8 panel A). Interestingly the latter showed a coexistence of a lamellar and a cubic Pn3m lattice. The appearance of a cubic phase suggests membrane fusion. An increase in peptide concentration to $P/L = 1:25$ led to lamellar phases also for the individual peptides (Figure 3.8 panel B). Additionally, there was a broad feature for M11 and the hybrid at low q-angles visible. The lamellar repeat spacing of any peptide application as function of temperature are shown in Figure 3.8 panel C. Structural paramaters like the lipid bilayers head-head distance D_{HH}, estimates of its steric D'_B and water layer D_W thickness for the equimolar mixture and the hybrid peptide were retrieved from corresponding scattering data (Table 3.4).

Water layers below ≈ 7 Å are undoubtedly proof of highly condensed lamellar systems with peptides possibly acting as spacers in between. Further, the temperature response of each system exhibited similar decreasing rates of the lamellar repeat distance until $45°C$. At $45°C$ the equimolar mixture started to deviate from its monotonic decreasing trend and increased until values of single MG2a application at 65°C were reached (Figure 3.8 panel C). All others followed the steady monotonic decrease.

The difference between the hybrid and M11 might be due to less translational degrees of freedom for the hybrid and most likely that M11 was present as a heterodimer, stabilized via salt bridges and hydrophobic interactions between the peptides which start to fail at $45°C$. Since the lamellar systems is strongly collapsed it is plausible that the more bulky furthest outward positioned MG2a led to the highest repeat distance. This is consistent with

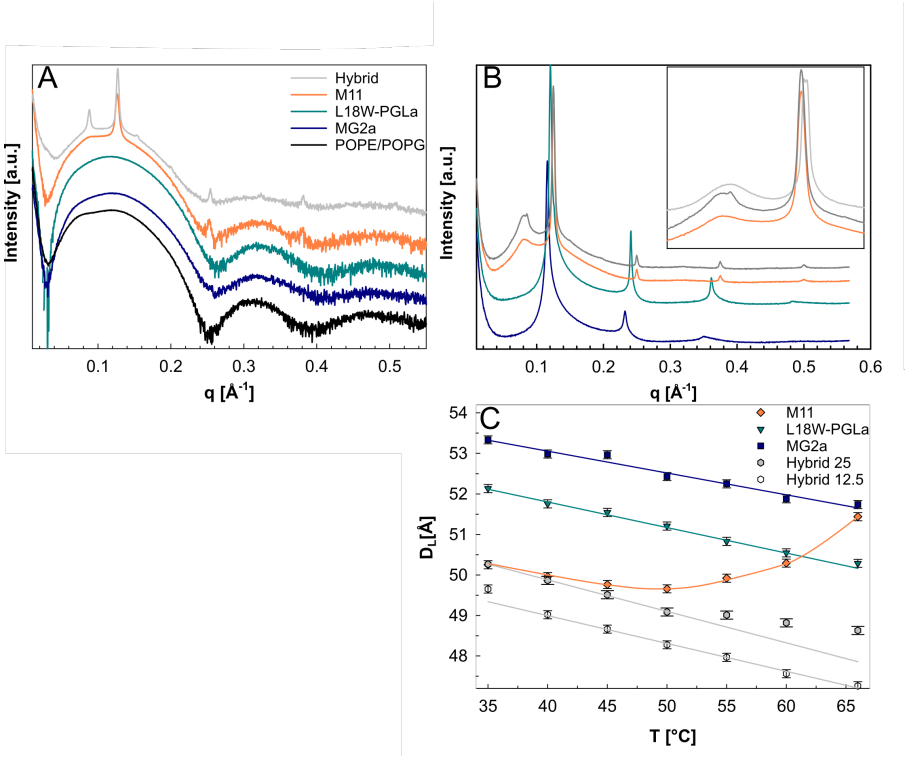

Figure 3.8.: Scattering patterns of 100 nm LUVs composed from POPE/POPG (3:1 mol/mol) in the presence and absence of magainins at P/L of 1:50 (A) and 1:25 (B) at 35°C. The inset in (B) is a zoom of the region around the broad peak at low q-angles and additionally displays the hybrid at a P/L of 1:12.5. Lamellar repeat distances as function of temperature induced in 100 nm LUVs upon exposure of magainins at P/L 1:25 and P/L 1:12.5 are shown in panel (C). Linear curves represent fits, solid orange line is a guide to the eye.

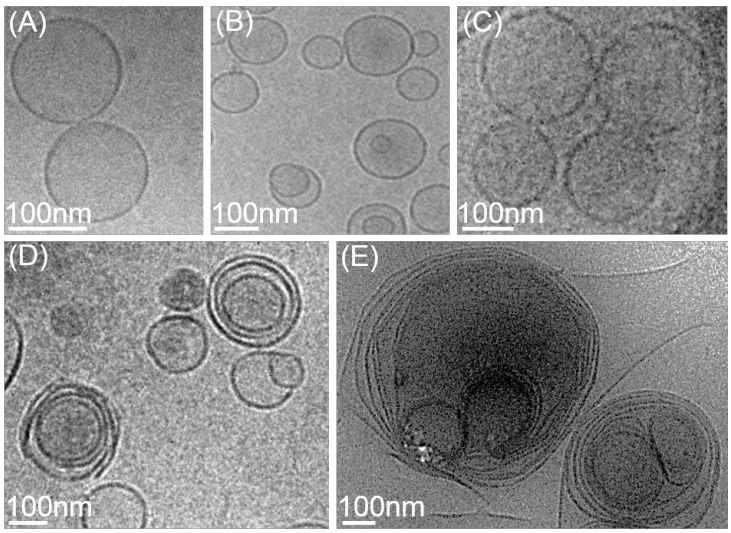

Figure 3.9.: Cryo-TEM images of 100 nm LUVs composed of POPE/POPG (3/1 mol/mol) in the absence (A) and presence of the peptides (P/L = 1:50) L18W-PGLa (B), MG2a (C), M11 (D) and the hybrid peptide (E) at 35°C.

earlier observations of peptide positioning at lower peptide concentrations [45].

At this point the microscopic structure was clear, however information on the aggregate shape was still lacking. Lamellar stacks or multilamellar vesicles both would result in identical scattering patterns for the investigated q-range. To explore the morphology at microscopic scale cryo-TEM experiments at $P/L = 1 : 50$ were carried out. Those measurements provided evidence that the equimolar mixture created morphologies different than single peptide applications and that the observed correlations in scattering patterns originated from multilamellar vesicles (Figure 3.9). Starting vesicles were perfectly spherical large unilamellar vesicles. Single peptide application increased vesicle size slightly and addition of the peptide cocktail led to the formation of multilamellar vesicles.

Additional cryo-TEM measurements showed a simultaneous presence of unilamellar vesicles with dense spherical aggregates (Figure 3.10 A, B) indicating vesicle adhesion, fusion and aggregation. Images of the hybrid peptide also showed dense particles D and a lattice of aggregates C.

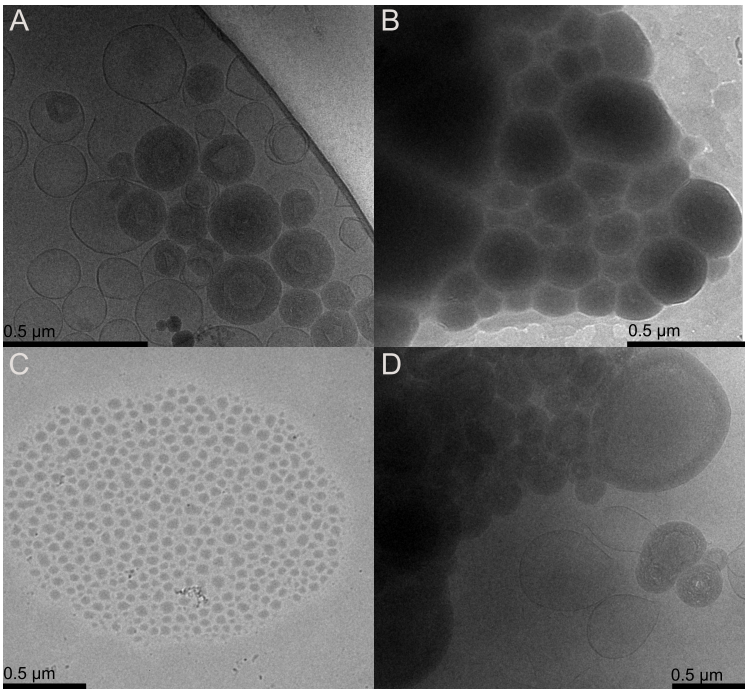

Figure 3.10.: Cryo-TEM images of 100 nm LUVs composed of POPE/POPG (3:1 mol/mol) upon addition of the equimolar mixture (A,B) and the hybrid (C,D) at a molar P/L of 1:50.

Complementary MD simulations showed in all atom production dynamic calculations as well as in Martini simulations membrane adhesion, fusion stalk and peptide fibril formation for the equimolar mixture. The mechanism of the stalk formation is displayed in Figure 3.12. For more detail please see publication [4]. Stalks have been previously shown to be precursors for membrane fusion [64–66] and cubic phase formation [67]. Indeed a cubic Pn3m phase was observed for the hybrid peptide during scattering experiments (figure 3.9 panel A).

Figure 3.11 shows the last simulation snap shots of coarse-grained Martini simulations after 20 µs. Based on X-ray diffraction results a stack of bilayers composed of POPE/POPG (3:1) with 50 Å repeat spacing was prepared (panel A). Addition of MG2a+L18W-PGLa at P/L 1:42 (panel B) and 1:21 (panel C) both consistently showed the formation of an alternating pattern between solvent pockets and nodes with the peptides located at the bilayer contact points (nodes). At P/L 1:42 the peptides on opposite membranes aggregated resulting in a height modulation of the membrane and the creation of solvent pockets. Twofold increase in peptide concentration (P/L 1:21) led to the formation of fiber-like structures for L18W-PGLa and MG2a mixtures along the contact nodes between the two membranes (3.11 panel D). Note, the alternating pattern corresponds to a certain spatial frequency which in MD simulations is affected by the simulation box size. In X-ray diffraction experiments a broad peak at low q values of unknown origin was observed for the hybrid peptide and the equimolar mixture (figure 3.13 panel A and B). Data of the hybrid peptide additionally showed a coexistence of the cubic Pn3m phase with the broad peak and an additional lamellar diffraction pattern at a P/L of 1:25. An increase of peptide concentration (P/L 1:12.5) led to the disappearance of the Pn3m Phase. Only the broad peak and the lamellar phase prevailed (Figure 3.13 panel A). The same broad feature was seen for the equimolar mixture (Figure 3.13 panel B). The similar peak shape and position of the feature suggested that this peak also originated from the same source. A small contribution of the broad peak could also be observed at a P/L 1:100 for M11.

Together with MD simulations two possible explanations for this feature were found. First, the peak is connected to the frequency of the above mentioned modulated pattern also resembling it's increase in frequency upon addition of more peptide. Second, it could be related to a molten

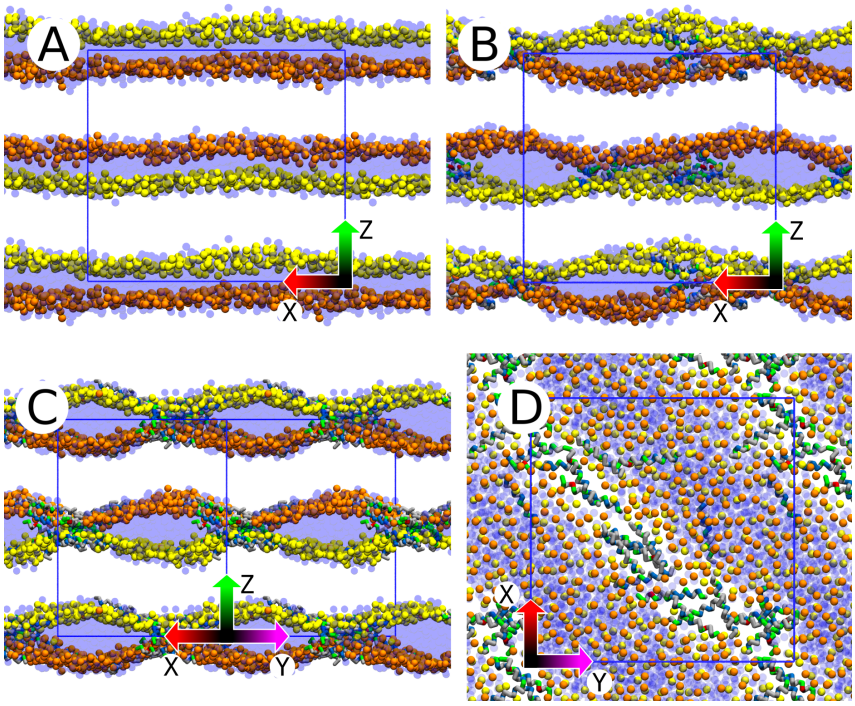

Figure 3.11.: Simulation snapshots of coarse-grained Martini systems with two lipid bilayers in the absence (A) and presence of MG2a+L18W-PGLa at P/L 1:41 (B) and 1:21 (C) after 20 μs. (D) corresponds to a top a view of the fiber-like peptide structures. The blue rectangle marks the simulation cell. Phosphate atoms are shown as orange and yellow spheres and the peptides are displayed in cartoon representation with the color coded residues (Nonpolar: gray, polar: green, acidic: red, and basic: blue). Water beads are illustrated as half transparent dark-blue spheres.

cubic Pn3m phase (sponge phase) which no longer exhibits a long range crystalline order. This scenario is strongly supported by the X-ray data due to the coexistence of the broad peak with the cubic Pn3m at P/L of 1:25 and the final loss of the Pn3m correlation peaks at P/L 1:12.5. Further evidence is provided by the distance between the water channels of the sponge (Figure 3.13 panel C) and cubic phase. The D spacing of the broad peak is significantly larger than then the distance between the pores in the cubic system ($D_{(1,1,0)}$). Therefore, the broad peak observed only in the presence of the hybrid and the equimolar mixture originated in both cases from a sponge phase.

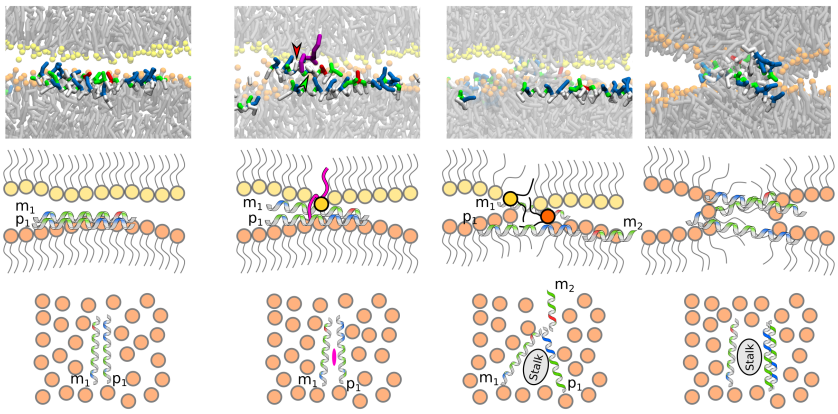

Figure 3.12.: Simulation snapshots (top) and schematics from the bilayer fusion process with MG2a (m1) and L18W-PGLa (p1) arranged as parallel heterodimers. The bilayer fusion was initiated by the purple lipid, followed by a V-shaped configuration of the peptides that caused the formation of a fusion stalk. In images 1), 2) and 3), phosphate beads of the first and second bilayer are shown in yellow and orange, respectively. In image 4), all phosphate beads are shown orange due to lipid mixing. Fore more details seen [4].

Reviewing all previous observations we propose that a transition from LUV to MLV alone is not a sufficient condition for enhanced dye release observed in [17]. Additionally, synergistic leakage is coupled to the increase of membrane curvature induced by dimers or peptide-fibril structures, followed by fusion events (fusion stalk) and the consecutive development of a sponge or cubic phase. Both structures are due to their porous nature leaky and therefore account for the increased amount of fluorescence in leakage experiments. Also, the substantial difference between the $D_{(110)} \approx 73$ Å of the cubic Pn3m phase and the lattice parameter of the lamellar phase D $\approx$ 50 Å suggests that there is no epitaxial relationship between them. This indicates a defect-rich transition zone between both structures, which may also contribute to the dye-release.

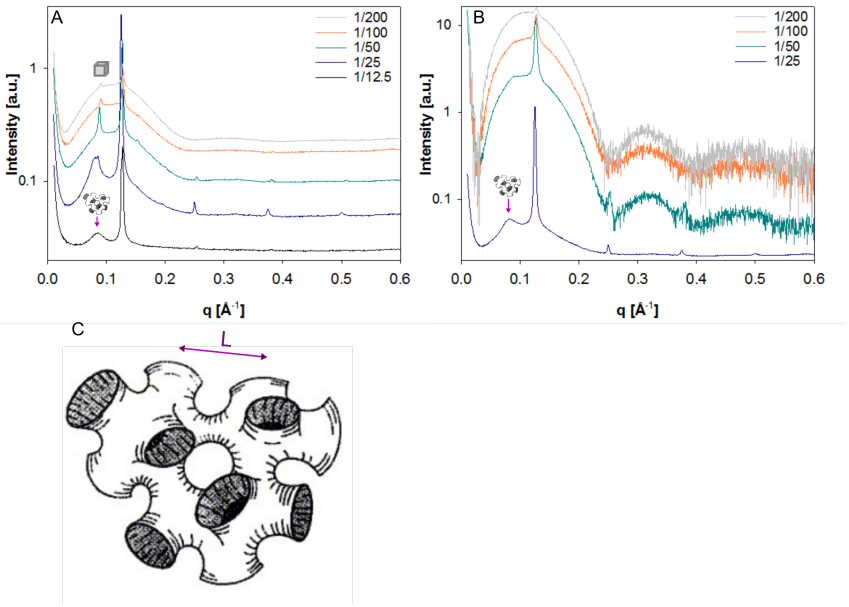

Figure 3.13.: SAXS patterns of 100 nm LUVs composed of POPE/POPG (3/1 mol/mol) in the presence of the chemically linked hybrid peptide (A) and the equimolar mixture M11 (B) at 35°C as function of P/L molar ratio. The purple arrow marks the broad peak of the sponge phase. Panel (C) shows a schematic of the sponge structure, adapted from Snabre 1990 [5].

4. Conclusion

We quantified the lipid membranes microscopic structural response induced by attacking magainins (L18W-PGLa, MG2a, Mix, Hybrid) under physiological conditions. Further the peptides transbilayer position was determined with less then 1 Å uncertainty via a custom tailored analysis developed during this thesis. Ultimately a model for the synergistic activity of L18W-PGLa and MG2a on a molecular level was proposed.

Experimentally we demonstrated that 100 nm large unilamellar vesicles composed of POPE/POPG (3/1) mimic *E. coli's* response towards an attack by AMPs in terms of biophysics remarkable. Also, by testing various mimics we found that the synergistic activity of the L18W-PGLa/MG2a cocktail was only observed when the membrane exhibited a tight polar/apolar interface (J_0). This key requirement states clearly how crucial the proper choice of lipids for a membrane mimic is. Next we found by application of the developed analysis for samples below synergistic peptide concentrations that any of the investigated peptides induced hydrocarbon core thinning and when the peptides were applied as equimolar mixture both L18W-PGLa and MG2a relocated within the transbilayer profile with respect to their single peptide positions. Ancillary biophysical studies at synergistic conditions informed on the presence of a lamellar lattice which was related to the formation of multilamellar aggregates via cryo-TEM experiments. In addition, the high dye- release observed in [17] was correlated with the occurrence of either a sponge or a cubic Pn3m phase [4]. Lipid demixing due to the cationic nature of the peptides was discarded via zero contrast neutron scattering experiments. Complementary MD simulations showed peptide induced membrane oscillations with solvent pockets and peptides positioned at the nodes. Peptide fiber formation along the contact points of the membranes was observed at elevated peptide concentrations.

Based on our observations we postulated a possible mode of action for the synergistic interaction of L18W-PGLa and MG2a in our test system. Synergism is coupled to an early onset of parallel heterodimer formation which inserted less deep into the membrane and caused vesicles to adhere and eventually to aggregate (LUV-MLV transition). An increase in peptide concentration led to the formation of peptide-fibril-structures. The partial insertion of those aggregates induced strong local membrane curvatures and cross-linked bilayers in close proximity. Those connections (fusion-stalks) transformed the system over time into a sponge phase. In the case of the hybrid, the Pn3m phase transformed into a sponge phase upon an increase of peptide content. Both structures account due to their leaky nature for the observed enhanced fluorescence reported in [17]. It is important to mention that our MD results showed that both peptides always remained in a surface state topology, even during fusion stalk formation. This is a direct result of POPE's negative intrinsic curvature and the accordingly tight packed polar/apolar interface. Therefore, Gram-negative bacterial mimics lacking the contribution of negatively curved lipids will lead to wrong results! Further, pores of sponge or cubic phases observed during this work resulted from the bridging of two closely located bilayers with any involved peptide in a surface state topology and are consequently fundamentally different compared to peptide pores proposed for synergism in literature [3, 13].

The above described model for the synergistic action of L18W-PGLa and MG2a is conform with the reported surface state orientation in literature for POPE/POPG (3:1) mixtures [18, 19]. Also it is topologically different from the models postulated by Ulrich (tetrameric heterocomplex [3]), Matsuzaki (toroidal pore [13]) and Bechinger (lipid-mesophase like peptide structures [2]). The first two are pore based models whereas the latter corresponds to a surface aligned topology. In particular the structure of the tetrameric heterocomplex was derived with NMR experiments on DMPC/DMPG lipid bilayers. This is a critical point, since it has been shown that short fully saturated lipid chains facilitate a transmembrane orientation of PGLa [18, 19, 61]. Further they are not representative for bacterial membranes. More adequate lipid mimics for Gram-negative bacteria should be enriched in POPE and POPG. Both are mixed-chain phospholipids and for both it has been shown that PGLa and MG2a never adopt a transmembrane positioning, not even when present simultaneously. During the attribution

of the toroidal pore model to PGLa/MG2a synergism by Matsuzaki natural lipids like EYPC, EYPG and BBPS were used. Those lipids do not exhibit well defined hydrocarbon chains and consequently the proposed model could be due to the nature of the hydrocarbon chain composition at least for PGLa. Based on NMR studies on DPPC in the presence of MG2a [19] and the fact that exchanging the PC headgroup by either PG or PE will lead to a significant tighter polar/apolar interface it is unlikely that MG2a will adopt a transmembrane state. Last but not least Bechinger proposed in 2016 lipid-mesophase like structures for PGLa and MG2a synergism. Topologically there is a similarity to the observed fibers, however their formation is driven by the tendency of peptides to form parallel heterodimeres followed by aggregation with peptides located on neighboring membranes.

The here derived model for the synergistic activity of PGLa and MG2a mixtures provides up to date the most comprehensive view of the phenomenon. It is consistent with previous observations in literature and supplies not only a non transmembrane pore centered mechanism ascribed to synergism but equally important supplies a novel way of viewing their synergistic killing at a molecular level.

5. Outlook

The state of the art analysis developed during this thesis provides the field with a tool to model diffusive scattering including an explicit term for the peptides contribution. It provides structural information on the membrane's response towards peptide attacks at highest possible resolution. Further, it offers the possibility to accurately determine the peptide's insertion depth if neutron contrasts are available. A parameter which was previously hard to pinpoint. In general the mathematical framework behind it is capable of describing any admixed molecule as long as its located in the bilayers headgroup region and follows a Gaussian distribution profile. Minor modifications of the code are going to allow for arbitrary positioning and distribution profiles. Further advancements of the model towards transmembrane states could potentially provide the capability to judge from scattering experiments alone which peptide insertion state is present. The present thesis showed that the derived framework functions remarkable well for symmetric unilamellar vesicles with peptides in surface state topologies. Given its success it would be advisable to advance the SDP towards asymmetric lipid membranes and as mentioned earlier towards transmembrane peptide orientations. Further the analysis could be based on Bayesian probability theory, similar to Frewein et al. [68, 69]. The different states observed during the simulation/calculation and their likeliness could be exploited to further substantiate which peptide insertion state is present. The model itself could be improved by the introduction of tilt angles for various lipid groups as fitting parameters, e.g. headgroup angles. Also a complexer parsing for the peptides of interest could be employed as e.g. recently shown by SAXS experiments and MD simulations for cholesterol [53, 70]. This could provide additional information on the peptides orientation. Next, when applying the SDP on data from deuterated samples exchangeable hydrogens have a massive influence on the retrieved structural parameters. Therefore, it should be identified which and how many of the hydrogen atoms of the

peptide will be exchanged. This might also effect the peptides parsing and is definitely going to enhance the achievable results. Further if a peptide parsing with at least two terms is present it could be possible to study data from peptide flip flops across the membrane.

Bibliography

[1] Tresset, G., 2009. The multiple faces of self-assembled lipidic systems. *PMC Biophysics* 2:3. https://doi.org/10.1186/1757-5036-2-3.

[2] Arnaud, M., Salnikov E.S., Glattard E.., Aisenbrey C., and Burkhard B., 2016. Magainin 2-PGLa Interactions in Membranes - Two Peptides that Exhibit Synergistic Enhancement of Antimicrobial Activity. *Curr Top Med Chem* 16:65–75.

[3] Zerweck, J., E. Strandberg, O. Kukharenko, J. Reichert, J. Bürck, P. Wadhwani, and A. S. Ulrich, 2017. Molecular mechanism of synergy between the antimicrobial peptides PGLa and magainin 2. *Sci Rep* 7:13153. https://www.nature.com/articles/s41598-017-12599-7.pdf.

[4] Kabelka, I., M. Pachler, M. S. Appavou, K. Lohner, R. Vachea, and G. Pabst, 2019. Magainin 2 and PGLa in Bacterial Membrane Mimics II: Membrane Fusion and Sponge Phase Formation. *submitted* https://doi.org/10.1101/763383.

[5] Snabre, P., and G. Porte, 1990. Viscosity of theL3Phase in Amphiphilic Systems. *EPL* 13:641–645.

[6] Munita, J. M., and C. A. Arias, 2016. Mechanisms of Antibiotic Resistance. *Microbiol Spectr* 4.

[7] Freire, J. M., D. Gaspar, A. S. Veiga, and M. A. R. B. Castanho, 2015. Shifting gear in antimicrobial and anticancer peptides biophysical studies: from vesicles to cells. *J Pept Sci* 21:178–185.

[8] Wimley, W. C., and K. Hristova, 2011. Antimicrobial Peptides: Successes, Challenges and Unanswered Questions. *J Membr Biol* 239:27–34. https://doi.org/10.1007/s00232-011-9343-0.

[9] Lohner, K., and S. Blondelle, 2005. Molecular Mechanisms of Membrane Perturbation by Antimicrobial Peptides and the Use of Biophysical Studies in the Design of Novel Peptide Antibiotics. *CCHTS* 8:241–256.

[10] Hoffmann, W., K. Richter, and G. Kreil, 1983. A novel peptide designated PYLa and its precursor as predicted from cloned mRNA of Xenopus laevis skin. *EMBO J* 2:711–714.

[11] Soravia, E., G. Martini, and M. Zasloff, 1988. Antimicrobial properties of peptides from Xenopus granular gland secretions. *FEBS Lett* 228:337–340.

[12] Hara, T., Y. Mitani, K. Tanaka, N. Uematsu, A. Takakura, T. Tachi, H. Kodama, M. Kondo, H. Mori, A. Otaka, F. Nobutaka, and K. Matsuzaki, 2001. Heterodimer Formation between the Antimicrobial Peptides Magainin 2 and PGLa in Lipid Bilayers: A Cross-Linking Study †. *Biochemistry* 40:12395–12399.

[13] Matsuzaki, K., Y. Mitani, K. Y. Akada, O. Murase, S. Yoneyama, M. Zasloff, and K. Miyajima, 1998. Mechanism of synergism between antimicrobial peptides magainin 2 and PGLa. *Biochemistry* 37:15144–15153.

[14] Nishida, M., Y. Imura, M. Yamamoto, S. Kobayashi, Y. Yano, and K. Matsuzaki, 2007. Interaction of a magainin-PGLa hybrid peptide with membranes: insight into the mechanism of synergism. *Biochemistry* 46:14284–14290.

[15] Westerhoff, H. V., M. Zasloff, J. L. Rosner, R. W. Hendler, A. de Waal, A. Vaz Gomes, P. M. Jongsma, A. Riethorst, and D. Juretić, 1995. Functional synergism of the magainins PGLa and magainin-2 in Escherichia coli, tumor cells and liposomes. *Eur J Biochem* 228:257–264.

[16] Williams, R. W., R. Starman, K. M. P. Taylor, K. Gable, T. Beeler, M. Zasloff, and D. Covell, 1990. Raman spectroscopy of synthetic antimicrobial frog peptides magainin 2a and PGLa. *Biochemistry* 29:4490–4496.

[17] Leber, R., M. Pachler, I. Kabelka, I. Svoboda, D. Enkoller, R. Vácha, K. Lohner, and G. Pabst, 2018. Synergism of Antimicrobial Frog Peptides Couples to Membrane Intrinsic Curvature Strain. *Biophys J* 114:1945–1954.

[18] Harmouche, N., and B. Bechinger, 2018. Lipid-Mediated Interactions between the Antimicrobial Peptides Magainin 2 and PGLa in Bilayers. *Biophys J* 115:1033–1044.

[19] Strandberg, E., J. Zerweck, P. Wadhwani, and A. S. Ulrich, 2013. Synergistic insertion of antimicrobial magainin-family peptides in membranes depends on the lipid spontaneous curvature. *Biophys J* 104:L9–11.

[20] Leikin, S., M. M. Kozlov, N. L. Fuller, and R. P. Rand, 1996. Measured effects of diacylglycerol on structural and elastic properties of phospholipid membranes. *Biophys J* 71:2623–2632.

[21] Kozlov, M., 2007. Determination of Lipid Spontaneous Curvature From X-Ray Examinations of Inverted Hexagonal Phases, volume 400 of *Methods in Molecular Biology*. Springer-Verlag Berlin Heidelberg, Berlin, Heidelberg.

[22] Malanovic, N., and K. Lohner, 2016. Gram-positive bacterial cell envelopes: The impact on the activity of antimicrobial peptides. *Biochim Biophys Acta* 1858:936–946.

[23] C.Ratledge and S.G. Wilkinson, editor, 1988. Gram negative bacteria: Wilkinson SG (1988) Gram-Negative Bacteria. Eds Microbial Lipids. Academic Press, London, UK.

[24] Chen, Y.-F., K.-Y. Tsang, W.-F. Chang, and Z.-A. Fan, 2015. Differential dependencies on [Ca2+] and temperature of the monolayer spontaneous curvatures of DOPE, DOPA and cardiolipin: effects of modulating the strength of the inter-headgroup repulsion. *Soft Matter* 11:4041–4053. `http://dx.doi.org/10.1039/C5SM00577A`.

[25] Heberle, F. A., and G. Pabst, 2017. Complex biomembrane mimetics on the sub-nanometer scale. *Biophys Rev* 9:353–373. `https://doi.org/10.1007/s12551-017-0275-5`.

[26] Hancock, R. E., and R. Lehrer, 1998. Cationic peptides: a new source of antibiotics. *Trends Biotechnol* 16:82–88.

[27] Zasloff, M., 2002. Antimicrobial peptides of multicellular organisms. *Nature* 415:389–395.

[28] Wade, D., A. Boman, B. Wåhlin, C. M. Drain, D. Andreu, H. G. Boman, and R. B. Merrifield, 1990. All-D amino acid-containing channel-forming antibiotic peptides. *Proc Natl Acad Sci U S A.* 87:4761–4765.

[29] Oren, Z., J. Hong, and Y. Shai, 1997. A repertoire of novel antibacterial diastereomeric peptides with selective cytolytic activity. *J Biol Chem* 272:14643–14649.

[30] Pirtskhalava, M., A. Gabrielian, P. Cruz, H. L. Griggs, R. B. Squires, D. E. Hurt, M. Grigolava, M. Chubinidze, G. Gogoladze, B. Vishnepolsky, V. Alekseyev, A. Rosenthal, and M. Tartakovsky, 2016. DBAASP v.2: an enhanced database of structure and antimicrobial/cytotoxic activity of natural and synthetic peptides. *Nucleic Acids Res* 44:6503.

[31] Wang, G., X. Li, and Z. Wang, 2016. APD3: the antimicrobial peptide database as a tool for research and education. *Nuleic Acids Res* 44:D1087–93.

[32] Rapaport, D., and Y. Shai, 1991. Interaction of fluorescently labeled pardaxin and its analogues with lipid bilayers. *J Biol Chem* 266:23769–23775.

[33] Ludtke, S. J., K. He, W. T. Heller, T. A. Harroun, L. Yang, and H. W. Huang, 1996. Membrane pores induced by magainin. *Biochemistry* 35:13723–13728.

[34] Gazit, E., I. R. Miller, P. C. Biggin, M. S. Sansom, and Y. Shai, 1996. Structure and orientation of the mammalian antibacterial peptide cecropin P1 within phospholipid membranes. *J Mol Biol* 258:860–870.

[35] Ostolaza, H., B. Bartolomé, I. Ortiz de Zárate, F. de La Cruz, and F. M. Goñi, 1993. Release of lipid vesicle contents by the bacterial protein toxin alpha-haemolysin. *Biochim Biophys Acta* 1147:81–88.

[36] Hristova, K., M. E. Selsted, and S. H. White, 1997. Critical Role of Lipid Composition in Membrane Permeabilization by Rabbit Neutrophil Defensins. *J Biol Chem* 272:24224–24233.

[37] Bechinger, B., and K. Lohner, 2006. Detergent-like actions of linear amphipathic cationic antimicrobial peptides. *Biochim Biophys Acta* 1758:1529–1539.

[38] Bechinger, B., 2009. Rationalizing the membrane interactions of cationic amphipathic antimicrobial peptides by their molecular shape. *Curr Opin Colloid In* 14:349–355.

[39] Epand, R. M., and R. F. Epand, 2009. Lipid domains in bacterial membranes and the action of antimicrobial agents. *Biochem Biophys Acta* 1788:289–294.

[40] Epand, R. F., W. L. Maloy, A. Ramamoorthy, and R. M. Epand, 2010. Probing the "charge cluster mechanism" in amphipathic helical cationic antimicrobial peptides. *Biochemistry* 49:4076–4084.

[41] Pokorny, A., and P. F. F. Almeida, 2004. Kinetics of dye efflux and lipid flip-flop induced by delta-lysin in phosphatidylcholine vesicles and the mechanism of graded release by amphipathic, alpha-helical peptides. *Biochemistry* 43:8846–8857.

[42] Almeida, P. F., and A. Pokorny, 2009. Mechanisms of antimicrobial, cytolytic, and cell-penetrating peptides: from kinetics to thermodynamics. *Biochemistry* 48:8083–8093.

[43] Rathinakumar, R., W. F. Walkenhorst, and W. C. Wimley, 2009. Broad-spectrum antimicrobial peptides by rational combinatorial design and high-throughput screening: the importance of interfacial activity. *J Am Chem Soc* 131:7609–7617.

[44] Wimley, W. C., 2010. Describing the mechanism of antimicrobial peptide action with the interfacial activity model. *ACS Chem Biol.* 5:905–917.

[45] Pachler, M., I. Kabelka, S. Prevos, K. Lohner, R. Vachea, and G. Pabst, 2019. Magainin 2 and PGLa in a Bacterial Cytoplasmic Membrane Mimic: Part I – Peptide-Peptide and Lipid-Peptide Interactions. *submitted* `https://doi.org/10.1101/664359`.

[46] Rieder, A. A., 2014. Aufbau und Optimierung einer Rapid Solvent Exchange Aufbau und Optimierung einer Rapid Solvent Exchange Apparatur zur Herstellung künstlicher Zellmembranen. Master thesis, Graz University of Technology, Graz.

[47] Buboltz, J. T., and G. W. Feigenson, 1999. A novel strategy for the preparation of liposomes: rapid solvent exchange. *Biochim Biophys Acta* 1417:232–245.

[48] Buboltz, J. T., 2009. A more efficient device for preparing model-membrane liposomes by the rapid solvent exchange method. *Rev Sci Instrum* 80:124301.

[49] Kollmitzer, B., P. Heftberger, M. Rappolt, and G. Pabst, 2013. Monolayer spontaneous curvature of raft-forming membrane lipids. *Soft Matter* 9:10877–10884. 24672578.

[50] Kingsley, P. B., and G. W. Feigenson, 1979. The synthesis of a perdeuterated phospholipid: 1,2-dimyristoyl-sn-glycero-3-phosphocholine-d72. *Chem Phys Lipids* 24:135–147.

[51] Kiselev, M. A., P. Lesieur, A. M. Kisselev, D. Lombardo, and V. L. Aksenov, 2002. Model of separated form factors for unilamellar vesicles. *Applied Physcis A* 74:s1654–s1656. https://doi.org/10.1007/s003390201837.

[52] Pencer, J., S. Krueger, C. P. Adams, and J. Katsaras, 2006. Method of separated form factors for polydisperse vesicles. *J Appl Crystallogr* 39:293–303.

[53] Kucerka, N., J. D. Perlmutter, J. Pan, S. Tristram-Nagle, J. Katsaras, and J. N. Sachs, 2008. The effect of cholesterol on short- and long-chain monounsaturated lipid bilayers as determined by molecular dynamics simulations and X-ray scattering. *Biophys J* 95:2792–2805.

[54] Kučerka, N., B. van Oosten, J. Pan, F. A. Heberle, T. A. Harroun, and J. Katsaras, 2015. Molecular structures of fluid phosphatidylethanolamine bilayers obtained from simulation-to-experiment comparisons and experimental scattering density profiles. *J Phys Chem B* 119:1947–1956.

[55] Pan, J., D. Marquardt, F. A. Heberle, N. Kučerka, and J. Katsaras, 2014. Revisiting the bilayer structures of fluid phase phosphatidylglycerol lipids: Accounting for exchangeable hydrogens. *Biochim Biophys Acta* 1838:2966–2969.

[56] Belička, M., A. Weitzer, and G. Pabst, 2017. High-resolution structure of coexisting nanoscopic and microscopic lipid domains. *Soft Matter* 13:1823–1833.

[57] Tristram-Nagle, S., H. I. Petrache, and J. F. Nagle, 1998. Structure and Interactions of Fully Hydrated Dioleoylphosphatidylcholine Bilayers. *Biophys J* 75:917–925.

[58] Rappolt, M., 2006. Chapter 9 The Biologically Relevant Lipid Mesophases as "Seen" by X-Rays. *Advances in Planar Lipid Bilayers and Liposomes* 5:253–283.

[59] Rappolt, M., 2010. Bilayer thickness estimations with "poor" diffraction data. *J Appl Physics* 107:084701–084701.

[60] Warren, B. E., 2014. X-ray diffraction. Dover Books on Physics. Dover Publications, New York.

[61] Salnikov, E. S., and B. Bechinger, 2011. Lipid-controlled peptide topology and interactions in bilayers: structural insights into the synergistic enhancement of the antimicrobial activities of PGLa and magainin 2. *Biophys J* 100:1473–1480.

[62] Lohner, K., 2009. New strategies for novel antibiotics: peptides targeting bacterial cell membranes. *Gen Physiol Biophys* 28:105–116.

[63] Nagle, J. F., and S. Tristram-Nagle, 2000. Structure of lipid bilayers. *Biochim Biophys Acta* 1469:159 – 195. `http://www.sciencedirect.com/science/article/pii/S0304415700000162`.

[64] Siegel, D. P., 1999. The Modified Stalk Mechanism of Lamellar/Inverted Phase Transitions and Its Implications for Membrane Fusion. *Biophys J* 76:291–313.

[65] Tamm, L. K., J. Crane, and V. Kiessling, 2003. Membrane fusion: a structural perspective on the interplay of lipids and proteins. *Curr Opin Struct Biol* 13:453 – 466.

[66] Chernomordik, L. V., and M. M. Kozlov, 2008. Mechanics of membrane fusion. *Nat Struct Mol Biol* 15:675–83.

[67] Salditt, T., I. Koltover, J. O. Rädler, and C. R. Safinya, 1998. Self-assembled DNA–cationic-lipid complexes: Two-dimensional smectic ordering, correlations, and interactions. *Phys Rev E* 58:889–904.

[68] Frewein, M. P., M. Rumetshofer, and G. Pabst, 2019. Global small-angle scattering data analysis ofinverted hexagonal phases. *J App Crystallogr* 52:403–414.

[69] Linden, W. v. d., V. Dose, and U. v. Toussaint, 2014. Bayesian Probability Theory: Applications in the Physical Sciences. Cambridge University Press.

[70] Pan, J., X. Cheng, F. A. Heberle, B. Mostofian, N. Kučerka, P. Drazba, and J. Katsaras, 2012. Interactions between ether phospholipids and cholesterol as determined by scattering and molecular dynamics simulations. *J Phys Chem B* 116:14829–14838.

Appendix A.

List of Publications

A.1. Attached Publications

Leber R., M.Pachler, I. Kabelka, I. Svoboda, D. Enkoller, R. Vácha, K. Lohner and G. Pabst, 2018. Synergism of Antimicrobial Frog Peptides Couples to Membrane Intrinsic Curvature Strain. *Biophysical Journal*. 114(8), 1945-1954.

Author contributions:
R.L. performed the experimental research, analyzed the data, and wrote the article.
M.P. performed research and analyzed data.
I.K. performed MC simulations.
I.S. performed experiments on *E. Coli.*
D.E. performed research.
R.V., K.L. and G.P. designed the research and wrote the article.

Pachler M.[†], I. Kabelka[†], M.S. Appavou, K. Lohner, R. Vácha and G. Pabst, 2019. Magainin 2 and PGLa in a Bacterial Cytoplasmic Membrane Mimic: Part I – Peptide-Peptide and Lipid-Peptide Interactions. *submitted*. `https://doi.org/10.1101/664359`.

[†]contributed equally

Author contributions:
M.P. performed the experimental research, analyzed the data, and wrote the article.
I.K. carried out all simulations, analyzed the data, and wrote the article.

M.-S.A. performed SANS experiments.
R.V., K.L. and G.P. designed the research and wrote the article.

Kabelka I.†, M.Pachler†, M.S. Appavou, K. Lohner, R. Vácha and G. Pabst, 2019. Magainin 2 and PGLa in Bacterial Membrane Mimics II: Membrane Fusion and Sponge Phase Formation. *submitted*. https://doi.org/10.1101/763383. †contributed equally

Author contributions:
M.P. performed the experimental research, analyzed the data, and wrote the article.
I.K. carried out all simulations, analyzed the data, and wrote the article.
M.-S.A. performed SANS experiments.
R.V., K.L. and G.P. designed the research and wrote the article.

Appendix B.

Scientific publications

Biophysical *Journal*
Article

Biophysical Society

Synergism of Antimicrobial Frog Peptides Couples to Membrane Intrinsic Curvature Strain

Regina Leber,[1,2] Michael Pachler,[1,2] Ivo Kabelka,[3,4] Irene Svoboda,[1,2] Daniel Enkoller,[5] Robert Vácha,[3,4] Karl Lohner,[1,2] and Georg Pabst[1,2,*]

[1]Institute of Molecular Biosciences, Biophysics Division, University of Graz, NAWI Graz, Graz, Austria; [2]BioTechMed Graz, Graz, Austria; [3]Central European Institute of Technology, Brno, Czech Republic; [4]Faculty of Science, Masaryk University, Brno, Czech Republic; and [5]Fresenius Kabi Austria GmbH, Graz, Austria

ABSTRACT Mixtures of the frog peptides magainin 2 and PGLa are well-known for their pronounced synergistic killing of Gram-negative bacteria. We aimed to gain insight into the underlying biophysical mechanism by interrogating the permeabilizing efficacies of the peptides as a function of stored membrane curvature strain. For Gram-negative bacterial-inner-membrane mimics, synergism was only observed when the anionic bilayers exhibited significant negative intrinsic curvatures imposed by monounsaturated phosphatidylethanolamine. In contrast, the peptides and their mixtures did not exhibit significant activities in charge-neutral mammalian mimics, including those with negative curvature, which is consistent with the requirement of charge-mediated peptide binding to the membrane. Our experimental findings are supported by computer simulations showing a significant decrease of the peptide-insertion free energy in membranes upon shifting intrinsic curvatures toward more positive values. The physiological relevance of our model studies is corroborated by a remarkable agreement with the peptide's synergistic activity in *Escherichia coli*. We propose that synergism is related to a lowering of a membrane-curvature-strain-mediated free-energy barrier by PGLa that assists membrane insertion of magainin 2, and not by strict pairwise interactions of the two peptides as suggested previously.

INTRODUCTION

Antimicrobial peptides (AMPs) are highly effective components of the innate immune system of most living organisms. AMPs respond to invading pathogens and are optimized to kill bacteria either by direct interaction or by immunomodulatory activities (1–3). Ever since the discovery of AMPs in prokaryotes in the 1930s and a few decades later in eukaryotes, research efforts devoted to the molecular mechanisms of their direct antimicrobial activities have revealed several modes of interaction (for review, see, e.g., (4,5)). A general consensus has been reached in recognizing that the positive charge of the peptide is essential for initial binding to the anionic bacterial membrane surface, a factor which allows discrimination between bacterial and host cell membranes, whereas hydrophobicity is needed for insertion into and disruption of the target membrane (see, e.g., (6,7)). Magainin 2 (MG2) and PGLa, two members of the magainin family isolated from the skin of the African clawed frog *Xenopus laevis* (8,9), are among the best-studied AMPs. They exhibit a broad spectrum of activity against microorganisms with minimal inhibitory concentration (MIC) values ranging from 5 to >100 μg/mL (10). Of particular interest is their synergistic activity, which has been observed in bacteria but also in lipid-only model membranes (11–16). Notably, MG2/PGLa synergism is most pronounced for Gram-negative strains such as *Escherichia coli* (13).

Unraveling the molecular origin of this synergistic activity has not been without disparity. Early biophysical studies on lipid-only systems suggested enhanced membrane-pore-formation capabilities of equimolar peptide mixtures (13–15). Indeed, a stable transmembrane orientation of PGLa/MG2 dimers, as reported from solid-state NMR measurements, supported this model (17). A few years later, however, Salnikov and Bechinger showed that the topology of PGLa and MG2 (i.e., their orientation with respect to the bilayer surface), and in particular that of MG2, depends on the hydrophobic thickness of the lipid bilayer (18). The important role of membrane physical parameters was further emphasized by Strandberg et al. (19) by correlating the topology of both peptides with the intrinsic curvature of lipids. In particular, these authors suggested that the

Submitted January 9, 2018, and accepted for publication March 12, 2018.

*Correspondence: georg.pabst@uni-graz.at

Editor: Kalina Hristova.

https://doi.org/10.1016/j.bpj.2018.03.006

© 2018 Biophysical Society.

This is an open access article under the CC BY license (http://creativecommons.org/licenses/by/4.0/).

synergistic insertion of MG2 and PGLa into membranes couples to a positive intrinsic curvature.

Intriguingly, however, cytoplasmic membranes of Gram-negative bacteria are enriched in lipids with negative intrinsic curvature, such as phosphatidylethanolamine (PE) (20). This prompted us to correlate membrane-permeabilizing activities of magainin monomers and dimers in different lipid-only model systems with various intrinsic curvatures J_0 determined from small-angle x-ray scattering (SAXS). In particular, we studied the activity of L18W-PGLa and MG2a, as well as their analogs containing GGC linkers, which were used to form the L18W-PGLa-MG2a hybrid peptide (Fig. 1). The choice of L18W-PGLa is motivated to facilitate better comparison to a previous study on magainin heterodimers (15). Note that the dye release from lipid vesicles induced by L18W-PGLa is almost identical to that induced by native PGLa (13). Thus, our results can be generalized to PGLa in our comparison to other reports. Likewise, MG2a is discussed synonymously with MG2.

The choice of lipid-only mimics is delicate. In addition to the PE enrichment, cytoplasmic membranes of Gram-negative bacteria also contain anionic phospholipids such as phosphatidylglycerol (PG) and cardiolipin (CL). The relative abundance of anionic lipids strongly depends on the strain (20) and growth conditions (21). For instance, the inner membrane of *Pseudomonas cepacia* contains 82% PE and 18% PG (wt% of total phospholipid), whereas *E. coli* also contains ~10 wt% CL (20). The focus of the present work is on the role of intrinsic curvature strain in magainin synergism. Because the sign of J_0 of CL strongly depends on the ionic composition of the aqueous buffer (22), we decided to mimic the inner membrane of Gram-negative bacteria to first order with a binary lipid mixture of POPE/POPG 3:1 mol/mol to avoid any ambiguities resulting from this issue. Additionally, phosphatidylcholine (PC)/cholesterol (Chol) mixtures served as a simple first-order model of human erythrocyte membranes considered as archetypes of mammalian plasma membranes. Again, PC/Chol mimics do not capture the full compositional complexity of such plasma membranes, but serve here to address the role of intrinsic curvature in a system lacking electrostatic interactions between anionic lipids and cationic peptide residues. Our results provide evidence that PGLa/MG2 synergism is tightly coupled to negative lipid intrinsic curvature and to negative surface charge of membranes but does not necessarily require, nor exclude, the formation of PGLa/MG2 pairs. Although electrostatic interactions between AMPs and lipid headgroups are crucial for significantly long retention time (binding) of the peptides to the bilayer surface, lipid intrinsic curvatures contribute to an activation free-energy barrier $\Delta G^{\ddagger}$ for membrane insertion of the peptides. We propose that PGLa, because of its higher affinity for the hydrophobic core of the bilayer, lowers $\Delta G^{\ddagger}$ for MG2 by reducing the curvature-mediated tension at the polar-apolar membrane interface and thereby potentiates the effect of MG2.

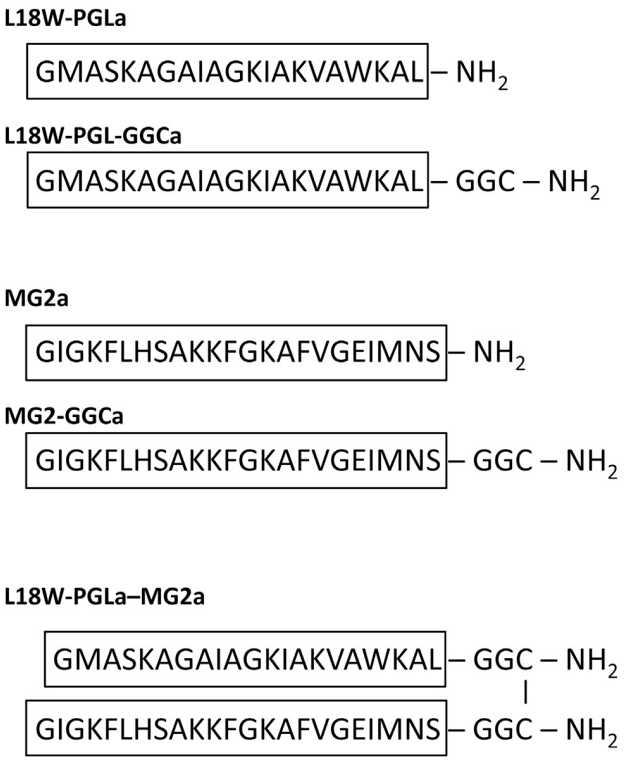

FIGURE 1 Primary structures of studied magainins.

MATERIALS AND METHODS

Lipids, peptides, and chemicals

Palmitoyl-oleoyl-phosphatidylethanolamine (POPE), dioleoyl-phosphatidylethanolamine (DOPE), palmitoyl-oleoyl-phosphatidylglycerol (POPG), palmitoyl-oleoyl-phosphatidylcholine (POPC), and 1-palmitoyl-2-hydroxy-PE (lyso-PE) were purchased from Avanti Polar Lipids, Alabaster, AL (purity >99%) as powder. Cholesterol, *cis*-9-tricosene, and Triton X-100 were obtained from Sigma-Aldrich, Vienna, Austria. L18W-PGLa and MG2a, as well as their analogs containing GGC linkers and L18W-PGLa-MG2a heterodimers, were obtained in lyophilized form (purity >95%) from PolyPeptide Laboratories (San Diego, CA). ANTS (8-aminonaphthalene-1,3,6-trisulfonic acid, disodium salt) and DPX (p-xylene-bis-pyridinium bromide) were purchased from Molecular Probes (Eugene, OR). Chemicals used for sodium dodecyl sulfate polyacrylamide gel electrophoresis (SDS-PAGE) as well as antibiotics (ampicillin sodium salt, gentamicin sulfate solution), 1,4-dithiothreitol (DTT), and Mueller-Hinton broth were obtained from Carl Roth (Karlsruhe, Germany). The Ultra-Low Range Marker for SDS-PAGE was purchased from Sigma-Aldrich.

Lipid stock solutions for sample preparation were prepared in organic solvent. In particular, lyso-PE was dissolved in chloroform/methanol/water 65:35:8 (v/v/v), whereas all other lipids, including *cis*-9-tricosene, were dissolved in chloroform/methanol (9:1; v/v). Peptide stock solutions were prepared in 0.01% acetic acid, and aliquots of the stock solutions were stored in silanized glass tubes at −20°C until use.

Methods

Large unilamellar vesicles (LUVs) of ~100 nm size were prepared and assayed for AMP-induced fluorescence leakage as described previously

(23). Intrinsic lipid curvatures were determined using a SAXSpace small-angle x-ray camera (Anton Paar, Graz, Austria) applying previously developed procedures (24). Monte Carlo (MC) simulations were performed using the Metropolis scheme and computationally efficient implicit-solvent coarse-grained models. Lipids were described by a three-bead model developed by Cooke and Deserno (25), and the peptide was modeled by a patchy spherocylinder (26). Free-energy calculations for peptide translocation were performed using the Wang-Landau method (27). For details of experimental and simulation procedures, see the Supporting Material.

RESULTS

Intrinsic curvatures of biomimetic membranes

We first determined estimates for J_0 of the studied lipids and their mixtures using SAXS as detailed in (24) (see also Supporting Material and Fig. S1 for x-ray data). Intrinsic curvatures relate to the elastic curvature energy stored in lipid membranes (see, e.g., (28)). The following lipid mixtures are relevant for the present study: POPE/POPG (3:1, mol/mol) as a mimic of the inner membrane of Gram-negative bacteria (29), and POPC/POPG (3:1, mol/mol) as an alternative and frequently used lipid-only model of bacterial membranes (see, e.g., (18,19)). Based on the intrinsic curvatures of the individual lipids (Table S2), we calculate, assuming linear additivity, a significantly negative value for POPE/POPG ($J_0^{mix} = -0.26$ nm^{-1}), whereas POPC/POPG is found to have $J_0^{mix} \sim 0$ (Table 1). To investigate the role of intrinsic curvature, we further studied lyso-PE/POPE/POPG (1.6:1.4:1, mol/mol/mol), which has an overall 3:1 PE/PG molar ratio but $J_0^{mix} \sim 0$. Two charge-neutral mimics of mammalian membranes were considered for testing the role of Coulomb interactions in addition to the effect of stored energy strain. Our choice was to use POPC and its 3:1 (mol/mol) mixture with cholesterol, which, because of the negative intrinsic curvature of cholesterol (24), has $J_0^{mix} = -0.14$ nm^{-1}, which served as a first-order approximate to mammalian plasma membranes.

Effect of intrinsic curvature and membrane charge

In the next step, we determined ANTS/DPX leakage in LUVs induced by L18W-PGLa, MG2a, and their equimolar mixture to exploit the effect of J_0 on AMP activity. The L18W-PGLa/MG2a mixture is motivated by previous studies (13) suggesting a pairwise interaction of the peptides to achieve synergism. In POPC/POPG ($J_0^{mix} \sim 0$), we found significant peptide activities (Fig. 2 *A*). Specifically, MG2a and L18W-PGLa were similarly permeabilizing vesicles at low concentrations, whereas L18W-PGLa was more effective than MG2a for $c_{peptide} \gtrsim 0.3$ μM. The equimolar L18W-PGLa/MG2a mixture, in turn, was less active than the peptides individually below that concentration, suggesting some antagonizing effect of unknown origin, but one

TABLE 1 Intrinsic Curvatures J_0^{mix} of Membrane Mimetics and Peptide Synergy Σ

Mimic (molar ratio)	J_0^{mix} [nm^{-1}]	Σ
POPE:POPG (3:1)	−0.258 ± 0.013	0.4 ± 0.1
POPC/POPG (3:1)	−0.012 ± 0.015	0.8 ± 0.2
lyso-PE/POPE/POPG (1.6:1.4:1)	−0.044 ± 0.059	1.3 ± 0.3
POPC	−0.022 ± 0.010	2.2 ± 0.4
POPC:Chol (3:1)	−0.140 ± 0.011	1.2 ± 0.3

For definition of Σ, see Eq. 1.

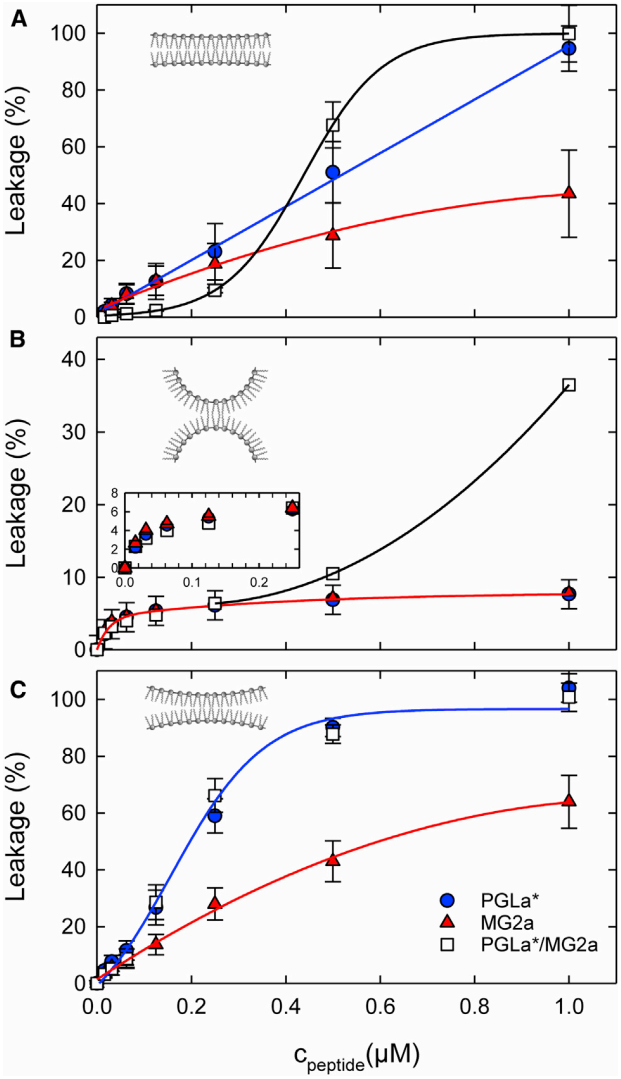

FIGURE 2 Leakage of POPC/POPG (3:1 mol/mol) (*A*), POPE/POPG (3:1 mol/mol) (*B*), and lyso-PE/POPE/POPG (1.6:1.4:1 mol/mol/mol) (*C*) LUVs as a function of L18W-PGLa and MG2a concentration, as well as their equimolar mixture. The lipid concentration was 50 μM. Experimental uncertainties are determined from three independent measurements. The solid lines are guides to the eye. The membrane insets in each panel represent the monolayer curvatures as determined in Table 1. To see this figure in color, go online.

which was reproduced in several replicas. The focus of the present report is at higher concentrations, however. Here, the peptide mixture was more active than L18W-PGLa and MG2a alone for $c_{peptide} \gtrsim 0.4$ μM. At $c_{peptide} = 1$ μM, leakage induced by just L18W-PGLa was within an experimental resolution equal to that of L18W-PGLa/MG2a.

In POPE/POPG vesicles, in turn, all studied combinations of peptides caused identical leakage ($\leq 6\%$) up to $c_{peptide} \approx 0.25$ μM and remained at the same level for the individual peptides at higher concentrations (Fig. 2 *B*). The peptide mixture, however, exhibited a strong increase of efficacy and was about six times more active than L18W-PGLa and MG2a alone at 1 μM. To see whether the different AMP activities are related to intrinsic curvature, we repeated the leakage assay for lyso-PE/POPE/POPG, which has the same lipid headgroup composition as POPE/POPG but $J_0^{mix} \sim 0$, just as POPC/POPG. Indeed, the peptides regained membrane-permeabilizing efficacy, with L18W-PGLa and L18W-PGLa/MG2a causing full LUV leakage at 1 μM concentration, just as observed for POPC/POPG (Fig. 2 *C*).

For mammalian mimics, in turn, our experiments revealed low activity for all peptides. L18W-PGLa exhibited the highest activity, although its maximal leakage did not exceed 10% within the studied concentration range for POPC (Fig. 3 *A*). The activity of the L18W-PGLa/MG2a was between that of L18W-PGLa and MG2a at all concentrations. Most likely this is related to the reduced number of L18W-PGLa molecules in the peptide mixture. Introducing cholesterol, which shifts J_0^{mix} to negative values, did not lead to an increase of activity of L18W-PGLa/MG2a relative to the peptide monomers as in POPE/POPG. Instead, the overall leakage dropped for all peptides almost to the noise level of the measurement (Fig. 3 *B*).

The diverse activities of the presently studied peptides can be summarized by the definition of a synergy parameter. For antimicrobial activity, this is usually based on the MIC (30). In analogy, we define

$$\Sigma = \frac{L_{L18W-PGLa} + L_{MG2a}}{L_{L18W-PGLa/MG2a}}, \quad (1)$$

where $L_{L18W\text{-}PGLa}$ and L_{MG2a} are the leakage values for the individual peptides at half of the peptide concentration used to determine the leakage $L_{L18W\text{-}PGLa/MG2a}$ of their mixture. Hence, $\Sigma < 0.5$ if both peptides act synergistically. Table 1 lists the results for the highest peptide concentration measured. Except for POPE/POPG, all model systems exhibited $\Sigma > 0.5$. This is consistent with a recent report on an increase of PGLa/MG2 synergy for PE/PG mixtures as compared to PC/PG (31). We thus conclude that L18W-PGLa/MG2a act synergistically only in POPE/POPG.

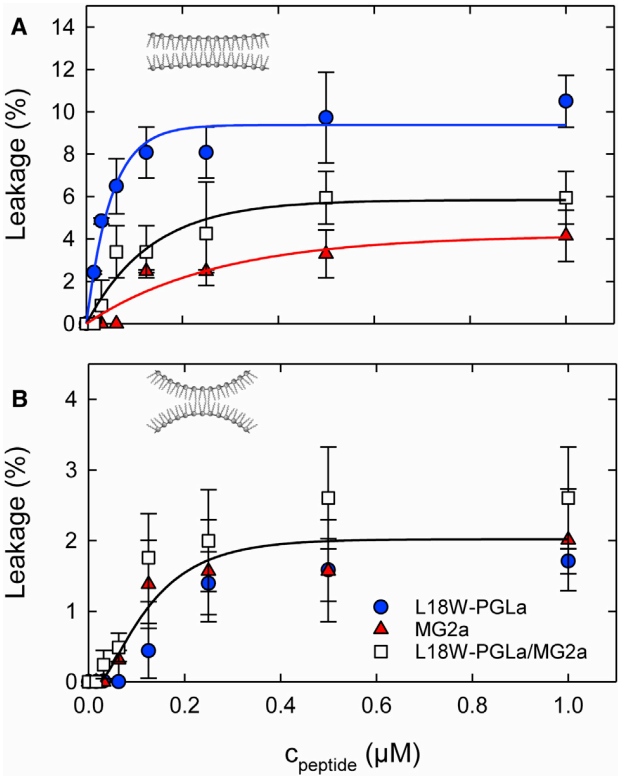

FIGURE 3 Leakage of POPC (*A*) and POPC/Chol (3:1 mol/mol) (*B*) LUVs as a function of L18W-PGLa, MG2a, and their equimolar mixture. The lipid concentration was 50 μM. Experimental uncertainties are determined from three independent measurements. The solid lines are guides to the eye. The membrane insets in each panel represent the monolayer curvatures as determined in Table 1. To see this figure in color, go online.

Effect of peptide dimerization

Synergistic effects of L18W-PGLa and MG2a have been proposed to result from pairwise peptide interaction in membranes (13). Following (16), we therefore constructed L18W-PGLa-MG2a heterodimers using L18W-PGL-GGCa and MG2-GGCa (Fig. 1). Further, L18W-PGL-GGCa and MG2-GGCa form in buffer solution (pH ~7) homodimers (15) as verified by SDS-PAGE (Fig. S2). This enabled us to compare the activities of the diverse magainin dimers. Fig. 4 *A* shows results from leakage experiments on POPE/POPG vesicles. In general, all dimers were able to permeabilize lipid bilayers more strongly than the equimolar mixture of L18W-PGLa and MG2a. More specifically, homodimers of L18W-PGLa and MG2a exhibited similar activities for $c_{peptide} < 0.1$ μM. At higher peptide concentrations, homodimers of L18W-PGLa exhibited a sigmoidal increase reaching nearly 100% leakage, whereas the activity of MG2a homodimers saturated at much lower leakage values (~60%). Turning to L18W-PGLa-MG2a heterodimers, we observed leakage superior to L18W-PGLa and MG2a homodimers already at

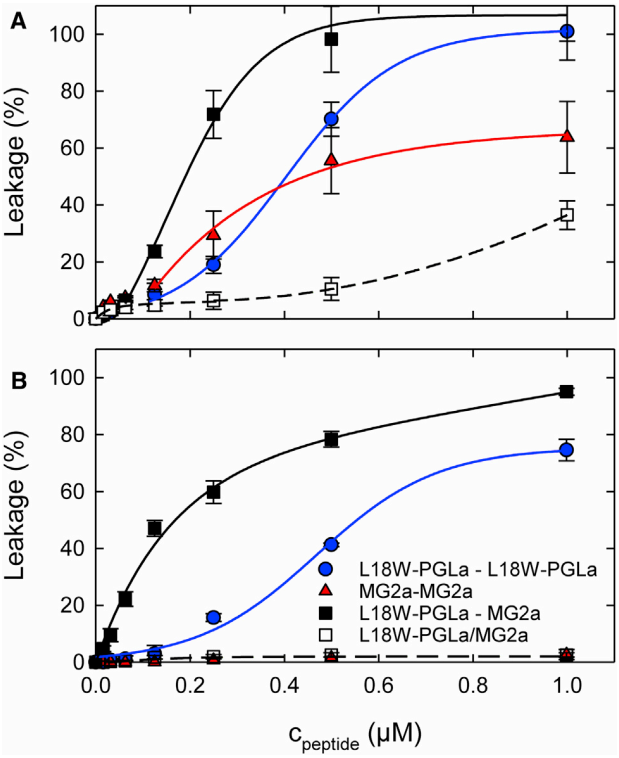

FIGURE 4 Dye release induced by L18W-PGLa/MG2a homodimers and heterodimers. (*A*) compares the activities of L18W-PGLa-L18W-PGLa and MG2a-MG2a homodimers, L18W-PGLa-MG2a heterodimers, and L18W-PGLa/MG2a equimolar mixtures in POPE/POPG LUVs. (*B*) presents results for the same peptides in POPC/Chol LUVs. Note that the results for MG2a homodimers and L18W-PGLa/MG2a are identical within experimental resolution. The lipid concentration was 50 μM. The lines are guides to the eye. To see this figure in color, go online.

low peptide concentration. Final leakage values at $c_{peptide} = 1$ μM were comparable to those of L18W-PGLa homodimers, however.

In the POPC/Chol mixture, effects were significantly different (Fig. 4 *B*). L18W-PGLa-MG2a heterodimers successfully permeabilized the LUVs and induced close to 100% leakage at 1 μM peptide concentration. L18W-PGLa homodimers were active above concentrations of 0.1 μM but reached only ~74% leakage at the highest concentration studied. In contrast, MG2a homodimers, just like L18W-PGLa/MG2a equimolar mixtures, were not able to induce significant dye release from the vesicles. Finally, we performed a control experiment on POPE/POPG vesicles by adding DTT (40 μM), which is known to reduce disulfide bonds (32), to the L18W-PGLa-L18W-PGLa solution before mixing the peptides with LUVs. This in situ transformation of L18W-PGLa homodimers to monomers resulted in permeabilization capabilities identical with that of L18W-PGLa peptide (Fig. S3). Thus, the membrane-lytic activity of L18W-PGLa can be increased strongly by chemical fixation as dimers.

Free energy of peptide translocation

To get deeper insight on the influence of intrinsic curvature on peptide insertion, we performed coarse-grained MC simulations on the translocation of an MG2a mimic through lipid bilayers of different J_0. The sign of intrinsic curvatures of the simulated systems corresponded to those of the measured systems and also included a system of positive intrinsic curvature (see Supporting Material). Simulations clearly show that membrane composition affects the free-energy profiles (Fig. 5). In particular, the system with the most negative J_0 exhibits the highest free-energy penalty for translocation of the peptide across the membrane. The barrier decreases significantly with shifting J_0 toward positive values, which makes the peptide translocation much easier. The translocation is mainly determined by the insertion step, which requires a change in orientation from a parallel to perpendicular/tilted peptide alignment with respect to the membrane surface. Note that the free-energy minimum corresponds to the peptide position in the membrane adsorbed state, which shifts progressively toward the membrane center with increasing J_0, i.e., positive curvature.

Antimicrobial activity of peptide monomers and dimers against *E. coli*

To correlate our results on membrane mimetics to biological activities toward bacteria, we determined the effect of peptides on *E. coli* growth. We observed distinct MIC values for the individual peptides (Fig. 6). In agreement with (16,31), we found synergistic activity of L18W-PGLa/MG2 mixtures ($\Sigma \sim 0.25$) as compared to single-peptide applications. Further, chemically fixed peptide homodimers were significantly more active than their

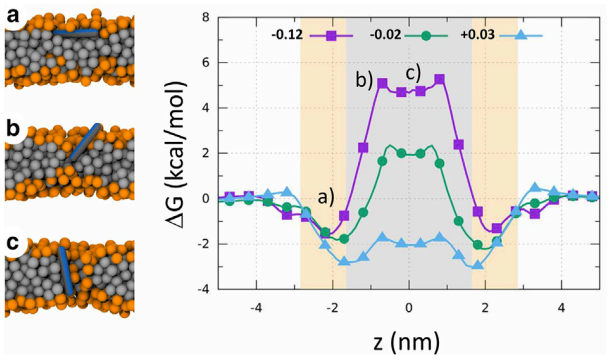

FIGURE 5 Calculated free energy profiles of peptide translocation across membranes with different intrinsic curvature (numbers in legend correspond to J_0 in nm^{-1}). The headgroup and tail regions are shown as orange and gray areas, respectively. The left-hand side shows simulation screen shots of the most important steps of peptide translocation: (*a*) surface adsorption, (*b*) peptide tilting, and (*c*) peptide insertion. To see this figure in color, go online.

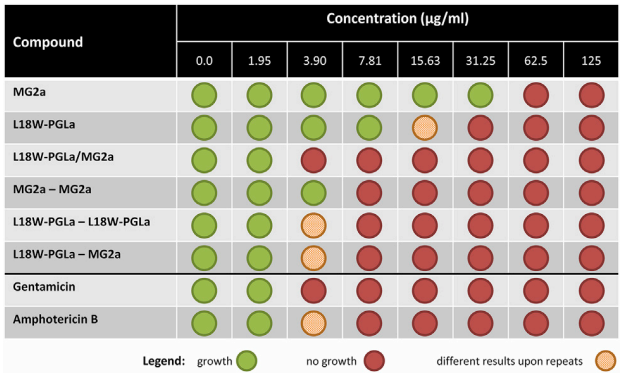

FIGURE 6 Effect of different magainins on the growth of *E. coli* K12. The antibiotics gentamicin and amphotericin B serve as positive controls. To see this figure in color, go online.

monomers. MG2a dimers reduced the MIC from 62.5 to 7.8 μg/mL and L18W-PGLa dimers from $\sim$31.25 to $\sim$7.8 μg/mL, respectively. In particular, L18W-PGLa homodimers exhibited the same efficacy as L18W-PGLa-MG2a heterodimers.

The MIC values can be compared qualitatively to our dye-release experiments on vesicles using the leakage intensities observed at the highest-measured peptide concentrations. Notably, the synergistic activity of the equimolar peptide mixture (Fig. 2 *B*), the similar activities of L18W-PGLa homodimers and L18W-PGLa-MG2a (Fig. 4 *A*), and the high efficacy of L18W-PGLa homodimers compared to individual L18W-PGLa peptide applications (Fig. S3) are well-captured by the POPE/POPG (3:1 mol/mol) mimic. Other features, such as the different antimicrobial activities of L18W-PGLa and MG2, as well as the almost equal efficacy of equimolar peptide mixtures and L18W-PGLa-MG2a hybrids, are not observed in our simple *E. coli* inner membrane mimics, which may be explained by the vastly more complex structure of the *E. coli* cell envelope that consists of an outer membrane, periplasm, and inner membrane. We emphasize, however, that the synergistic activity of L18W-PGLa and MG2a, which is the main focus of this work, is reproduced in POPE/POPG 3:1 (mol/mol).

We can further compare our leakage results on POPC/Chol vesicles to the peptide's hemolytic activity. Nishida et al. (16) reported a sixfold increase of erythrocyte hemolysis for PGLa-MG2a heterodimers as compared to the PGLa/MG2a equimolar mixture. Further, compared to single peptides, the heterodimer's hemolytic activity was even 40- to 60-fold increased. This latter result correlates qualitatively with our findings in POPC/Chol (3:1 mol/mol) vesicles, in which the heterodimers showed a 50 times higher activity than the L18W-PGLa/MG2a mixture (Fig. 4 *B*). Hence, POPC/Chol appears to be a reasonable first-order lipid-only model to estimate the hemolytic potential of magainins.

DISCUSSION

Synergism is coupled to negative intrinsic curvature

Coupling experimental data for intrinsic curvatures and AMP-induced ANTS/DPX dye release from selected lipid-only mimics of bacterial and mammalian membranes provided clear evidence for the delicate balance of membrane curvature elasticity, overall bilayer surface charge, and peptide properties in promoting or obstructing the synergistic activity of L18W-PGLa/MG2a mixtures. The synergism of PGLa and MG2 has been studied before by leakage assays on diverse lipid vesicles, showing significant enhancement of peptide activity for PGLa/MG2 equimolar mixtures (13,33).

Pronounced synergism was observed only in POPE/POPG bilayers (Fig. 2 *B*). The requirement of high peptide concentration to permeabilize PE-enriched bilayers may be additionally enhanced by extensive intermolecular H-bonding of PEs (34,35). Most interestingly, however, L18W-PGLa/MG2a synergism is fully abolished in lyso-PE/POPE/POPG (Fig. 2 *C*). This system was designed to have 1) the same overall charge as POPC/POPG and POPE/POPG, 2) the same headgroup composition as POPE/POPG (i.e., the same abilities to form H-bonds), and 3) the overall same intrinsic curvature as POPC/POPG ($J_0 \sim 0$). The loss of synergism in lyso-PE/POPE/POPG hence provides unambiguous evidence for a coupling to negative intrinsic curvature.

It has been recognized for some time that protein/peptide activity couples to intrinsic lipid curvatures (36–38). Intrinsic lipid curvature is a property of lipid monolayers (i.e., each membrane leaflet) that gives rise to an elastic energy stored in flat lipid bilayers (see, e.g., (39)), which may be released upon interaction with a membrane active compound (36). That is, lateral strain, in particular at the polar/apolar interface, is significantly larger for lipids with a more negative J_0, whereas lipid membranes with a positive J_0 have a looser polar/apolar interface. Membrane intrinsic curvature has been previously related to MG2 activity (40) or synergism (19). Conversely, the latter authors concluded that synergistic interactions between PGLa/MG2 are related to positive J_0 that would allow the peptides to penetrate into the bilayer more easily (19). This assessment was based on the assumption that synergism is related to the adoption of a tilted or inserted PGLa topology in the presence of MG2. This hypothesis has been cast into doubt by (41,42), which show that the peptides develop synergistic activities in an in-planar topology. Strandberg et al. (19) also notably reported mainly surface aligned PGLa/MG2 for POPC/POPG bilayers, whereas MG2-mediated PGLa insertion was reported only for lipid mixtures with disaturated hydrocarbon chains (17,19).

Based on our results, we agree with (17,19) that membranes with a more positive curvature facilitate peptide insertion into the bilayer interface because of reduced lateral stress at the bilayer's polar/apolar interface (i.e., looser

packing). However, at the same time, this hampers the development of synergy because both magainins are able to disrupt the polar/apolar interface at low energetic cost. POPE/POPG (3:1 mol/mol), in turn, displays substantial interfacial stress, and indeed both magainins did not induce significant vesicle leakage (Fig. 2 *B*). However, when applied as an equimolar mixture, they clearly showed synergy with $\Sigma = 0.4$ (Table 1), which is in good agreement with recent observations from Zerweck et al. (31). Corroborated by our MC simulations (Fig. 5), these findings strongly suggest an activation barrier for vesicle leakage, $\Delta G^{\ddagger}$, that is mediated by the interfacial packing density and hence lipid composition. In addition, synergy requires anionic lipids for increased affinity of peptides to the membrane surface. This is clearly demonstrated by POPC/Chol, which contains significant intrinsic negative curvature energies but resulted in a synergy parameter $\Sigma = 1.2$ (Table 1).

To appreciate the different activities of L18W-PGLa and MG2a, it is instructive to consider the energetics of membrane insertion based on the Wimley-White hydrophobicity scale (43). We thus calculated estimates for the Gibbs free energy of insertion into the bilayer nonpolar region (44)

$$\Delta G^{o}_{ins} \approx \Delta G^{o}_{f} + \Delta G^{o}_{oct} - \Delta G^{o}_{if} \approx \Delta G^{o}_{oct} - \Delta G^{o}_{if} = \Delta G^{o}_{oct-if}, \quad (2)$$

using the Membrane Protein Explorer (MPEx, http://blanco.biomol.uci.edu/mpex/), where ΔG^{o}_{f} is the free energy from peptide conformational changes in the aqueous phase (assumed to be insignificant), ΔG^{o}_{oct} is the free energy of peptide transfer from water to octanol, and ΔG^{o}_{if} is the free energy of binding to the membrane-water interface. Calculation of ΔG^{o}_{if} requires knowledge of the peptide's helicity taken up at the membrane surface. For charged membranes, electrostatic interactions need to be considered (45). However, corrections calculated via the Gouy-Chapman theory for melittin yielded the same surface-partition coefficient for charged and charge-neutral bilayers (45). For our semiquantitative discussion, it thus suffices to derive ΔG^{o}_{if} based on the peptide's helicity in PC bilayers (Table 2). Our ΔG^{o}_{ins} estimates show that L18W-PGLa has a higher propensity for being located within the membrane core than MG2a. This agrees with previous NMR data showing that PGLa may tilt into the bilayer core, whereas MG2 always remained parallel at the membrane surface (18,19).

TABLE 2 Thermodynamics of AMP Insertion in PC Membranes According to the Wimley-White Hydrophobicity Scale

	% helix in PC	ΔG^{o}_{if} (kcal/mol)	ΔG^{o}_{oct} (kcal/mol)	ΔG^{o}_{ins} (kcal/mol)	μ_H
MG2a	83[a]	−7.3	16.9	24.2	14.1
L18W-PGLa	72[b]	−6.1	16.2	22.3	10.9

The Wimley-White hydrophobicity scale is from Ref. (43).
[a]Taken from (66).
[b]Taken from (67).

To correlate these considerations with our leakage data, it is further necessary to consider $\Delta G^{\ddagger}$ as introduced above. Inspired by (44), we can draw a hypothetical energy path for AMP insertion and synergism (Fig. 7). In particular, the difference in ΔG_{if} between L18W-PGLa and MG2a (Table 2) should lead to a higher $\Delta G^{\ddagger}$ for MG2a in bilayers of equal lipid composition, which would explain why MG2a is always less active than L18W-PGLa. In the case of synergistic interaction between L18W-PGLa and MG2a, the activation barrier also appears to be lowered. We speculate in particular that the perturbation of the lipid bilayer by L18W-PGLa helps to lower $\Delta G^{\ddagger}$ for MG2a, which, because of its higher mean hydrophobic moment μ_H (Table 2), i.e., amphipathicity, will cause a stronger impairment of the bilayer's permeability barrier because of a larger mismatch with the polarity profile of the lipid bilayer. This agrees with a previous analysis of properties of α-helical antimicrobial peptides showing that their efficacy is dominated by their overall amphipathicity (46). Note that previous solid-state NMR measurements did not report on PGLa-mediated insertion of MG2 (18,19). However, detection of such states could have been impeded by a limited degree of sample hydration, which has been shown previously to significantly increase threshold concentrations for peptide insertion into lipid bilayers (see, e.g., (47)).

Synergism is not necessarily coupled to L18W-PGLa/MG2a pair formation

Motivated by a maximum of antimicrobial activity at equimolar peptide ratio, a number of studies claim that

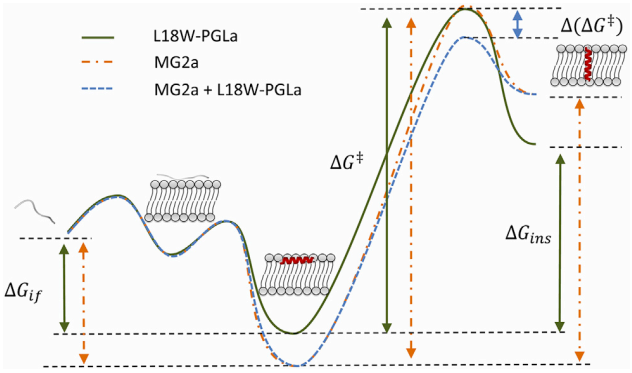

FIGURE 7 Schematic free-energy landscape with different states during the peptide-insertion process into a lipid bilayer, including adsorption to and folding at the membrane surface ΔG_{if}, as well as insertion into the hydrophobic core ΔG_{ins}, for which the peptide has to overcome an activation barrier $\Delta G^{\ddagger}$. Depending on the energy difference between the transition state ($\ddagger$) and the peptide's interfacial state, $\Delta G^{\ddagger}$ can vary significantly. ΔG_{if} is assumed to be smaller for L18W-PGLa than for MG2a. Synergistic interactions between the peptides may lower the barrier by $\Delta(\Delta G^{\ddagger})$. To see this figure in color, go online.

synergism of magainins is due to a pairwise interaction of the two AMPs (formation of physical heterodimers) in the presence of the lipid bilayer (13,15,16,33). Further, molecular dynamics simulations (48) and mutation studies (31) suggest that close contact interactions between glycine and alanine residues on PGLa support the formation of an antiparallel (physical) homodimer. Indeed, chemically cross-linked L18W-PGLa homodimers are almost as active as L18W-PGLa-MG2a heterodimers in POPE/POPG (Fig. 4 *A*). These results are in good agreement with several previous studies demonstrating that peptide aggregates (dimers) are in general—due to their larger size—significantly more perturbing bilayers than their monomers (see, e.g., (49–52)). Nishida et al. (16) argued that association of L18W-PGLa and MG2a is concentration-dependent and that cysteine-linked L18W-PGLa-MG2a mimic high peptide concentrations. However, even at our highest peptide concentration, which is ~5 times larger than that applied in (16), the heterodimers are still 2–3 times more effective than the equimolar L18W-PGLa/MG2a mixture. Considering that peptides diffuse in membranes at a similar rate to lipids (53,54), it thus occurs that L18W-PGLa/MG2a pairs should have formed rapidly on the time scale of our experiment. Thus, aggregation of L18W-PGLa and MG2a is not a strict prerequisite for developing synergism. In turn, our conclusion is in agreement with (41), who found that carboxyterminal-GGS or -GGA analogs of PGLa and MG2 are more active than PGLa/MG2a mixtures, although they are not able to form cysteine cross-links.

Correlation of membrane-lytic activities of magainins between plasma membrane mimics and live cells

The role of membrane lipid architecture in AMP selectivity has been extensively discussed before (see, e.g., (29)). One of the most obvious differences in lipid architecture is the absence of charged lipid species in the outer leaflet of mammalian plasma membranes, whereas bacterial plasma membranes contain anionic lipid species. Thus, attractive electrostatic interactions between cationic residues on AMP and anionic lipids are an essential first step of discrimination that has been already recognized for several years (for review, see, e.g., (6)). However, the effects of membrane elasticity in particular at the polar/apolar interface are of similar importance to consider. This is convincingly demonstrated by comparing the synergistic peptide activities found for POPE/POPG with the peptide activity on *E. coli*. For POPC/POPG, in turn, we found no such agreement. Moreover, the increased activity of L18W-PGLa-MG2a in POPC/Chol mixtures correlates well with their increased hemolysis of erythrocytes (16). We note, however, that other aspects, such as differences in L18W-PGLa and MG2a activities or the almost-equal killing efficacy of equimolar L18W-PGLa/MG2a mixtures and L18W-PGLa-MG2a heterodimers, are not mirrored in our leakage experiments on POPE/POPG (3:1 mol/mol) LUVs. This indicates limitations of the currently applied lipid-only model systems, which are unable to capture the full complexity of the *E. coli* cell envelope. We are currently developing more complex membrane mimetic systems.

CONCLUSION

We have provided experimental evidence for the significance of combining a negatively charged membrane surface with a tightly packed polar/apolar interface for synergistic interactions of L18W-PGLa and MG2a with lipid membranes. Tight packing of this interface is achieved here by POPE, which has a significant negative intrinsic curvature. Cardiolipin, which is also present in cytoplasmic membranes of Gram-negative bacteria (20) and which has negative J_0 in the presence of divalent ions (22), may further add to the interfacial packing strain. If bilayers have negligible overall intrinsic curvature, L18W-PGLa and MG2a permeabilize the membrane much more easily and do not develop synergism. This effect is expected to be even more pronounced for lipids with positive intrinsic curvature, which agrees well with previous observations (18,19). Consequently, "softening up" the polar/apolar interface by a concerted action of MG2a and L18W-PGLa appears to be the underlying mechanism of synergism for the two peptides. We speculate that L18W-PGLa is the "helper molecule" that preconditions the bilayer and thereby allows MG2a, which, due to its more pronounced amphipathicity, is less compatible with the distribution of polar and nonpolar moieties in lipid membranes, to increase its activity. In addition, synergism also requires electrostatic interactions between the peptides and membrane lipids to anchor the AMPs more strongly within the membrane interface. Importantly, however, pairwise interactions of L18W-PGLa and MG2a are not strictly required for this scenario, which is supported by our experiments on homo- and heterodimers of the two peptides and which agrees with a recent report (41). Additional effects, such as peptide-induced lipid phase separation, may further influence this mechanism. Corresponding experiments will be performed in our laboratory in the near future. The correlation of synergistic activity of L18W-PGLa and MG2a in *E. coli* with dye-release experiments in POPE/POPG LUVs but the inability to reproduce other features of AMP activity in bacteria strongly supports a proper choice of the lipid mimetic system for unraveling the biophysics of AMP-membrane interactions.

SUPPORTING MATERIAL

Supporting Materials and Methods, five figures, and two tables are available at http://www.biophysj.org/biophysj/supplemental/S0006-3495(18)30323-0.

AUTHOR CONTRIBUTIONS

R.L. performed research, analyzed data, and wrote the article. M.P. performed research and analyzed data. I.K. performed MC simulations. I.S. performed experiments on *E. coli*. D.E. performed research. R.V., G.P., and K.L. designed research and wrote the article.

ACKNOWLEDGMENTS

The authors thank Christopher Aisenbrey and Burkhard Bechinger for stimulating discussions.

This work was supported by the Austrian Science Fund FWF, project No. I 1763-B21 (to K.L.), as well as the Czech Science Foundation (grant 17-11571S to R.V.) and the Central European Institute of Technology 2020 (LQ1601) project, with financial contribution made by the Ministry of Education, Youths and Sports of the Czech Republic and special support paid from the National Programme for Sustainability II funds. Computational resources were provided by the CESNET LM2015042 and the IT4Innovations National Supercomputing Center–LM2015070, provided under the program Projects of Large Research, Development, and Innovations Infrastructures.

SUPPORTING CITATIONS

References (55–65) appear in the Supporting Material.

REFERENCES

1. Mayer, M. L., D. M. Easton, and R. E. W. Hancock. 2010. Fine tuning host responses in the face of infection: emerging roles and clinical applications of host defence peptides. *In* Antimicrobial Peptides: Discovery, Design and Novel Therapeutic Strategies. G. Wang, ed. CABI, pp. 195–220.
2. Steinstraesser, L., U. Kraneburg, …, S. Al-Benna. 2011. Host defense peptides and their antimicrobial-immunomodulatory duality. *Immunobiology.* 216:322–333.
3. Hancock, R. E., E. F. Haney, and E. E. Gill. 2016. The immunology of host defence peptides: beyond antimicrobial activity. *Nat. Rev. Immunol.* 16:321–334.
4. Wimley, W. C., and K. Hristova. 2011. Antimicrobial peptides: successes, challenges and unanswered questions. *J. Membr. Biol.* 239:27–34.
5. Lohner, K. 2017. Membrane-active antimicrobial peptides as template structures for novel antibiotic agents. *Curr. Top. Med. Chem.* 17:508–519.
6. Lohner, K., and S. E. Blondelle. 2005. Molecular mechanisms of membrane perturbation by antimicrobial peptides and the use of biophysical studies in the design of novel peptide antibiotics. *Comb. Chem. High Throughput Screen.* 8:241–256.
7. Henderson, J. M., and K. Y. C. Lee. 2013. Promising antimicrobial agents designed from natural peptide templates. *Curr. Opin. Solid State Mater. Sci.* 17:175–192.
8. Hoffmann, W., K. Richter, and G. Kreil. 1983. A novel peptide designated PYLa and its precursor as predicted from cloned mRNA of Xenopus laevis skin. *EMBO J.* 2:711–714.
9. Soravia, E., G. Martini, and M. Zasloff. 1988. Antimicrobial properties of peptides from Xenopus granular gland secretions. *FEBS Lett.* 228:337–340.
10. Zasloff, M. 1987. Magainins, a class of antimicrobial peptides from Xenopus skin: isolation, characterization of two active forms, and partial cDNA sequence of a precursor. *Proc. Natl. Acad. Sci. USA.* 84:5449–5453.
11. Williams, R. W., R. Starman, …, D. Covell. 1990. Raman spectroscopy of synthetic antimicrobial frog peptides magainin 2a and PGLa. *Biochemistry.* 29:4490–4496.
12. Westerhoff, H. V., M. Zasloff, …, D. Juretić. 1995. Functional synergism of the magainins PGLa and magainin-2 in Escherichia coli, tumor cells and liposomes. *Eur. J. Biochem.* 228:257–264.
13. Matsuzaki, K., Y. Mitani, …, K. Miyajima. 1998. Mechanism of synergism between antimicrobial peptides magainin 2 and PGLa. *Biochemistry.* 37:15144–15153.
14. Wieprecht, T., O. Apostolov, …, J. Seelig. 2000. Membrane binding and pore formation of the antibacterial peptide PGLa: thermodynamic and mechanistic aspects. *Biochemistry.* 39:442–452.
15. Hara, T., Y. Mitani, …, K. Matsuzaki. 2001. Heterodimer formation between the antimicrobial peptides magainin 2 and PGLa in lipid bilayers: a cross-linking study. *Biochemistry.* 40:12395–12399.
16. Nishida, M., Y. Imura, …, K. Matsuzaki. 2007. Interaction of a magainin-PGLa hybrid peptide with membranes: insight into the mechanism of synergism. *Biochemistry.* 46:14284–14290.
17. Tremouilhac, P., E. Strandberg, …, A. S. Ulrich. 2006. Synergistic transmembrane alignment of the antimicrobial heterodimer PGLa/magainin. *J. Biol. Chem.* 281:32089–32094.
18. Salnikov, E. S., and B. Bechinger. 2011. Lipid-controlled peptide topology and interactions in bilayers: structural insights into the synergistic enhancement of the antimicrobial activities of PGLa and magainin 2. *Biophys. J.* 100:1473–1480.
19. Strandberg, E., J. Zerweck, …, A. S. Ulrich. 2013. Synergistic insertion of antimicrobial magainin-family peptides in membranes depends on the lipid spontaneous curvature. *Biophys. J.* 104:L9–L11.
20. Wilkinson, S. G. 1988. Gram-negative bacteria. *In* Microbial Lipids S. G. Wilkinson, and C. Ratledge, eds. . Academic Press, pp. 299–488.
21. Morein, S., A. Andersson, …, G. Lindblom. 1996. Wild-type Escherichia coli cells regulate the membrane lipid composition in a "window" between gel and non-lamellar structures. *J. Biol. Chem.* 271:6801–6809.
22. Chen, Y. F., K. Y. Tsang, …, Z. A. Fan. 2015. Differential dependencies on [Ca2+] and temperature of the monolayer spontaneous curvatures of DOPE, DOPA and cardiolipin: effects of modulating the strength of the inter-headgroup repulsion. *Soft Matter.* 11:4041–4053.
23. Zweytick, D., G. Deutsch, …, K. Lohner. 2011. Studies on lactoferricin-derived Escherichia coli membrane-active peptides reveal differences in the mechanism of N-acylated versus nonacylated peptides. *J. Biol. Chem.* 286:21266–21276.
24. Kollmitzer, B., P. Heftberger, …, G. Pabst. 2013. Monolayer spontaneous curvature of raft-forming membrane lipids. *Soft Matter.* 9:10877–10884.
25. Cooke, I. R., K. Kremer, and M. Deserno. 2005. Tunable generic model for fluid bilayer membranes. *Phys. Rev. E Stat. Nonlin. Soft Matter Phys.* 72:011506.
26. Vácha, R., and D. Frenkel. 2011. Relation between molecular shape and the morphology of self-assembling aggregates: a simulation study. *Biophys. J.* 101:1432–1439.
27. Wang, F., and D. P. Landau. 2001. Efficient, multiple-range random walk algorithm to calculate the density of states. *Phys. Rev. Lett.* 86:2050–2053.
28. Marsh, D. 1996. Intrinsic curvature in normal and inverted lipid structures and in membranes. *Biophys. J.* 70:2248–2255.
29. Lohner, K., E. Sevcsik, and G. Pabst. 2008. Liposome-based biomembrane mimetic systems: implications for lipid-peptide interactions. *In* Advances in Planar Lipid Bilayers and Liposomes (Vol. 6). A. Leitmannova-Liu, ed. Elsevier, pp. 103–137.
30. Meletiadis, J., S. Pournaras, …, T. J. Walsh. 2010. Defining fractional inhibitory concentration index cutoffs for additive interactions based on self-drug additive combinations, Monte Carlo simulation analysis, and in vitro-in vivo correlation data for antifungal drug combinations against Aspergillus fumigatus. *Antimicrob. Agents Chemother.* 54:602–609.

31. Zerweck, J., E. Strandberg, …, A. S. Ulrich. 2017. Molecular mechanism of synergy between the antimicrobial peptides PGLa and magainin 2. *Sci. Rep.* 7:13153.
32. Liang, H. P., T. M. Brophy, and P. J. Hogg. 2011. Redox properties of the tissue factor Cys186-Cys209 disulfide bond. *Biochem. J.* 437:455–460.
33. Zerweck, J., E. Strandberg, …, A. S. Ulrich. 2016. Homo- and heteromeric interaction strengths of the synergistic antimicrobial peptides PGLa and magainin 2 in membranes. *Eur. Biophys. J.* 45:535–547.
34. Boggs, J. M. 1980. Intermolecular hydrogen bonding between lipids: influence on organization and function of lipids in membranes. *Can. J. Biochem.* 58:755–770.
35. Pink, D. A., S. McNeil, …, M. J. Zuckermann. 1998. A model of hydrogen bond formation in phosphatidylethanolamine bilayers. *Biochim. Biophys. Acta.* 1368:289–305.
36. Koller, D., and K. Lohner. 2014. The role of spontaneous lipid curvature in the interaction of interfacially active peptides with membranes. *Biochim. Biophys. Acta.* 1838:2250–2259.
37. Dan, N., and S. A. Safran. 1998. Effect of lipid characteristics on the structure of transmembrane proteins. *Biophys. J.* 75:1410–1414.
38. Botelho, A. V., N. J. Gibson, …, M. F. Brown. 2002. Conformational energetics of rhodopsin modulated by nonlamellar-forming lipids. *Biochemistry.* 41:6354–6368.
39. Shearman, G. C., O. Ces, …, J. M. Seddon. 2006. Inverse lyotropic phases of lipids and membrane curvature. *J. Phys. Condens. Matter.* 18:S1105–S1124.
40. Matsuzaki, K., K. Sugishita, …, R. M. Epand. 1998. Relationship of membrane curvature to the formation of pores by magainin 2. *Biochemistry.* 37:11856–11863.
41. Glattard, E., E. S. Salnikov, …, B. Bechinger. 2016. Investigations of the synergistic enhancement of antimicrobial activity in mixtures of magainin 2 and PGLa. *Biophys. Chem.* 210:35–44.
42. Marquette, A., E. S. Salnikov, …, B. Bechinger. 2016. Magainin 2-PGLa interactions in membranes - two peptides that exhibit synergistic enhancement of antimicrobial activity. *Curr. Top. Med. Chem.* 16:65–75.
43. White, S. H., and W. C. Wimley. 1999. Membrane protein folding and stability: physical principles. *Annu. Rev. Biophys. Biomol. Struct.* 28:319–365.
44. Almeida, P. F., and A. Pokorny. 2009. Mechanisms of antimicrobial, cytolytic, and cell-penetrating peptides: from kinetics to thermodynamics. *Biochemistry.* 48:8083–8093.
45. Beschiaschvili, G., and J. Seelig. 1990. Melittin binding to mixed phosphatidylglycerol/phosphatidylcholine membranes. *Biochemistry.* 29:52–58.
46. Pathak, N., R. Salas-Auvert, …, R. G. Harrison. 1995. Comparison of the effects of hydrophobicity, amphiphilicity, and alpha-helicity on the activities of antimicrobial peptides. *Proteins.* 22:182–186.
47. Huang, H. W., and Y. Wu. 1991. Lipid-alamethicin interactions influence alamethicin orientation. *Biophys. J.* 60:1079–1087.
48. Ulmschneider, J. P., J. C. Smith, …, E. Strandberg. 2012. Reorientation and dimerization of the membrane-bound antimicrobial peptide PGLa from microsecond all-atom MD simulations. *Biophys. J.* 103:472–482.
49. Takei, J., A. Remenyi, and C. E. Dempsey. 1999. Generalised bilayer perturbation from peptide helix dimerisation at membrane surfaces: vesicle lysis induced by disulphide-dimerised melittin analogues. *FEBS Lett.* 442:11–14.
50. Dempsey, C. E., S. Ueno, and M. B. Avison. 2003. Enhanced membrane permeabilization and antibacterial activity of a disulfide-dimerized magainin analogue. *Biochemistry.* 42:402–409.
51. Lorenzón, E. N., N. A. Santos-Filho, …, E. M. Cilli. 2016. C-terminal lysine-linked magainin 2 with increased activity against multidrug-resistant bacteria. *Protein Pept. Lett.* 23:738–747.
52. Verly, R. M., J. M. Resende, …, B. Bechinger. 2017. Structure and membrane interactions of the homodimeric antibiotic peptide homotarsinin. *Sci. Rep.* 7:40854.
53. Frey, S., and L. K. Tamm. 1990. Membrane insertion and lateral diffusion of fluorescence-labelled cytochrome c oxidase subunit IV signal peptide in charged and uncharged phospholipid bilayers. *Biochem. J.* 272:713–719.
54. Gambin, Y., R. Lopez-Esparza, …, W. Urbach. 2006. Lateral mobility of proteins in liquid membranes revisited. *Proc. Natl. Acad. Sci. USA.* 103:2098–2102.
55. Broekhuyse, R. M. 1968. Phospholipids in tissues of the eye. I. Isolation, characterization and quantitative analysis by two-dimensional thin-layer chromatography of diacyl and vinyl-ether phospholipids. *Biochim. Biophys. Acta.* 152:307–315.
56. Buboltz, J. T., and G. W. Feigenson. 1999. A novel strategy for the preparation of liposomes: rapid solvent exchange. *Biochim. Biophys. Acta.* 1417:232–245.
57. Rieder, A. A., D. Koller, …, G. Pabst. 2015. Optimizing rapid solvent exchange preparation of multilamellar vesicles. *Chem. Phys. Lipids.* 186:39–44.
58. Alley, S. H., O. Ces, …, R. H. Templer. 2008. X-ray diffraction measurement of the monolayer spontaneous curvature of dioleoylphosphatidylglycerol. *Chem. Phys. Lipids.* 154:64–67.
59. Leikin, S., M. M. Kozlov, …, R. P. Rand. 1996. Measured effects of diacylglycerol on structural and elastic properties of phospholipid membranes. *Biophys. J.* 71:2623–2632.
60. Israelachvili, J. N. 2011. Intermolecular and Surface Forces, Third Edition. Academic Press, Burlington, MA.
61. Ellens, H., J. Bentz, and F. C. Szoka. 1985. H+- and Ca2+-induced fusion and destabilization of liposomes. *Biochemistry.* 24:3099–3106.
62. Ladokhin, A. S., W. C. Wimley, and S. H. White. 1995. Leakage of membrane vesicle contents: determination of mechanism using fluorescence requenching. *Biophys. J.* 69:1964–1971.
63. Laemmli, U. K. 1970. Cleavage of structural proteins during the assembly of the head of bacteriophage T4. *Nature.* 227:680–685.
64. Frenkel, D., and B. Smit. 2002. Understanding Molecular Simulation. Academic Press, San Diego, CA.
65. Mueller, J. H., and J. Hinton. 1941. A protein-free medium for primary isolation of the gonococcus and meningococcus. *Proc. Soc. Exp. Biol. Med.* 48:330–333.
66. Gesell, J., M. Zasloff, and S. J. Opella. 1997. Two-dimensional 1H NMR experiments show that the 23-residue magainin antibiotic peptide is an α-helix in dodecylphosphocholine micelles, sodium dodecylsulfate micelles, and trifluoroethanol/water solution. *J. Biomol. NMR.* 9:127–135.
67. Bechinger, B., M. Zasloff, and S. J. Opella. 1998. Structure and dynamics of the antibiotic peptide PGLa in membranes by solution and solid-state nuclear magnetic resonance spectroscopy. *Biophys. J.* 74:981–987.

Biophysical Journal, Volume *114*

Supplemental Information

Synergism of Antimicrobial Frog Peptides Couples to Membrane Intrinsic Curvature Strain

Regina Leber, Michael Pachler, Ivo Kabelka, Irene Svoboda, Daniel Enkoller, Robert Vácha, Karl Lohner, and Georg Pabst

Supplementary Information

Synergism of Antimicrobial Frog Peptides Couples to Membrane Intrinsic Curvature Strain

Regina Leber, Michael Pachler, Ivo Kabelka, Irene Svoboda, Daniel Enkoller, Robert Vácha, Karl Lohner, and Georg Pabst

PREPARATION OF LIPOSOMES

Lipid films (20 mg total lipid) for dye-release experiments were prepared by mixing the appropriate amounts of dissolved phospholipids before evaporation of solvents under a stream of nitrogen and stored in vacuum overnight. After addition of Hepes buffer containing the fluorophor/quencher ANTS/DPX (10 mM Hepes, 68 mM NaCl, 12.5 mM ANTS, 45 mM DPX, pH 7.4), formation of lipid vesicles was achieved by equilibration at 15°C above the lipid's melting temperature and intermittent vigorous vortex mixing. PE/PG-mixtures were additionally homogenized by six freeze/thaw-cycles. Large unilamellar vesicles (LUVs) were obtained by 25 cycles of extrusion of the hydrated liposomes through a polycarbonate filter (Millipore-Isopore^{TM}, Merck, Vienna) of 0.1 µm pore size above the lipid's melting temperature. Non-encapsulated fluorophore and quencher were removed by size-exclusion chromatography using SephadexTM G-75 (Sigma-Aldrich, Vienna) gel as described earlier (1). LUVs were eluted with Hepes buffer (10 mM Hepes, 140 mM NaCl, pH 7.4). Liposomal lipids were quantified by the determination of lipid phosphorus according the method described by (2). The final LUV concentration for dye-release experiments was adjusted to 50 µM in Hepes buffer (10 mM Hepes, 140 mM NaCl, pH 7.4).

PREPARATION AND ANALYSIS OF INVERTED HEXAGONAL PHASES BY SAXS

Samples for X-ray analysis were prepared by rapid solvent exchange (RSE) (3) using an adapted method that allows control of temperature (4). Here we focus in particular on the intrinsic curvatures of POPG and lyso-PE, whose values have to the best of our knowledge not been reported before. Both lipids do not form H_{II} phases and were therefore mixed with DOPE at various amounts as detailed above. In brief, appropriate amounts of lipid stock solution were pipetted into test tubes containing NaPi buffer (20 mM Na-phosphate, 130 mM NaCl, pH 7.4) and which were pre-equilibrated at a given temperature. The test tubes were quickly mounted onto the RSE apparatus, setting the argon flow to 60 ml/min and the vortex speed to 1000-1200 rpm. Rapid evaporation was initiated by opening the valve to a vacuum

pump set to a pressure in between the vapor pressure of solvent and water leading to the formation of lipid aggregates. Sample preparation was terminated after six minutes. Details of RSE settings are listed in supplementary Table S1. Control experiments using ^{1}H NMR showed no contamination of the samples with organic solvent.

Table S1: Settings used for the rapid solvent exchange.

Lipids	Temperature [°C]	Pressure [mbar]	Vortex speed [U/min]
DOPE	45	200	1200
POPG/DOPE	60	300	1000
lyso-PE/DOPE	70	900	1000
POPE	55	360	1000

All samples contained 12 wt% tricosene, which is needed to reduce the packing frustration of the inverted hexagonal phase (H_{II}) (see, e.g., (5)). This effect decreases the lamellar-to-H_{II} phase transition of POPE close to room temperature (6). POPG and lyso-PE do not form H_{II} phases. Therefore they were mixed with DOPE at various concentrations using a previously reported protocol (6). Samples containing DOPE and POPG were measured immediately after preparation, while lyso-PE containing samples were equilibrated for three days at room temperature in argon atmosphere to avoid lipid oxidation.

SAXS measurements were performed using a SAXSpace compact camera from Anton Paar (Austria), equipped with a Pilatus 100K-S detector system (Dectris, Switzerland) and a Genix 3D microfocus X-ray generator from Xenocs (Grenoble, France) [beam-size (Cu-Kα): ~ 300 µm (diameter)]. A scattering vector range of q = 0.6 nm^{-1} o 10.9 nm^{-1} was covered by setting the sample-to-detector distance to 308 mm. Temperature control was provided by a Peltier unit to within ± 0.1 °C. All samples were transferred into a paste cell holder (Anton Paar, Austria) and equilibrated for 10 minutes at 35°C before exposing to X-rays for one hour. Data reduction was performed with SAXStreat (Anton Paar, Austria). Note that temperature dependencies of intrinsic curvatures are in the range of $\frac{\Delta J_0}{T} = -1 \times 10^{-3}$ nm^{-1}/K^{-1} to -3×10^{-3} nm^{-1}/K^{-1} (6). Temperature corrections to adjust the here reported J_0's to 37°C used for vesicle leakage assays are consequently within experimental error.

SAXS data analysis was performed according to Kollmitzer et al. (6). In brief, intensities and peak positions of H_{II} phase patterns $I_{h,k}$ were used to construct electron density maps

$$\rho(\vec{r}) = \sum_{h,k} \alpha_{h,k} \sqrt{\frac{I_{h,k} q_{h,k}^2}{m_{h,k}}} \cos\left(2\pi \overrightarrow{q_{h,k}}\, \vec{r}\right), \quad \text{(S1)}$$

where *h*, *k* are the Miller indices, $m_{h,k}$ is the multiplicity of equivalent diffraction planes and $\alpha_{h,k}$ is the phase. Subsequently, electron density maps were radially integrated over azimuthal angles between 0° and 60° to yield one-dimensional electron density profiles. The maximum of these profiles was fitted with a Gaussian to determine the position of the lipid headgroup R_p. The intrinsic curvature $J_0 = -1/R_0$ is then determined by finding the position of the neutral plane $R_0 = R_p + d_{H1}$ (7), which is assumed to be located at the glycerol backbone (6). Specifically, we used $d_{H1} = 0.44$ nm as estimate for the distance between the lipid heads and the backbone (6).

The intrinsic curvature of non H_{II}-phase forming lipids was estimated assuming linear additivity using

$$J_0 = \frac{J_0^{mix} - (1-\chi) J_0^{DOPE}}{\chi}, \quad \text{(S2)}$$

where χ is the mole fraction of the respective 'guest' lipid in DOPE, which is used as a H_{II}-phase forming template ('host'). To increase the reliability of the J_0 estimates for guest lipids several guest/host mixtures were measured and interpolated, ensuring full miscibility of the guest lipids within the host structure (Fig. S1) and (6).

Figure S1 shows the SAXS patterns of 9:1 (molar ratio) lipid mixtures used to calculate J_0. The intrinsic curvatures of both DOPE mixtures increased with concentration of the guest lipid (Fig. S1, insert), albeit stronger for lyso-PE, as can be expected from its cone-like molecular shape, due to the difference of projected lateral areas of the PE head and the single hydrocarbon chain (8). The resulting J_0's for all lipids relevant for this study are listed in Tab. S2. In agreement with the qualitative assessment based on the molecular shape we found a significant positive J_0 for lyso-PE, while J_0 of POPG was, within experimental uncertainty, essentially zero. In order to test the effect of buffer on intrinsic lipid curvatures we also measured POPE, which readily forms in the presence of 12 wt.% tricosene a H_{II} phase at 35°C (Fig. S1), see also (6). The derived J_0 = -0.35 nm^{-1} is slightly more negative than our previously reported value. We attribute this to the effect of buffer ions on PE headgroup hydration, which is further supported by a similar decrease of J_0 for DOPE (-0.45 nm^{-1}) as compared to the value found in pure water (6). For the present study such subtleties are, however, of less significance. Here we are interested in estimates for net intrinsic curvatures

of lipid mixtures, which were calculated by their molecular averages upon assuming linear additivity

$$J_0^{mix} = \sum_i \chi_i J_0^{(i)}. \quad (3)$$

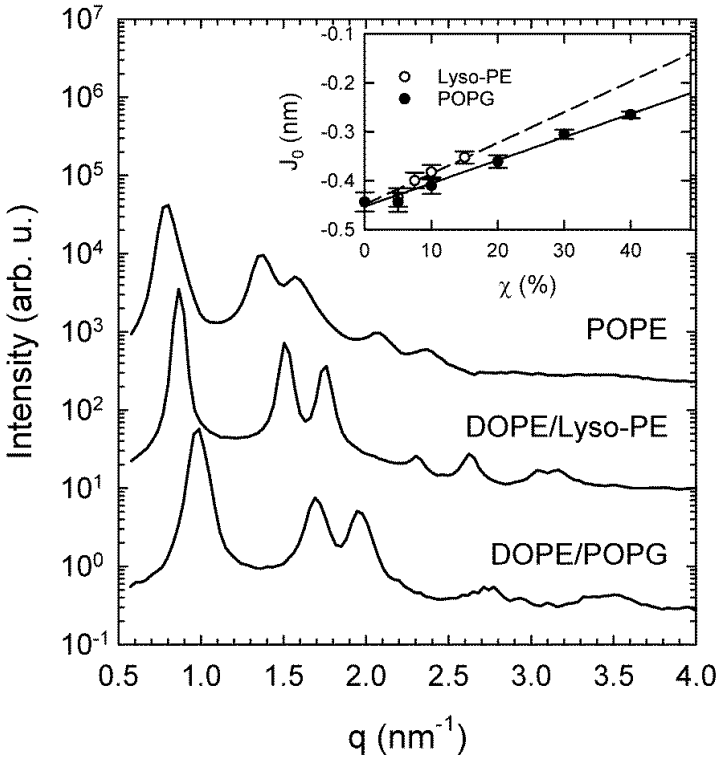

Figure S1: SAXS patterns of DOPE/POPG (9:1 mol/mol), DOPE/lyso-PE (9:1 mol/mol) and POPE at 35°C. All samples contained 12 wt% tricosene. Data are offset vertically for clarity of presentation. The insert shows the change of intrinsic curvatures as a function of POPG and lyso-PE concentration in DOPE, which is used to estimate their J_0's.

Table S2: Intrinsic curvatures of presently studied lipids at 35°C.

Lipid	J_0 **[nm^{-1}]**
lyso-PE	0.180 ± 0.123
POPG	0.020 ± 0.030
POPE	-0.350 ± 0.007
POPC*	-0.022 ± 0.010
Chol*	-0.494 ± 0.013

* Data taken from ref. (6)

FLUORESCENCE SPECTROSCOPY - LEAKAGE ASSAY

Leakage of the aqueous content of ANTS/DPX-loaded LUVs upon incubation with peptides was determined according to (9) and as detailed previously (1). Briefly, 2 ml of LUV suspension was filled into quartz cuvettes and equilibrated at 37°C for 5 minutes. Incremental amounts of peptide solutions prepared in Hepes buffer were added to the LUV suspension with µ-pipettes and mixed using a magnetic stirrer to achieve final peptide concentrations ranging from 0.016 - 1 µM, corresponding to peptide-to-lipid molar ratios from 1:3200 to 1:50. Fluorescence emission was recorded 5 minutes before and after the addition of peptides on a Cary Eclipse Fluorescence Spectrophotometer (Varian Inc., now Agilent Technologies, California, US) using an excitation wavelength of λ_{ex} = 360 nm and an emission wavelength λ_{em} = 530 nm. The slit widths for excitation and emission monochromators were set to 10 nm. Percentage of leakage was calculated from the fraction of the leakage (10)

$$I_F = \frac{(F-F_0)}{(F_{max}-F_0)}, \qquad \text{(S4)}$$

where F is the measured fluorescence, F_0 is the initial fluorescence without peptide, and F_{max} is the fluorescence corresponding to 100% leakage gained by addition of 1% Triton X-100.

SODIUM DODECYL SULFATE POLYACRYLAMIDE GEL ELECTROPHORESIS (SDS-PAGE)

In order to verify the dimeric or monomeric state of peptides, 2 µg of peptides were dissolved in loading buffer without DTT and separated by a one-dimensional SDS-PAGE using 5 % stacking and 18 % separating gels according to the method of Laemmli (11). Peptides were stained for 30 min with Coomassie brilliant blue after electrophoretic separation (11). An ultra-low range molecular weight marker was used to estimate the size of peptides after separation via SDS-PAGE. Experiments show that L18W-PGL-GGCa and MG2-GGCa form homodimers in buffer solution (pH ~ 7) (Fig. S2), in agreement with (12). Application of DTT leads to a drop of peptide activity to levels observed for single peptides, consistent with monomer formation (Fig. S3).

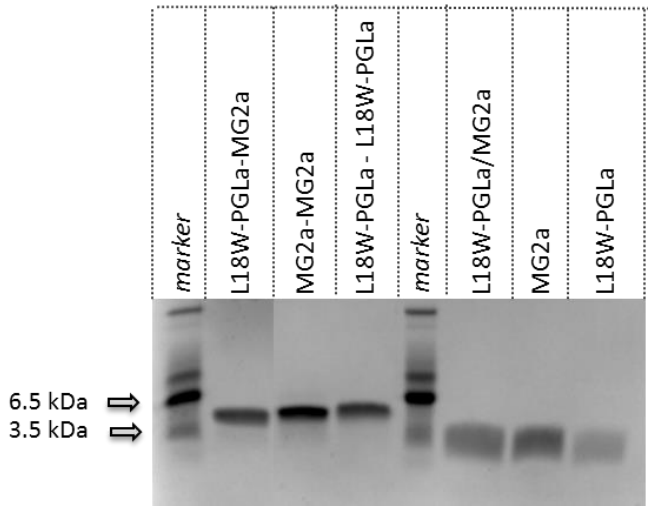

Figure S2: SDS-PAGE verifying dimeric and monomeric forms of magainins

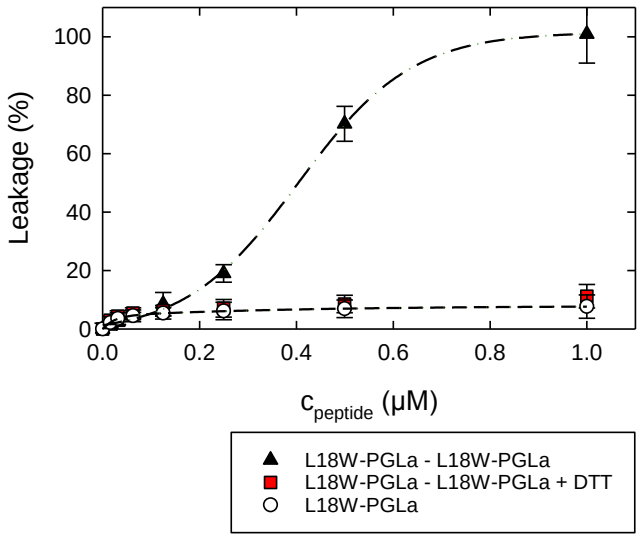

Figure S3: Effect of DTT addition to L18W-PGLa homodimers on leakage of POPE/POPG 3:1 mol/mol LUVs. For comparison, leakage induced by L18W-PGLa is shown as well (see also Fig. 2 *B*). The lipid concentration was 50 µM. Lines are guides to the eye.

MC SIMULATIONS

Monte Carlo simulations were performed using the Metropolis scheme and computationally efficient implicit solvent coarse-grained models. Sizes and distances of the models were calculated in reduced units, which (based on real particle dimensions) roughly translate to nm. The studied systems were composed of 200 lipid molecules and a single peptide. Lipids were

described by a three-bead model developed by Cooke and Deserno (13), using one bead for the head group of diameter d_h and two beads for tails each of diameter d_t (Fig. S4 *A*).

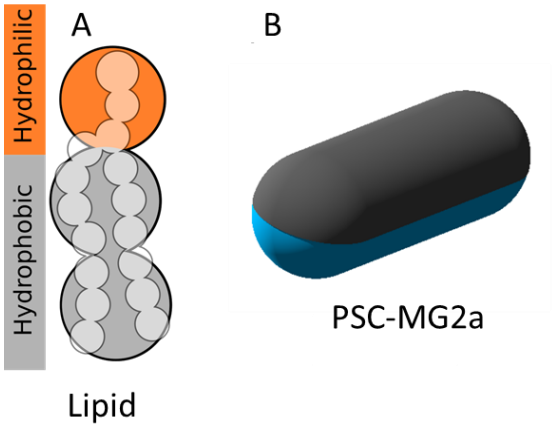

Figure S4: Schematic representations of the employed models. Panel A: Three-bead lipid model with lipid mapping (shown as silhouette). Panel B: PSC model of MG2a. Hydrophobic patches/regions are represented in grey, while orange and blue depict hydrophilic parts of lipid and peptide, respectively.

Three lipids with different intrinsic curvatures were simulated by variation of headgroup size (Fig. S5). The size of head bead affects J_0. Assuming cylindrical geometry of lipids one can calculate the intrinsic curvature by (14)

$$J_0 = \frac{2}{l}\left(1 - \frac{V}{A_h l}\right), \tag{S5}$$

where l is the length of the hydrophobic tails, A_h is the effective headgroup area and V is the hydrocarbon chain volume. However, there are more possibilities to calculate the l and $V/(A_h l)$. The first possibility is based on the geometry of individual molecules with $A_h = \pi d_h^2/4$, $V = \pi d_t^2 l/4$, and $l = 2d_t$. For $d_h = 0.85$ nm, 0.95 nm and 1.05 nm, this results for $d_t = 1$ nm in $J_0 = -0.38$ nm^{-1}, -0.11 nm^{-1}, and $+0.09$ nm^{-1}, respectively. However, this considers only excluded volume interactions between lipid molecules in ideal configuration. We therefore adhere to the second possibility, which derives J_0 from MC simulations and consequently include also contributions from temperature and the lipid parametrization (bonds, bending, and tail attraction). In this case the length of hydrophobic tails is calculated from the average distance of headgroup beads from the bilayer center, i.e. $d_l = 2.5$ nm. The headgroup areas are derived from the simulation box size of the equilibrated membrane at zero tension, which yields $A_h = 1.025$ nm^2, 1.145 nm^2 and 1.215 nm^2 with increasing d_h. Assuming that $A_h \propto d_h^2$ we can interpolate the headgroup area to perfectly cylindrical lipids (i.e., $d_h = d_t$ and $J_0 = 0$), yielding $A_h^0 = 1.176$ nm^2. Consequently Eq. (S5) is modified to

$$J_0 = \frac{2}{l}\left(1 - \frac{A_h^0}{A_h}\right), \quad \text{(S6)}$$

leading to $J_0 = -0.12$ nm^{-1}, -0.02 nm^{-1}, and $+0.03$ nm^{-1} for $d_h = 0.85$ nm, 0.95 nm and 1.05 nm, respectively. The lipid with the largest headgroup leads to $J_0 > 0$.

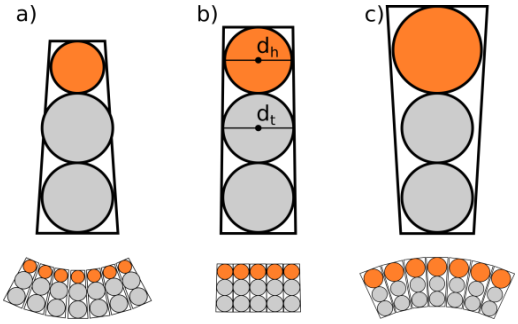

Figure S5: Schematic representation of lipid shape and induced curvature. Diameters of lipid heads and tails are denoted as d_h and d_t, respectively, with d_t = 1 nm. Conical lipids a) and c) had d_h = 0.85 and 1.05 nm, respectively. For cylindrical lipids b) d_h = 0.95 nm. The corresponding intrinsic curvatures are a) J_0 = -0.12 nm^{-1}, b) J_0 = -0.02 nm^{-1}, and c) J_0 = +0.03 nm^{-1}.The induced curvature is shown below each lipid. Differences in headgroup sizes are magnified for clarity.

The peptide was modelled by a patchy spherocylinder (PSC) (15), setting the peptide length to 4 nm and its diameter to 1 nm to roughly match the size and polarity of MG2a, i.e. half of the peptide surface was hydrophobic (Fig. S4 *B*). At either side of the patch, there is a 5° switching range to linearly scale the interaction potential to zero. The remaining surface is purely repulsive and thus considered to be hydrophilic. For more details on the model, see (15).

To mimic the hydrophobic effect, effective tail-tail interactions were used to drive membrane self-assembly leading to an effective attractive potential with a cos^2 profile. Further, the same potential was used to describe interactions between lipid tails and the peptide's hydrophobic patch. Repulsive interactions were modeled by Weeks-Chandler-Anderson (shifted and truncated Lennard-Jones) potential. The PSC-MG2a switching range between hydrophobic and hydrophilic surfaces was set to 1.0 nm. As described in the original article, the switching range of lipids was extended to 1.6 nm to keep the membrane in the fluid phase (13). The depth of the attractive potential well was -1 kT (k is the Boltzmann constant and T is the temperature) for lipid-tail particles and -1 kT per unit length of PSC line segment.

The membrane bilayer was assembled in the XY-plane of a rectangular box. The initial box size was about 11 × 11 × 50 nm. Periodic boundary conditions were applied in all three

dimensions, forming “infinite” membrane plane. Simulations were performed under constant temperature and number of particles, while keeping zero lateral tension in the XY-plane. We used standard MC trial moves to move the peptide/lipid beads/whole lipids and to modify the box size (16). All simulations were carried out using our in-house software (freely available github.com/robertvacha/SC).

Free energy calculations for peptide translocation were performed using the Wang-Landau method (17). The free energy surface was considered converged once the modification factor was below 10^{-7}. Subsequently, simulations maintaining detailed balance of peptide translocation were performed and the obtained free energy surface was used as an external bias. The obtained histogram was then used to further improve the previously calculated free energy surface. The error of the free energy profiles is about 1 kT.

For proper sampling of peptide insertion, two collective variables (CVs) were used. First CV is the distance between peptide and the membrane center of mass. The free energy profile is symmetrical around the membrane center and asymmetry shows the calculation error. Second CV is the peptide orientation with respect to the membrane normal. The orientation is expressed as the cosine of the angle. Change of orientation from perpendicular to parallel (with respect to the membrane normal) is considered. For clarity, the second collective variable is averaged out and only the dependence on peptide position is shown.

IN VITRO ASSAY FOR AMP ACTIVITY

To study the effect of magainins on metabolically active bacteria, we assessed the antimicrobial activity of the peptides by determining the MIC values according to Clinical and Laboratory Standards Institute (CLSI, formerly National Committee for Clinical Laboratory Standards) guidelines.

Inhibition of bacterial growth by frog peptides was determined using an automated turbidimetric-based system (Bioscreen C, Labsystem, Helsinki, Finland), which measures absorbance of cell cultures in 100-well plates at regular time intervals (λ = 580 nm). Assays were performed in Mueller-Hinton (MH) broth without Ca^{2+} (18) using Bioscreen polystyrene honeycomb 100-well plates. Briefly, serial dilutions of the AMPs or control antibiotics (gentamicin and ampicillin B) were made in MH broth and dispensed with a multi-pipette into

polystyrene honeycomb 100-well plates. *E. coli* K12 cells grown for 18–20 h on agar plates were suspended in saline adjusting the turbidity to an optical density at λ=565 nm (OD_{565}) of 0.5 (~1×10^8 cells/mL) using a DEN-1B densitometer (Grant Instruments, Cambridge, UK). A fifty-fold dilution of this *E. coli* suspension prepared in MH broth was mixed with 50 µL (1:1 volume ratio) of a given peptide solution by three times up and down pipetting. Resulting cell suspensions were grown at 37°C with continuous, low amplitude shaking. The turbidity was measured in intervals of 5 minutes (filter bandwidth: λ= 420 – 580 nm). MIC was considered as the minimum concentration of peptide that inhibited any increment of turbidity after 48 h.

REFERENCES

1. Zweytick, D., G. Deutsch, J. Andrä, S. E. Blondelle, E. Vollmer, R. Jerala, and K. Lohner. 2011. Studies on lactoferricin-derived Escherichia coli membrane-active peptides reveal differences in the mechanism of N-acylated versus nonacylated peptides. J Biol Chem 286:21266–21276.
2. Broekhuyse, R. M. 1968. Phospholipids in tissues of the eye. I. Isolation, characterization and quantitative analysis by two-dimensional thin-layer chromatography of diacyl and vinyl-ether phospholipids. Biochim Biophys Acta 152:307–315.
3. Buboltz, J. T., and G. W. Feigenson. 1999. A novel strategy for the preparation of liposomes: rapid solvent exchange. Biochim Biophys Acta 1417:232–245.
4. Rieder, A. A., D. Koller, K. Lohner, and G. Pabst. 2015. Optimizing rapid solvent exchange preparation of multilamellar vesicles. Chemistry and physics of lipids 186:39–44.
5. Alley, S. H., O. Ces, M. Barahona, and R. H. Templer. 2008. X-ray diffraction measurement of the monolayer spontaneous curvature of dioleoylphosphatidylglycerol. Chemistry and physics of lipids 154:64–67.
6. Kollmitzer, B., P. Heftberger, M. Rappolt, and G. Pabst. 2013. Monolayer spontaneous curvature of raft-forming membrane lipids. Soft Matter 9:10877.
7. Leikin, S., M. M. Kozlov, N. L. Fuller, and R. P. Rand. 1996. Measured effects of diacylglycerol on structural and elastic properties of phospholipid membranes. Biophys J 71:2623–2632.
8. Israelachvili, J. N. 2011. Intermolecular and surface forces, 3rd ed. Academic Press, Burlington, MA.
9. Ellens, H., J. Bentz, and F. C. Szoka. 1985. H+- and Ca2+-induced fusion and destabilization of liposomes. Biochemistry 24:3099–3106.
10. Ladokhin, A. S., W. C. Wimley, and S. H. White. 1995. Leakage of membrane vesicle contents: Determination of mechanism using fluorescence requenching. Biophys J 69:1964–1971.

11. Laemmli, U. K. 1970. Cleavage of structural proteins during the assembly of the head of bacteriophage T4. Nature 227:680–685.

12. Hara, T., Y. Mitani, K. Tanaka, N. Uematsu, A. Takakura, T. Tachi, H. Kodama, M. Kondo, H. Mori, A. Otaka, F. Nobutaka, and K. Matsuzaki. 2001. Heterodimer formation between the antimicrobial peptides magainin 2 and PGLa in lipid bilayers: a cross-linking study. Biochemistry 40:12395–12399.

13. Cooke, I. R., K. Kremer, and M. Deserno. 2005. Tunable generic model for fluid bilayer membranes. Phys Rev E 72:11506.

14. Marsh, D. 1996. Intrinsic curvature in normal and inverted lipid structures and in membranes. Biophys J 70:2248–2255.

15. Vácha, R., and D. Frenkel. 2011. Relation between molecular shape and the morphology of self-assembling aggregates: a simulation study. Biophys J 101:1432–1439.

16. Frenkel, D., and B. Smit. 2002. Understanding Molecular Simulation. Academic Press, San Diego, CA.

17. Wang, F., and D. P. Landau. 2001. Efficient, multiple-range random walk algorithm to calculate the density of states. Phys Rev Lett 86:2050–2053.

18. Mueller, J. H., and J. Hinton. 1941. A protein-free medium for primary isolation of the gonococcus and meningococcus. Proc Soc Exp Biol Med 48:330–333.

Biophysical Journal, Volume *114*

Supplemental Information

Synergism of Antimicrobial Frog Peptides Couples to Membrane Intrinsic Curvature Strain

Regina Leber, Michael Pachler, Ivo Kabelka, Irene Svoboda, Daniel Enkoller, Robert Vácha, Karl Lohner, and Georg Pabst

Supplementary Information

Synergism of Antimicrobial Frog Peptides Couples to Membrane Intrinsic Curvature Strain

Regina Leber, Michael Pachler, Ivo Kabelka, Irene Svoboda, Daniel Enkoller, Robert Vácha, Karl Lohner, and Georg Pabst

PREPARATION OF LIPOSOMES

Lipid films (20 mg total lipid) for dye-release experiments were prepared by mixing the appropriate amounts of dissolved phospholipids before evaporation of solvents under a stream of nitrogen and stored in vacuum overnight. After addition of Hepes buffer containing the fluorophor/quencher ANTS/DPX (10 mM Hepes, 68 mM NaCl, 12.5 mM ANTS, 45 mM DPX, pH 7.4), formation of lipid vesicles was achieved by equilibration at 15°C above the lipid's melting temperature and intermittent vigorous vortex mixing. PE/PG-mixtures were additionally homogenized by six freeze/thaw-cycles. Large unilamellar vesicles (LUVs) were obtained by 25 cycles of extrusion of the hydrated liposomes through a polycarbonate filter (Millipore-Isopore^{TM}, Merck, Vienna) of 0.1 µm pore size above the lipid's melting temperature. Non-encapsulated fluorophore and quencher were removed by size-exclusion chromatography using SephadexTM G-75 (Sigma-Aldrich, Vienna) gel as described earlier (1). LUVs were eluted with Hepes buffer (10 mM Hepes, 140 mM NaCl, pH 7.4). Liposomal lipids were quantified by the determination of lipid phosphorus according the method described by (2). The final LUV concentration for dye-release experiments was adjusted to 50 µM in Hepes buffer (10 mM Hepes, 140 mM NaCl, pH 7.4).

PREPARATION AND ANALYSIS OF INVERTED HEXAGONAL PHASES BY SAXS

Samples for X-ray analysis were prepared by rapid solvent exchange (RSE) (3) using an adapted method that allows control of temperature (4). Here we focus in particular on the intrinsic curvatures of POPG and lyso-PE, whose values have to the best of our knowledge not been reported before. Both lipids do not form H_{II} phases and were therefore mixed with DOPE at various amounts as detailed above. In brief, appropriate amounts of lipid stock solution were pipetted into test tubes containing NaPi buffer (20 mM Na-phosphate, 130 mM NaCl, pH 7.4) and which were pre-equilibrated at a given temperature. The test tubes were quickly mounted onto the RSE apparatus, setting the argon flow to 60 ml/min and the vortex speed to 1000-1200 rpm. Rapid evaporation was initiated by opening the valve to a vacuum

pump set to a pressure in between the vapor pressure of solvent and water leading to the formation of lipid aggregates. Sample preparation was terminated after six minutes. Details of RSE settings are listed in supplementary Table S1. Control experiments using ^{1}H NMR showed no contamination of the samples with organic solvent.

Table S1: Settings used for the rapid solvent exchange.

Lipids	Temperature [°C]	Pressure [mbar]	Vortex speed [U/min]
DOPE	45	200	1200
POPG/DOPE	60	300	1000
lyso-PE/DOPE	70	900	1000
POPE	55	360	1000

All samples contained 12 wt% tricosene, which is needed to reduce the packing frustration of the inverted hexagonal phase (H_{II}) (see, e.g., (5)). This effect decreases the lamellar-to-H_{II} phase transition of POPE close to room temperature (6). POPG and lyso-PE do not form H_{II} phases. Therefore they were mixed with DOPE at various concentrations using a previously reported protocol (6). Samples containing DOPE and POPG were measured immediately after preparation, while lyso-PE containing samples were equilibrated for three days at room temperature in argon atmosphere to avoid lipid oxidation.

SAXS measurements were performed using a SAXSpace compact camera from Anton Paar (Austria), equipped with a Pilatus 100K-S detector system (Dectris, Switzerland) and a Genix 3D microfocus X-ray generator from Xenocs (Grenoble, France) [beam-size (Cu-Kα): ~ 300 µm (diameter)]. A scattering vector range of q = 0.6 nm^{-1} o 10.9 nm^{-1} was covered by setting the sample-to-detector distance to 308 mm. Temperature control was provided by a Peltier unit to within ± 0.1 °C. All samples were transferred into a paste cell holder (Anton Paar, Austria) and equilibrated for 10 minutes at 35°C before exposing to X-rays for one hour. Data reduction was performed with SAXStreat (Anton Paar, Austria). Note that temperature dependencies of intrinsic curvatures are in the range of $\frac{\Delta J_0}{T} = -1 \times 10^{-3}$ nm^{-1}/K^{-1} to -3×10^{-3} nm^{-1}/K^{-1} (6). Temperature corrections to adjust the here reported J_0's to 37°C used for vesicle leakage assays are consequently within experimental error.

SAXS data analysis was performed according to Kollmitzer et al. (6). In brief, intensities and peak positions of H_{II} phase patterns $I_{h,k}$ were used to construct electron density maps

$$\rho(\vec{r}) = \sum_{h,k} \alpha_{h,k} \sqrt{\frac{I_{h,k} q_{h,k}^2}{m_{h,k}}} \cos\left(2\pi \overrightarrow{q_{h,k}}\, \vec{r}\right), \quad \text{(S1)}$$

where *h*, *k* are the Miller indices, $m_{h,k}$ is the multiplicity of equivalent diffraction planes and $\alpha_{h,k}$ is the phase. Subsequently, electron density maps were radially integrated over azimuthal angles between 0° and 60° to yield one-dimensional electron density profiles. The maximum of these profiles was fitted with a Gaussian to determine the position of the lipid headgroup R_p. The intrinsic curvature $J_0 = -1/R_0$ is then determined by finding the position of the neutral plane $R_0 = R_p + d_{H1}$ (7), which is assumed to be located at the glycerol backbone (6). Specifically, we used $d_{H1} = 0.44$ nm as estimate for the distance between the lipid heads and the backbone (6).

The intrinsic curvature of non H_{II}-phase forming lipids was estimated assuming linear additivity using

$$J_0 = \frac{J_0^{mix} - (1-\chi) J_0^{DOPE}}{\chi}, \quad \text{(S2)}$$

where χ is the mole fraction of the respective 'guest' lipid in DOPE, which is used as a H_{II}-phase forming template ('host'). To increase the reliability of the J_0 estimates for guest lipids several guest/host mixtures were measured and interpolated, ensuring full miscibility of the guest lipids within the host structure (Fig. S1) and (6).

Figure S1 shows the SAXS patterns of 9:1 (molar ratio) lipid mixtures used to calculate J_0. The intrinsic curvatures of both DOPE mixtures increased with concentration of the guest lipid (Fig. S1, insert), albeit stronger for lyso-PE, as can be expected from its cone-like molecular shape, due to the difference of projected lateral areas of the PE head and the single hydrocarbon chain (8). The resulting J_0's for all lipids relevant for this study are listed in Tab. S2. In agreement with the qualitative assessment based on the molecular shape we found a significant positive J_0 for lyso-PE, while J_0 of POPG was, within experimental uncertainty, essentially zero. In order to test the effect of buffer on intrinsic lipid curvatures we also measured POPE, which readily forms in the presence of 12 wt.% tricosene a H_{II} phase at 35°C (Fig. S1), see also (6). The derived J_0 = -0.35 nm^{-1} is slightly more negative than our previously reported value. We attribute this to the effect of buffer ions on PE headgroup hydration, which is further supported by a similar decrease of J_0 for DOPE (-0.45 nm^{-1}) as compared to the value found in pure water (6). For the present study such subtleties are, however, of less significance. Here we are interested in estimates for net intrinsic curvatures

of lipid mixtures, which were calculated by their molecular averages upon assuming linear additivity

$$J_0^{mix} = \sum_i \chi_i J_0^{(i)}. \quad (3)$$

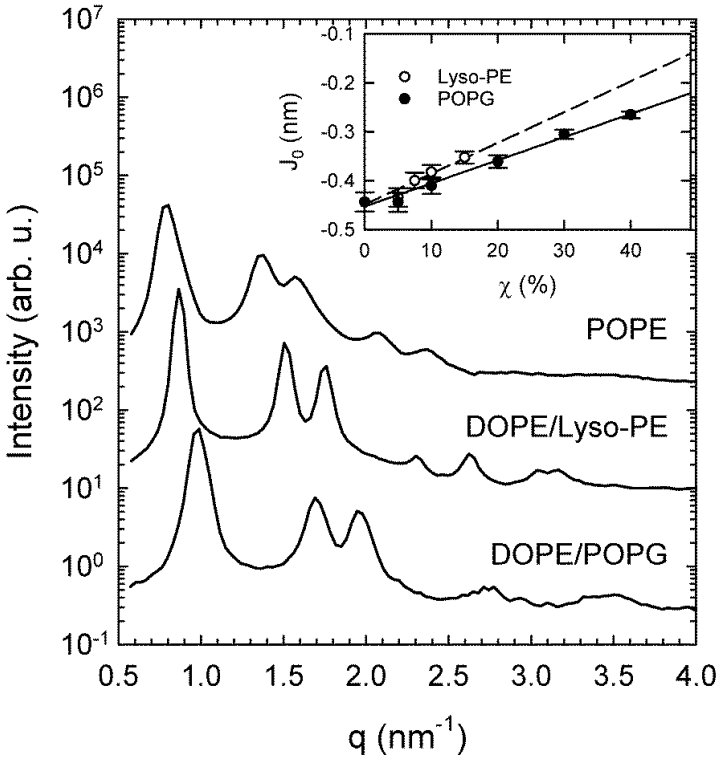

Figure S1: SAXS patterns of DOPE/POPG (9:1 mol/mol), DOPE/lyso-PE (9:1 mol/mol) and POPE at 35°C. All samples contained 12 wt% tricosene. Data are offset vertically for clarity of presentation. The insert shows the change of intrinsic curvatures as a function of POPG and lyso-PE concentration in DOPE, which is used to estimate their J_0's.

Table S2: Intrinsic curvatures of presently studied lipids at 35°C.

Lipid	J_0 **[nm^{-1}]**
lyso-PE	0.180 ± 0.123
POPG	0.020 ± 0.030
POPE	-0.350 ± 0.007
POPC*	-0.022 ± 0.010
Chol*	-0.494 ± 0.013

* Data taken from ref. (6)

FLUORESCENCE SPECTROSCOPY - LEAKAGE ASSAY

Leakage of the aqueous content of ANTS/DPX-loaded LUVs upon incubation with peptides was determined according to (9) and as detailed previously (1). Briefly, 2 ml of LUV suspension was filled into quartz cuvettes and equilibrated at 37°C for 5 minutes. Incremental amounts of peptide solutions prepared in Hepes buffer were added to the LUV suspension with µ-pipettes and mixed using a magnetic stirrer to achieve final peptide concentrations ranging from 0.016 - 1 µM, corresponding to peptide-to-lipid molar ratios from 1:3200 to 1:50. Fluorescence emission was recorded 5 minutes before and after the addition of peptides on a Cary Eclipse Fluorescence Spectrophotometer (Varian Inc., now Agilent Technologies, California, US) using an excitation wavelength of λ_{ex} = 360 nm and an emission wavelength λ_{em} = 530 nm. The slit widths for excitation and emission monochromators were set to 10 nm. Percentage of leakage was calculated from the fraction of the leakage (10)

$$I_F = \frac{(F-F_0)}{(F_{max}-F_0)}, \qquad \text{(S4)}$$

where F is the measured fluorescence, F_0 is the initial fluorescence without peptide, and F_{max} is the fluorescence corresponding to 100% leakage gained by addition of 1% Triton X-100.

SODIUM DODECYL SULFATE POLYACRYLAMIDE GEL ELECTROPHORESIS (SDS-PAGE)

In order to verify the dimeric or monomeric state of peptides, 2 µg of peptides were dissolved in loading buffer without DTT and separated by a one-dimensional SDS-PAGE using 5 % stacking and 18 % separating gels according to the method of Laemmli (11). Peptides were stained for 30 min with Coomassie brilliant blue after electrophoretic separation (11). An ultra-low range molecular weight marker was used to estimate the size of peptides after separation via SDS-PAGE. Experiments show that L18W-PGL-GGCa and MG2-GGCa form homodimers in buffer solution (pH ~ 7) (Fig. S2), in agreement with (12). Application of DTT leads to a drop of peptide activity to levels observed for single peptides, consistent with monomer formation (Fig. S3).

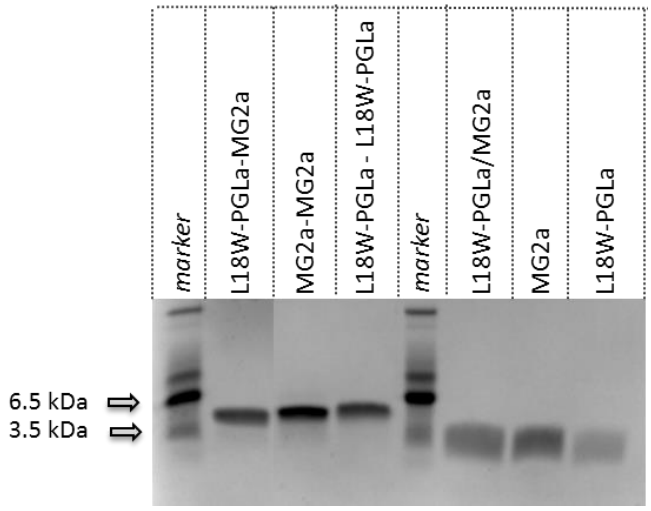

Figure S2: SDS-PAGE verifying dimeric and monomeric forms of magainins

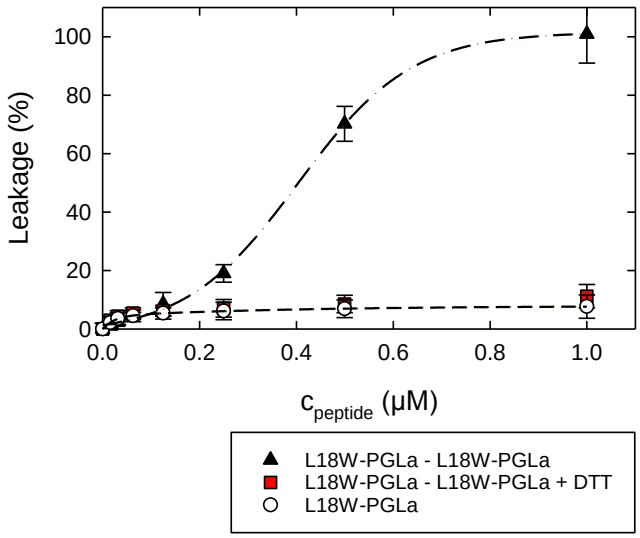

Figure S3: Effect of DTT addition to L18W-PGLa homodimers on leakage of POPE/POPG 3:1 mol/mol LUVs. For comparison, leakage induced by L18W-PGLa is shown as well (see also Fig. 2 *B*). The lipid concentration was 50 µM. Lines are guides to the eye.

MC SIMULATIONS

Monte Carlo simulations were performed using the Metropolis scheme and computationally efficient implicit solvent coarse-grained models. Sizes and distances of the models were calculated in reduced units, which (based on real particle dimensions) roughly translate to nm. The studied systems were composed of 200 lipid molecules and a single peptide. Lipids were

described by a three-bead model developed by Cooke and Deserno (13), using one bead for the head group of diameter d_h and two beads for tails each of diameter d_t (Fig. S4 *A*).

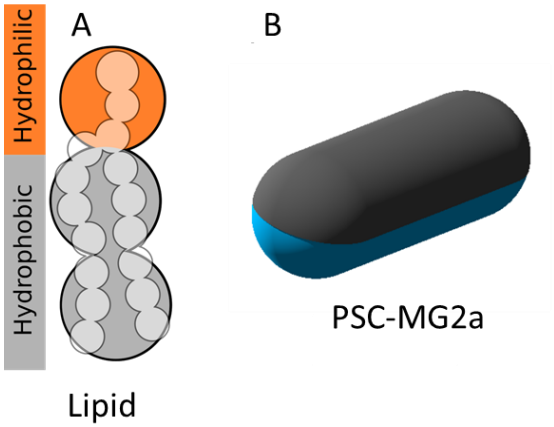

Figure S4: Schematic representations of the employed models. Panel A: Three-bead lipid model with lipid mapping (shown as silhouette). Panel B: PSC model of MG2a. Hydrophobic patches/regions are represented in grey, while orange and blue depict hydrophilic parts of lipid and peptide, respectively.

Three lipids with different intrinsic curvatures were simulated by variation of headgroup size (Fig. S5). The size of head bead affects J_0. Assuming cylindrical geometry of lipids one can calculate the intrinsic curvature by (14)

$$J_0 = \frac{2}{l}\left(1 - \frac{V}{A_h l}\right), \tag{S5}$$

where l is the length of the hydrophobic tails, A_h is the effective headgroup area and V is the hydrocarbon chain volume. However, there are more possibilities to calculate the l and $V/(A_h l)$. The first possibility is based on the geometry of individual molecules with $A_h = \pi d_h^2/4$, $V = \pi d_t^2 l/4$, and $l = 2d_t$. For $d_h = 0.85$ nm, 0.95 nm and 1.05 nm, this results for $d_t = 1$ nm in $J_0 = -0.38$ nm^{-1}, -0.11 nm^{-1}, and $+0.09$ nm^{-1}, respectively. However, this considers only excluded volume interactions between lipid molecules in ideal configuration. We therefore adhere to the second possibility, which derives J_0 from MC simulations and consequently include also contributions from temperature and the lipid parametrization (bonds, bending, and tail attraction). In this case the length of hydrophobic tails is calculated from the average distance of headgroup beads from the bilayer center, i.e. $d_l = 2.5$ nm. The headgroup areas are derived from the simulation box size of the equilibrated membrane at zero tension, which yields $A_h = 1.025$ nm^2, 1.145 nm^2 and 1.215 nm^2 with increasing d_h. Assuming that $A_h \propto d_h^2$ we can interpolate the headgroup area to perfectly cylindrical lipids (i.e., $d_h = d_t$ and $J_0 = 0$), yielding $A_h^0 = 1.176$ nm^2. Consequently Eq. (S5) is modified to

$$J_0 = \frac{2}{l}\left(1 - \frac{A_h^0}{A_h}\right), \quad \text{(S6)}$$

leading to $J_0 = -0.12$ nm^{-1}, -0.02 nm^{-1}, and $+0.03$ nm^{-1} for $d_h = 0.85$ nm, 0.95 nm and 1.05 nm, respectively. The lipid with the largest headgroup leads to $J_0 > 0$.

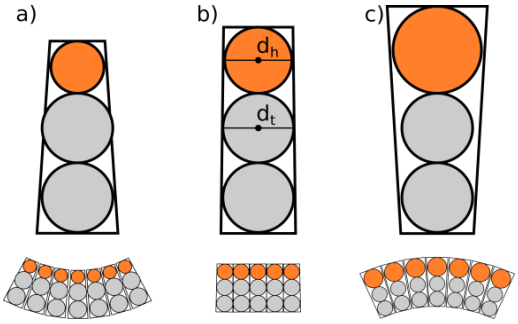

Figure S5: Schematic representation of lipid shape and induced curvature. Diameters of lipid heads and tails are denoted as d_h and d_t, respectively, with d_t = 1 nm. Conical lipids a) and c) had d_h = 0.85 and 1.05 nm, respectively. For cylindrical lipids b) d_h = 0.95 nm. The corresponding intrinsic curvatures are a) J_0 = -0.12 nm^{-1}, b) J_0 = -0.02 nm^{-1}, and c) J_0 = +0.03 nm^{-1}.The induced curvature is shown below each lipid. Differences in headgroup sizes are magnified for clarity.

The peptide was modelled by a patchy spherocylinder (PSC) (15), setting the peptide length to 4 nm and its diameter to 1 nm to roughly match the size and polarity of MG2a, i.e. half of the peptide surface was hydrophobic (Fig. S4 *B*). At either side of the patch, there is a 5° switching range to linearly scale the interaction potential to zero. The remaining surface is purely repulsive and thus considered to be hydrophilic. For more details on the model, see (15).

To mimic the hydrophobic effect, effective tail-tail interactions were used to drive membrane self-assembly leading to an effective attractive potential with a cos^2 profile. Further, the same potential was used to describe interactions between lipid tails and the peptide's hydrophobic patch. Repulsive interactions were modeled by Weeks-Chandler-Anderson (shifted and truncated Lennard-Jones) potential. The PSC-MG2a switching range between hydrophobic and hydrophilic surfaces was set to 1.0 nm. As described in the original article, the switching range of lipids was extended to 1.6 nm to keep the membrane in the fluid phase (13). The depth of the attractive potential well was -1 kT (k is the Boltzmann constant and T is the temperature) for lipid-tail particles and -1 kT per unit length of PSC line segment.

The membrane bilayer was assembled in the XY-plane of a rectangular box. The initial box size was about 11 × 11 × 50 nm. Periodic boundary conditions were applied in all three

dimensions, forming “infinite” membrane plane. Simulations were performed under constant temperature and number of particles, while keeping zero lateral tension in the XY-plane. We used standard MC trial moves to move the peptide/lipid beads/whole lipids and to modify the box size (16). All simulations were carried out using our in-house software (freely available github.com/robertvacha/SC).

Free energy calculations for peptide translocation were performed using the Wang-Landau method (17). The free energy surface was considered converged once the modification factor was below 10^{-7}. Subsequently, simulations maintaining detailed balance of peptide translocation were performed and the obtained free energy surface was used as an external bias. The obtained histogram was then used to further improve the previously calculated free energy surface. The error of the free energy profiles is about 1 kT.

For proper sampling of peptide insertion, two collective variables (CVs) were used. First CV is the distance between peptide and the membrane center of mass. The free energy profile is symmetrical around the membrane center and asymmetry shows the calculation error. Second CV is the peptide orientation with respect to the membrane normal. The orientation is expressed as the cosine of the angle. Change of orientation from perpendicular to parallel (with respect to the membrane normal) is considered. For clarity, the second collective variable is averaged out and only the dependence on peptide position is shown.

IN VITRO ASSAY FOR AMP ACTIVITY

To study the effect of magainins on metabolically active bacteria, we assessed the antimicrobial activity of the peptides by determining the MIC values according to Clinical and Laboratory Standards Institute (CLSI, formerly National Committee for Clinical Laboratory Standards) guidelines.

Inhibition of bacterial growth by frog peptides was determined using an automated turbidimetric-based system (Bioscreen C, Labsystem, Helsinki, Finland), which measures absorbance of cell cultures in 100-well plates at regular time intervals (λ = 580 nm). Assays were performed in Mueller-Hinton (MH) broth without Ca^{2+} (18) using Bioscreen polystyrene honeycomb 100-well plates. Briefly, serial dilutions of the AMPs or control antibiotics (gentamicin and ampicillin B) were made in MH broth and dispensed with a multi-pipette into

polystyrene honeycomb 100-well plates. *E. coli* K12 cells grown for 18–20 h on agar plates were suspended in saline adjusting the turbidity to an optical density at λ=565 nm (OD_{565}) of 0.5 (~1×10^8 cells/mL) using a DEN-1B densitometer (Grant Instruments, Cambridge, UK). A fifty-fold dilution of this *E. coli* suspension prepared in MH broth was mixed with 50 µL (1:1 volume ratio) of a given peptide solution by three times up and down pipetting. Resulting cell suspensions were grown at 37°C with continuous, low amplitude shaking. The turbidity was measured in intervals of 5 minutes (filter bandwidth: λ= 420 – 580 nm). MIC was considered as the minimum concentration of peptide that inhibited any increment of turbidity after 48 h.

REFERENCES

1. Zweytick, D., G. Deutsch, J. Andrä, S. E. Blondelle, E. Vollmer, R. Jerala, and K. Lohner. 2011. Studies on lactoferricin-derived Escherichia coli membrane-active peptides reveal differences in the mechanism of N-acylated versus nonacylated peptides. J Biol Chem 286:21266–21276.
2. Broekhuyse, R. M. 1968. Phospholipids in tissues of the eye. I. Isolation, characterization and quantitative analysis by two-dimensional thin-layer chromatography of diacyl and vinyl-ether phospholipids. Biochim Biophys Acta 152:307–315.
3. Buboltz, J. T., and G. W. Feigenson. 1999. A novel strategy for the preparation of liposomes: rapid solvent exchange. Biochim Biophys Acta 1417:232–245.
4. Rieder, A. A., D. Koller, K. Lohner, and G. Pabst. 2015. Optimizing rapid solvent exchange preparation of multilamellar vesicles. Chemistry and physics of lipids 186:39–44.
5. Alley, S. H., O. Ces, M. Barahona, and R. H. Templer. 2008. X-ray diffraction measurement of the monolayer spontaneous curvature of dioleoylphosphatidylglycerol. Chemistry and physics of lipids 154:64–67.
6. Kollmitzer, B., P. Heftberger, M. Rappolt, and G. Pabst. 2013. Monolayer spontaneous curvature of raft-forming membrane lipids. Soft Matter 9:10877.
7. Leikin, S., M. M. Kozlov, N. L. Fuller, and R. P. Rand. 1996. Measured effects of diacylglycerol on structural and elastic properties of phospholipid membranes. Biophys J 71:2623–2632.
8. Israelachvili, J. N. 2011. Intermolecular and surface forces, 3rd ed. Academic Press, Burlington, MA.
9. Ellens, H., J. Bentz, and F. C. Szoka. 1985. H+- and Ca2+-induced fusion and destabilization of liposomes. Biochemistry 24:3099–3106.
10. Ladokhin, A. S., W. C. Wimley, and S. H. White. 1995. Leakage of membrane vesicle contents: Determination of mechanism using fluorescence requenching. Biophys J 69:1964–1971.

11. Laemmli, U. K. 1970. Cleavage of structural proteins during the assembly of the head of bacteriophage T4. Nature 227:680–685.

12. Hara, T., Y. Mitani, K. Tanaka, N. Uematsu, A. Takakura, T. Tachi, H. Kodama, M. Kondo, H. Mori, A. Otaka, F. Nobutaka, and K. Matsuzaki. 2001. Heterodimer formation between the antimicrobial peptides magainin 2 and PGLa in lipid bilayers: a cross-linking study. Biochemistry 40:12395–12399.

13. Cooke, I. R., K. Kremer, and M. Deserno. 2005. Tunable generic model for fluid bilayer membranes. Phys Rev E 72:11506.

14. Marsh, D. 1996. Intrinsic curvature in normal and inverted lipid structures and in membranes. Biophys J 70:2248–2255.

15. Vácha, R., and D. Frenkel. 2011. Relation between molecular shape and the morphology of self-assembling aggregates: a simulation study. Biophys J 101:1432–1439.

16. Frenkel, D., and B. Smit. 2002. Understanding Molecular Simulation. Academic Press, San Diego, CA.

17. Wang, F., and D. P. Landau. 2001. Efficient, multiple-range random walk algorithm to calculate the density of states. Phys Rev Lett 86:2050–2053.

18. Mueller, J. H., and J. Hinton. 1941. A protein-free medium for primary isolation of the gonococcus and meningococcus. Proc Soc Exp Biol Med 48:330–333.

Manuscript submitted to **Biophysical** *Journal*
Article

Magainin 2 and PGLa in Bacterial Membrane Mimics I: Peptide-Peptide and Lipid-Peptide Interactions

M.P., I.K., M.-S. A., K.L., R.V., G.P.

ABSTRACT We addressed the onset of synergistic activity of the two well-studied antimicrobial peptides magainin 2 (MG2a) and PGLa using lipid-only mimics of Gram-negative cytoplasmic membranes. Specifically, we coupled a joint analysis of small-angle X-ray and neutron scattering experiments on fully hydrated lipid vesicles in the presence of MG2a and L18W-PGLa to all-atom and coarse-grained molecular dynamics simulations. In agreement with previous studies both peptides, as well as their equimolar mixture, were found to remain in a surface-aligned topology upon membrane insertion and to induce significant membrane perturbation as evidenced by membrane thinning and hydrocarbon order parameter changes in the vicinity of the inserted peptide. These effects were particularly pronounced for the so called synergistic mixture of 1:1 (mol/mol) L18W-PGLa/MG2a and cannot be accounted for by a linear combination of the membrane perturbations of two peptides individually. Our data are consistent with parallel heterodimers forming at much lower concentrations than previously considered, but which do not induce a synergistic leakage of dyes. Our simulations further show that the heterodimers interact via salt bridges and hydrophobic forces, which apparently makes them more stable than putatively formed antiparallel L18W-PGLa and MG2a homodimers. Moreover, dimerization of L18W-PGLa and MG2a leads to a relocation of the peptides within the lipid headgroup regime as compared to the individual peptides. The early onset of dimerization of L18W-PGLa and MG2a at low peptide concentrations consequently appears to be key to their synergistic dye-releasing activity from lipid vesicles at high concentrations.

STATEMENT OF SIGNIFICANCE

We demonstrate that specific interactions of the antimicrobial peptides MG2a and PGLa with each other in POPE/POPG bilayers lead to the formation of surface-aligned parallel dimers, which provide already at low peptide concentrations the nucleus for the peptides' well-known synergistic activity.

INTRODUCTION

The steady increase of antibiotic resistance of pathogenic bacteria combined with the decline of approved antimicrobial agents is considered to be a severe threat to global health. In view of these developments, considerable research efforts have been devoted to understanding the mode of action of antimicrobial peptides (AMPs), considered as alternative for the development of novel antibiotics. AMPs are effector molecules of the innate immune system, whose main targets are bacterial membranes. AMPs kill bacteria within minutes, which makes it more difficult for bacteria to develop resistance mechanisms (for review see e.g. (1, 2)). Applying diverse biophysical techniques on lipid-only membrane mimics, several interaction models have been conceived for AMPs (1, 3, 4). Pore-formation is arguably the most widely discussed membrane disruptive mechanism.

Choosing a specific membrane mimic requires a delicate balance between experimental or computational tractability and physiological relevance. This leads to a search for the minimum realistic lipid mixture which yields a similar response to AMPs as in live bacteria. Phosphatidylethanolamine, phosphatidylglycerol, and cardiolipin represent the main lipid components of Gram-negative cytoplasmic membranes. Yet, we demonstrated previously that lipid bilayers composed of palmitoyl-oleoyl-phosphatidylethanolamine (POPE) and palmitoyl-oleoyl-phosphatidylglycerol (POPG) (molar ratio: 3:1) respond similarly to PGLa and Magainin 2-amide (MG2a), in agreement with their antimicrobial activity toward *Escherichia coli* K12 (5), despite the lack of cardiolipin or other cell wall components. Hence POPE/POPG (3:1 mol/mol) bilayers appear to be valid first order mimics for biophysical studies on the activity of AMPs with Gram-negative bacteria.

Studying the activity of PGLa and MG2a is of specific interest due to synergistic effects, first described by Matsuzaki and coworkers (6–8). Equimolar mixtures of the two peptides reduced the minimum inhibitory concentration of the individual peptides in *E. coli* K12 by about one order of magnitude. The molecular mechanism of the observed synergy remains controversial, however. Originally, synergism was associated with the formation of a transmembrane pore with a 1:1 peptide stoichiometry (6–8). In contrast, solid state NMR experiments from the Ulrich and Bechinger groups demonstrated that MG2a never adopts a transmembrane topology and that PGLa may insert perpendicularly in the presence of MG2a into

the membrane only in phosphatidylcholine-enriched or short chain disaturated phosphatidylethanolamine-enriched bilayers, respectively (9–13). None of these latter lipids are of significance for Gram-negative cytoplasmic membranes, however.

The dependence of MG2a mediated PGLa insertion into bilayers was attributed to the intrinsic lipid curvature, which leads to a tight packing of the bilayer's polar-apolar interface in the case of cone-shaped lipids, such as POPE, and increases the energy barrier for peptide translocation (5, 14). Of recent, this was refined by considering also details of hydrocarbon chain configurations (13).

The topologies of PGLa and MG2a within the synergistic regime as proposed from the above mentioned data differ significantly. Zerweck et al. postulated a pore formed by a tetrameric heterocomplex of transmembrane PGLa and surface aligned MG2a, which is stabilized by intimate Gly-Gly contacts between antiparallel PGLa dimers and C-terminal interactions between PGLa and MG2a (12). This contrasts, however, the surface topology of both peptides reported in POPE enriched bilayers (11, 13). Notably some of the observed effects on peptide topology might be also related to the relatively low water content of solid state NMR experiments. We are thus currently lacking insight that would explain how PGLa and MG2a remain surface bound, but disrupt membrane at the same time synergistically (5).

We therefore performed a comprehensive study using a broad selection of experimental and computational tools in order to reveal the effects of PGLa and MG2a in fully hydrated POPE/POPG (3:1 mol/mol) bilayers on nanoscopic to macroscopic length scales. Specific care was given to ensure that conditions allow a direct comparison to our previously reported leakage experiments, including the use of L18W-PGLa instead of native PGLa (5). Note that L18W-PGLa was reported to behave analogously to native PGLa (6).

Due to the large number of produced data, we decided to present the results in a paper series. The present paper focuses on low peptide concentrations, i.e. where L18W-PGLa/MG2a mixtures do not cause synergistic dye-release from POPE/POPG vesicles (5). This allowed us to investigate the peptides influence on the membrane structure in great detail by using combined joint small-angle X-ray and neutron scattering (SAXS/SANS) as well as all-atom and coarse-grained molecular dynamics (MD) simulations. We found, for example, that membrane-mediated interactions between the two peptides lead to an early onset of dimerization causing a shift of L18W-PGLa from slightly below to slightly above the lipid's glycerol backbone, while remaining surface aligned. This effect leads to a perturbation of membrane structure, which is more pronounced than in the case of non-interacting individual peptides. The resulting remodelling of membrane structure thus appears as a precursor to synergistic dye release at higher peptide concentrations.

MATERIALS AND METHODS

Lipids, Peptides and Chemicals

POPE and POPG were purchased from Avanti Polar Lipids (Alabaster, AL, USA, purity>99%) as powder and used without further purification. L18W-PGLa (GMASKAGAIAGKIAKVAWKAL-NH_2) and MG2a (GIGKFLHSAKKFGKAFVGEIMNS-NH_2) were obtained in lyophilized form (purity >95%) from PolyPeptide Laboratories (San Diego, CA, USA). Deuterium dioxide (purity 99.8 atom %) and HEPES (purity >99.5) were purchased from Carl Roth (Karlsruhe, Baden-Wüttenberg, Germany). All other chemicals were obtained from Sigma-Aldrich (Vienna, Austria) in *pro analysis* quality. Lipid stock solutions for sample preparation were prepared in organic solvent chloroform/methanol (9:1; v/v); lipid concentration was determined using a phosphate assay (15). Peptide stock solutions were prepared in 10 mM HEPES 140 mM NaCl buffer solution (pH 7.4).

Sample Preparation

Lipid thin films were prepared by mixing appropriate amounts of lipid stock solutions to obtain samples composed of POPE:POPG (3:1, mol/mol), followed by solvent evaporation under a nitrogen stream at 35°C and overnight storage in a vacuum chamber. Dry lipid films were hydrated in 10 mM HEPES, containing 140 mM NaCl (pH 7.4). For neutron experiments the H_2O/D_2O ratio in the buffer was varied as detailed below. Hydrated samples were equilibrated for one hour at 55°C followed by 8 freeze-and-thaw cycles using liquid N_2 and intermittent vortex mixing. Large unilamellar vesicles (LUVs) were obtained by 31 extrusions with a hand held mini extruder (Avanti Polar Lipids, Alabaster, AL) using a 100 nm pore diameter polycarbonate filter. Vesicle size and polydispersity was determined via dynamic light scattering using a Zetasizer NANO ZSP (Malvern Instruments, Malvern, United Kingdom). LUVs were again phosphate assayed and mixed with appropriate amounts of peptide stock solution to obtain peptide/lipid (P/L) molar ratios in the range of P/L = 1/400 – 1/50. LUVs were equilibrated at a given peptide concentration for 4 days prior to measurement.

Small-angle X-ray scattering

Small-angle X-ray scattering (SAXS) data were collected at the SWING beamline (Soleil, Saint-Aubin, France) using X-ray photons of wavelength $\lambda = 10$ Å and an Eiger 4M detector (Dectris, Baden-Daetwill, Switzerland). Samples were manually loaded in 1.5 mm path length quartz capillaries and mounted in a capillary holder, whose temperature was controlled with a circulating water bath. The sample-to-detector distance (SDD) was set to 1 m, which allowed us to cover scattering vectors in the range from $q = 0.0098$ Å^{-1} to 0.9 Å^{-1}. Data correction (integration, normalization and background subtraction) was performed using the software Foxtrot (Xenocs, Sassenage, France).

Small-angle neutron scattering

Neutron scattering experiments (SANS) were performed at KWS-1 (FRM II, Munich-Garching, Germany (16). Using 2D scintillation detector, a wavelength of 5 Å ($\Delta\lambda/\lambda = 0.1$) and SDD = 1.21 m and 7.71 m, allowed us to cover a q-range from 0.005 – 0.42 Å^{-1}. Samples were kept in 1 mm path length quartz cuvettes QX-404 (Helmma, Jena, Germany) and equilibrated at 35°C, using a circulating water bath. Used contrast conditions were 100, 75 and 50 % v/v D2O/H2O. Data correction was performed using the QTIKWS software from JCNS (Gaching, Germany).

Joint SAXS/SANS analysis

For the P/L ratios used in the present study no peptide-mediated aggregation of LUVs was observed, i.e. scattering data did not exhibit any Bragg peak scattering. This allowed us to treat SAXS/SANS data in terms of dilute particle scattering, that is we were able to neglect any contribution from LUV-LUV or bilayer-bilayer positional correlations. Moreover, we focused our analysis on peptide-induced changes of the membrane structure by analyzing scattering data for $q > 0.05$ Å^{-1}. In this q-range overall vesicle size and morphology do not contribute (17), which allowed us to model the scattered intensities as $I(q) \propto |F_{\mathrm{FB}}(q)|^2/q^2$, where $F_{\mathrm{FB}}(q)$ is the flat bilayer form factor.

The form factor was derived within the framework of the scattering density profile (SDP) model (18). In brief, the SDP analysis is based on a composition-dependent parsing of membrane structure into quasi-molecular fragments, whose distribution along the bilayer normal is described in terms of Gaussian-type volume probability functions. Parsing is guided by MD simulations (for a recent review, see e.g., (19)). The volume probability functions can be easily scaled with the neutron or X-ray scattering lengths of each group entailing a joint SAXS/SANS analysis that combines the differently contrasted samples into one underlying membrane structure. Analogous strategies have been reported previously, see e.g. (20–23).

Parsing. Considering previously reported SDP data for POPE (24), POPG (25), and by using all-atom MD simulations (see below) the lipid part of the membrane structure was parsed into the ethanolamine (ENX), glycerol (PG2), phosphate (PO_4), carbonyl glycerol (CG), CH, CH_2, and CH_3 groups (see Fig. 1 and supplementary Fig. S1). Following our previous SDP analysis of coexisting lipid domains (26, 27), we combined the individual groups of POPE and POPG into one hybrid lipid structure, using molecular averaging. In particular, we paired all hydrocarbon, CG and PO_4 groups, assuming that they align at the same transbilayer position. This is reasonable considering the identical hydrocarbon chain composition of both lipids. That is, only the ENX and PG2 groups were adjusted independently.

Based on experimental evidence for surface-aligned topologies of MG2a and L18W-PGLa in POPE/POPG (3:1 mol/mol) (13), as well as our own MD simulations results, we modelled the contribution of the peptides by a single Gaussian volume probability function centered at z_{P} in the headgroup regime. Further, we assumed that peptides (i) distribute equally in both leaflets and (ii) fully partition into the lipid membrane. The first assumption is motivated by the long sample equilibration times, during which peptides are able to translocate spontaneously through the bilayer. The second assumption is corroborated by the absence of scattering from unbound peptides in our data (28) and previous partitioning experiments (29). For the equimolar mixture, we combined L18W-PGLa and MG2a into a single Gaussian as supported by MD simulations (see below).

The individual volume distribution functions are detailed in the SI. The area per unit cell A_{U} is a common scaling factor for all distribution functions and therefore was chosen as fit parameter (see also (27)). From the analysis we determined several structural parameters, such as, e.g., the Luzzati bilayer thickness (30)

$$D_B = \frac{2V_{\mathrm{LP}}}{A_{\mathrm{U}}}, \tag{1}$$

where V_{VP} is the total volume of the lipid/peptide unit cell (Eq. S9), the hydrocarbon chain length $D_{\mathrm{C}} = z_{\mathrm{CH_2}}$, where $z_{\mathrm{CH_2}}$ is the outer terminal position of the methylene group, and the distance from the CG to PO_4 groups $D_{\mathrm{HD}} = z_{\mathrm{PO_4}} - z_{\mathrm{CG}}$.

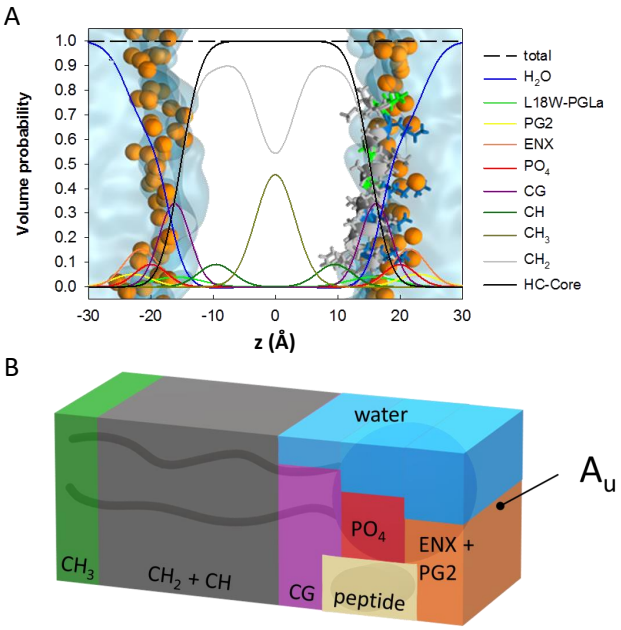

Figure 1: Schematic of the applied SDP model. Panel A shows the distribution functions of the different quasimolecular groups (see also Fig. S1). The spheres in the overlayed MD simulations represent phosphor atoms. Panel B gives a schematic of the unit cell of cross sectional area A_U with different contributions from lipid, peptide and water.

Data fitting. To obtain robust fitting parameters and estimates for their uncertainties every data set was fitted 400 times using a genetic algorithm (31) with random starting parameters. This gave us Gaussian-like distributions for each adjustable parameter. We report the average (center of mass) of these distributions; uncertainties where calculated from second moments. For details regarding constraints and cost function, see the SI.

Molecular dynamics simulations

Molecular dynamics (MD) simulations were performed using GROMACS version 2016.2 (32, 33).

All-atom simulations

Simulation Settings. Protein and solvent molecules were described by Amberff99SB-ILDN (34, 35), and lipids by Slipids (36, 37) force fields. The simulation time step was set to 2 fs. A temperature of 308.15 K was maintained by using a Nosé-Hoover thermostat (38–40), with a coupling constant of 0.5 ps. Two separate coupling groups for protein-lipid and solvent atoms were used. 3D periodic boundary conditions were applied and a Parrinello-Rahman barostat (41, 42) with semi-isotropic coupling scheme was employed for keeping the pressure at 1 bar with a coupling constant of 2 ps. Long-ranged electrostatic interactions were treated with particle mesh Ewald method (43) with the real-space cutoff set to 1.2 nm.Lennard-Jones interactions were cutoff at 1.2 nm. All bonds were constrained using the LINCS algorithm; long-range dispersion corrections (44) were applied for energy and pressure.

System Preparation. Lipid bilayers composed of 192 POPE and 64 POPG molecules were assembled in the XY-plane by distributing lipids equally in both leaflets using the CHARMM-GUI interface (45). The system was hydrated by more than 40 water molecules per lipid and NaCl ions were added at 130 mM concentration. The initial box dimensions were $8.9 \times 8.9 \times 8.5$ nm. MG2a and L18W-PGLa were prepared in α-helical conformation.

The following starting configurations were considered. System (1): A single peptide was placed into each membrane leaflet in a surface-aligned topology. System (2): A parallel L18W-PGLa/MG2a heterodimer was placed into each membrane leaflet in a surface-aligned topology.

All systems were equilibrated using similar protocols. Firstly, energy minimization was performed using the steepest descent algorithm. Then, an equilibration with positional restraints on peptide backbone was performed for 60 ns followed by an

equilibration with dihedral restraints, in order to maintain the peptide's secondary structure. The length of simulations with dihedral restrains were 105 ns (system (1)), or 180 ns (system (2)). Finally, unrestrained production dynamics simulation were performed for 500 ns.

Coarse-grained Simulations

Simulation Settings. Computationally-efficient coarse-grained simulations were performed using the MARTINI 2.2 force field (46–48) with a simulation time step of 20 fs. A velocity-rescaling thermostat (modified with a stochastic term) (49) was employed with coupling constant of 1.0 ps to maintain the temperature at 310 K. Protein-lipid and solvent beads were coupled to separate baths to ensure correct temperature distribution. The pressure was kept at 1 bar using a Parrinello-Rahman barostat with a semi-isotropic coupling scheme and a coupling constant of 12 ps. All non-bonded interactions, including van der Waals forces were cut-off at 1.1 nm. The relative dielectric constant was set to 15.

Since MARTINI does not explicitly describe backbone hydrogen bonds, we imposed the secondary structures (α-helices) on the peptides throughout the entire simulation run. The peptide C-terminal capping was modeled by removal of the charge and changing the backbone bead type to neutral.

System Preparation. The membrane was assembled in the XY-plane using the CHARMM-GUI web server (50). The lipid bilayer was composed of 378 POPE and 126 POPG equally distributed lipids in both leaflets. Roughly 30 water beads per lipid were added (a single bead corresponds to four water molecules) and also NaCl ions were added at a concentration of 130 mM. Two P/L ratios – 1/42 and 1/21, were considered for MG2a, L18W-PGLa and MG2a/L18W-PGLa (1:1 mol/mol) placing an equal number of randomly distributed peptides into each membrane leaflet. Dimerization was derived from analyzing distances between the peptide centers of mass and the peptide termini. If at least two of these distances were smaller than 1 nm, then the peptides were considered to be in a dimer. As control we performed an unbiased simulation starting with peptide heterodimers taking all parallel/antiparallel variants of mutual peptide alignment into accoun and analyzed as a function of time. Finally, we performed a biased simulation, where MG2a and L18W-PGLa were restrained in heterodimers via a flat-bottom potential. The potential was applied to the distances between peptide centers of mass for separations larger than 1 nm with a force constant of 1000 kJ mol^{-1} nm^{-2}.

RESULTS

Scattering Experiments

Membrane structure and peptide location

We determined the structural response of POPE/POPG (3:1 mol/mol) LUVs to both peptides, including their equimolar mixture (P/L = 1/200, T = 35°C) using a joint analysis of scattering data with a total of four contrasts (SAXS, SANS: 50, 75 100% D_2O). No vesicle aggregation or formation of multilamellar aggregates occurred at this peptide concentration as evidenced by the pure diffuse nature of all scattering patterns (Fig. 2, Figs. S2–S4). This enabled us to derive the peptides' effect on membrane structure in detail using the analysis described in the previous section.

Pure POPE/POPG bilayers serve as a reference system for the present study. Our SDP analysis yields 60.56 ± 0.10 Å^2 for the lateral area per lipid (Tab. 1), see Fig. S2, for corresponding fits and Tab. S1 for all parameter values. This value compares well to A_U = 59.8 Å^2 obtained by molecular averaging the individual areas per lipid reported for POPE and POPG (24, 25), which supports our analysis. Moreover, our model shows a good agreement with the scattered intensities in the presence of peptides (Fig. 2), Fig. S3, S4), which further supports our assumption of evenly distributed peptides. An equal distribution of peptides in both leaflets is expected to need extended sample equilibration times, such as realized for the here presented data, during which peptides may spontaneously translocate through the membranes. We note, however, that we cannot fully exclude the presence of asymmetric transleaflet distributions of the peptides. Disentangling leaflet compositional differences is beyond the resolution of the here presented experiments.

All peptides caused significant modulations of membrane structure (Tabs. 1) with L18W-PGLa having the least effect, e.g., the decrease of thickness of the hydrophobic core $2\Delta D_C \sim -0.4$ Å and $\Delta A_U \sim 0.7$ Å^2. Interestingly, D_B increased slightly. This can be mainly attributed to the increased volume of the unit cell due to contributions from L18W-PGLa (see Eq. (1)). For MG2a in turn, no significant changes were observed for D_B, while $2D_C$ and A_U changed about twice as much compared to L18W-PGLa. In case of the equimolar peptide mixture $\Delta A_U \sim 2.7$ Å^2 is most significant, leading even to a decrease of D_B. Since $2\Delta D_C$ does not contain contributions from peptide volumes, it consequently is the appropriate parameter to measure membrane thinning. For the studied peptides membrane thinning follows the order L18W-PGLa/MG2a > MG2a > L18W-PGLa. We note that the thinning observed for L18W-PGLa/MG2a cannot be explained by a simple linear combination of the thinning

Table 1: Effect of magainins on the structure of POPE/POPG (3:1 mol/mol) bilayers.

sample	A_U [Å^2]	D_B [Å]	D_C [Å]	z_P [Å]	D_{HD} [Å]
POPE/POPG	60.56±0.10	39.15±0.06	15.34±0.02 (15.10)^a		4.19±0.05
+ L18W-PGLa	61.26±0.13	39.49±0.08	15.16±0.03 (15.06)^a	15.75±0.44	4.07±0.06
+ MG2a	62.00±0.09	39.17±0.06	14.98±0.02 (15.01)^a	16.29±0.50	3.80±0.06
+ L18W-PGLa/MG2a	63.29±0.06	38.31±0.03	14.68±0.01 (14.93)^a	15.98±0.43	4.45±0.04

^{a} values in brackets are derived from all-atom MD simulations.

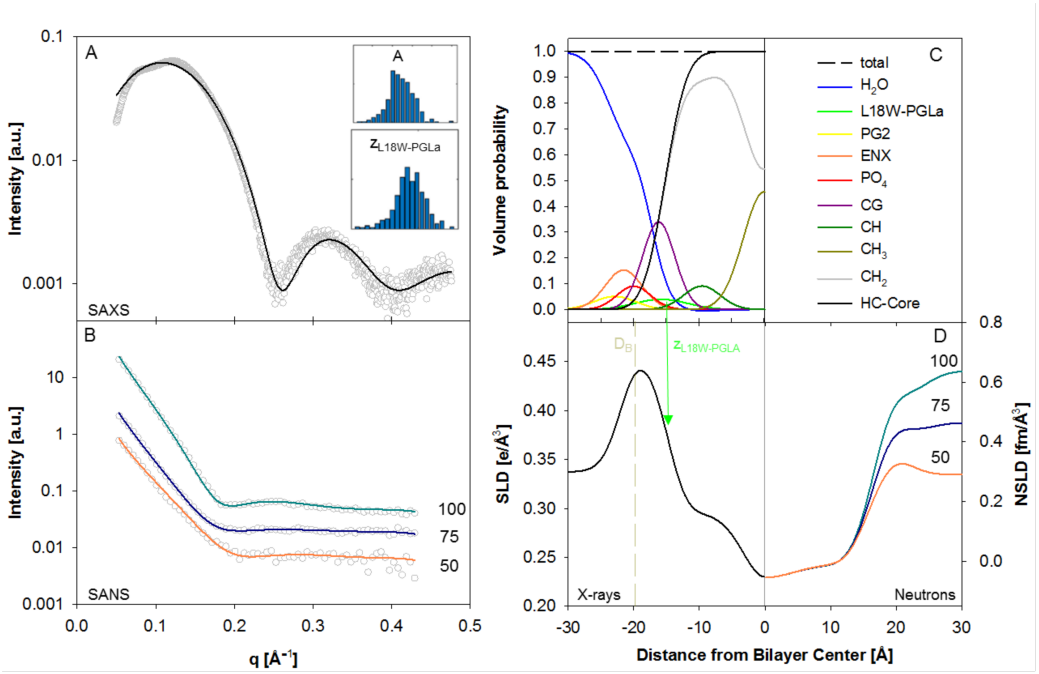

Figure 2: SDP analysis of POPE/POPG (3:1 mol/mol) in the presence of L18W-PGLa (P/L = 1/200). Panels (A) and (B) show the calculated model fits from averaged parameters (solid lines) for SAXS an SANS data, obtained from 400 independent optimization runs. Insets in (A) show histograms of the area per unit cell, A_U, and the position of the peptide in the bilayer, z_P. Panel (C) shows the volume probability distribution of the bilayer and panel (D) displays the corresponding electron and neutron scattering length densities. The arrow indicates location of z_P and the dashed-line shows the position of $D_B/2$.

effects of the individual peptides. In particular the experimental form factors of POPE/POPG in the presence of L18W-PGLa and MG2a cannot be averaged to yield the form factor observed upon addition of the equimolar mixture, which should be possible if the two peptides were not interacting with each other (Fig. S5). This supports the formation of heterodimers at significantly lower P/L than previously reported (7, 9).

It is particular interesting to relate membrane thinning to the location of the peptides within the bilayer (Tab. 1). L18W-PGLa is positioned slightly below, and MG2a slightly above the glycerol backbone (CG group), respectively as observed by comparing z_P and D_C. The peptide mixture behaved similar to MG2a with a preferential location just above the lipid backbone. Thus, pronounced thinning effects are observed for peptides located further away from the membrane center, as well as for L18W-PGLa/MG2a, presumably due to dimer formation.

Finally, we present results for the distance between CG and the PO_4 groups, D_{HD}. Because of the rotational flexibility of the lipid head group, this value is a measure of the average headgroup tilt projected on to the normal of the lipid bilayer. That is, the lowest D_{HD} found in the presence of MG2a indicates that the lipid headgroups are more tilted toward the membrane than for L18W-PGLa/MG2a with the largest D_{HD}-value.

Effect of Temperature and Peptide Concentration

We varied the temperature in the range from 35 – 50°C to see whether the two peptides and their mixture induce specific changes to membrane structure (Figs. S6–S8). Additionally, we increased the peptide concentration ensuring that Bragg peaks resulting from vesicle aggregate changes do not dominate the scattered intensities. In the case of MG2a and L18W-PGLa this allowed us to go up to P/L = 1/50 (Figs. S7 and S8). For the 1:1 peptide mixture we observed the onset of MLV formation (indicated by a low intensity peak) already at P/L = 1/200 (Fig. S9). We thus restricted our analysis to P/L = 1/400 – 1/200 for the equimolar mixture. Peptide induced formation of coupled bilayers will be discussed in the subsequent paper.

Compared to the above discussed joint SAXS/SANS data, the performed temperature-dependent SAXS experiments provided limited structural resolution. Nevertheless relative structural changes of structural parameters such as A_U as a function of temperature can be retrieved reliably (Figs. S10, S11), using reported lipid volume temperature dependencies (24, 25). Figure 3 shows the thermal expansion of the area per unit cell for POPE/POPG bilayers ($\Delta A_U/\Delta T$), for the presently studied magainins as function of peptide concentration resulting from this analysis. In general we find that the area expansion decreases with peptide concentration and levels off at about 0.22Å^2/K, independent of the specific structure of the added peptides including their mixture. This shows that membranes are increasingly less able to expand laterally with increasing temperature as a result of the peptide induced membrane perturbation.

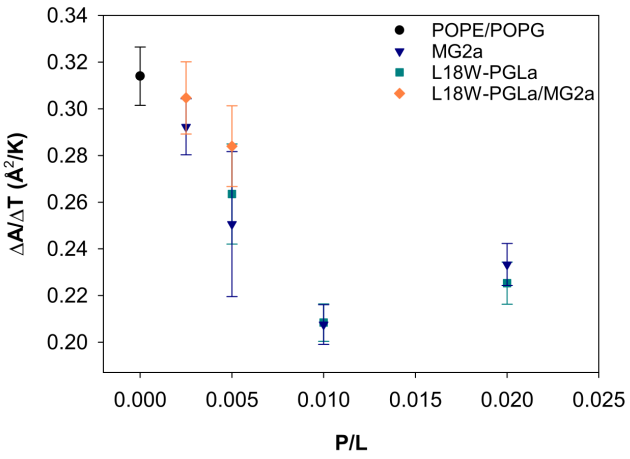

Figure 3: Dependence of the thermal area expansion coefficient of POPE/POPG (3:1 mol/mol) bilayers on peptide concentration (circles: pure bilayer, triangles: MG2a, squares: L18W-PGLa, diamonds: L18W-PGLa/MG2a (1:1 mol/mol)).

All-atom and coarse-grained simulations

To gain additional insights on the molecular level, we performed MD simulations of both peptides within POPE/POPG (3:1 mol/mol) bilayers. Figure S12 compares the form factors derived from all-atom MD simulations to experimental data. The remarkable agreement in particular for $q > 0.15$ Å provides a valuable validation of the results presented below.

Individual peptides

Firstly, we performed all-atom simulations with peptide monomers, where each membrane leaflet contained a single peptide to ensure membrane and system symmetry. Throughout the simulations, both peptides retained their mostly α-helical conformation and remained oriented parallel with respect to the membrane plane (Fig. 4). The exception was MG2a, which showed a partial loss of helicity at the C-terminus in one leaflet. Figure 4 shows snapshots from the end of the 500 ns long simulations together with the depth of peptide insertion. L18W-PGLa was found to be slightly deeper in the headgroup region compared to MG2, which is consistent with our SANS/SAXS analysis.

We observed a local membrane modification in the vicinity of the peptides in agreement with our scattering data analysis. Lipids changed their tilt and conformation in order to fill the hydrophobic void below the inserted peptide, as shown previously (51). To quantify this effect, we calculated the density distribution of the methyl groups of the lipid tails in the peptide aligned trajectories (Fig. 5 *A*, *B*). The methyl density was locally increased below the peptides filling the available space

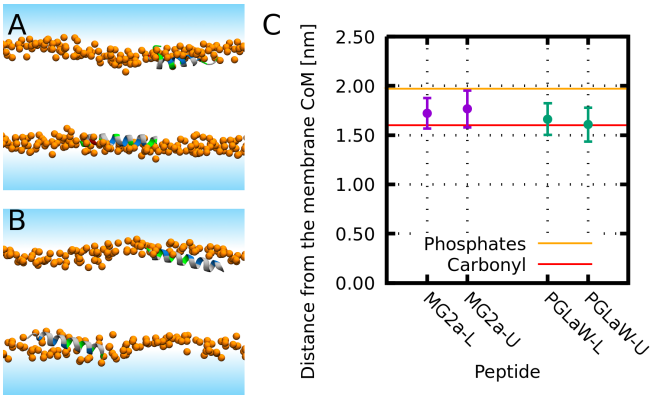

Figure 4: Membrane positioning of MG2a and L18W-PGLa peptides. Left side shows the snapshots from the end of 500 ns long MD simulations of (A) MG2a and (B) L18W-PGLa adsorbed at the membrane surface. Panel C shows the peptide positions in both leaflets averaged over trajectories. Snapshots color coding: Lipid phosphate atoms are shown as orange spheres. Solvent is represented by a blue-shaded area and lipid tails are not shown for clarity. The peptide secondary structure is shown in a cartoon representation, colored by residue type (nonpolar: gray, polar: green, acidic: red, and basic: blue).

between peptide side-chains. The consequent effects on hydrocarbon chain packing are observed in the order parameter profiles dependence as a function of the distance from the peptides Fig.6 *A*, *B* (see also Figs. S13, S14). In general, our analysis showed that palmitoyl chains are mostly affected at intermediate segments, whereas oleoyl hydrocarbons experience most significant changes toward the hydrocarbon tails. Moreover, MG2a appears to induce a slight increase of order close to the POPG glycerol backbone of the unsaturated and a more pronounced disordering of its saturated hydrocarbon chain, respectively. Overall, the effects on hydrocarbon packing lead to membrane thinning in good agreement with our scattering data analysis (see Tab. 1). The changes in density distributions for individual groups of membrane are depicted in Figs. S15 and S16.

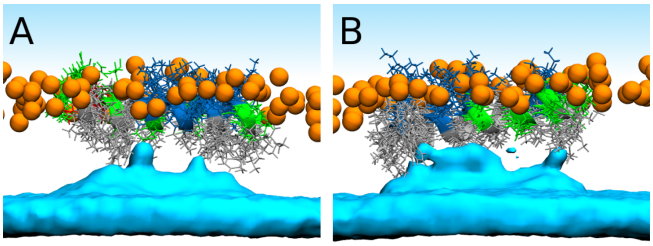

Figure 5: Averaged densities of terminal hydrocarbon CH_3 groups (cyan surfaces) after insertion of MG2a (A) and L18W-PGLa (B) in POPE/POPG bilayers.

Effects of peptide dimers

MG2a and PGLa peptides were previously shown to prefer parallel dimers using a coarse-grained model (52), which also agrees with experimental findings (7, 9). We verified this tendency also for our bacterial membrane mimic. Due to the low number of dimer formation events at low peptide concentrations within the length of our simulations (20 μs), we had to increase P/L ratios from 1/42 to 1/21 in order to facilitate the analysis. We note, however, that this did not lead to the formation of a transmembrane pore as observed in simulations using dilaureoylphosphatidylcholine bilayers (52). This is due to the larger membrane thickness and tighter interfacial lipid packing of POPE/POPG (3:1 mol/mol) bilayers (5) and allowed us to derive the dimerization behavior even at elevated peptide levels. MG2a/L18W-PGLa mixtures starting from random configuration showed the strongest preference for dimerization, followed by MG2a and L18W-PGLa (Fig. 7). MG2a/L18W-PGLa mixtures mainly formed parallel heterodimers, while MG2a and L18W-PGLa preferentially formed anti-parallel homodimers. An additional independent 40 μs long coarse-grained simulations starting with peptides preformed in various heterodimer configurations further corroborated the higher stability of parallel heterodimers as compared to other peptide-peptide alignments (Fig. S20).

Since the peptide-peptide interactions might be overestimated in coarse-grained simulations (53), we performed additional

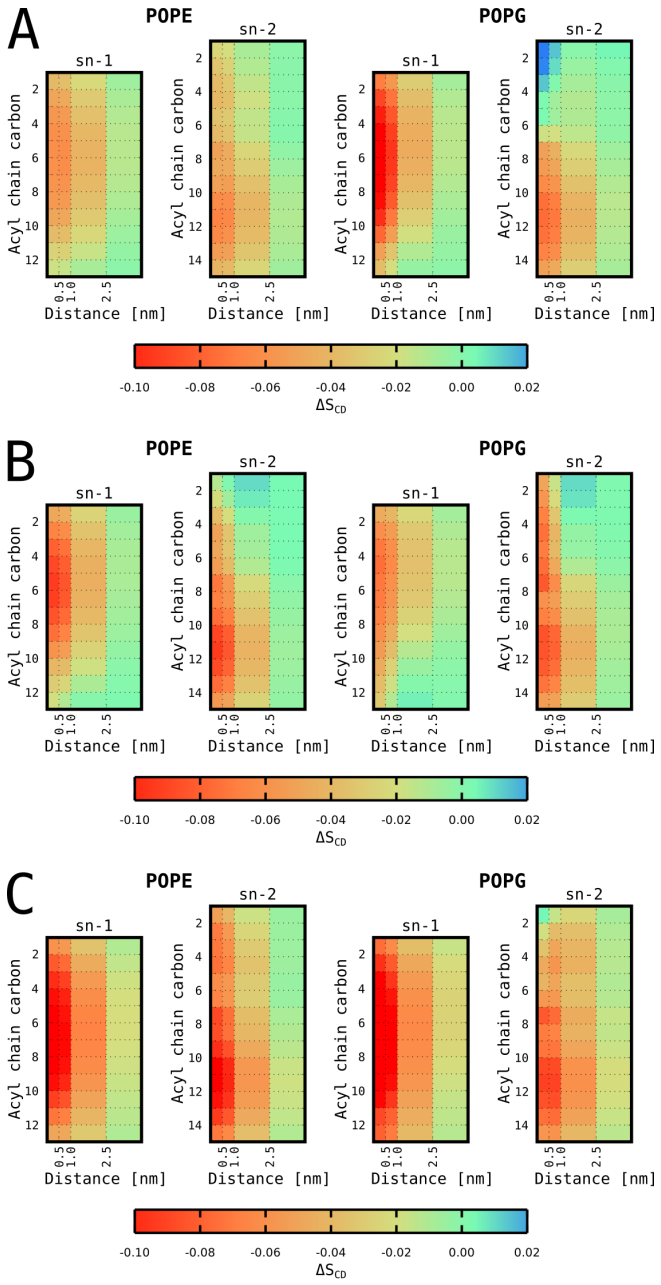

Figure 6: Changes of the lipid tail order parameters as a function of distance from the peptide (A) MG2a, (B) L18W-PGLa, and (C) MG2a+L18W-PGLa.

all-atom simulations starting from preformed dimers. In agreement with our coarse-grained simulations, we found that parallel heterodimers were stable on the simulated timescale.

Based on the preference of MG2a/L18W-PGLa mixtures to form parallel MG2a/L18W-PGLa heterodimers, we investigated the effect of this heterodimer on membrane structure using all-atom simulations of parallel heterodimers in both membrane leaflets (see Fig. S17 for final snapshot of the 500 ns trajectory). In agreement with experimental data heterodimers lead to increased membrane thinning (Tab. 1) and significantly pronounced hydrocarbon chain packing defects (Fig. 6 *C*) as compared to the individual peptides. This supports our above notion that the experimentally observed enhanced membrane perturbation is a result of L18W-PGLa/MG2a dimer formation at low peptide concentrations.

In the next step we interrogated our all-atom simulations for the effect of dimerization on peptide location within bilayers.

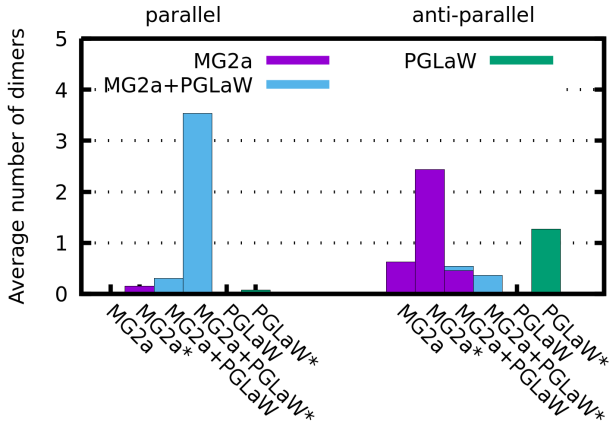

Figure 7: Time averaged number of dimers formed in all simulated coarse-grained systems. Left group corresponds to parallel dimers, while anti-parallel dimers are in the right group. Systems were simulated at either 1/42 or 1/21 (denoted by asterisk) peptide-to-lipid ratio. Purple bars represent MG2a homodimers, L18W-PGLa homodimers are green, and MG2a+L18-WPGLa heterodimers are shown in cyan.

Compared to MG2a and L18W-PGLa (Fig. 4 *C*), L18W-PGLa/MG2a heterodimers inserted more shallow into the membrane (Fig. S18). An analysis of our coarse-grained Martini simulations at both peptide concentrations showed that the transbilayer position of the heterodimers was within uncertainty almost equal to that of MG2a (Fig. 8, Fig. S19). In order to see, whether the dynamics of dimer formation might affect their insertion depth, we artificially kept the peptides in parallel heterodimer configuration in an additional simulation (for details see the Methods section). This simulation decreased the uncertainty of the peptide position significantly, but gave the overall same result for the dimer position as the unconstrained coarse grained simulations, i.e. dimers are located closely to the phosphate group. The main difference compared to all-atom simulations is the slightly less deeper insertion of MG2a, which could be due to force field issues. However, on an absolute scale these differences are only minor. Moreover, results of both simulation models even agree considering the positional uncertainty of the peptides (Fig. 8, Figs. S18, S19). Regarding experimental data (Tab. 1), we find an overall reasonable agreement, with respect to the peptide position. Specifically, there is broad consensus between the here applied different experimental and computational techniques that L18W-PGLa positions itself further out from the bilayer center, when dimerizing with MG2a.

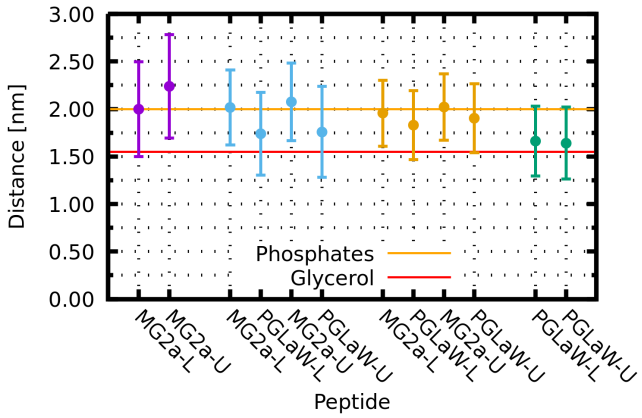

Figure 8: Effect of peptide dimerization on the insertion depth of peptides in POPE/POPG bilayers from coarse-grained simulations. Data show the distances of the peptides from the membrane's center of mass for the individual peptides (MG2a (purple), L18W-PGLa (green))
, as well as unconstrained (blue) and constrained (orange) L18W-PGLa/MG2a (P/L = 1/21). The distances were averaged over 20 μs for all peptides and are presented for (L)ower and (U)pper membrane leaflets individually. Error bars represent the standard deviation. Orange and red horizontal lines represent the approximate position of phosphate and glycerol groups.

DISCUSSION

We combined SAXS/SANS experiments with all-atom and coarse-grained MD simulations to interrogate mutual interactions between L18W-PGLa, MG2a, and fully hydrated POPE/POPG (3:1 mol/mol) bilayers. The focus of the present work is on low peptide concentrations, i.e. where equimolar mixtures of both peptide do not permeabilize POPE/POPG bilayers synergistically (5). Yet, we demonstrate that the peptide mixture leads to significantly enhanced membrane perturbations even at low concentrations.

We developed a SDP analysis for peptide containing lipid membranes, which allowed us to determine the peptide position in the bilayer with high accuracy at low peptide concentrations by a simultaneous statistical analysis of four differently contrasted SAXS/SANS experiments. The observables were in excellent agreement with our MD simulations, enabling additional insight on lipid-peptide and peptide-peptide interactions. Note that previous reports on similar systems using solid state ^{15}N-NMR were not sensitive to the penetration depth of peptides within the headgroups. Both our experimental and simulation data consistently showed that MG2a inserts slightly less into the bilayer than L18W-PGLa (Tab. 1, Fig. 4 *C*). This can be understood in terms of the larger hydrophilic surface of MG2a compared to L18W-PGLa due the larger number of polar residues (5).

In agreement with ^{15}N-NMR data on POPE/POPG (3:1 mol/mol) (13) and POPE-enriched bilayers (11) we found that both peptides adopt a surface-aligned topology, even in the case of equimolar L18W-PGLa/MG2a mixtures. The surface-aligned topology caused significant disorder of hydrocarbon chain packing, which was most pronounced in the vicinity of the peptides. In particular, we observed that the methyl termini of the hydrocarbons filled large fractions of the void below the peptide (Fig. 5), consistent with previous reports on dimple formation and membrane thinning (54). Membrane thinning was observed for both peptides (Tab. 1), consistent with a surface-aligned topology. The pronounced membrane thinning for equimolar mixtures of the two peptides provides indirect evidence for dimer formation. This is further supported by our experimental form factors, which were determined from a statistical data analysis and which clearly show that the effects of the individual peptides cannot be simply combined to yield the membrane structure in the presence of both peptides (Fig. S5). Hence, PGLa and MG2a seem to form dimers at concentrations much lower than reported previously (7, 9, 52).

Using all-atom MD simulations we derived order parameter profiles as a function of distance from the peptides. In agreement with a previous NMR study (13) both peptides were found to perturb the saturated hydrocarbons of surrounding lipids (Fig. 6). Our results suggest that MG2a is more effective than L18W-PGLa in doing so, which correlates with the further outward location of MG2a within the membrane and its increased bulkiness (molecular volumes: $V_{\mathrm{L18W\text{-}PGLa}} = 4927.8$ Å^3, and $V_{\mathrm{MG2a}} = 5748.0$ Å^3). MD simulations additionally allowed us to probe order parameter profiles of unsaturated hydrocarbons. Interestingly, we found that MG2a increased the order of the oleoyl chain close to the glycerol backbone of POPG only, while a general decrease of this chain's order parameter was observed for POPE at all segments for both peptides (Fig. 6 *A*, *B*, Figs. S13, S14). This indicates specific interactions of MG2a with POPG, which are located around the positively charged amino acids as revealed a detailed analysis of MD data (Fig. S21). Finally, assuming heterodimers, all effects observed with respect to the order of hydrocarbon chains were significantly more pronounced as compared to single peptides (Fig. 6 *C*), in agreement with our experimentally observed changes of membrane structure. This is also consistent with previous reports (see, e.g. (55)), showing that the formation of dimers amplifies the perturbation of the lipid tails in the vicinity of peptide dimer as compared to monomers.

Our simulations indicated that homodimers formed preferentially in antiparallel configuration, while L18W-PGLa/MG2a formed mainly parallel heterodimers (Fig. 7), which is in agreement with a previous study (52). Interestingly, heterodimer formation has been reported for significantly different lipid bilayers. Thus, dimerization of PGLa and MG2a, does not appear to be highly specific to lipid composition, although we cannot comment on the onset of dimerization in other lipid bilayers from the present study. The analysis of enthalpic interactions between different amino acids showed that dimer formation is stabilized by salt bridges between MG2a-Glu19 and Lys12 or Lys15 residues of L18W-PGLa (Fig. S22) in agreement with (52). Moreover, there are significant hydrophobic interactions between the peptides. For example, Ulmschneider *et al.* reported a stabilization of PGLa homodimers by Gly/Ala interactions at high P/L ratios (56). It appears, however, that the sum of all these interactions leads to a preferential formation of L18W-PGLa/MG2a heterodimers as compared to L18W-PGLa/L18W-PGLa or MG2a/MG2a homodimers, which is consistent with previous observations (6).

Most interestingly, peptide dimerization affects the penetration depth of the surface-aligned peptides. In particular L18W-PGLa moves somewhat further out in the headgroup region, when it associates with MG2a (Tab. 1, Fig. 8, Figs. S18, S19). This leads to a larger void created in the membrane interior just below the peptides, causing an increased change of membrane structure. Hence, the ability to form a dimers appears to be important for the membrane perturbation efficacy of the studied peptides.

CONCLUSION

Our study suggests that an early onset of the formation of peptide dimers is the key event to the enhanced activity of L18W-PGLa/MG2a mixtures. Previously, we speculated that L18W-PGLa causes a deeper insertion of MG2a into the bilayer (5). Indeed, the present work shows the opposite, i.e. that L18W-PGLa moves further out from the membrane center when forming a heterodimer with MG2a. These heterodimers perturb membranes significantly more than the sum of the effects induced by individual (non-interacting) peptides. Apparently, this 'synergistic' dimerization is not sufficient to allow enhanced leakage of dyes (although smaller polar molecules might already permeate the bilayer) (5). For membrane leakage to occur, higher peptide concentrations are required. The corresponding membrane restructuring effects will be described in the subsequent paper.

SUPPORTING MATERIAL

Supporting Materials and Methods, twenty three figures, and one table are available at ...

AUTHOR CONTRIBUTIONS

M.P. performed the experimental research, analyzed the data, and wrote the article. I.K. carried out all simulations, analyzed the data, and wrote the article. M.-S.A. performed SANS experiments. R.V., K.L. and G.P. designed the research and wrote the article.

ACKNOWLEDGMENTS

This work was supported by the Austrian Science Funds FWF (project No. I1763-B21 to K.L.), the Czech Science Foundation (grant 17-11571S to R.V.) and the CEITEC 2020 (LQ1601) project with financial contribution made by the Ministry of Education, Youths and Sports of the Czech Republic within special support paid from the National Programme for Sustainability II funds. Computational resources were provided by the CESNET LM2015042 and the CERIT Scientific Cloud LM2015085, provided under the programme 'Projects of Large Research, Development, and Innovations Infrastructures'. This work was supported by The Ministry of Education, Youth and Sports from the Large Infrastructures for Research, Experimental Development and Innovations project 'IT4Innovations National Supercomputing Center – LM2015070'. We acknowledge SOLEIL for provision of synchrotron radiation facilities and we would like to thank Javier Perez for assistance in using beamline SWING. This work is based upon experiments performed at the KWS-1 instrument operated by JCNS at the Heinz Maier-Leibnitz Zentrum (MLZ), Garching, Germany.

SUPPORTING CITATIONS

Reference (57) appears in the Supporting Material.

REFERENCES

1. Wimley, W. C., and K. Hristova, 2011. Antimicrobial peptides: successes, challenges and unanswered questions. *J Membr Biol* 239:27–34.

2. Lohner, K., 2016. Membrane-active Antimicrobial Peptides as Template Structures for Novel Antibiotic Agents. *CTMC* 17:508–519.

3. Zasloff, M., 2002. Antimicrobial peptides of multicellular organisms. *Nature* 415:389–395.

4. Bechinger, B., 2015. The SMART model: Soft Membranes Adapt and Respond, also Transiently, in the presence of antimicrobial peptides. *J Pept Sci* 21:346–355.

5. Leber, R., M. Pachler, I. Kabelka, I. Svoboda, D. Enkoller, R. Vácha, K. Lohner, and G. Pabst, 2018. Synergism of Antimicrobial Frog Peptides Couples to Membrane Intrinsic Curvature Strain. *Biophys J* 114:1945–1954.

6. Matsuzaki, K., Y. Mitani, K. Y. Akada, O. Murase, S. Yoneyama, M. Zasloff, and K. Miyajima, 1998. Mechanism of synergism between antimicrobial peptides magainin 2 and PGLa. *Biochemistry* 37:15144–15153.

7. Hara, T., Y. Mitani, K. Tanaka, N. Uematsu, A. Takakura, T. Tachi, H. Kodama, M. Kondo, H. Mori, A. Otaka, F. Nobutaka, and K. Matsuzaki, 2001. Heterodimer Formation between the Antimicrobial Peptides Magainin 2 and PGLa in Lipid Bilayers: A Cross-Linking Study †. *Biochemistry* 40:12395–12399.

8. Nishida, M., Y. Imura, M. Yamamoto, S. Kobayashi, Y. Yano, and K. Matsuzaki, 2007. Interaction of a magainin-PGLa hybrid peptide with membranes: insight into the mechanism of synergism. *Biochemistry* 46:14284–14290.

9. Tremouilhac, P., E. Strandberg, P. Wadhwani, and A. S. Ulrich, 2006. Synergistic transmembrane alignment of the antimicrobial heterodimer PGLa/magainin. *J Biol Chem* 281:32089–32094.

10. Salnikov, E. S., and B. Bechinger, 2011. Lipid-controlled peptide topology and interactions in bilayers: structural insights into the synergistic enhancement of the antimicrobial activities of PGLa and magainin 2. *Biophys J* 100:1473–1480.

11. Strandberg, E., J. Zerweck, P. Wadhwani, and A. S. Ulrich, 2013. Synergistic insertion of antimicrobial magainin-family peptides in membranes depends on the lipid spontaneous curvature. *Biophys J* 104:L9–11.

12. Zerweck, J., E. Strandberg, O. Kukharenko, J. Reichert, J. Bürck, P. Wadhwani, and A. S. Ulrich, 2017. Molecular mechanism of synergy between the antimicrobial peptides PGLa and magainin 2. *Sci Rep* 7:13153.

13. Harmouche, N., and B. Bechinger, 2018. Lipid-Mediated Interactions between the Antimicrobial Peptides Magainin 2 and PGLa in Bilayers. *Biophys J* 115:1033–1044.

14. Kabelka, I., and R. Vácha, 2018. Optimal Hydrophobicity and Reorientation of Amphiphilic Peptides Translocating through Membrane. *Biophys J* 115:1045–1054.

15. Kingsley, P. B., and G. W. Feigenson, 1979. The synthesis of a perdeuterated phospholipid: 1,2-dimyristoyl-sn-glycero-3-phosphocholine-d72. *Chem Phys Lipids* 24:135–147.

16. Feoktystov, A. V., H. Frielinghaus, Z. Di, S. Jaksch, V. Pipich, M.-S. Appavou, E. Babcock, R. Hanslik, R. Engels, G. Kemmerling, H. Kleines, A. Ioffe, D. Richter, and T. Brückel, 2015. KWS-1 high-resolution small-angle neutron scattering instrument at JCNS: current state. *J Appl Crystallogr* 48:61–70.

17. Pencer, J., S. Krueger, C. P. Adams, and J. Katsaras, 2006. Method of separated form factors for polydisperse vesicles. *J Appl Crystallogr* 39:293–303.

18. Kucerka, N., J. F. Nagle, J. N. Sachs, S. E. Feller, J. Pencer, A. Jackson, and J. Katsaras, 2008. Lipid bilayer structure determined by the simultaneous analysis of neutron and X-ray scattering data. *Biophys J* 95:2356–2367.

19. Heberle, F. A., and G. Pabst, 2017. Complex biomembrane mimetics on the sub-nanometer scale. *Biophys Rev* 9:353–373.

20. Pan, J., D. P. Tieleman, J. F. Nagle, N. Kucerka, and S. Tristram-Nagle, 2009. Alamethicin in lipid bilayers: combined use of X-ray scattering and MD simulations. *Biochim Biophys Acta* 1788:1387–1397.

21. Dupuy, F. G., I. Pagano, K. Andenoro, M. F. Peralta, Y. Elhady, F. Heinrich, and S. Tristram-Nagle, 2018. Selective Interaction of Colistin with Lipid Model Membranes. *Biophys J* 114:919–928.

22. Khondker, A., R. J. Alsop, A. Dhaliwal, S. Saem, J. M. Moran-Mirabal, and M. C. Rheinstädter, 2017. Membrane Cholesterol Reduces Polymyxin B Nephrotoxicity in Renal Membrane Analogs. *Biophys J* 113:2016–2028.

23. Nielsen, J. E., V. A. Bjørnestad, and R. Lund, 2018. Resolving the structural interactions between antimicrobial peptides and lipid membranes using small-angle scattering methods: the case of indolicidin. *Soft Matter* 14:8750–8763.

24. Kučerka, N., B. van Oosten, J. Pan, F. A. Heberle, T. A. Harroun, and J. Katsaras, 2015. Molecular structures of fluid phosphatidylethanolamine bilayers obtained from simulation-to-experiment comparisons and experimental scattering density profiles. *J Phys Chem B* 119:1947–1956.

25. Pan, J., D. Marquardt, F. A. Heberle, N. Kučerka, and J. Katsaras, 2014. Revisiting the bilayer structures of fluid phase phosphatidylglycerol lipids: Accounting for exchangeable hydrogens. *Biochim Biophys Acta* 1838:2966–2969.

26. Heftberger, P., B. Kollmitzer, A. A. Rieder, H. Amenitsch, and G. Pabst, 2015. In situ determination of structure and fluctuations of coexisting fluid membrane domains. *Biophys J* 108:854–862.

27. Belička, M., A. Weitzer, and G. Pabst, 2017. High-resolution structure of coexisting nanoscopic and microscopic lipid domains. *Soft Matter* 13:1823–1833.

28. Narayanan, T., D. Weerakkody, A. G. Karabadzhak, M. Anderson, O. A. Andreev, and Y. K. Reshetnyak, 2016. pHLIP Peptide Interaction with a Membrane Monitored by SAXS. *J Phys Chem B* 120:11484–11491.

29. Wieprecht, T., O. Apostolov, M. Beyermann, and J. Seelig, 2000. Interaction of a mitochondrial presequence with lipid membranes: role of helix formation for membrane binding and perturbation. *Biochemistry* 39:15297–15305.

30. Nagle, J. F., and S. Tristram-Nagle, 2000. Structure of lipid bilayers. *Biochim Biophys Acta* 1469:159–195.

31. Storn, R., and K. Price, 1997. Differential Evolution – A Simple and Efficient Heuristic for global Optimization over Continuous Spaces. *J GLOBAL OPTIM* 11:341–359.

32. Abraham, M. J., T. Murtola, R. Schulz, S. Páll, J. C. Smith, B. Hess, and E. Lindahl, 2015. GROMACS: High performance molecular simulations through multi-level parallelism from laptops to supercomputers. *SoftwareX* 1-2:19–25.

33. Páll, S., M. J. Abraham, C. Kutzner, B. Hess, and E. Lindahl, 2015. Tackling Exascale Software Challenges in Molecular Dynamics Simulations with GROMACS. *In* E. Laure, and S. Markidis, editors, Solving software challenges for exascale, Springer, Cham, volume 8759 of *LNCS Sublibrary: SL 1 - Theoretical Computer Science and General Issues*, 3–27.

34. Lindorff-Larsen, K., S. Piana, K. Palmo, P. Maragakis, J. L. Klepeis, R. O. Dror, and D. E. Shaw, 2010. Improved side-chain torsion potentials for the Amber ff99SB protein force field. *Proteins* 78:1950–1958.

35. Sorin, E. J., and V. S. Pande, 2005. Exploring the helix-coil transition via all-atom equilibrium ensemble simulations. *Biophys J* 88:2472–2493.

36. Jämbeck, J. P. M., and A. P. Lyubartsev, 2012. Derivation and systematic validation of a refined all-atom force field for phosphatidylcholine lipids. *J Phys Chem B* 116:3164–3179.

37. Jämbeck, J. P. M., and A. P. Lyubartsev, 2012. An Extension and Further Validation of an All-Atomistic Force Field for Biological Membranes. *J Chem Theory Comput* 8:2938–2948.

38. Nosé, S., 1984. A unified formulation of the constant temperature molecular dynamics methods. *J Chem Phys* 81:511–519.

39. Nosé, S., 1984. A molecular dynamics method for simulations in the canonical ensemble. *Mol Phys* 52:255–268.

40. Hoover, W. G., 1985. Canonical dynamics: Equilibrium phase-space distributions. *Phys. Rev. A* 31:1695–1697.

41. Parrinello, M., and A. Rahman, 1980. Crystal Structure and Pair Potentials: A Molecular-Dynamics Study. *Phys. Rev. Lett.* 45:1196–1199.

42. Parrinello, M., and A. Rahman, 1981. Polymorphic transitions in single crystals: A new molecular dynamics method. *J Appl Phys* 52:7182–7190.

43. Essmann, U., L. Perera, M. L. Berkowitz, T. Darden, H. Lee, and L. G. Pedersen, 1995. A smooth particle mesh Ewald method. *J Chem Phys* 103:8577–8593.

44. Allen, M. P., and D. J. Tildesley, 2017. volume 1. Oxford University Press.

45. Jo, S., T. Kim, V. G. Iyer, and W. Im, 2008. CHARMM-GUI: a web-based graphical user interface for CHARMM. *J Comput Chem* 29:1859–1865.

46. Marrink, S. J., H. J. Risselada, S. Yefimov, D. P. Tieleman, and A. H. de Vries, 2007. The MARTINI force field: coarse grained model for biomolecular simulations. *J Phys Chem B* 111:7812–7824.

47. Monticelli, L., S. K. Kandasamy, X. Periole, R. G. Larson, D. P. Tieleman, and S.-J. Marrink, 2008. The MARTINI Coarse-Grained Force Field: Extension to Proteins. *J Chem Theory Comput* 4:819–834.

48. de Jong, D. H., G. Singh, W. F. D. Bennett, C. Arnarez, T. A. Wassenaar, L. V. Schäfer, X. Periole, D. P. Tieleman, and S. J. Marrink, 2013. Improved Parameters for the Martini Coarse-Grained Protein Force Field. *J Chem Theory Comput* 9:687–697.

49. Bussi, G., D. Donadio, and M. Parrinello, 2007. Canonical sampling through velocity rescaling. *J Chem Phys* 126:014101.

50. Lee, J., X. Cheng, J. M. Swails, M. S. Yeom, P. K. Eastman, J. A. Lemkul, S. Wei, J. Buckner, J. C. Jeong, Y. Qi, S. Jo, V. S. Pande, D. A. Case, C. L. Brooks, A. D. MacKerell, J. B. Klauda, and W. Im, 2016. CHARMM-GUI Input Generator for NAMD, GROMACS, AMBER, OpenMM, and CHARMM/OpenMM Simulations Using the CHARMM36 Additive Force Field. *J Chem Theory Comput* 12:405–413.

51. Mihailescu, M., R. G. Vaswani, E. Jardón-Valadez, F. Castro-Román, J. A. Freites, D. L. Worcester, A. R. Chamberlin, D. J. Tobias, and S. H. White, 2011. Acyl-chain methyl distributions of liquid-ordered and -disordered membranes. *Biophys J* 100:1455–1462.

52. Han, E., and H. Lee, 2015. Synergistic effects of magainin 2 and PGLa on their heterodimer formation, aggregation, and insertion into the bilayer. *RSC Adv.* 5:2047–2055.

53. Javanainen, M., H. Martinez-Seara, and I. Vattulainen, 2017. Excessive aggregation of membrane proteins in the Martini model. *PLoS ONE* 12:1–20.

54. Ludtke, S., K. He, and H. Huang, 1995. Membrane thinning caused by magainin 2. *Biochemistry* 34:16764—16769.

55. Hristova, K., C. E. Dempsey, and S. H. White, 2001. Structure, Location, and Lipid Perturbations of Melittin at the Membrane Interface. *Biophys J* 80:801–811.

56. Ulmschneider, J. P., J. C. Smith, M. B. Ulmschneider, A. S. Ulrich, and E. Strandberg, 2012. Reorientation and dimerization of the membrane-bound antimicrobial peptide PGLa from microsecond all-atom MD simulations. *Biophys J* 103:472–482.

57. Cieplak, P., W. d. Cornell, C. Bayly, and P. A. Kollman, 1995. Application of the multimolecule and multiconformational RESP methodology to biopolymers: Charge derivation for DNA, RNA, and proteins. *J. Comput. Chem.* 16:1357–1377.

Supporting Material

Magainin 2 and PGLa in Bacterial Membrane Mimics I: Peptide-Peptide and Lipid-Peptide Interactions

M.P., I.K., M.-S.A., K.L., R.V., G. P.

Scattering Density Profile Model for a symmetric Membrane

POPE and POPG were parsed into CH_3, CH_2, CH, CG, PO_4, ENX and PG2 groups as reported previously (1, 2) (Fig. S1). Since we studied POPE/POPG mixtures the several of these groups were combined in order to reduce the number of adjustable parameters. In particular, we merged the CH_3, CH_2, CH, CG, PO_4 groups and fitted only ENX and PG2 individually. Except for CH_2 all lipid groups were modelled with Gaussians

$$P_i^X(z) = S_i^X \frac{n_i V_i}{A_U \sigma_i} \left[e^{-\frac{(z+z_i)^2}{2\sigma^2}} + e^{-\frac{(z-z_i)^2}{2\sigma^2}} \right] \tag{S1}$$

of width σ_i with $i \in \{CH_3, CH, CG, PO_4, ENX \text{ and } PG2\}$, where V_i is the volume of each group and n_i is number of type i components (e.g. $n_{CH_3} = 2$).

NMR experiments demonstrated that L18W-PGLa and MG2a align parallel to the membrane surface in POPE/POPG bilayers (3). Their volume distribution functions were therefore described analogously to Eq. (S1). The scaling factor S_i^X ($X \in \{L, P\}$) accounts for the fraction of lipid

$$S_i^L = \frac{n_i^L}{\sum_i^n n_i^L} \tag{S2}$$

and peptide per unit cell

$$S_i^P = \frac{n_i^P}{\sum_i^n n_i^L}, \tag{S3}$$

respectively.

The overall hydrocarbon core of the unit cell was described with error functions

$$P_{HC}^L(z) = \frac{1}{2} \left[\frac{2}{\sqrt{\pi}} \int_0^{\frac{z+z_i}{\sqrt{2}\sigma}} e^{-x^2} dx + \frac{2}{\sqrt{\pi}} \int_0^{\frac{z-z_i}{\sqrt{2}\sigma}} e^{-x^2} dx \right], \tag{S4}$$

from which the CH_2 distribution is obtained via

$$P_{CH_2}^L(z) = P_{HC}^L(z) - P_{CH3}^L(z) - P_{CH}^L(z). \tag{S5}$$

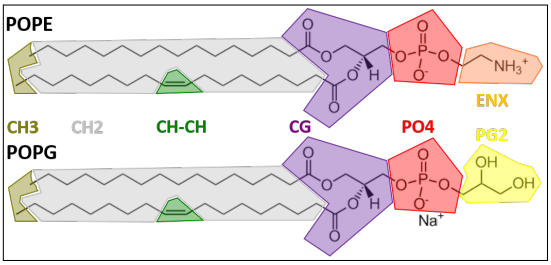

Figure S1: Schematic of POPE and POPG parsing into quasimolecular fragments. The chains consist of terminal methyl (CH_3), methylene (CH_2) and methine (CH), whereas the headgroup region is composed of carbonyl+glycerol (CG), phosphate (PO_4), ethanolamine (ENX) and glycerol (PG2).

Assuming ideal volume filling at every position z along the bilayer normal, we obtain the water distributions by using

$$P_W(z) = 1 - \sum_k P(z)_k, \tag{S6}$$

with $k \in \{CH_3, CH_2, CH, CG, PO_4, ENX, PG2, \text{and } P\}$.

Finally, the neutron and X-ray form factors were calculated through

$$F(q) = 2 \int_0^{\frac{D}{2}} \Delta\rho(z) cos(qz) dz, \tag{S7}$$

where

$$\Delta\rho(z) = \sum_k \left[\rho_k(z) - \rho_W\right] P_k(z), \tag{S8}$$

is the scattering length density (SLD) contrast with respect to water ρ_W and D/2 refers to any position outside the bilayer for which $\Delta\rho(z) = 0$.

The total volumes of the individual components needs to be supplied to the analysis. For example, the volume of the unit cell containing lipid and peptide

$$V_{\mathrm{LP}} = \frac{n_{\mathrm{POPE}} V_{\mathrm{POPE}}}{n_{\mathrm{POPE}} + n_{\mathrm{POPG}}} + \frac{n_{\mathrm{POPG}} V_{\mathrm{POPG}}}{n_{\mathrm{POPE}} + n_{\mathrm{POPG}}} + \frac{n_{\mathrm{P}} V_{\mathrm{P}}}{n_{\mathrm{POPE}} + n_{\mathrm{POPG}}}, \tag{S9}$$

where n_{POPE}, n_{POPG} and n_{P} are the total numbers of POPE, POPG and peptide molecules, and $V_{\mathrm{POPE}} = 1175.1$ Å^3, $V_{\mathrm{POPG}} = 1216.55$ Å^3 (1, 2) are the corresponding volumes. The peptide volumes $V_{\mathrm{P}} = 4927.8$ Å^3 for L18W-PGLa and 5748.0 Å^3 for MG2a were obtained from MD simulations.

The scattered intensity is then given by

$$I(q) = \frac{K}{q^2} F(q)^2 + I_{inc}, \tag{S10}$$

where I_{inc} is the incoherent background and K is the instrumental scaling constant.

SAXS/SANS data were jointly fitted with a combined cost function

$$\chi^2 = \sum_{i,j} \left(\frac{I_i^j - I_{\mathrm{fit_i}}^j}{w_i^j \sigma_i^j} \right)^2, \tag{S11}$$

where I_i^j is the recorded intensity of contrast j (e.g. SAXS or SANS including differently contrasted samples), $\mathrm{I}_{\mathrm{fit_i}}^j$ is the calculated intensity, and σ_i^j corresponds to the experimental error of the measured intensities. Additionally, specific weighting schemes were employed to account for the importance of the first minimum as well as the intensity modulations at high q. This was achieved by introducing weighting factors w_i^j in order to decrease experimental uncertainties by in specific q-regions of the scattering data.

To ensure connectivity of the lipid structure and to further reduce the number of adjustable parameters, we coupled the CG group to the boundary of the hydrocarbon core analogously to a previous report (4), $z_{\mathrm{CG}} = D_{\mathrm{C}} + 1$ Å, and fixed relative distances between $z_{\mathrm{ENX}} - z_{\mathrm{PO_4}} = 1.57$ Å and $z_{\mathrm{PG2}} - z_{\mathrm{PO_4}} = 2.92$ Å, as reported in (1, 2). By definition, the position of the CH_2 group is constrained by $z_{\mathrm{CH_2}} = V_{\mathrm{HC}}/A_{\mathrm{U}}$, thus leaving only $z_{\mathrm{CH_3}}$, z_{CH}, $z_{\mathrm{PO_4}}$ and the position of the peptide z_{P}, as well as the corresponding widths as freely adjustable parameters. In cases, where only SAXS data was available a quadratic penalty function for negative water probabilities was utilized, which were caused by inappropriate positioning of the peptides. The corresponding prefactor was chosen to be as small as possible, in order to prevent a trapping of the fitting routine in a local minimum.

Supplementary Figures

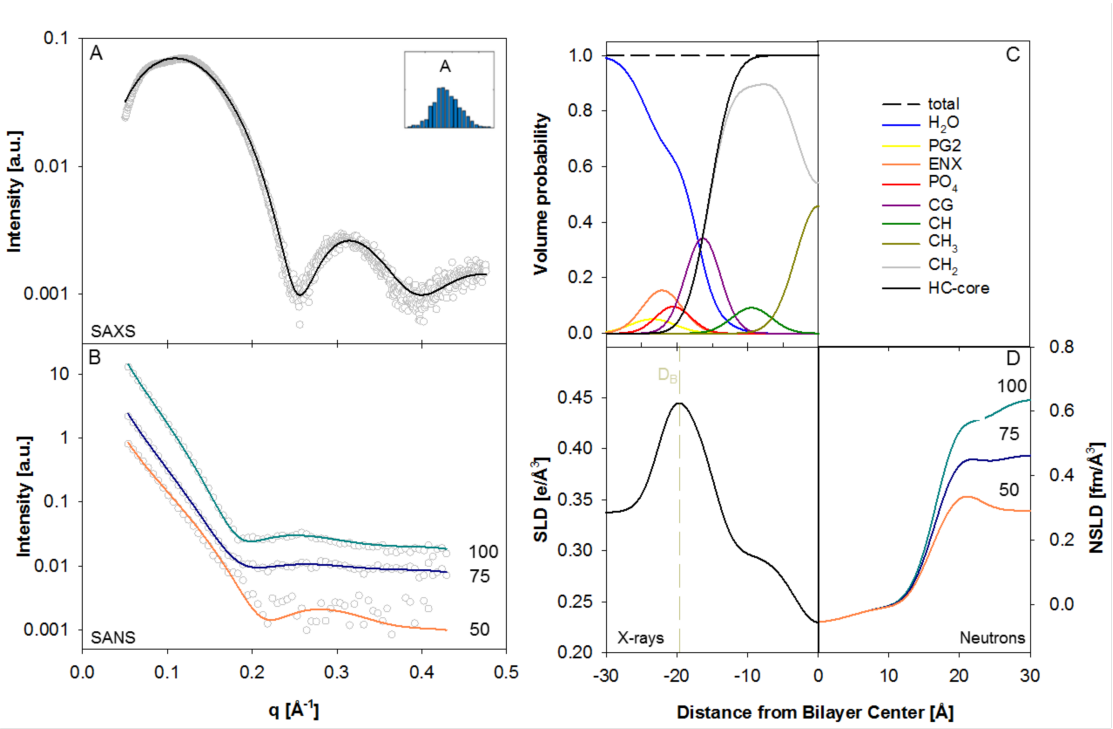

Figure S2: Joint analysis of SAXS and SANS data of LUVs (size $\sim$ 100 nm) composed POPE/POPG (3:1 mol/mol) at 35°C. Panels (A) and (B) show the fits (solid lines) of the joint analysis. The insert to (A) shows a histogram of the area per unit cell obtained from the statistical analysis. Panel (C) shows the volume probability distribution of the bilayer and panel (D) displays the corresponding electron and neutron scattering length densities. The Luzzati thickness, D_B, is marked in the electron density profile.

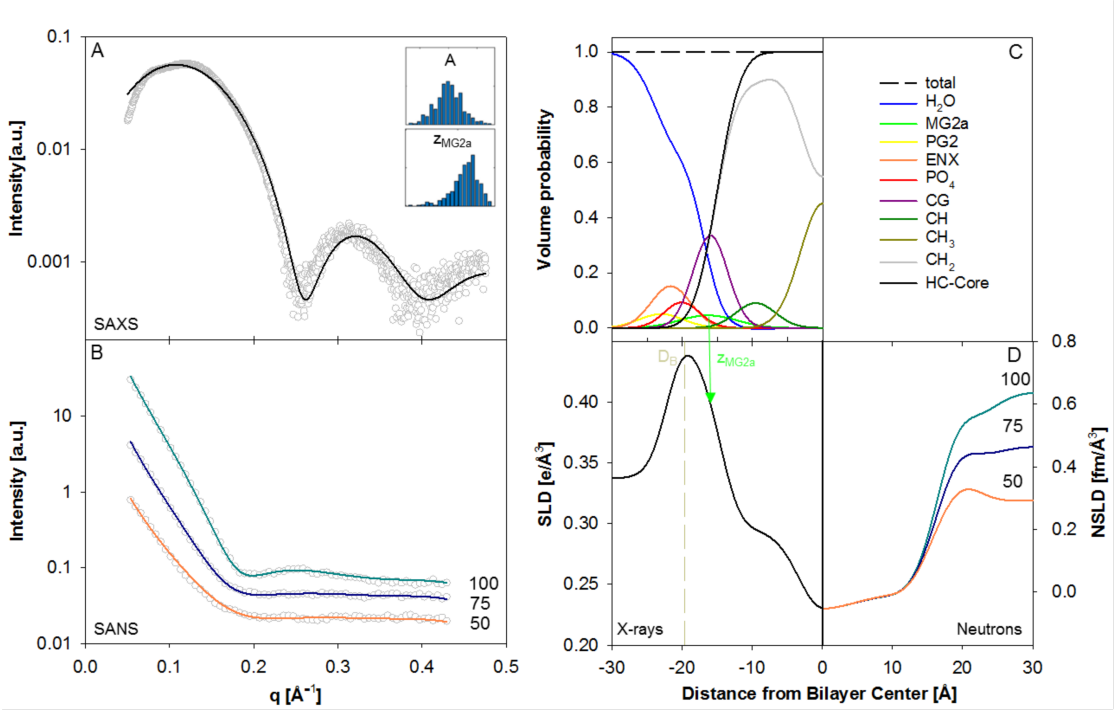

Figure S3: Joint analysis of SAXS and SANS data of liposomes composed POPE/POPG (3:1 mol/mol) in the presence of MG2a (P/L = 1/200) at 35°C. Panels (A) and (B) show the fits (solid lines) of the joint analysis. Inserts to (A) show histograms of the area per unit cell and the position of the peptide in the bilayer as obtained from the statistical data analysis. Panel (C) shows the volume probability distribution of the bilayer and panel (D) displays the corresponding electron and neutron scattering length densities. The Luzzati thickness, D_B, and the transbilayer position of MG2a, z_{MG2a}, are marked in the electron density profile.

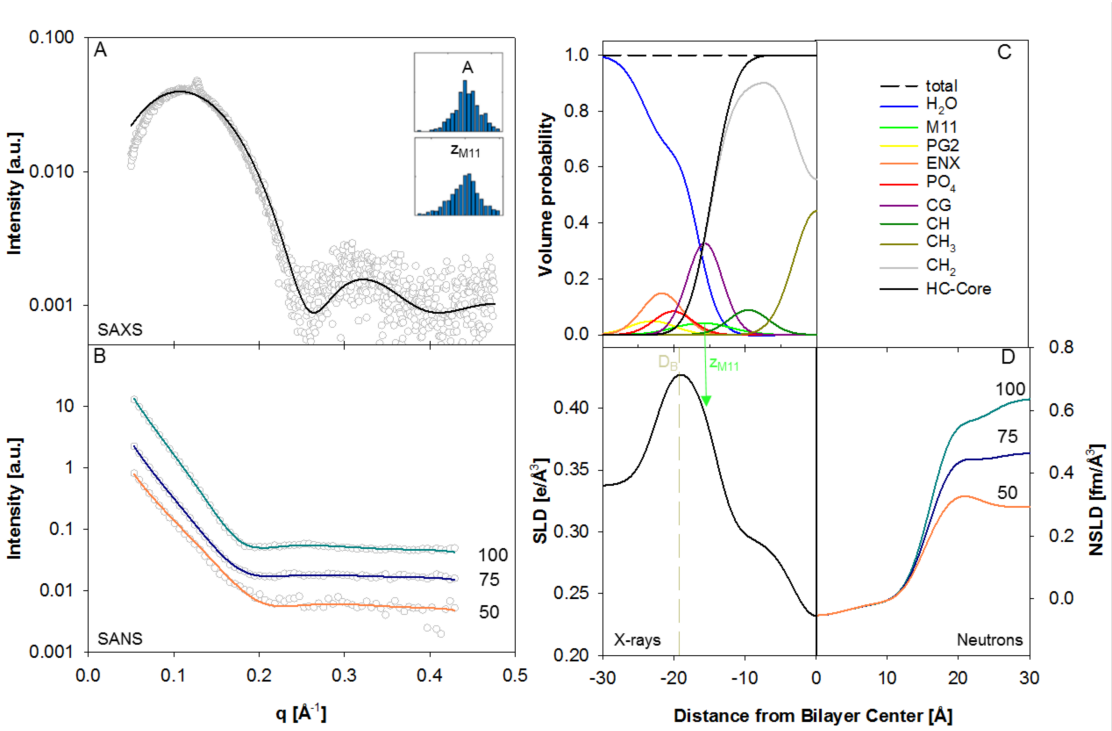

Figure S4: Joint analysis of SAXS and SANS data of liposomes composed POPE/POPG (3:1 mol/mol) in the presence of a equimolar mixture of L18W-PGLa and MG2a (M11) (P/L = 1/200) at 35°C. Panel (A) and (B) show the fits (solid lines) of the joint analysis. Inserts to (A) show histograms of the area per unit cell and the position of the peptide in the bilayer as obtained from the statistical data analysis. Panel (C) shows the volume probability distribution of the bilayer and panel (D) displays the corresponding electron and neutron scattering length densities. The Luzzati thickness, D_B, and the average transbilayer peptide position, z_{M11}, are marked in the electron density profile.

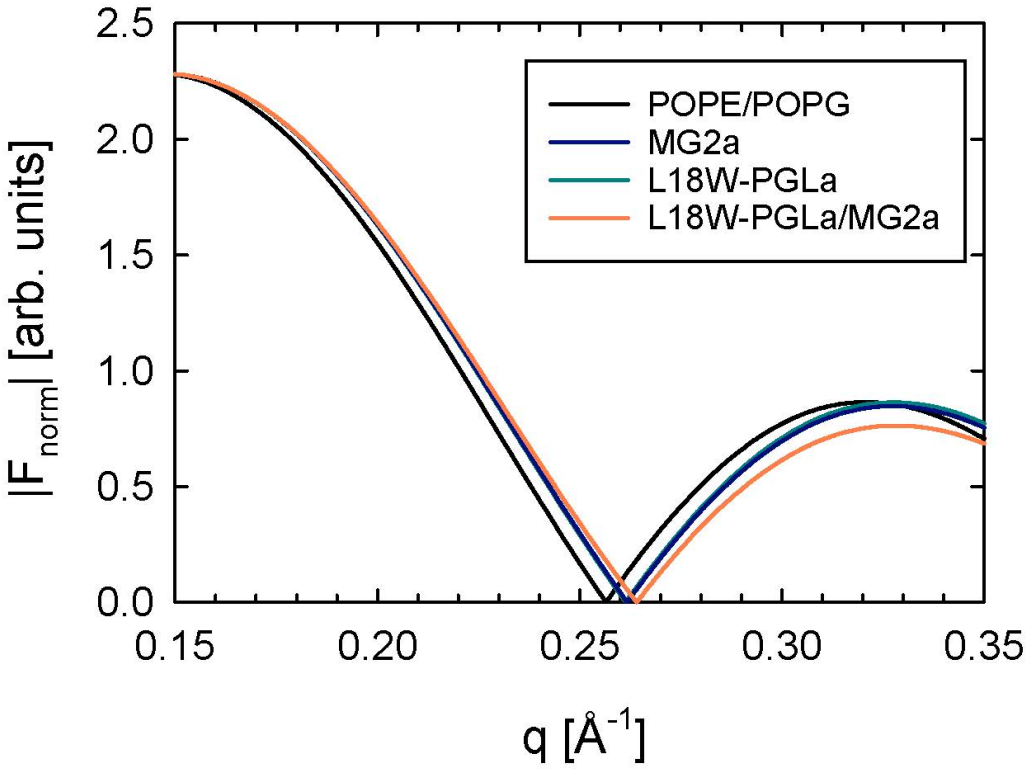

Figure S5: Normalized experimental SAXS form factors for POPE/POPG in the absence and presence of the different peptides obtained from statistical data fitting.

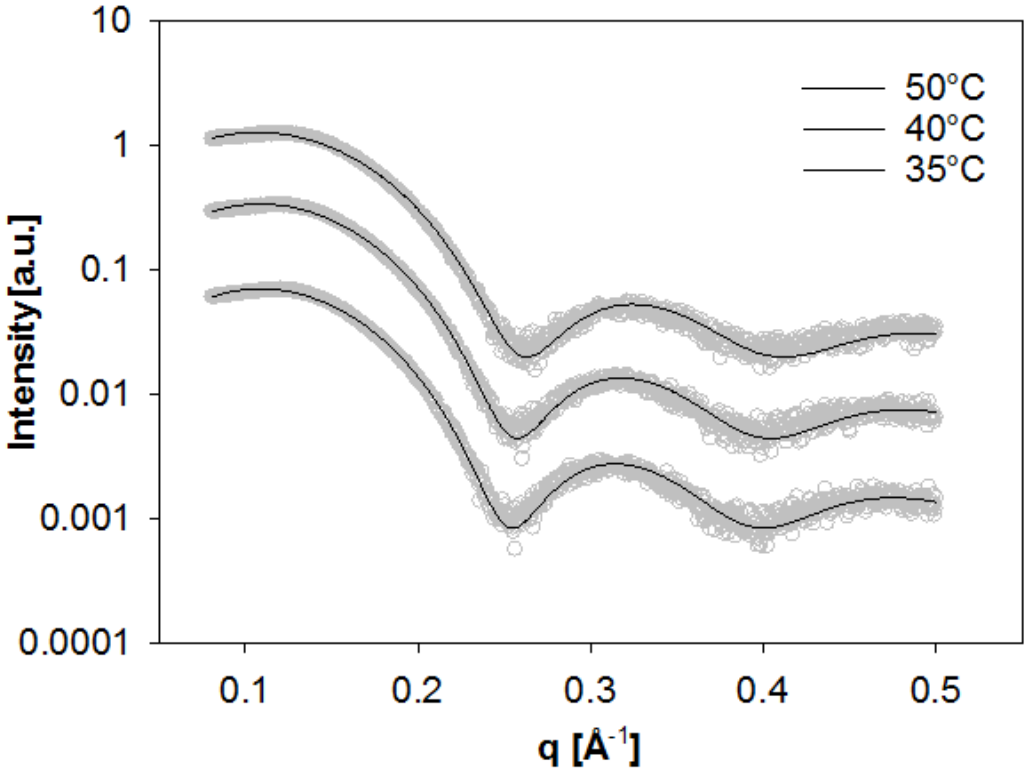

Figure S6: SAXS data of 100 nm unilamellar vesicles composed of POPE/POPG (3:1 mol/mol, open circles) at 35, 40 and 50°C. Solid lines correspond to fits with the SDP model.

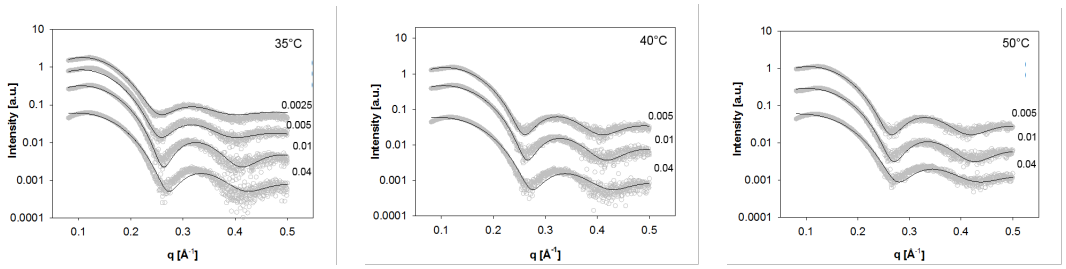

(a) (b) (c)

Figure S7: SAXS data of 100 nm unilamellar vesicles composed of POPE/POPG (3:1 mol/mol) in the presence of L18W-PGLa as a function temperature and P/L (numbers right to the scattering data). Solid lines correspond to fits.

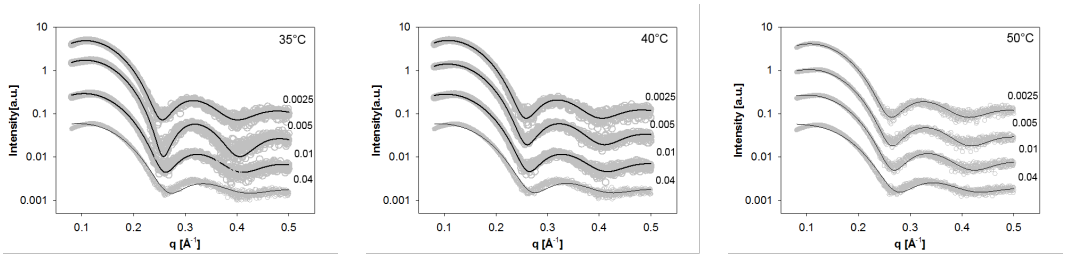

(a) (b) (c)

Figure S8: SAXS data of 100 nm unilamellar vesicles composed of POPE/POPG (3:1 mol/mol) in the presence of MG2a as a function temperature and P/L (numbers right to the scattering data). Solid lines correspond to fits.

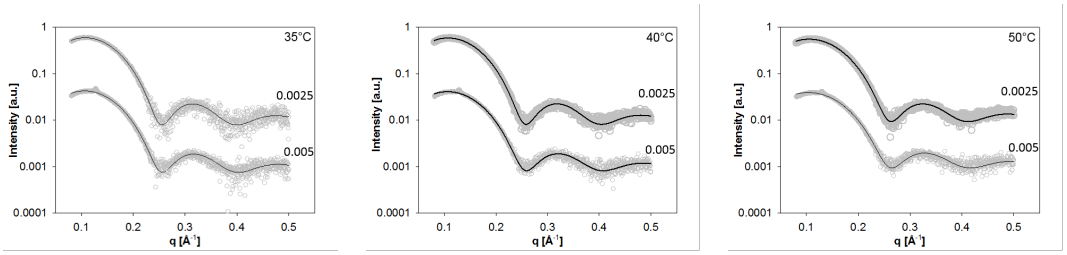

(a) (b) (c)

Figure S9: SAXS data of 100 nm unilamellar vesicles composed of POPE/POPG (3:1 mol/mol) in the presence of a equimolar mixture of L18W-PGLa and MG2a as a function temperature and P/L (numbers right to the scattering data). Solid lines correspond to fits.

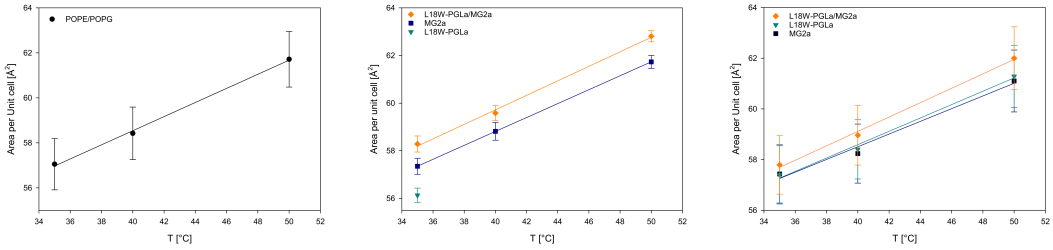

(a) (b) (c)

Figure S10: Temperature dependencies of the area per unit cell, in the absence of peptide (a) and for P/L = 1/400 (b) and 1/200 (c). Solid lines represent the fits.

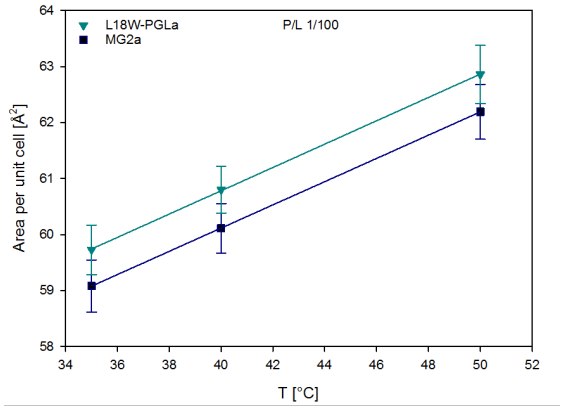

(a)

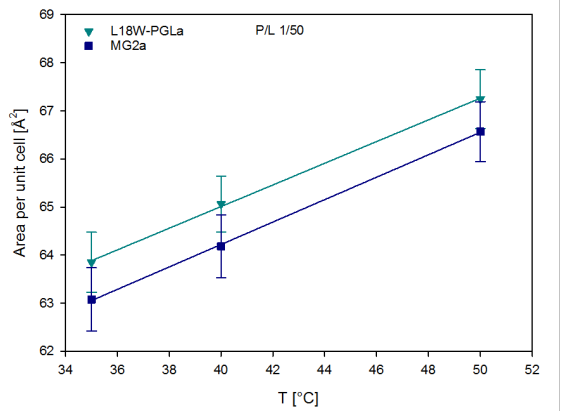

(b)

Figure S11: Temperature dependencies of the area per unit cell for P/L = 1/100 (a) and 1/50 (b). Solid line represent the fits.

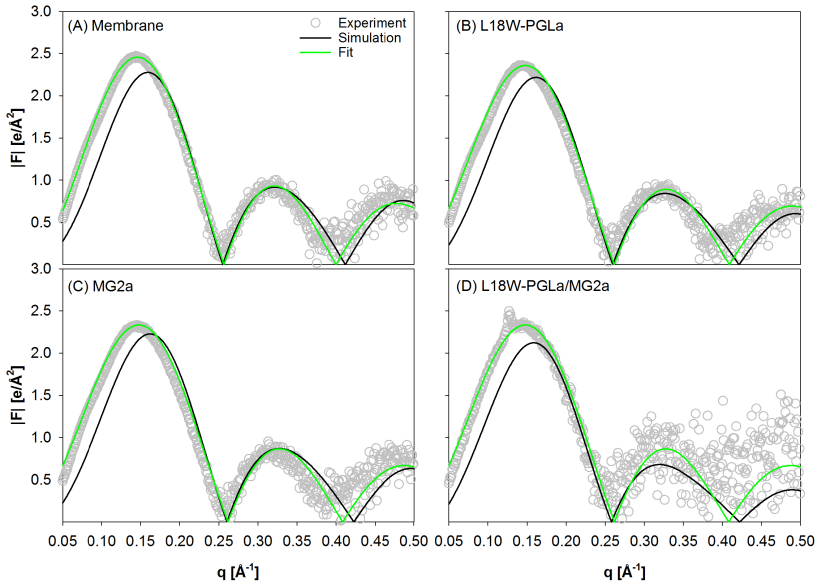

Figure S12: Comparison of experimental form factors for POPE/POPG (3:1 mol/mol) with and without peptides at P/L= 1/200 and 35°C for the pure lipid system (A), L18W-PGLa (B), MG2a (C) and the equimolar mixture (D) to those obtained from MD simulations and global fits. Global fits and simulations are in absolute units while experimental form factors haven been scaled. Note that the global fits include an optimization three additional contrasts from neutron experiments.

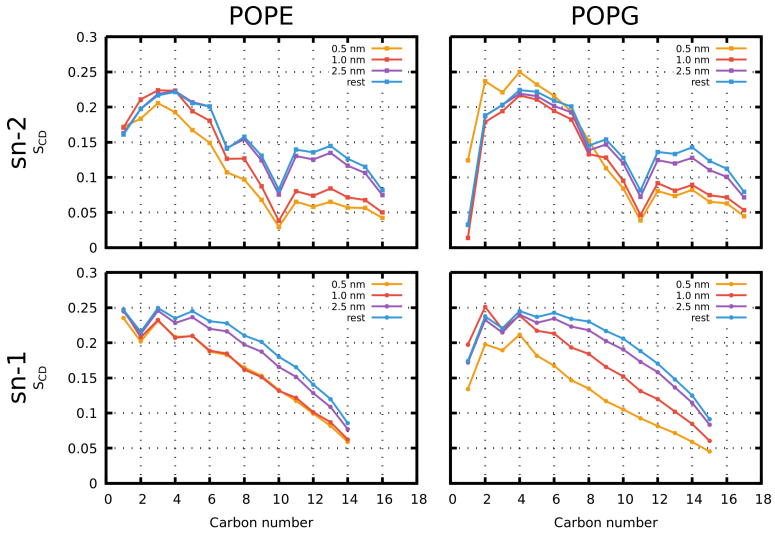

Figure S13: Calculated lipid order parameter of POPE (left) and POPG (right) acyl chains. The data were collected from a 500 ns long all-atom simulation with single MG2a peptide on each membrane leaflet. The distance is given by lipid phosphate to the nearest MG2a peptide Cα atom.

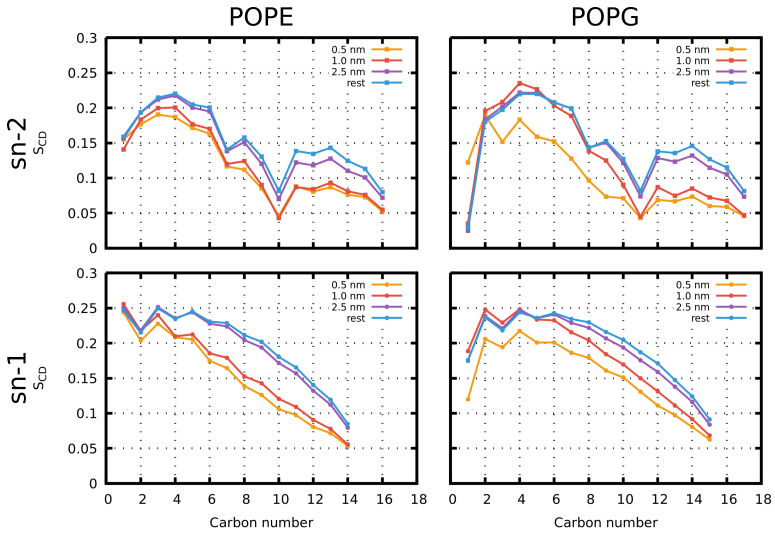

Figure S14: Calculated lipid order parameter of POPE (left) and POPG (right) acyl chains. The data were collected from a 500 ns long all-atom simulation with single L18W-PGLa peptide on each membrane leaflet. The distance is given by lipid phosphate to the nearest L18W-PGLa peptide Cα atom.

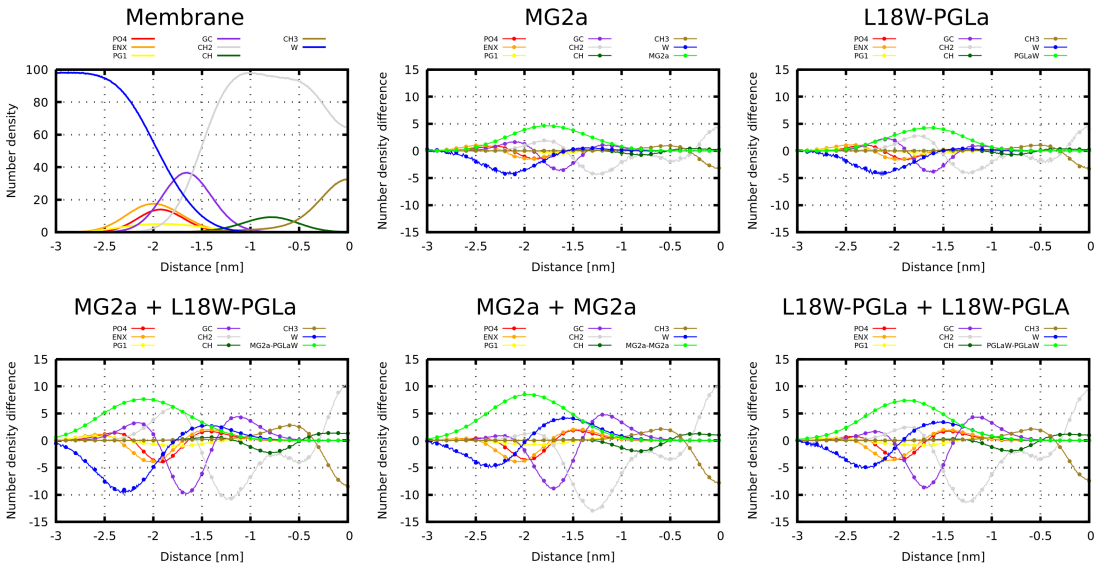

Figure S15: Calculated density profiles from 500 ns long all-atom simulations as a function of distance from the membrane center of mass. (A) Number density of POPE/POPG (3:1 mol/mol) membrane. (B–F) Difference in the number density after the addition of peptides.

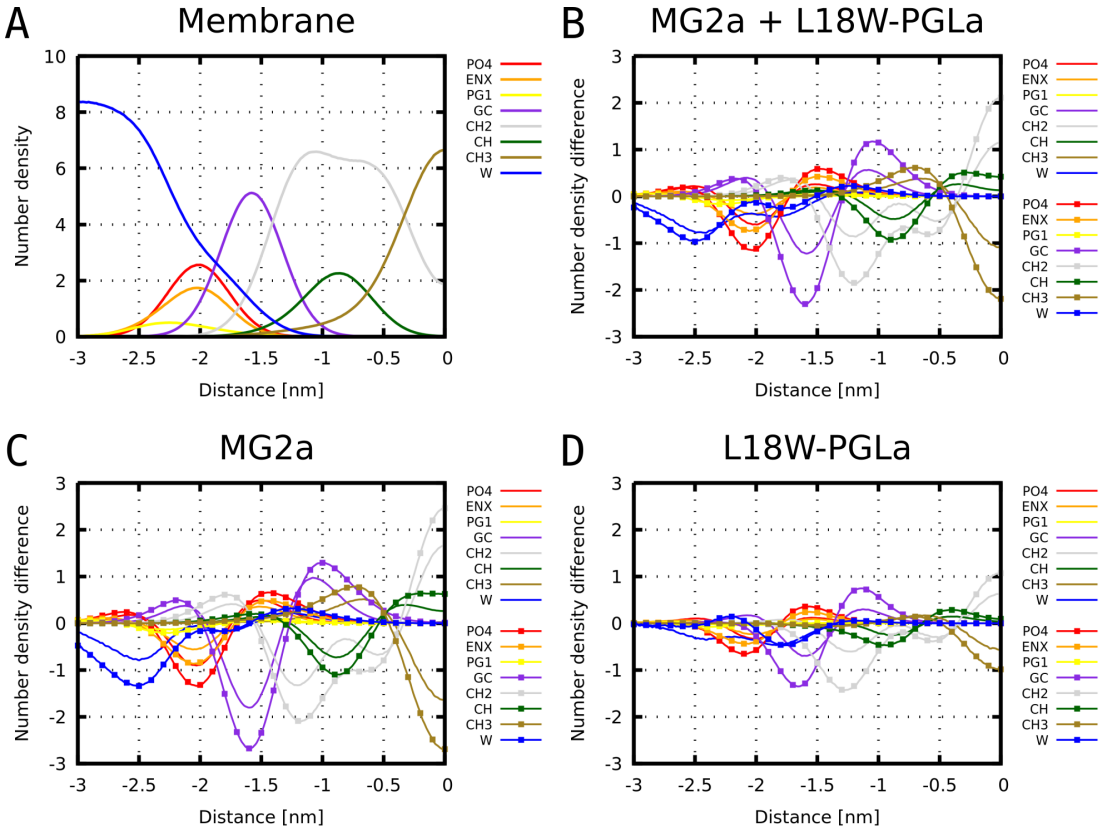

Figure S16: Calculated density profiles from 20 μs long coarse-grained simulations as a function of distance from the membrane center of mass. (A) Number density of POPE/POPG (3:1 mol/mol) membrane. (B–D) Difference in the number density after the addition of peptides. Systems with P/L = 1/42 and 1/21 are shown with smooth lines and lines with squares, respectively.

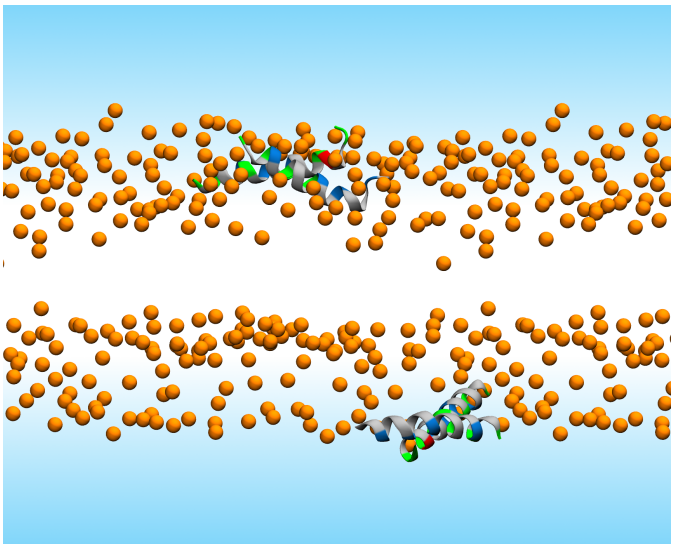

Figure S17: Last snapshots from a 500 ns long MD simulations of MG2a+L18W-PGLa heterodimer adsorbed at the membrane surface. Initially, the peptide pairs were prepared as parallel dimers. Lipid phosphate atoms are shown as orange spheres. Solvent is represented by a blue-shaded area and lipid tails are not shown for clarity. Peptide secondary structure is shown in cartoon representation and colored by residue type. Nonpolar: gray, polar: green, acidic: red, and basic: blue.

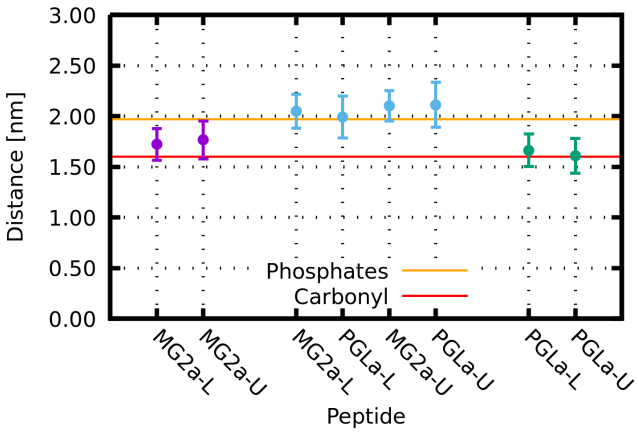

Figure S18: The distance between the peptide and membrane centers of mass. Monomers of (A) MG2a and (C) L18W-PGLa, and heterodimer (B) MG2a+L18W-PGLa are shown. Either (A,C) one monomer or (B) one parallel dimer was adsorbed on (L)ower and (U)pper membrane leaflet. Data are averaged over 500 ns long all-atom trajectory and the bars represent the standard deviation.

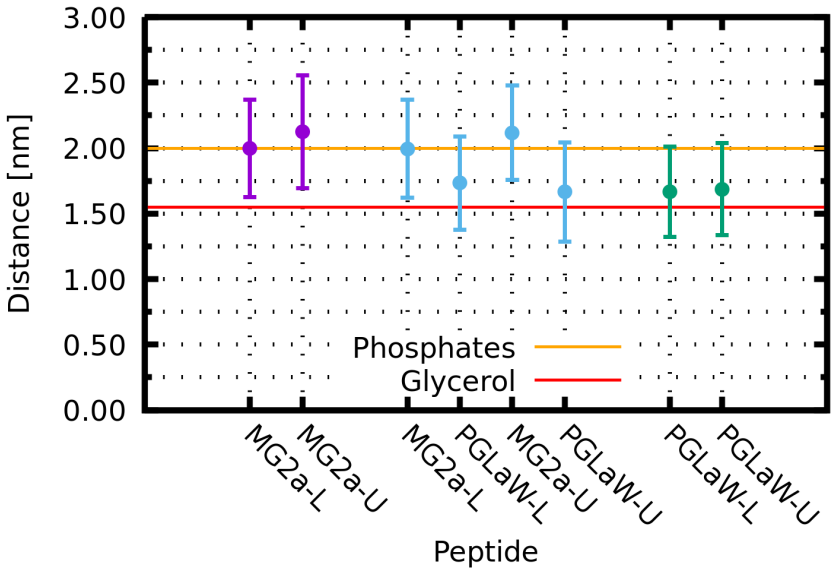

Figure S19: The distance between the peptide and membrane center of mass as obtained from coarse-grained MD simulations. Six peptides (MG2a: purple; 1:1 MG2a+L18W-PGLa: cyan; PGLa: green) were placed on each membrane leaflet (P/L ratio 1/42). Under these conditions, MG2a+L18W-PGLa peptides form parallel heterodimers only occasionally (see Fig. 9 in the main text), causing the L18W-PGLa peptide to be positioned slightly closer towards the membrane surface. The distances are averaged over 20 μs for all peptides (MG2a or L18W-PGLa) on either the (L)ower or (U)pper membrane leaflets. The bars represent the standard deviation. Orange and red horizontal lines represent the approximate position of phosphate and glycerol groups.

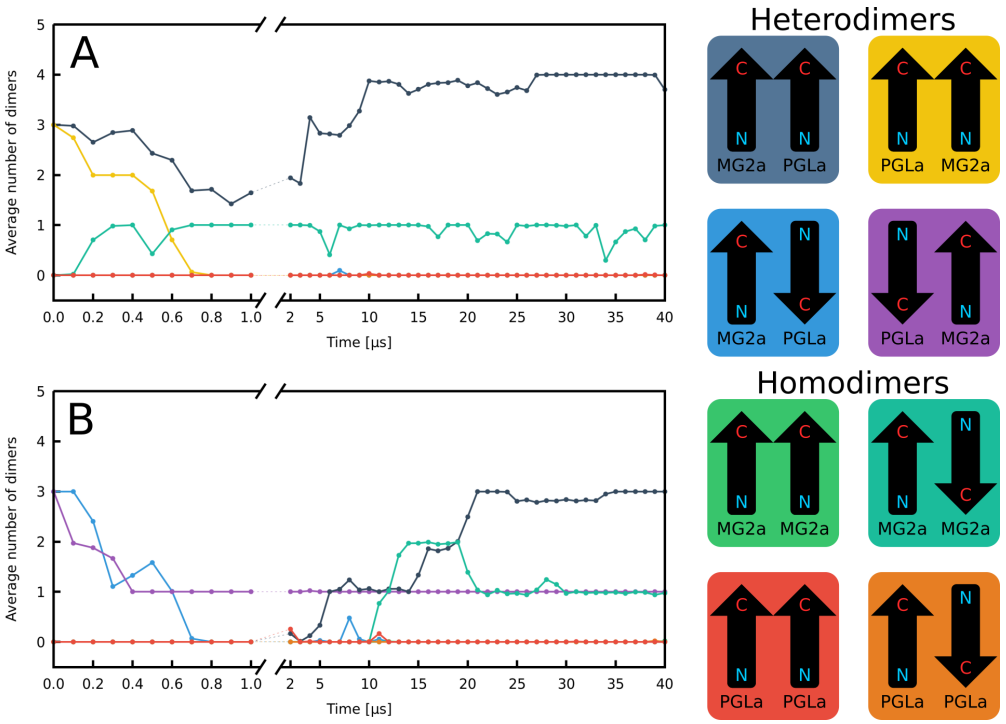

Figure S20: Average number of peptide dimers as a function of time in a system with 12 peptides on each leaflet (P/L = 1/21). Four different heterodimeric starting configurations (each prepared three times) were considered. These configurations are shown in the upper part of the legend. A) On the first leaflet, there were six parallel heterodimers (three of each configuration – gray and yellow) and B) six antiparallel heterodimers (three of each configuration – blue and violet) in the second leaflet. Parallel heterodimers (gray) seem to have the highest stability followed by MG2a homodimers (dark-green). In addition, newly formed dimers were only parallel heterodimers and MG2a antiparallel homodimers, first of which formed more in both A) and B). These results are consistent with simulations starting from random configurations (Fig. 7). Data from the first 1 μs of the trajectory are averaged every 100 ns. Then, each point is an average from a 1 μs long trajectory. Color coding of dimers is displayed in the legend on the right side. The instability of parallel PGLa-MG2a heterodimers (yellow) as apposed to MG2a-PGLa heterodimers (grey) is due to the inability to form salt bridge between the residues E19-K15 and stronger tryptophan interactions S23-W18 and I20-W18 of MG2a and L18W-PGLa in such configuration (see Figs. S22 and S23).

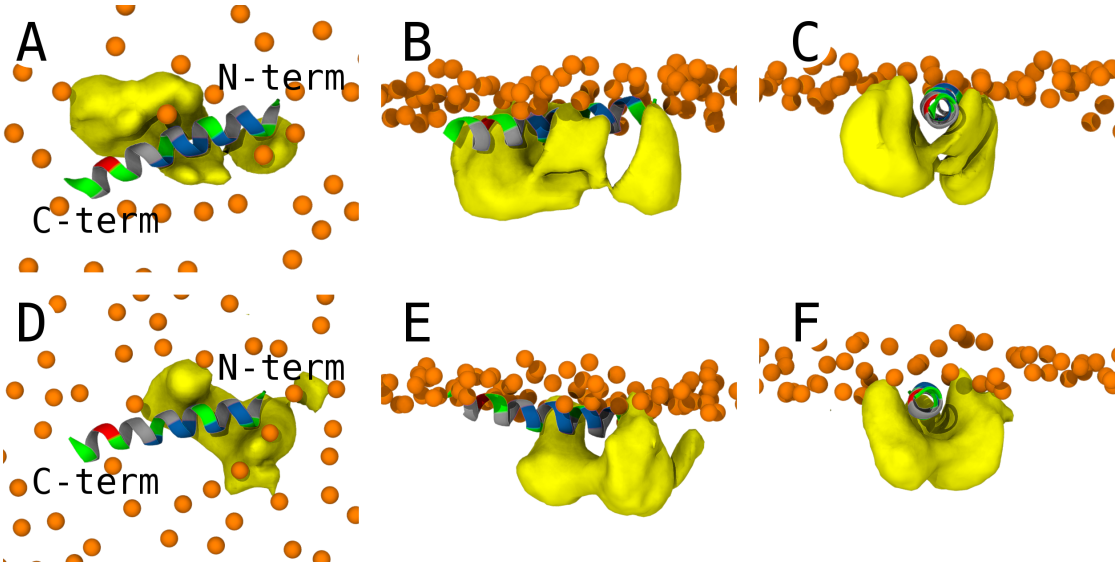

Figure S21: Averaged densities of POPG sn-2 acyl chains from a 500 ns long all-atom MD simulations in the vicinity of MG2a. Lipids with increased order parameter were selected and used for the analysis. In the simulation each membrane leaflet contained one MG2a molecule. Peptides on top (A–C) and bottom (D–E) leaflets were individually analyzed to evaluate the agreement. (A,D) top view on the simulated system, (B,E) side view, and (C,F) view along the peptide long axis. Snapshot color coding: Yellow surfaces represent the average densities of the acyl chain carbons. Lipid phosphate atoms are shown as orange spheres. Solvent and lipid tails are not shown for clarity. The peptide secondary structure is shown in cartoon representation colored by residue type (nonpolar: gray, polar: green, acidic: red, and basic: blue).

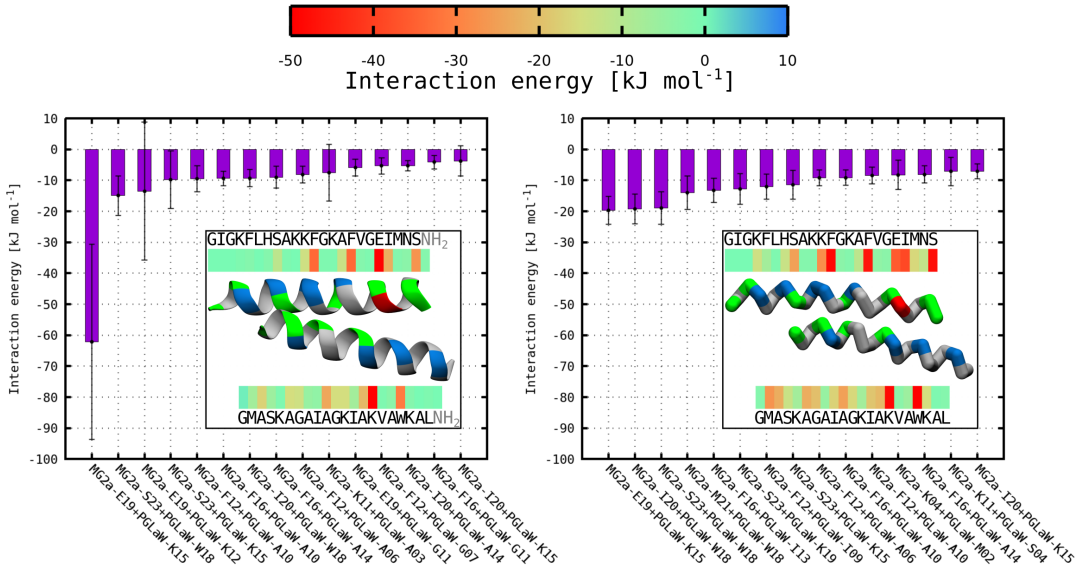

Figure S22: Averaged enthalpic interaction energies between the MG2a and L18W-PGLa heterodimers. Fifteen residue pair interactions with the lowest average energies are shown for both all-atom (left) and coarse-grained (right) simulations. The insets show representative snapshots of MG2a (top) and L18W-PGLa (bottom) peptides in a parallel heterodimer. Color bars show the total average interaction of a residue from one peptide with all residues of the other peptide. The corresponding color scale is presented at the top of the figure. Terminal capping groups were considered as a separate residues according to Amber force field settings (5). Error bars correspond to standard deviations. The large error bars in the all-atom simulations are caused by the possibility of formation of two salt bridges between E19 of MG2a and either K15 and K12 of L18W-PGLa with long residence times. To reach convergence, longer time scale of our all-atom simulation would be required. The peptide secondary structure is shown in cartoon representation colored by residue type (nonpolar: gray, polar: green, acidic: red, and basic: blue).

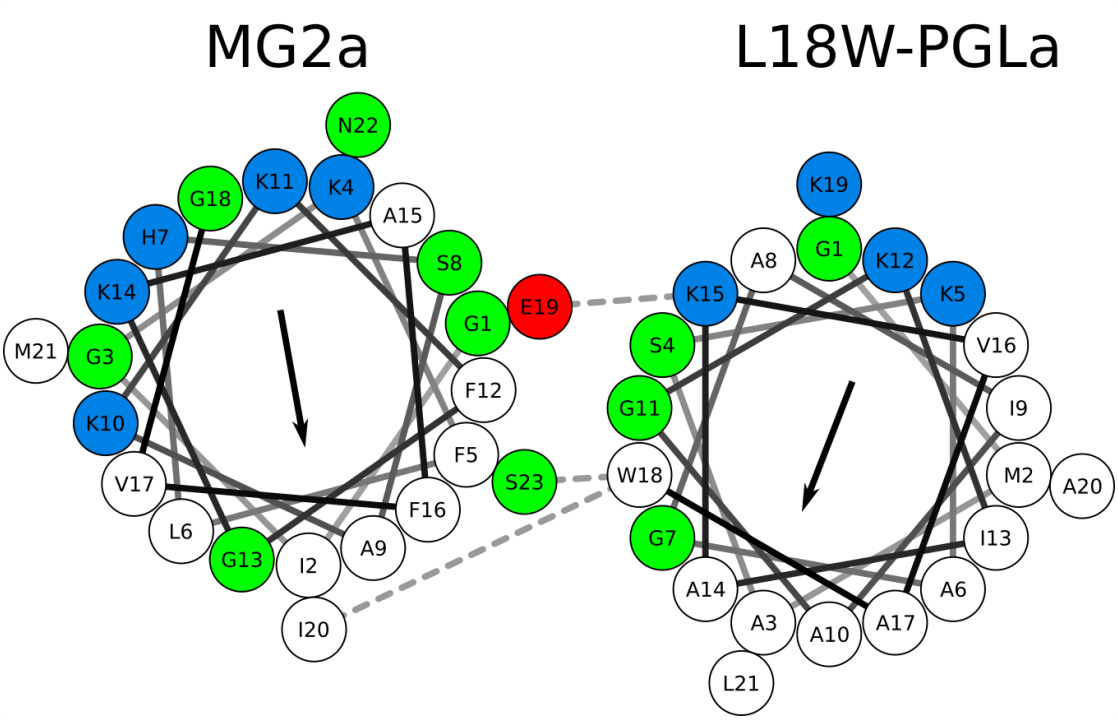

Figure S23: Helical wheels of MG2a and L18W-PGLa arranged in a parallel heterodimer with hydrophobic moments pointing in the same direction. The strongest interactions between peptide residues are marked by dashed lines demonstrating a preference for the displayed conformation. Residues are colored by residue type: nonpolar – white, polar – green, acidic – red, and basic – blue).

Supplementary Tables

Table S1: Summary of the joint analysis of 100 nm LUVs composed of POPE / POPG (3:1) in the absence and presence of L18W-PGLa, MG2a and their equimolar mixture at P/L = 1/200 and 35°C

Paramters	POPE/POPG	L18W-PGLa	MG2a	L18W-PGLa / MG2a
z_{CH_2} [Å]	15.34±0.02	15.16±0.03	14.98±0.02	14.68±0.01
z_{CH} [Å]	9.45±0.22	9.53±0.23	9.53±0.2	9.53±0.21
z_{GC} [Å]	16.34±0.02	16.16±0.03	15.98±0.03	15.68±0.01
z_{PO_4} [Å]	20.53±0.02	19.96±0.03	20.06±0.03	20.13±0.03
z_{ENX} [Å]	22.10±0.02	21.53±0.03	21.62±0.03	21.70±0.03
z_{PG_2} [Å]	23.45±0.02	22.89±0.03	22.98±0.03	23.05±0.03
z_P [Å]		15.76±0.44	16.29±0.50	15.98±0.43
σ_{CH_3} [Å]	2.64± 0.02	2.65±0.02	2.65±0.02	2.65±0.02
σ_{CH_2} [Å]	3.21±0.05	3.19±0.04	3.19±0.04	3.18±0.04
σ_{CH} [Å]	2.82± 0.04	2.82±0.04	2.81±0.03	2.81±0.04
σ_{GC} [Å]	2.49± 0.03	2.48±0.03	2.49±0.04	2.49±0.03
σ_{PO_4} [Å]	2.47±0.11	2.60±0.13	2.51±0.16	2.72±0.09
σ_{ENX} [Å]	2.81±0.04	2.81±0.04	2.81±0.04	2.80±0.04
σ_{PG_2} [Å]	3.15±0.04	3.16±0.04	3.16±0.04	3.16±0.04
σ_P [Å]		4.02±0.14	4.04±0.15	4.00±0.14

References

1. Kučerka, N., B. van Oosten, J. Pan, F. A. Heberle, T. A. Harroun, and J. Katsaras, 2015. Molecular structures of fluid phosphatidylethanolamine bilayers obtained from simulation-to-experiment comparisons and experimental scattering density profiles. *J Phys Chem B* 119:1947–1956.

2. Pan, J., D. Marquardt, F. A. Heberle, N. Kučerka, and J. Katsaras, 2014. Revisiting the bilayer structures of fluid phase phosphatidylglycerol lipids: Accounting for exchangeable hydrogens. *Biochim Biophys Acta* 1838:2966–2969.

3. Harmouche, N., and B. Bechinger, 2018. Lipid-Mediated Interactions between the Antimicrobial Peptides Magainin 2 and PGLa in Bilayers. *Biophys J* 115:1033–1044.

4. Belička, M., A. Weitzer, and G. Pabst, 2017. High-resolution structure of coexisting nanoscopic and microscopic lipid domains. *Soft Matter* 13:1823–1833.

5. Cieplak, P., W. d. Cornell, C. Bayly, and P. A. Kollman, 1995. Application of the multimolecule and multiconformational RESP methodology to biopolymers: Charge derivation for DNA, RNA, and proteins. *J. Comput. Chem.* 16:1357–1377.

Manuscript submitted to **Biophysical***Journal*
Article

Magainin 2 and PGLa in Bacterial Membrane Mimics II: Membrane Fusion and Sponge Phase Formation

I.K., M.P., S.P., I.L.-P., K.L., G.P., R.V.

ABSTRACT We studied the synergistic mechanism of equimolar mixtures of magainin 2 (MG2a) and PGLa in phosphatidylethanolamine/phosphatidylglycerol mimics of Gram-negative cytoplasmic membranes. In a preceding paper [Pachler et al., Biophys. J. 2019 xxx], we reported on the early onset of parallel heterodimer formation of the two antimicrobial peptides already at low concentrations and the resulting defect formation in membranes. Here, we focus on the structures of the peptide/lipid aggregates occurring in the synergistic regime at elevated peptide concentrations. Using a combination of calorimetric, scattering, electron microscopic and *in silico* techniques, we demonstrate that the two peptides, even if applied individually, transform originally large unilamellar vesicles into multilamellar vesicles, with a collapsed interbilayer spacing resulting from peptide induced adhesion. Interestingly, the adhesion does not lead to a peptide induced lipid separation of charged and charge neutral species. In addition to this behavior, equimolar mixtures of MG2a and PGLa formed surface-aligned fibril-like structures, which induced adhesion zones between the membranes and the formation of transient fusion stalks in molecular dynamics simulations and a coexisting sponge phase observed by small-angle X-ray scattering. The previously reported increased leakage of lipid vesicles of identical composition in the presence of MG2a/PGLa mixtures is therefore related to a peptide-induced cross-linking of bilayers.

STATEMENT OF SIGNIFICANCE

We demonstrate that the synergistic activity of the antimicrobial peptides MG2a and PGLa correlates to the formation of surface-aligned fibril-like peptide aggregates, which cause membrane adhesion, fusion and finally the formation of a sponge phase.

INTRODUCTION

PGLa and Magainin 2 (MG2a) are two antimicrocial peptides (AMPs) derived from the African clawed frog, which are well known for their synergistic killing of bacteria (1). So far, no consensus has been reached regarding the biophysical mechanism though. While some groups proposed the formation of distinct transmembrane pores formed by PGLa/MG2a dimers (1) or complex peptide aggregates (2), others suggested the formation of mesophase-like structures by surface-aligned peptides (3). Recently, we reported that the activity of these peptides in *Escherichia coli* can be reasonably mimicked by mixtures of palmitoyl oleoyl phosphatidylethanolamine (POPE) and palmitoyl oleoyl phosphatidylglycerol (POPG) (molar ratio 3:1), while other lipid mixtures fail to capture synergistic effects (4). Intriguingly, both peptides, in particular when mixed at an equimolar ratio, were shown to adopt a surface-aligned topology in POPE-enriched bilayers (5, 6), thus questioning the formation of transmembrane pores. However, even if the peptides from mesophase-like structures at synergistic concentrations in POPE-enriched bilayers (3), it is far from being clear how that should cause enhanced leakage of dyes from large unilamellar vesicles (LUVs) (4). In order to address the synergistic mechanism, we applied several experimental and computational tools that allowed us to study the peptide-induced effects occurring on the nanoscopic to macroscopic length scales. In the preceding paper of this series, we combined small-angle X-ray and neutron scattering (SAXS/SANS) experiments with all-atom and coarse-grained molecular dynamics simulations to show that equimolar mixtures of L18W-PGLa and MG2a are prone to form surface-aligned parallel heterodimers already at low peptide concentrations and the dimerisation leads to an increase of the defects within the membrane interior (7).

The present paper focuses on the synergistic regime of the peptides at high concentrations (i.e. peptide to lipid molar ratio P/L $\leq 1/50$) (4). For direct comparison to our previous results including leakage assays, we used L18W-PGLa instead of native PGLa (4). Nevertheless, the mutant behavior was reported to be analogous to native PGLa (1). In addition to the experimental techniques applied in our first paper (7), we used differential scanning calorimetry (DSC) to reveal effects of the peptides on the cooperative melting of POPE/POPG bilayers, as well as cryogenic transmission electron microscopy (cryo-TEM) to capture the macroscopic equilibrium structure after incubating LUVs with the two peptides. Our results demonstrate that the peptides transform the LUVs at sufficiently high concentration into condensed multilamellar vesicles (MLVs) with the peptides sandwiched between the individual bilayers. Additionally, equimolar peptide mixtures formed surface-aligned fibril-like structures in the interstitial bilayer space, which finally lead to fusion events and to the formation of a leaky sponge phase.

MATERIALS AND METHODS

Experiments

Lipids, Peptids and Chemicals. POPE, POPG, palmitoyl-d31-oleoyl-phosphoethanolamine (POPE-d31) and palmitoyl-d31-oleoyl-phosphatidylglycerol (POPG-d31) were purchased from Avanti Polar Lipids (Alabaster, AL, USA, purity > 99%) as powder. L18W-PGLa, MG2a and the chemically linked heterodimer L18W-PGLa–MG2a, denoted in the following as hybrid peptide (Fig. S1), were obtained in lyophilized form (purity >95%) from PolyPeptide Laboratories (San Diego, CA, USA). Deuterium oxide (D_2O, purity 99.8 atom%) and HEPES (purity >99.5) were purchased from Carl Roth (Karlsruhe, Baden-Wüttenberg, Germany). All other chemicals were obtained from Sigma-Aldrich (Vienna, Austria) in *pro analysis* quality. Lipid stock solutions for sample preparation were prepared in organic solvent chloroform/methanol (9:1; v/v) and phosphate assayed for quantification of lipid content (8). Peptide stock solutions were prepared in 10 mM HEPES 140 mM NaCl buffer solution (pH 7.4).

Sample preparation Samples were prepared, assayed and controlled as described in (7). Samples for zero-contrast neutron experiments contained mixtures of protiated and deuterated lipids as detailed below and were hydrated in 10 mM HEPES (140 mM NaCl, pH 7.4) prepared in D_2O/H_2O (43.7 vol%). We emphasize that all lipid samples were extruded to ~ 100 nm-sized large unilamellar vesicles (LUVs) prior to the addition of the peptides. Further, all presented data have been recorded at least three days after peptide addition. We therefore refer to these data as end states.

Small-Angle X-ray Scattering (SAXS)

SAXS data were collected at the SWING beamline (Soleil, Saint-Aubin, France) as described in (7). Peptide induced aggregation of vesicles led to the formation of Bragg peaks, which impeded the data analysis developed in (7). Instead, data were analyzed based on Bragg peak positions and intensities only, see e.g. (9). In brief, the electron density for a centrosymetric lamellar structure is given by

$$\rho^*(z) = \frac{1}{|F_1|} \sum_{h=1}^{h_{max}} \alpha_h |F_h| \cos\left(\frac{2\pi h z}{D}\right) \qquad (1)$$

where $\alpha_h = \pm 1$ is the phase, F_h is the form factor of the h' reflection, and $D = 2\pi h/q_h$ is lamellar repeat distance. From the derived electron density profiles we calculated the head to headgroup distance D_{HH} from the distance between the maxima across the lipid bilayer. The steric bilayer thickness $D'_B = D_{HH} + 2D_{PO}$ can be estimated by using $D_{PO} = 2.92$ Å, which corresponds to a distance between the PO_4 group and the furthest outward lipid group (here the glycerol group) as determined from a joint SAXS/SANS data analysis (7).

Bragg peak positions of cubic phases index as

$$q_{hkl} = 2\pi \frac{\sqrt{h^2 + k^2 + l^2}}{a}, \qquad (2)$$

where h, k, l are the the Miller indices and a is the lattice parameter.

Small-Angle Neutron Scattering (SANS)

Zero-contrast SANS data were acquired on D11 at the Institut Laue-Langevin (ILL), Grenoble, France, with a multiwire ^{3}He detector of 256×256 pixels (3.75×3.75 mm^2), at a wavelength $\lambda = 0.53$ nm ($\Delta\lambda/\lambda = 9$ %), and three sample-to-detector distances: 1.4, 8 and 39 m (with corresponding collimations of 8 m, 8 m and 40.5 m, respectively, covering a q-range of 0.015–5 nm^{-1}. Samples were poured into quartz cuvettes of either 2 mm or 1 mm pathway and mounted in a thermostated rotating holder to minimize sample sedimentation. Data were reduced with BerSANS, accounting for flat field, solid angle, dead time, transmission, and background subtraction. Scattered intensities were placed on an absolute scale using the scattering by 1 mm H_2O as a secondary standard.

In general, the scattered intensity is proportional to the scattering contrast $\Delta\rho$

$$I(q) \propto \frac{\Delta\rho}{q^2} = \frac{\sum_i (\rho_W - \rho_i)}{q^2}, \qquad (3)$$

where ρ_W is the neutron scattering length density (NSLD) of the buffer, and ρ_i is the NSLD of a given slab of the lipid bilayer. For designing zero contrast conditions, we considered two slabs describing the lipid headgroup and hydrocarbon core, respectively. In this case it can be estimated that homogeneously distributed lipids match the 43.7 vol% deuterated buffer at a molar ratio of 78/22 deuterated/protiated hydrocarbons. That is, under these experimental conditions, the lipid headgroup and the hydrocarbon core are both fully contrast-matched and invisible to neutrons.

We used two lipid mixtures, both having a total deuterated/protiated hydrocarbon ratio of 78/22. System A with POPE-d31/ (POPG)/(POPG-d31) at (75)/(22 /3) mol/mol/mol and system B with (POPE/POPE-d31)/ (POPG/POPG-d31) at (16.5/58.5)/(5.5/19.5) mol/mol/mol/mol. The compositions were designed that a peptide-induced lipid separation will give rise lateral contrast and hence lead to detectable coherent scattering signal for the first mixture only. Analogous experiments have been reported for the formation of nanoscopic lipid domains (10). The second mixture was chosen to contrast-match each lipid component individually. Hence, no scattering contrast can be achieved upon lipid demixing. These samples, therefore served as negative controls.

Differential Scanning Calorimetry (DSC)

DSC experiments were carried out on a MicroCal VP high-sensitivity DSC (Microcal, Northhampton, MA, USA) at a

scan rate of 30 °C/h in the temperature regime of 5 to 60°C. Each experiment consisted of three subsequent heating and cooling scans. Baseline subtraction was performed using Origin (OriginLab, Northampton, MA, USA).

Cryo Transmission Electron Microscopy (TEM)

All cryo-TEM images were recorded with a Gatan system mounted on a Tecnai12 electron microscope (FEI Company, Hillsboro, OR), equipped with a LaB_6 filament as described previously (11).

Molecular dynamics simulations

Molecular dynamics (MD) simulations were performed using GROMACS version 2016.2 (12, 13).

All-atom simulations

Simulation Settings. POPE and POPG lipids were described using the Slipids force field (14, 15), while MG2a (GIGKFLHSAKKFGKAFVGEIMNS-NH_2) and L18W-PGLa (GMASKAGAIAGKIAKVAWKAL-NH_2) were simulated with Amberff99SB-ILDN force field (16, 17). The time integration was performed using the leap-frog algorithm with the time step set to 2 fs. A Nosé-Hoover thermostat (18–20) with a coupling constant of 0.5 ps was used to maintain the temperature at 308.15 K. To ensure proper heating of the system, two coupling groups for peptide+lipid and water+ion atoms were used. A Parrinello-Rahman barostat (21, 22) with a semi-isotropic coupling scheme and a coupling constant of 2 ps was employed for keeping the membrane tensionless and the system at a constant pressure of 1 bar. 3D periodic boundary conditions were applied. Long-ranged electrostatic interactions were treated with the particle mesh Ewald method (23) using the real-space cutoff to 1.2 nm. Lennard-Jones interactions were cutoff at 1.2 nm. All bonds were constrained using the LINCS algorithm. Long-range dispersion corrections were applied for both energy and pressure. (24) For equilibration, the protein backbone atoms were held by positional restraints during a 120 ns simulation of the system. For the next 180 ns long equilibration step, backbone dihedral angles were constrained to maintain a helical structure while letting the peptide free to move.

Membrane Stack system. The equlibrated bilayer with parallel MG2a+P18W-PGLa heterodimers in each membrane leaflet was duplicated and shifted by 5 nm in the Z-axis (direction of membrane normal). Each bilayer was composed of 192 POPE and 64 POPG lipids equally distributed in both leaflets. The initial box dimensions were 8.9×8.9×8.5 nm. This system with two stacked membranes was solvated and energy minimized using the steepest descent algorithm. Production MD was performed without any restraints for 1 μs.

Peptide Fiber system. A smaller membrane patch composed of 96 POPE and 32 POPG lipids (with initial dimensions of 6.9 x 6.9 x 10 nm) was prepared. Two parallel MG2a+L18W-PGLA heterodimers were inserted into the membrane center in parallel orientation with respect to the membrane plane. The dimers were placed in a fibril with the N-terminus of L18W-PGLa peptide (of the first dimer) interacting with C-terminus of MG2a (of the second dimer), see Fig. S8 *A*, *B*. Thus, the peptides formed an “infinite" fiber over periodic boundary conditions. The production MD was performed without any restraints for 330 ns.

Coarse-grained Simulations

Simulation Settings. We employed coarse-grained Martini 2.2 (25–27) force field with four-to-one atom mapping in combination with the leap-frog algorithm with an integration time step of 20 fs. A velocity-rescaling thermostat (modified with a stochastic term) (28) with a coupling constant of 1.0 ps maintained the temperature at 310 K. Protein-lipid and solvent beads were coupled to separate baths to ensure correct temperature distribution. The pressure was kept at 1 bar using the Parrinello-Rahman barostat (21, 22) with a semi-isotropic coupling scheme with coupling constant of 12 ps. All non-bonded interactions were cut off at 1.1 nm and the van der Waals potential was shifted to zero. The relative dielectric constant was set to 15.

As a consequence of coarse-graining, the Martini model does not explicitly describe backbone hydrogen bonds. Thus, the secondary structure has to be imposed on the peptides and maintained throughout the simulation. Both MG2a and L18W-PGLa peptides were modeled as α-helices. The peptide C-terminal capping was modeled by removing the charge and changing the backbone bead type to neutral.

System Preparation. The lipid membranes were assembled in the XY plane using the CHARMM-GUI web server. (29) All Lipid bilayers were formed from POPE and POPG lipids (3:1 mol:mol), equally distributed in both leaflets.

The following systems with two stacked membranes were prepared: (i) a membrane-only system with two 504-lipid bilayers, (ii) two 504-lipid bilayers containing MG2a and L18W-PGLa (1:1 ratio; P/L = 1:42), (iii) same as (ii) but with P/L = 1:21, (iv) two 2016-lipid bilayers containing MG2a and L18W-PGLa (P/L = 1:21), (v) same as (ii) but with but with the peptides placed only in one leaflet of each bilayer. Roughly four solvent beads were added per lipid and NaCl ions were added at 0.13 M concentration with an excess of sodium ions to neutralize the system net charge. In the coarse-grained representation, one water bead corresponds to four water molecule and ion beads are considered to implicitly contain its first hydration shell. The production dynamics simulation was performed for 20 μs with the exception of system (iv) with the simulation length of 100 μs.

RESULTS

Experiments

Peptides do not induce lipid domain formation, but distribute non-homogeneously

We first investigated the effects of the peptides on the thermotropic behavior of POPE/POPG (3:1 mol/mol) bilayers using DSC. The pure bilayer exhibited a broad, but single main transition at ~ 23°C, consistent with a previous report (30), and a hysteresis of $\Delta T_m \sim -2$°C, upon cooling (Fig. 1).

Equilibration of the LUVs in the presence of the peptides (P/L = 1:50) caused a splitting of the melting transition into at least two components, which was mostly pronounced upon cooling. Note that this peptide concentration corresponds to the synergistic regime of both L18W-PGLa/MG2a equimolar mixtures and their chemically-linked hybrid (4). In the case of the equimolar L18W-PGLa/MG2a mixture, denoted in the following as M11, and the hybrid peptide, the splitting of the transition upon cooling occurred over a larger temperature range – and in particular for the hybrid peptide – signifying a loss of cooperativity. Additionally, the maximum of the specific heat capacity shifted slightly to higher temperatures.

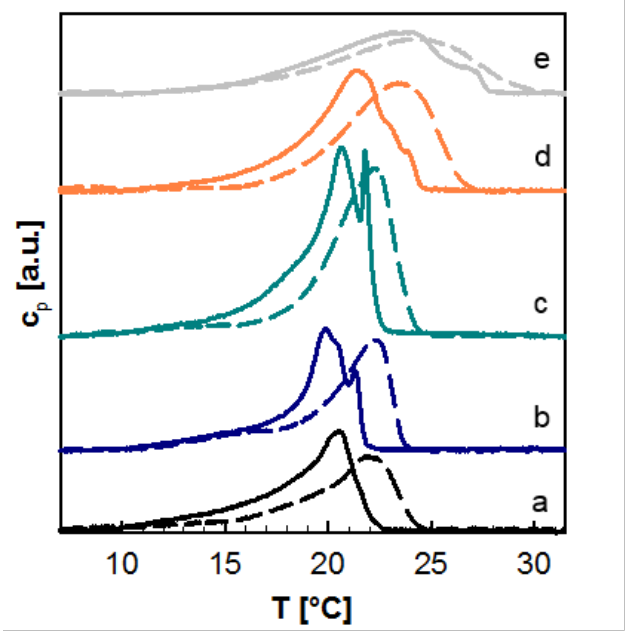

Figure 1: Melting of POPE/POPG (3:1 mol/mol) in the absence (a) and presence of the peptides MG2a (b), L18W-PGLa (c), their equimolar mixture M11 (d) and the hybrid peptide (e) at $P/L = 1:50$. Heating scans are shown as dashed lines and cooling scans as solid lines, respectively.

In order to test, whether the peptide-induced splitting of the melting transition is due to the formation of lipid domains, we performed zero-contrast SANS experiments. We prepared two lipid mixtures using a combination of perdeuterated and protiated POPE and POPG, which should give rise to a scattering signal in the case of lipid domain formation (system A). System B severed as a negative control and should not show any scattering features even in the case of domain formation (see Material and Methods for details).

Figure 2 shows the corresponding scattering data. Both systems (A and B) exhibited a flat scattering signal for $q > 0.1$ nm^{-1} and increased intensities at low q-vectors. The control experiment showed the same trend (Fig. 2 *B*). The increase at low q-values can be explained by residual scattering contrast, i.e. slightly imperfect contrast matching, which leads to an increase of scattered intensities due its dependency on q^{-2} (see Eq. 3). Additional experiments in the main phase transition regime at P/L = 1:50 yielded analogous results (Figs. S4 - S6). Therefore, we conclude that the addition of peptides does not induce the formation of domains enriched in either lipid species. Consequently, the complex thermotropic behavior revealed by DSC (Fig. 1) needs to be related to a non-homogeneous distribution of peptides.

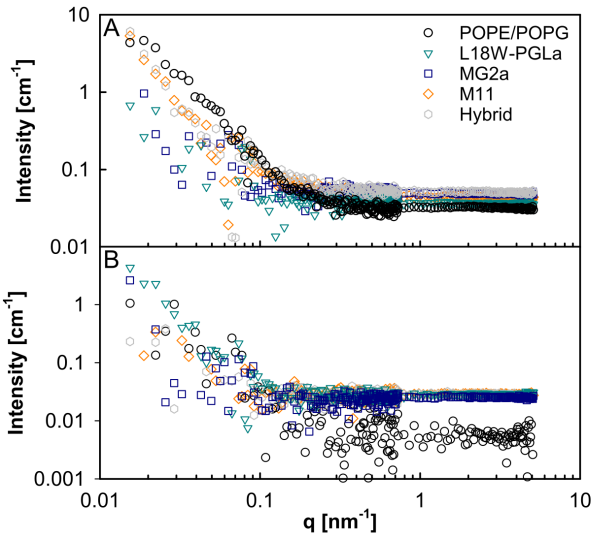

Figure 2: Zero-contrast SANS data of (POPEd31)/(POPG/POPGd31) (75)/(22/3) (Panel A) and the control sample (Panel B) in the absence (black circles) and presence of the peptides at 35°C and a P/L of 1:25.

Peptides transform LUVs to MLVs with collapsed layer spacing

In the following we focus on the end states (see the Methods section) of the systems well above the melting regime. SAXS data of the pure POPE/POPG samples showed a diffuse modulation of the scattered intensity, characteristic of positionally

Table 1: Structural parameters of peptide induced lamellar phases at P/L = 1:25.

POPE/POPG +	D [Å]	D_{HH}[Å]	D'_B[Å]	D_W[Å]
L18W-PGLa	52.1			
MG2a	53.3			
M11	50.3	37.6	43.4	6.9
Hybrid	50.3	37.6	43.4	6.9

uncorrelated bilayers, as present in LUV dispersions which was analyzed in detail in the preceding paper (7). Equilibration of the LUVs with L18W-PGLa or MG2a (P/L = 1:50) did not affect the diffuse character of the scattering patterns (Fig. 3 *A*). In contrast, additional sharp peaks occurred for M11 and the peptide hybrid at the same P/L. The peaks can be ascribed to a single lamellar lattice of d = 49.8 Å (Fig. S2 *A*) in case of M11. The hybrid peptide induced a similar lamellar phase coexisting with a cubic Pn3m phase with a lattice constant of a = 100 Å and a prominent $q_{(1,1,0)} \sim 0.088$ Å^{-1} peak (Fig. S2 *B*, Tab. S1). Note that we observed the Pn3m phase for the hybrid peptide already at P/L = 1 : 200 (Fig. 3 *B*, insert).

Doubling the amount of peptide concentration (P/L = 1 : 25) also caused a formation of a multilamellar phase for the individual peptides (Fig. 3 *B*) with $D^{\mathrm{MG2a}} > D^{\mathrm{L18W\text{-}PGLa}} > D^{\mathrm{M11}} = D^{\mathrm{hybrid}}$ (Tab. 1). While formation of a multilamellar aggregate was the only effect of L18W-PGLa or MG2a, their equimolar mixture induced an additional broad peak at q = 0.081 Å^{-1}. The significant different shape of this peak as compared to the Bragg peaks originating from the lamellar phase clearly shows that it originates from different positional correlations. In fact, this peak was even present, though much weaker, at P/L = 1:50 at slightly higher q-values. Interestingly, we observed it also for the hybrid peptide at P/L = 1:25, where it partially overlapped with the (1,1,0)-reflection of the Pn3m phase (Fig. 3 *B*, insert). No signatures of a cubic phase were detected at P/L = 1:12.5, but the broad peak was clearly present.

The SAXS patterns observed at P/L = 1:25 for M11 and the hybrid peptide both displayed four lamellar diffraction orders (Fig. 3 *B*). This enabled us to calculate the steric bilayer thickness as detailed in the Methods section and the thickness of the water layer according to $D_W = D - D'_B$. Our results show very small D_W values of $\sim$ 7 Å (Tab. 1). That is, the formed lamellar aggregates are almost completely collapsed and most likely separated only by the steric size of partially membrane-inserted peptides. The lower amount of Bragg reflections observed in the presence of L18W-PGLa or MG2a individually impedes us from deriving electron density profiles with comparable resolution. However, the similarly small D-values suggest that also these lamellar aggregates are almost completely collapsed.

Increasing temperature leads to a linear decrease of the lamellar repeat distance with a similar rate for MG2a, L18W-

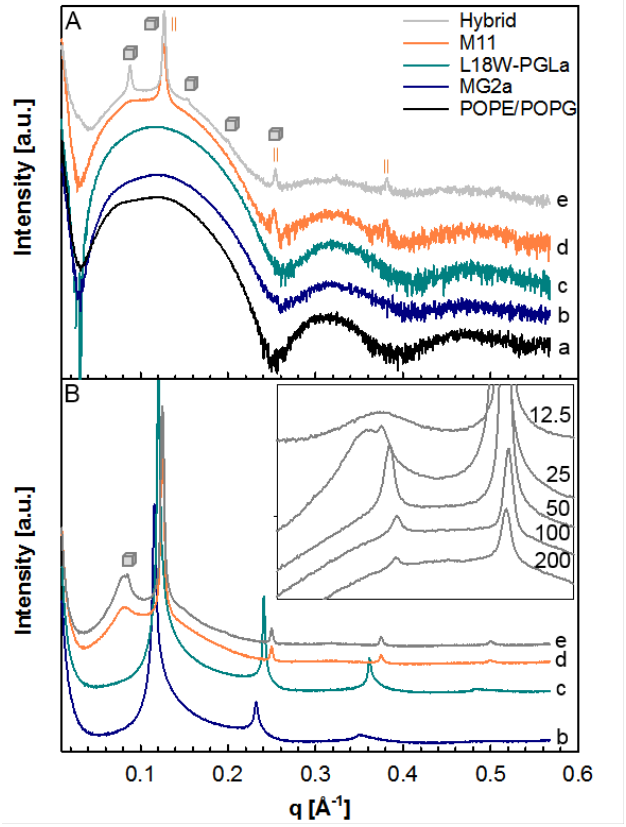

Figure 3: SAXS patterns of pure POPE/POPG LUVs (a) and in the presence of MG2a (b), L18W-PGLa (c), M11 (d) and the hybrid peptide (e) at P/L = 1:50 (panel A) and P/L = 1:25 (panel B), respectively at 35°C. The insert in panel B corresponds to a closeup of the scattering data in the low q region for the hybrid peptide. Numbers correspond to relative number of lipids for P/L, with P = 1.

PGLa and the hybrid peptide (Fig. 4), which is most likely due to a progressive thinning of the membrane, observed previously for other systems (see, e.g., (31)). The exception was M11, for which we observed the same D as for the hybrid peptide at low temperatures. However, D diverged from these data at 45°C and approached the D values of MG2a at 66°C. The difference between the hybrid and M11 is probably due to the decreased translational and configurational degrees of freedom for the hybrid, where both peptides are covalently coupled. In the case of M11 peptides interact only via weak forces, which seem to be overcome upon increasing temperature. Previously, we reported that MG2a inserts somewhat less deeply into the headgroup regime of POPE/POPG mixtures than L18W-PGLa (7). The temperature behavior of D for the equimolar mixture therefore indicates that the heterodimers dissociate for $T > 45$°C and peptides take up their 'original' positions within the bilayer.

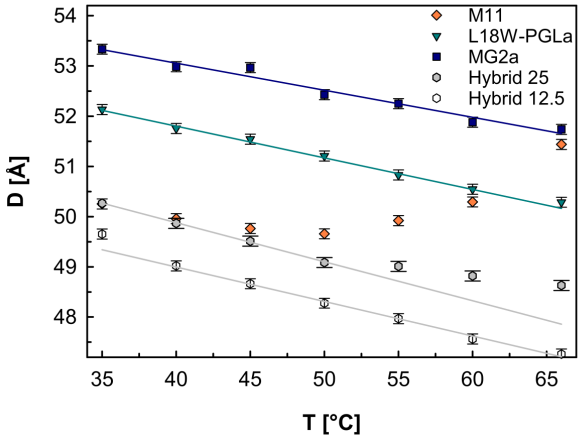

Figure 4: Temperature dependence of the lamellar repeat distance of POPE/POPG (3:1 mol/mol) multibilayers in the presence of magainins at P/L = 1:25 (full symbols) and P/L = 1:12.5 (open circle).

It is not clear from SAXS experiments, whether the lamellar phases observed in the presence of peptides correspond to a stack of sheets or multilamellar vesicles (MLVs). To differentiate between these two types of aggregates we performed cryo-TEM. Adding either L18W-PGLa or MG2a ($P/L = 1:50$) to POPE/POPG LUVs (Fig. 5 *A*) induced a significant variation of vesicle size without changing their lamellarity (Fig. 5 *B*, *C*). In contrast, the addition of M11 or the hybrid peptide induced clear signatures of MLVs (Fig. 5 *D*, *E*). We thus conclude that the peptides indeed lead to the formation of MLVs composed of tightly coupled bilayers. Note that the sharp peaks observed at P/L = 1:25 for the individual peptides (Fig. 3) indicate that MG2a and L18W-PGla are able to induce a LUV → MLV transition at sufficiently high concentration.

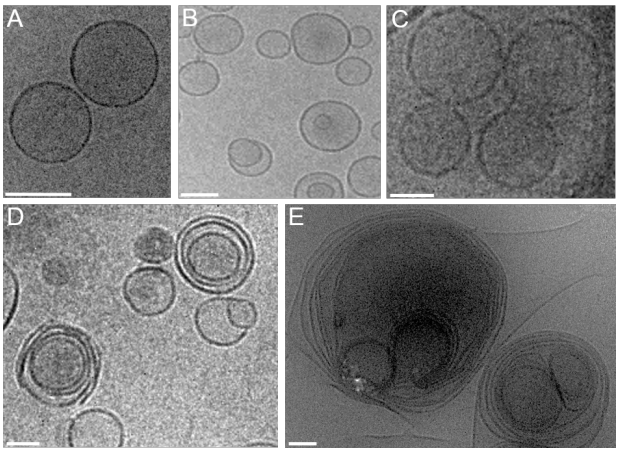

Figure 5: Cryo-TEM images of POPE/POPG (3:1 mol/mol) (A) and in the presence of the peptides (P/L = 1:50) L18W-PGLa (B), MG2a (C), M11 (D) and the hybrid peptide (E) at 35°C. All scale bars correspond to 100 nm.

MD simulations

Peptide mixtures are able to form surface-bound tetramers in isolated bilayers

In the preceding paper, we found that MG2a and L18W-PGLa alone prefer to form surface-aligned monomers or antiparallel homodimers in POPE/POPG (3:1) bilayers (7). In contrast, equimolar mixtures of the peptides resulted in the preferential formation of parallel heterodimers in the same lipid bilayers and concentrations. Here we extended the coarse-grained simulation of the peptide mixture and found that the parallel heterodimers of MG2a and L18W-PGLa can further assemble into tetramers (Fig. 6). In these aggregates, all four peptides interact via their C-termini. Both MG2as are aligned completely parallel to the membrane surface, while L18W-PGLa peptides are slightly tilted with their C-termini reaching into the membrane hydrophobic core. Due to the amidation of the terminal carboxyl group and the lack of complementary charged species, the tetramer is held together mainly by hydrophobic interactions (see Fig. S7 for calculated interaction energies between individual residues).

Since previous NMR experiments do not provide information on the penetration depth of the two peptides (6) we also tested the possible formation of peptide aggregates within the membrane's hydrophobic core. To do so, we inserted two parallel heterodimers in an alternating fashion in the membrane center, as shown in Fig. S8 *A*, *B*. Initially, the peptides were held in the position by restraints to equilibrate the membrane. Upon removal of these constraints, the peptide aggregate quickly fell apart and the peptides assumed surface-bound position (Fig. S8 (C)) .

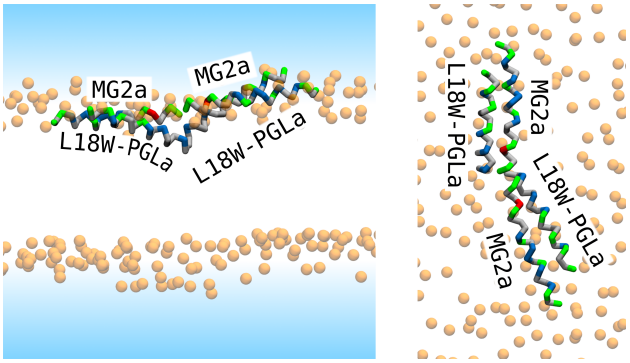

Figure 6: Representative simulation snapshots of two MG2a/L18W-PGLa parallel dimers forming a tetramer through the interaction of their C-termini. Side and top views on the tetramer are shown on left and right images, respectively. Lipid phosphate atoms are shown as orange spheres. Solvent is represented by a blue-shaded area and lipid tails are not shown for clarity. Peptide secondary structure is shown in cartoon representation and colored by residue type. Nonpolar: grey, polar: green, acidic: red, and basic: blue. Mag2a has a glutamic acid (red) in its sequence and is more polar, while L18W-PGLa is more hydrophobic.

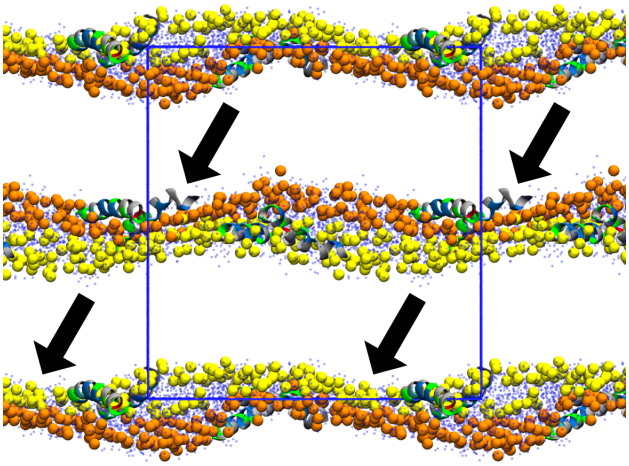

Figure 7: Final snapshot of two lipid bilayers after 1 μs long all-atom simulation. Blue rectangle marks the simulation cell. Lipid phosphate atoms of first and second bilayers are shown as orange and yellow spheres, respectively. Lipid tails are not shown for clarity. The peptides' secondary structures are displayed in cartoon representation and colored by residue type. Nonpolar: gray, polar: green, acidic: red, and basic: blue. Water oxygens are shown as semi-transparent dark-blue dots.

Formation of fibre-like structures in collapsed multibilayers

Motivated by our experimental evidence for the peptide-induced formation of MLVs with reduced intrinsic spacing, we prepared a stack of two membranes at P/L = 1:64 (see Methods section for details) and performed a 1 μs long all-atom dynamics simulation, see Fig. S11 and 7. To mimic the experimental conditions, the bilayers centers were initially displaced by 50 Å as determined from our SAXS measurements. Due to the slow diffusion of peptides on membranes, the peptides were prepared as parallel dimers and placed randomly on the membrane. All dimers remained stable and interacted with lipids of the adjacent membrane. These peptides interactions lead to the formation of an alternating pattern of peptide nodes and solvent pockets (see Fig. 7). Any further aggregation of peptides was not observed within the 1 μs time scale and all peptides remained within the initial membrane with their hydrophobic side facing the center of the bilayer. Note that the system size likely affected the size of the water pockets as water is constrained to remain within the simulation box.

To verify that the observed behavior is not an artifact, we extended the lateral system size to 504-lipid bilayers and performed 20 μs long coarse-grained Martini simulations in the presence and absence of L18W-PGLa and MG2a. No spontaneous membrane adhesion or appreciable interaction between the bilayers was observed for the pure membrane system (Fig. 8 *A*). Membrane adhesion with a concomitant formation of "pockets and nodes" was only observed in the presence of the peptide mixture. At P/L = 1:42, the peptides aggregated resulting in a height modulation of the membranes, where peptides were located at the nodes (Fig. 8 *B*), in agreement with all-atom simulations. The wavelength of the modulation is different from all-atom simulations and is likely to be affected by the system size. At higher peptide concentration (P/L=1:21), L18W-PGLa and MG2a formed fibril-like structures along the bilayer contact nodes (connected through the periodic boundary), as shown in Fig. 8 *C*, *D*. Interestingly, we also observed a temporary formation of membrane fusion stalk in the presence of the peptides (Fig. S12). The fusion stalk fell apart after the exchange of several lipids in tens of nanoseconds.

To investigate the effect of periodic boundary conditions, we prepared a much larger system with a stack of membranes each composed of 2016 lipid molecules. The peptides were added at random initial positions and orientations (P/L = 1 : 21), but distributed equally on the membrane surfaces. Fig. S9 *A* shows the initial configuration from the production dynamics simulation. During the simulation, a fusion stalk formed between two bilayers and remained stable for the remaining duration of the simulation, i.e., 100 μs. Fig. S9B shows the snapshot from the end of the simulation. Note that even during the stalk formation the peptides remained parallel or slightly tilted to the membrane plane. Irrespective of the fusion stalk, which occurred only at a single location of the simulated membrane stack, the peptides aggregated and formed fibril-like structures, analogously to the 504-lipid simulation (Fig. S10).

In order to interrogate, whether the presence of peptides

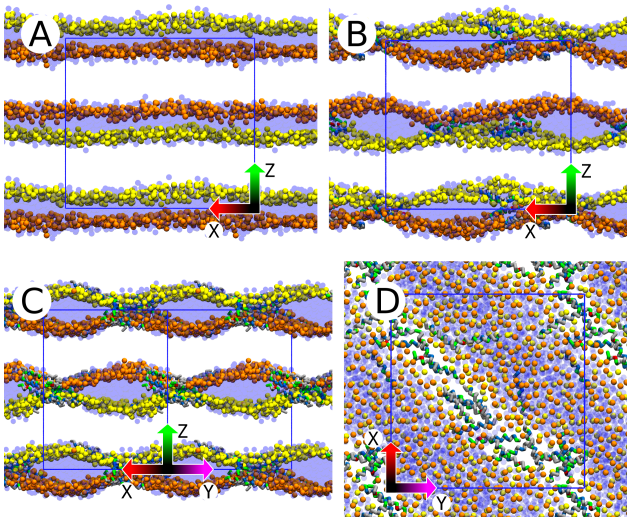

Figure 8: Last simulation snapshots of coarse-grained systems with two lipid bilayers and (A) without peptides, (B) with MG2a+L18W-PGLa at 1:42 peptide-to-lipid ratio, and (C, D) with MG2a+L18W-PGLa at 1:21 peptide-to-lipid ratio after 20 μs. Arrows indicate the system axes: (X) red, (Y) magenta, and (Z) green. Blue rectangle marks the simulation cell: (A, B) view along the Y axis, (C) cell is rotated by 45° (because nodes formed in that direction this time), and (D) top view along the Z axis. Lipid phosphate atoms of the first and second bilayers are shown as orange and yellow spheres, respectively. Lipid tails are not displayed for clarity. Peptide secondary structure is shown in cartoon representation and colored by residue type. Nonpolar: gray, polar: green, acidic: red, and basic: blue. Water beads are shown as semi-transparent dark-blue spheres.

in both leaflets of opposing bilayers is a necessary condition for bilayer adhesion we performed a coarse-grained simulation of a similar-sized system but placing the peptides in one leaflet of each bilayer, only. We again observed a membrane stalk. Interestingly, its formation was accompanied by a translocation of peptides between the membranes. Specifically, stalk-formation was initiated from a heterodimer by moving a MG2a toward the interbilayer space (Fig. 9). This caused one of the lipids from the opposite membrane to insert its tail between the peptide dimer. The insertion was stabilized by the hydrophobic interactions of the hydrocarbon chain with the phenylalanine residues of MG2a at position 12 and 16. Subsequently, the heterodimer split at the N-terminus leading to the formation of a fusion stalk, which was further stabilized by other peptides, which diffused into the stalk. Similar process of stalk formation was observed it in three independent simulations.

DISCUSSION

We used a combination of experimental and computational techniques to demonstrate that equimolar mixtures of L18W-PGLa and MG2a induce intricate topological changes in membranes composed of POPE/POPG (3:1 mol/mol) at synergistic peptide/lipid ratios. The peptide mixture caused a transformation of LUVs into MLVs with a collapsed interbilayer distance as evidenced by SAXS and cryo-TEM (Figs. 3, 5). MG2a and L18W-PGLa individually were also found to induce this transformation, however, only at doubled concentration. At the molecular level, our coarse-grained MD simulations showed that the formation of parallel L18W-PGLa/MG2a heterodimers observed in a previous report (7) progresses to a tetramer formation (or double heterodimers) stabilized by C-termini interactions, which can further assemble into fibril-like structures in presence of two close membranes (Figs. 6 - 8). These fibril-like structures are aligned parallel to the membrane surface and are sandwiched between the collapsed multibilayers, i.e. the peptides couple adjacent bilayers by peptide-peptide and peptide-lipid interactions. Interestingly, electrostatic interaction between POPG and the cationic residues of MG2a and L18W-PGLa does not induce lipid domain formation as evidenced by zero-contrast SANS (Fig. 2). Instead, the splitting of the main phase transition of the aggregates into multiple melting transitions appears to be due to a non-homogeneous distribution of peptides.(Fig. 1). We note, however, that the overall melting process was significantly less cooperative for the peptide mixture and the hybrid peptide, i.e., in the presence of their aggregates.

The formation of fibril-like structures induced a curvature modulation of membranes with peptides forming the connections between the membranes. These peptides aggregates were able to initiate the formation of fusion stalks (Figs. 9, S12). The smallest peptide aggregate, for which we observed stalk formation, was a parallel heterodimer, inserted only in one membrane leaflet, which induced a fusion to the proximal peptide-free bilayer. Interestingly, peptides remained parallel or slightly tilted from the membrane plane even during the stalk formation.

Stalks are well-known precursors to membrane fusion (32–34) and cubic phase formation (32). Indeed, we observed a Pn3m cubic phase coexisting with the collapsed multibilayers in case of chemically-linked heterdimers by SAXS (Fig. 3), thus supporting MD results. At elevated concentration of the hybrid peptide (P/L = 1:25), we observed an additional broad peak indicating the presence of an additional phase coexisting with the Pn3m and lamellar phases. The Pn3m completely vanished at P/L = 1:12.5, and the scattering pattern exhibited just a broad peak as well as the peaks arising from the collapsed multibilayers. A similar broad Bragg reflection was also observed for L18W-PGLa/MG2a mixtures, but not for the individual peptides (Fig. 3).

There are two possible scenarios for the origin of this broad peak, the first one being the peptide-induced curvature

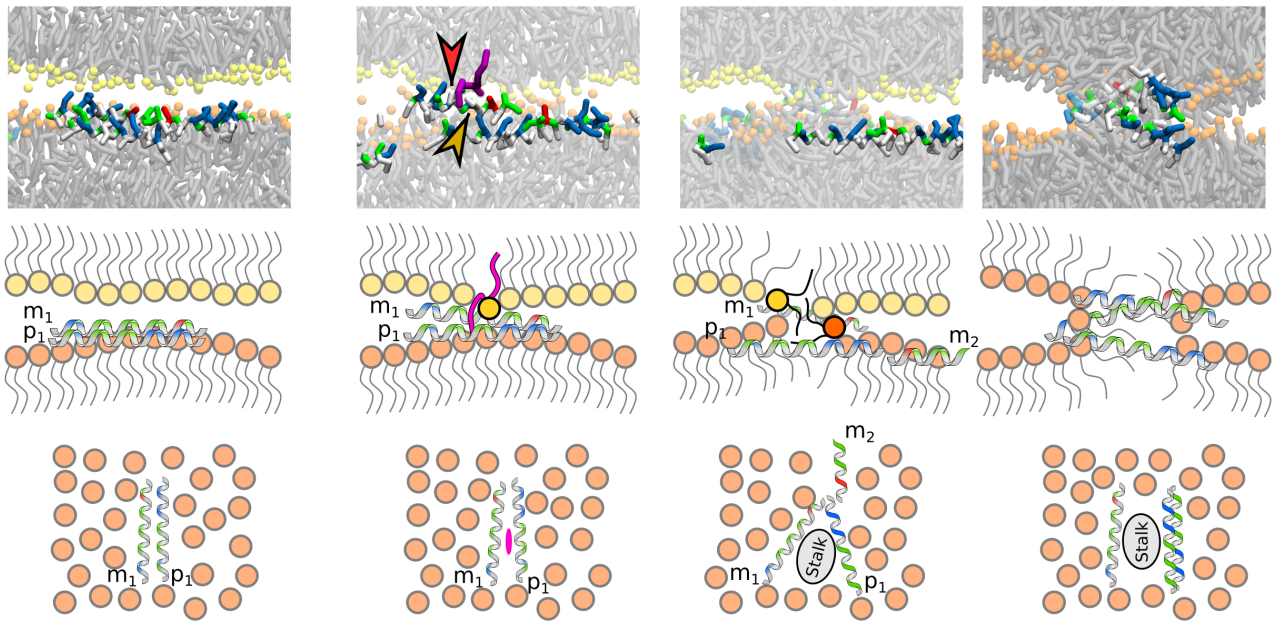

Figure 9: Simulation snapshots (top) and corresponding illustrative images from the side (middle) and top view (bottom) capturing the process of bilayer fusion. 1) MG2a (m1) and L18W-PGLa (p1) peptides arranged in a parallel dimer. 2) The bilayer fusion was initiated by one lipid (highlighted in purple). Single lipid tail was interacting with Phe12 (red arrow) and Phe16 (dark-yellow arrow) of the MG2a peptide and connected both bilayers. 3) MG2a and L18W-PGLa peptides assumed a V-shaped configuration that caused the formation of a fusion stalk. 4) Several peptides crossed from one bilayer to another and lipids from the two bilayers started to mix through the stalk. Later in the simulation, two L18W-PGLa peptides formed an antiparallel homodimer and the fusion stalk further expanded. One MG2a peptide was stabilizing the stalk from the other side. The stalk remained stable until the end of the 20 μs long simulation. In first three columns, phosphate beads of the first and second bilayer are shown in yellow and orange, respectively. In the most right column, all phosphate beads are shown orange due to lipid mixing.

modulation of the lamellar phase. In this case, the peak would emanate from the wavelength of the modulation. Somewhat similar patterns have been reported for sandwiched structures formed by DNA/surfactant complexes under specific conditions (35), where DNA aligned between the bilayers. A second scenario explaining the presence of the broad peak is the formation of a sponge phase. Sponge phases can be viewed as molten bicontinuous cubic phases, with a characteristic low-angle peak, whose position relates to the average distance between the water channels (36–38). Likewise, the $D_{(1,1,0)}$ of the Pn3m phase, gives the distance between the pores. The facts that (i) the D-spacing of the broad peak is larger than $D_{(1,1,0)}$ in the presence of the hybrid peptide at P/L = 1:25 and (ii) the Pn3m phase vanishes upon further increasing the peptide concentration (Fig. 3 *B*, insert) indeed support the formation of a sponge phase, which analogously to Pn3m consists of a network of water channels, but lacks 3D crystalline-like positional correlations. In other words, increasing hybrid peptide concentration appears to lead to an overall decrease of membrane curvature causing a melting of the Pn3m phase into a spongy structure. The similar position and shape of the broad Bragg peak formed in presence of M11 suggest also the formation of a sponge phase in the synergistic regime of the peptide mixture. Previously, Silva et al. reported a LUV → collapsed MLV transition for the same lipid mixture in the presence of cecropin A (39). However, no coexisting sponge phase or other curvature-related structures were observed. We found black featureless objects in samples with the equimolar mixture or the hybrid peptide (Fig. S13). These structures could contain cubic or sponge structures, but are too large/thick to be analyzed by cryo-TEM.

Finally, it is important to align our present findings with our previously reported leakage data for the same lipid system (4). Both L18W-PGLa and MG2a caused only minor release of fluorescent dye, whereas their equimolar mixture and the hybrid peptide induced significant leakage. Our present experiments revealed the formation of multibilayers with a collapsed D-spacing at high peptide concentration for all peptides, including their equimolar mixture (Figs. 3). Therefore, a LUV → MLV transition does not seem to be a sufficient condition for enhanced dye leakage. This suggests that there is a pathway transforming LUVs to MLVs without leaking their

content. In contrast, synergistically increased dye release is coupled to increased membrane curvature in the presence of fibril-like peptide structures leading to fusion events and the development of sponge or cubic phases. Importantly, fusion events could be leaky (40, 41) and both above phases are highly leaky structures able to account for the dye release. Additionally, the significant difference between $D_{(1,1,0)} \sim 73$ Å of the Pn3m phase and the $D \sim 50$ Å of the lamellar phase (Tab. 1) shows that there is no epitaxial relationship between the cubic and the lamellar phases. This indicates the formation of a defect-rich zone bridging the two structures, which could also give rise to significant membrane leakage (see, e.g., (38) for a detailed discussion).

An important aspect of our results is that both peptides remained in a surface-aligned topology even during the formation of fusion-stalks. This is specific to the significant negative intrinsic curvature of POPE, which leads to a tight packing of the bilayer's polar/apolar interface and a high energy barrier for peptide translocation (4). Therefore other membrane mimics, lacking contributions of lipids with negative intrinsic curvature – e.g. if lipids not occurring in bacteria are used –, may allow for a full insertion of peptides and the formation of specific transmembrane pores as suggested previously for MG2a and PGLa (1, 2). Pores of sponge or cubic phases essentially result from bridging two close bilayers and are consequently distinct from peptide transmembrane pores. Our results agree in part with the suggested mesophase-like peptide arrangement (3), which in a way are similar to the fibril-like structures observed here, although effects on membrane curvature were not considered. However, effective discharge of dyes from LUVs correlates with the formation of sponge or cubic phases.

Correlating our present findings to the biological activity of the peptides (4) is not straightforward, due significant differences between Gram-negative bacteria and here studied lipid vesicles. We are not aware of any observation of peptide-induced non-lamellar membrane structures in bacteria. However, inner mitochondrial membranes have been reported to form cubic phases under stress conditions (42). Moreover, bacterial lipid extracts have been shown to form cubic phase in the presence of surface-inserted AMPs (43). Observations of cubic phases formed by membranes enriched with lipids with negative intrinsic curvature (such as phosphatidylethanolamine and cardiolipin) are in line with our findings. Aggregates, as observed for L18W-PGLa and MG2a, seem to facilitate this effect leading to sponge or cubic phases even in the absence of cardiolipin, which might be even be exploited by PGLa and MG2a in bacteria. Moreover, constantly ongoing membrane remodelling processes such as bacterial endocytosis (44) or cell division provide membrane contact points for peptides to intercept these processes possibly by inducing non-lamellar membrane structures.

CONCLUSION

The synergistic mechanism of MG2a and L18W-PGLa is a complex process which evolves over several length scales. MG2a and L18W-PGla are able to dimerize already at low peptide concentrations (7), which progresses upon increasing their content into fibril-like structures inducing cross-links between proximate bilayers leading to the occurrence of fusion stalks. The membrane with synergistic peptides evolve over time into a sponge phase correlating with synergistic leakage of the vesicles as observed previously (4). If the peptides are strongly coupled, as in the case of the MG2a-L18W-PGLa hybrid, a cubic phase with high membrane curvature forms already at peptide concentrations as low as P/L = 1:200 (Fig. 3 *B*), tying in with the hybrid's even higher activity (see Fig. 4 *A* in (4)). One of remaining issue to address regarding the synergistic mechanism of PGLa and MG2a is the sequence of events, i.e. the kinetics of their activity. We are currently performing such studies in our laboratories.

AUTHOR CONTRIBUTIONS

I.K. carried out all simulations, analyzed the data, and wrote the article. M.P. performed SAXS, SANS, DSC experiments, analyzed the data, and wrote the article. S.P. performed SANS experiments and I.L-P. performed and analyzed TEM experiments. R.V., K.L. and G.P. designed the research and wrote the article.

ACKNOWLEDGMENTS

We thank Frederick A. Heberle for assistance in designing the zero-contrast SANS experiments and Michael Rappolt for helpful insights regarding cubic and sponge phases. This work was supported by the Czech Science Foundation (grant 17-11571S to R.V.), the Austrian Science Funds FWF (project No. I1763-B21 to K.L.), Grant Agency of Masaryk University (MUNI/G/ 1100/2016), and the CEITEC 2020 (LQ1601) project with financial contribution made by the Ministry of Education, Youths and Sports of the Czech Republic within special support paid from the National Programme for Sustainability II funds. Computational resources were provided by the CESNET LM2015042 and the CERIT Scientific Cloud LM2015085, provided under the programme 'Projects of Large Research, Development, and Innovations Infrastructures'. This work was supported by The Ministry of Education, Youth and Sports from the Large Infrastructures for Research, Experimental Development and Innovations project 'IT4Innovations National Supercomputing Center – LM2015070'. We acknowledge SOLEIL for provision of synchrotron radiation facilities and we would like to thank Javier Perez for assistance in using beamline SWING.

An online supplement to this article can be found by visiting BJ Online at http://www.biophysj.org.

REFERENCES

1. Matsuzaki, K., Y. Mitani, K. Y. Akada, O. Murase, S. Yoneyama, M. Zasloff, and K. Miyajima, 1998. Mechanism of synergism between antimicrobial peptides magainin 2 and PGLa. *Biochemistry* 37:15144–15153.

2. Zerweck, J., E. Strandberg, O. Kukharenko, J. Reichert, J. Bürck, P. Wadhwani, and A. S. Ulrich, 2017. Molecular mechanism of synergy between the antimicrobial peptides PGLa and magainin 2. *Sci Rep* 7:13153.

3. Marquette, A., E. S. Salnikov, E. Glattard, C. Aisenbrey, and B. Bechinger, 2016. Magainin 2-PGLa interactions in membranes - Two peptides that exhibit synergistic enhancement of antimicrobial activity. *Curr Top Med Chem* 16:65–75.

4. Leber, R., M. Pachler, I. Kabelka, I. Svoboda, D. Enkoller, R. Vácha, K. Lohner, and G. Pabst, 2018. Synergism of Antimicrobial Frog Peptides Couples to Membrane Intrinsic Curvature Strain. *Biophys J* 114:1945–1954.

5. Strandberg, E., J. Zerweck, P. Wadhwani, and A. S. Ulrich, 2013. Synergistic insertion of antimicrobial magainin-family peptides in membranes depends on the lipid spontaneous curvature. *Biophys J* 104:L9–11.

6. Harmouche, N., and B. Bechinger, 2018. Lipid-Mediated Interactions between the Antimicrobial Peptides Magainin 2 and PGLa in Bilayers. *Biophys J* 115:1033–1044.

7. Pachler, M., I. Kabelka, M.-S. Appavou, K. Lohner, R. Vácha, and G. Pabst, 2019. Magainin 2 and PGLa in Bacterial Membrane Mimics I: Peptide-Peptide and Lipid-Peptide Interactions. *bioRxiv* https://www.biorxiv.org/content/10.1101/664359v1.

8. Kingsley, P. B., and G. W. Feigenson, 1979. The synthesis of a perdeuterated phospholipid: 1,2-dimyristoyl-sn-glycero-3-phosphocholine-d72. *Chem Phys Lipids* 24:135–147.

9. Rappolt, M., 2006. Chapter 9 The Biologically Relevant Lipid Mesophases as "Seen" by X-Rays. *In* A. Leitmannova Liu, editor, Advances in Planar Lipid Bilayers and Liposomes: (Volume 5, Advances in Planar Lipid Bilayers and Liposomes), Elsevier Science & Technology, St. Louis, MO, volume 5 of *Advances in Planar Lipid Bilayers and Liposomes S*, 253–283.

10. Heberle, F. A., R. S. Petruzielo, J. Pan, P. Drazba, N. Kučerka, R. F. Standaert, G. W. Feigenson, and J. Katsaras, 2013. Bilayer Thickness Mismatch Controls Domain Size in Model Membranes. *J Am Chem Soc* 135:6853–6859. PMID: 23391155.

11. Eicher, B., D. Marquardt, F. A. Heberle, I. Letofsky-Papst, G. N. Rechberger, M.-S. Appavou, J. Katsaras, and G. Pabst, 2018. Intrinsic Curvature-Mediated Transbilayer Coupling in Asymmetric Lipid Vesicles. *Biophys J* 114:146–157.

12. Abraham, M. J., T. Murtola, R. Schulz, S. Páll, J. C. Smith, B. Hess, and E. Lindahl, 2015. GROMACS: High performance molecular simulations through multi-level parallelism from laptops to supercomputers. *SoftwareX* 1-2:19–25.

13. Páll, S., M. J. Abraham, C. Kutzner, B. Hess, and E. Lindahl, 2015. Tackling Exascale Software Challenges in Molecular Dynamics Simulations with GROMACS. *In* E. Laure, and S. Markidis, editors, Solving software challenges for exascale, Springer, Cham, volume 8759 of *LNCS Sublibrary: SL 1 - Theoretical Computer Science and General Issues*, 3–27.

14. Jämbeck, J. P. M., and A. P. Lyubartsev, 2012. An Extension and Further Validation of an All-Atomistic Force Field for Biological Membranes. *J Chem Theory Comput* 8:2938–2948.

15. Jämbeck, J. P. M., and A. P. Lyubartsev, 2012. Derivation and systematic validation of a refined all-atom force field for phosphatidylcholine lipids. *J Phys Chem B* 116:3164–3179.

16. Lindorff-Larsen, K., S. Piana, K. Palmo, P. Maragakis, J. L. Klepeis, R. O. Dror, and D. E. Shaw, 2010. Improved side-chain torsion potentials for the Amber ff99SB protein force field. *Proteins* 78:1950–1958.

17. Sorin, E. J., and V. S. Pande, 2005. Exploring the helix-coil transition via all-atom equilibrium ensemble simulations. *Biophys J* 88:2472–2493.

18. Nosé, S., 1984. A unified formulation of the constant temperature molecular dynamics methods. *J Chem Phys* 81:511–519.

19. Nosé, S., 1984. A molecular dynamics method for simulations in the canonical ensemble. *Mol Phys* 52:255–268.

20. Hoover, W. G., 1985. Canonical dynamics: Equilibrium phase-space distributions. *Phys Rev A* 31:1695–1697.

21. Parrinello, M., and A. Rahman, 1980. Crystal Structure and Pair Potentials: A Molecular-Dynamics Study. *Phys Rev Lett* 45:1196–1199.

22. Parrinello, M., and A. Rahman, 1981. Polymorphic transitions in single crystals: A new molecular dynamics method. *J Appl Phys* 52:7182–7190.

23. Essmann, U., L. Perera, M. L. Berkowitz, T. Darden, H. Lee, and L. G. Pedersen, 1995. A smooth particle mesh Ewald method. *J Chem Phys* 103:8577–8593.

24. Allen, M. P., and D. J. Tildesley, 2017. volume 1. Oxford University Press.

25. Marrink, S. J., H. J. Risselada, S. Yefimov, D. P. Tieleman, and A. H. de Vries, 2007. The MARTINI force field: coarse grained model for biomolecular simulations. *J Phys Chem B* 111:7812–7824.

26. Monticelli, L., S. K. Kandasamy, X. Periole, R. G. Larson, D. P. Tieleman, and S.-J. Marrink, 2008. The MARTINI Coarse-Grained Force Field: Extension to Proteins. *J Chem Theory Comput* 4:819–834.

27. de Jong, D. H., G. Singh, W. F. D. Bennett, C. Arnarez, T. A. Wassenaar, L. V. Schäfer, X. Periole, D. P. Tieleman, and S. J. Marrink, 2013. Improved Parameters for the Martini Coarse-Grained Protein Force Field. *J Chem Theory Comput* 9:687–697.

28. Bussi, G., D. Donadio, and M. Parrinello, 2007. Canonical sampling through velocity rescaling. *J Chem Phys* 126:014101.

29. Jo, S., T. Kim, V. G. Iyer, and W. Im, 2008. CHARMM-GUI: a web-based graphical user interface for CHARMM. *J Comput Chem* 29:1859–1865.

30. Pozo Navas, B., K. Lohner, G. Deutsch, E. Sevcsik, K. A. Riske, R. Dimova, P. Garidel, and G. Pabst, 2005. Composition dependence of vesicle morphology and mixing properties in a bacterial model membrane system. *Biochim Biophys Acta* 1716:40–48.

31. Pabst, G., J. Katsaras, V. A. Raghunathan, and M. Rappolt, 2003. Structure and Interactions in the Anomalous Swelling Regime of Phospholipid Bilayers †. *Langmuir* 19:1716–1722.

32. Siegel, D. P., 1999. The Modified Stalk Mechanism of Lamellar/Inverted Phase Transitions and Its Implications for Membrane Fusion. *Biophys J* 76:291–313.

33. Tamm, L. K., J. Crane, and V. Kiessling, 2003. Membrane fusion: a structural perspective on the interplay of lipids and proteins. *Curr Opin Struct Biol* 13:453 – 466.

34. Chernomordik, L. V., and M. M. Kozlov, 2008. Mechanics of membrane fusion. *Nat Struct Mol Biol* 15:675 EP –.

35. Salditt, T., I. Koltover, J. O. Rädler, and C. R. Safinya, 1998. Self-assembled DNA–cationic-lipid complexes: Two-dimensional smectic ordering, correlations, and interactions. *Phys Rev E* 58:889–904.

36. Roux, D., C. Coulon, and M. E. Cates, 1992. Sponge phases in surfactant solutions. *J Phys Chem* 96:4174–4187.

37. Lei, N., C. R. Safinya, D. Roux, and K. S. Liang, 1997. Synchrotron x-ray-scattering studies on the sodium dodecyl sulfate–water–pentanol–dodecane L3 sponge phase. *Phys Rev E* 56:608–613.

38. Angelov, B., A. Angelova, U. Vainio, V. M. Garamus, S. Lesieur, R. Willumeit, and P. Couvreur, 2009. Long-living intermediates during a lamellar to a diamond-cubic lipid phase transition: a small-angle X-ray scattering investigation. *Langmuir* 25:3734–3742.

39. Silva, T., B. Claro, B. F. B. Silva, N. Vale, P. Gomes, M. S. Gomes, S. S. Funari, J. Teixeira, D. Uhríková, and M. Bastos, 2018. Unravelling a Mechanism of Action for a Cecropin A-Melittin Hybrid Antimicrobial Peptide: The Induced Formation of Multilamellar Lipid Stacks. *Langmuir* 34:2158–2170. PMID: 29304549.

40. Risselada, H. J., G. Bubnis, and H. Grubmüller, 2014. Expansion of the fusion stalk and its implication for biological membrane fusion. *Proc Natl Acad Sci USA* 111:11043–11048.

41. Yang, S.-T., E. Zaitseva, L. V. Chernomordik, and K. Melikov. Cell-penetrating peptide induces leaky fusion of liposomes containing late endosome-specific anionic lipid. *Biophys J* 2525–2533.

42. Deng, Y., and M. Mieczkowski, 1998. Three-dimensional periodic cubic membrane structure in the mitochondria of amoebaeChaos carolinensis. *Protoplasma* 203:16–25.

43. Koller, D., and K. Lohner, 2014. The role of spontaneous lipid curvature in the interaction of interfacially active peptides with membranes. *Biochim Biophys Acta, Biomembr* 1838:2250 – 2259. Interfacially active peptides and proteins.

44. Lonhienne, T. G. A., E. Sagulenko, R. I. Webb, K.-C. Lee, J. Franke, D. P. Devos, A. Nouwens, B. J. Carroll, and J. A. Fuerst, 2010. Endocytosis-like protein uptake in the bacterium Gemmata obscuriglobus. *Proc Natl Acad Sci USA* 107:12883–12888.

SUPPORTING MATERIAL

Magainin 2 and PGLa in Bacterial Membrane Mimics II: Membrane Fusion and Sponge Phase Formation

I.K., M.P., S.P., I.L.-P., K.L., G.P., R.V.

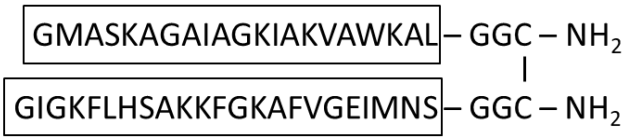

Figure S1: Chemical structure of the L18W-PGLa–MG2a hybrid peptide made of covalently bound peptides L18W-PGLa and MG2a.

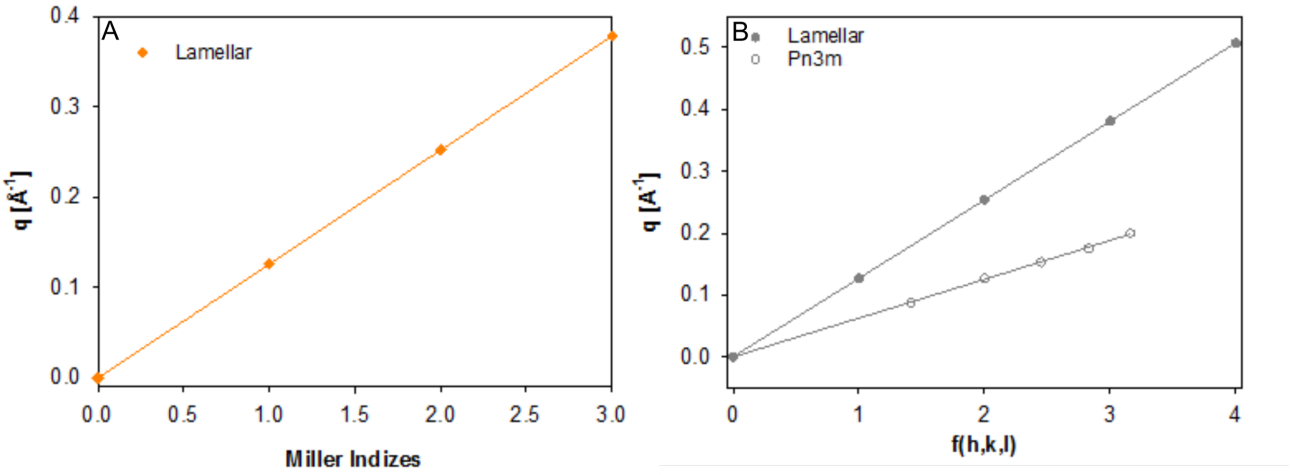

Figure S2: Indexation plots for the lamellar phase formed in the presence of M11 (A) and the coexisting lamellar and cubic phases formed by the chemically linked hybrid peptide (B) at a P/L of 1:50.

Table S1: Observed reflections of the lamellar and Pn3m phases.

lamellar (h)	Pn3m (h,k,l)
1	1,1,0
2	2,0,0
3	2,1,1
4	2,2,0
	3,1,0

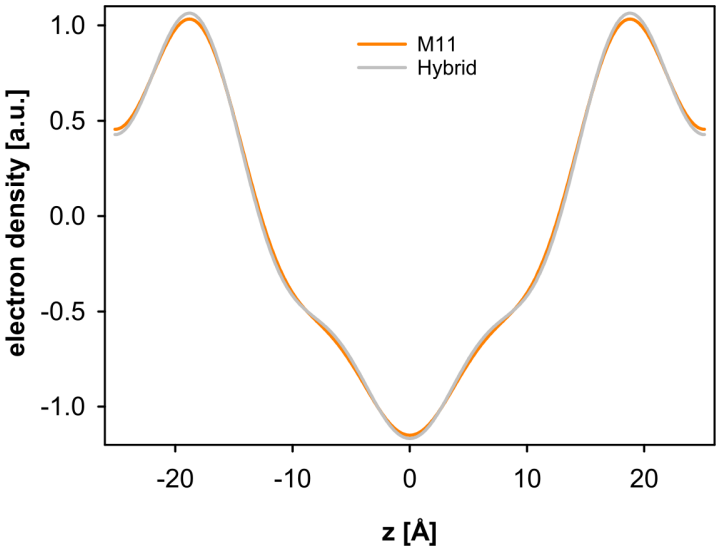

Figure S3: Electron density of 100 nm unilamellar vesicles composed of POPE/POPG (3:1 mol/mol) in the presence of M11 and the hybrid peptide at a P/L of 1/25 and 35°C.

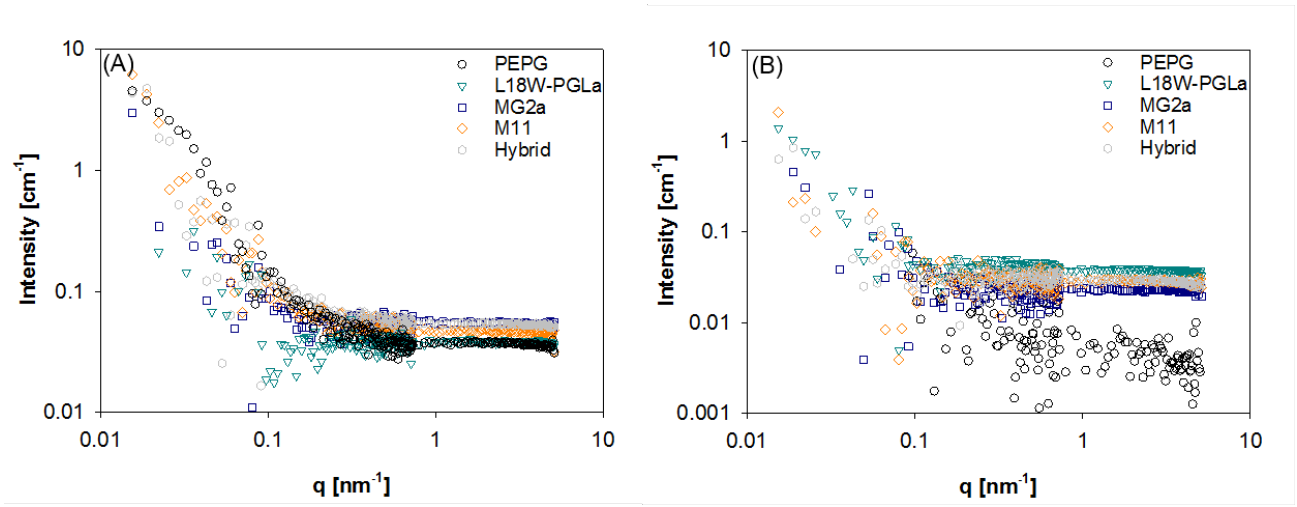

Figure S4: Zero-contrast SANS data of (POPEd31)/(POPG/POPGd31) (75)/(22/3) (Panel A) and the control sample (Panel B) in the absence (black circles) and presence of the peptides at 20°C (A) and 22°C (B) at a P/L of 1:25.

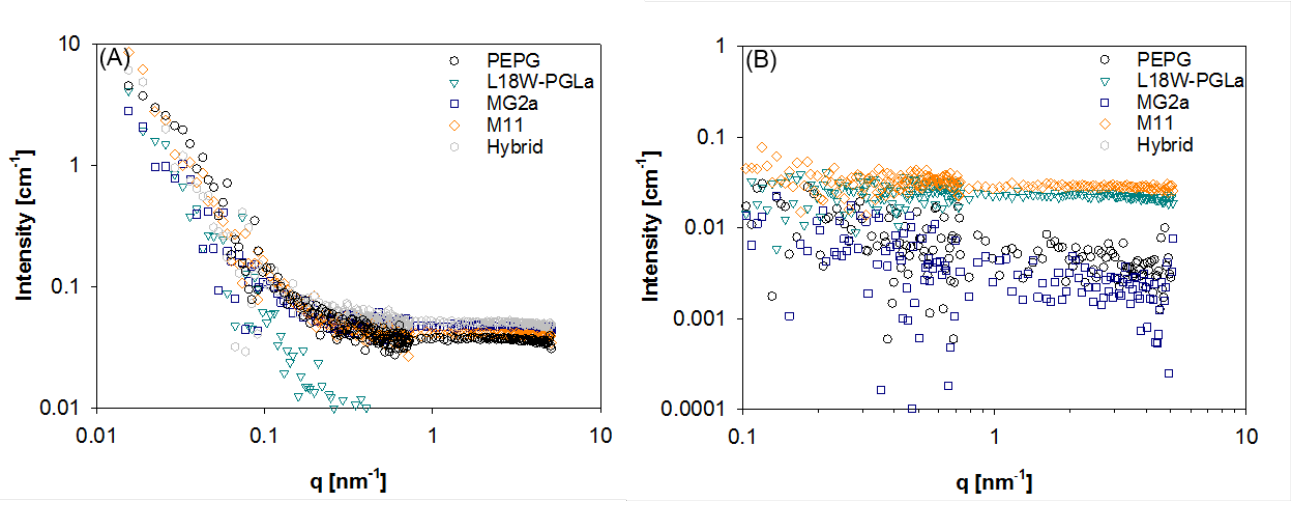

Figure S5: Zero-contrast SANS data of (POPEd31)/(POPG/POPGd31) (75)/(22/3) (Panel A) and the control sample (Panel B) in the absence (black circles) and presence of the peptides at 20°C (A) and 22°C (B) at a P/L of 1:50.

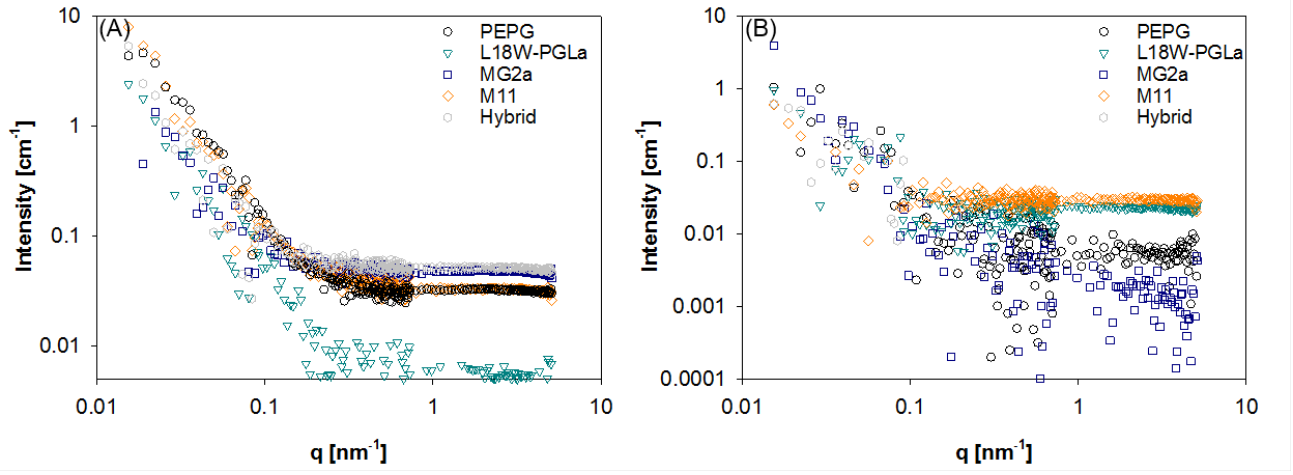

Figure S6: Zero-contrast SANS data of (POPEd31)/(POPG/POPGd31) (75)/(22/3) (Panel A) and the control sample (Panel B) in the absence (black circles) and presence of the peptides at 35°C° at a P/L of 1:50.

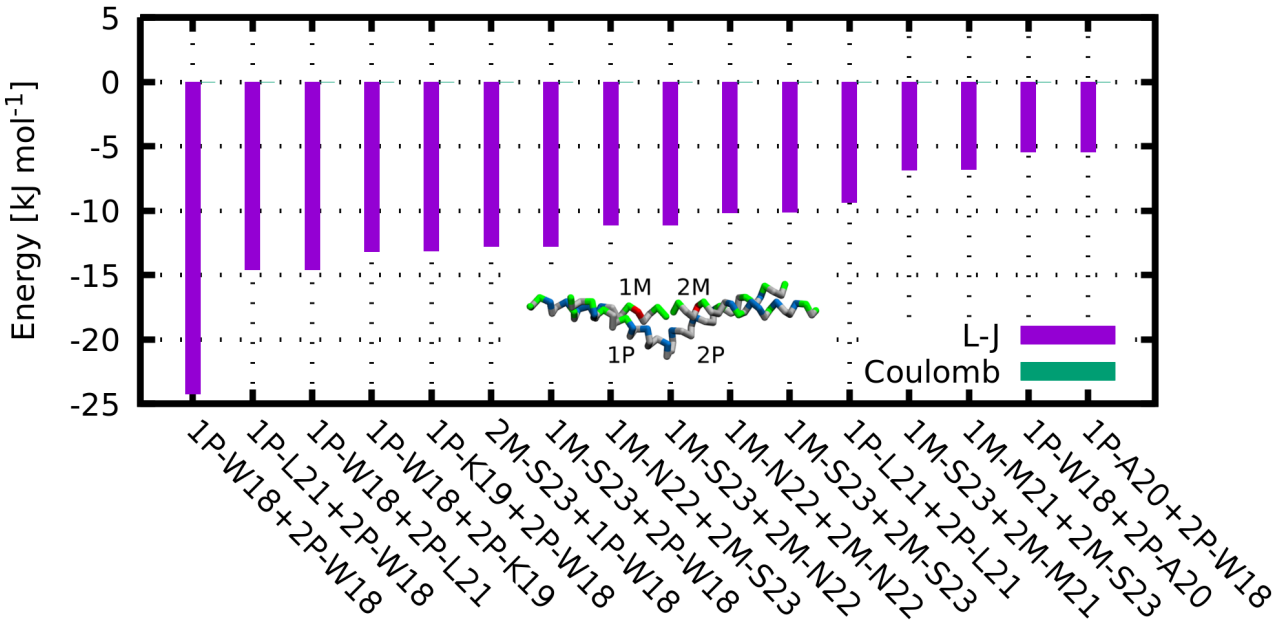

Figure S7: Calculated interaction energies between residues in opposing L18W-PGLa/MG2a heterodimers. Using single-letter amino acid codes, only residues with interaction energies larger than 5 kJ mol^{-1} are shown. MG2a and L18W-PGLaW are abbreviated as 'M' and 'P', respectively. The inset shows a representative structure of the tetramer formed by the heterodimers pointing with C-termini in the center. Purple and green bars represent Lennard-Jones and Coulomb interactions, respectively.

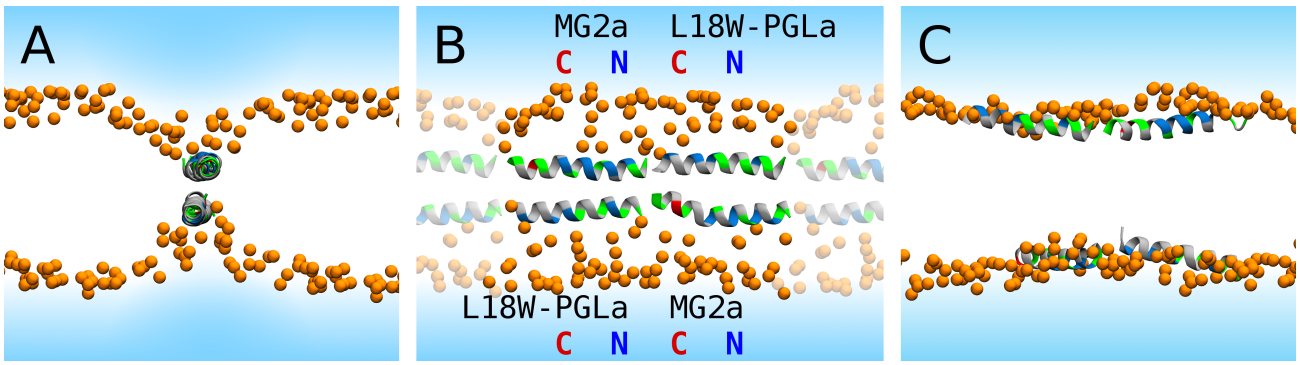

Figure S8: Initial and final simulation snapshots of a peptide fiber in the middle of the membrane. Initial system configuration with view along the fiber axis (A) and a sideview – rotated by 90° – (B). Periodic images are semi-transparent. (C) Final snapshot after 330 ns of production dynamics. Lipid phosphate atoms are shown as orange spheres. Lipid tails are not shown for clarity. The peptide secondary structure is shown in cartoon representation and colored by residue type. Nonpolar: gray, polar: green, acidic: red, and basic: blue.

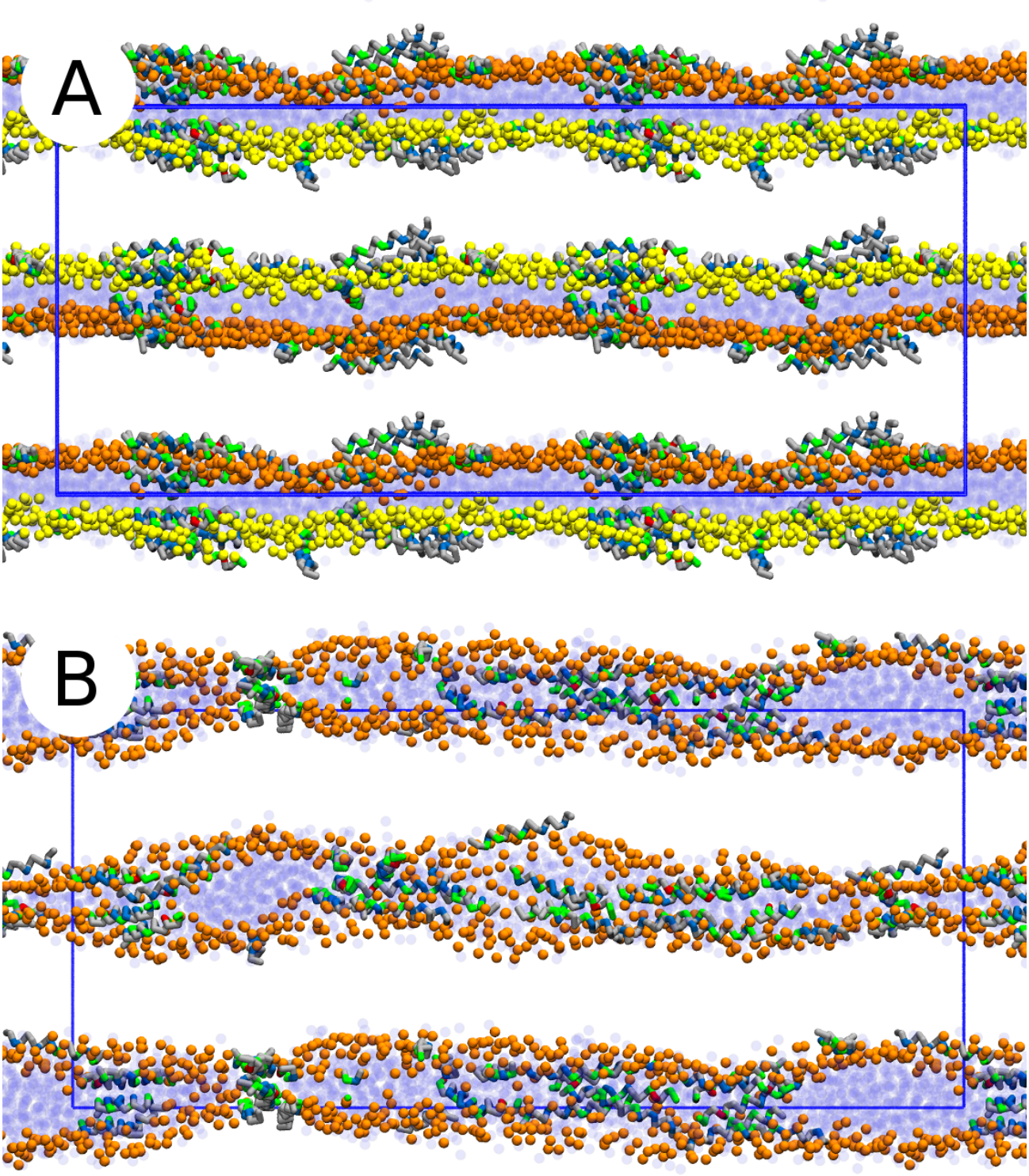

Figure S9: (A) Initial snapshot from the production simulation of a stack of two lipid bilayers with adsorbed peptides at 1:21 P/L. (B) Cut through the simulated system from the final simulation configuration after 100 μs. Due to the formation of a stable membrane stalk, lipids were mixed between bilayers. Lipid phosphate atoms of first and second bilayers before mixing are shown as orange and yellow spheres, respectively. Lipid tails are not shown for clarity. Nonpolar: gray, polar: green, acidic: red, and basic: blue. Water beads are shown as semi-transparent dark-blue spheres.

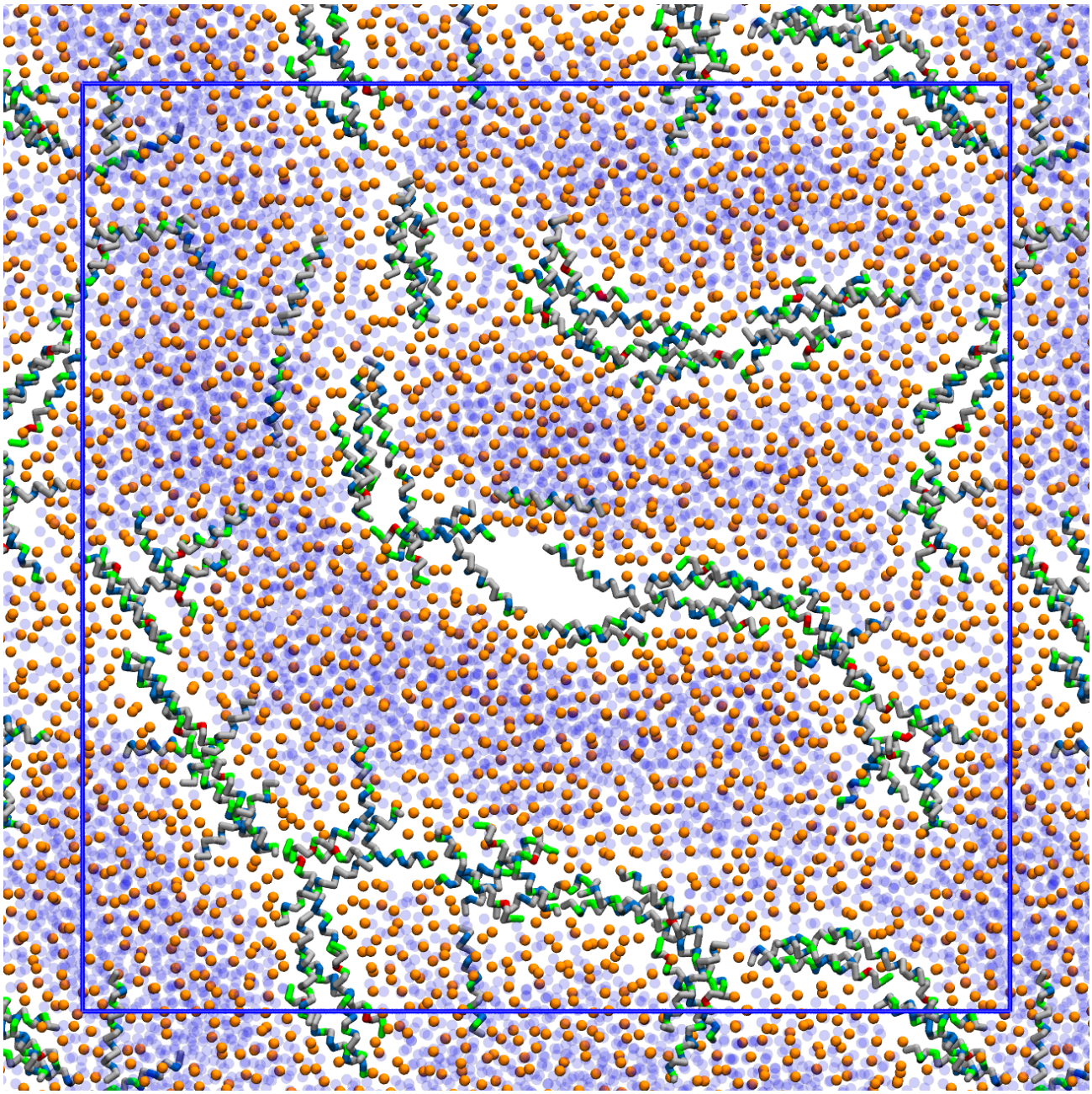

Figure S10: Top view on the interface between two lipid bilayers with adsorbed peptides at P/L= 1:21. The snapshot was taken from the end of a 100 μs. Peptides formed fiber-like structures and brought the membrane leaflets closer together. A stable fusion stalk is in the center of the image, surrounded by the peptides. Lipid phosphate atoms are shown as orange spheres. Lipid tails are not shown for clarity. Nonpolar: gray, polar: green, acidic: red, and basic: blue. Water beads are shown as semi-transparent dark-blue spheres.

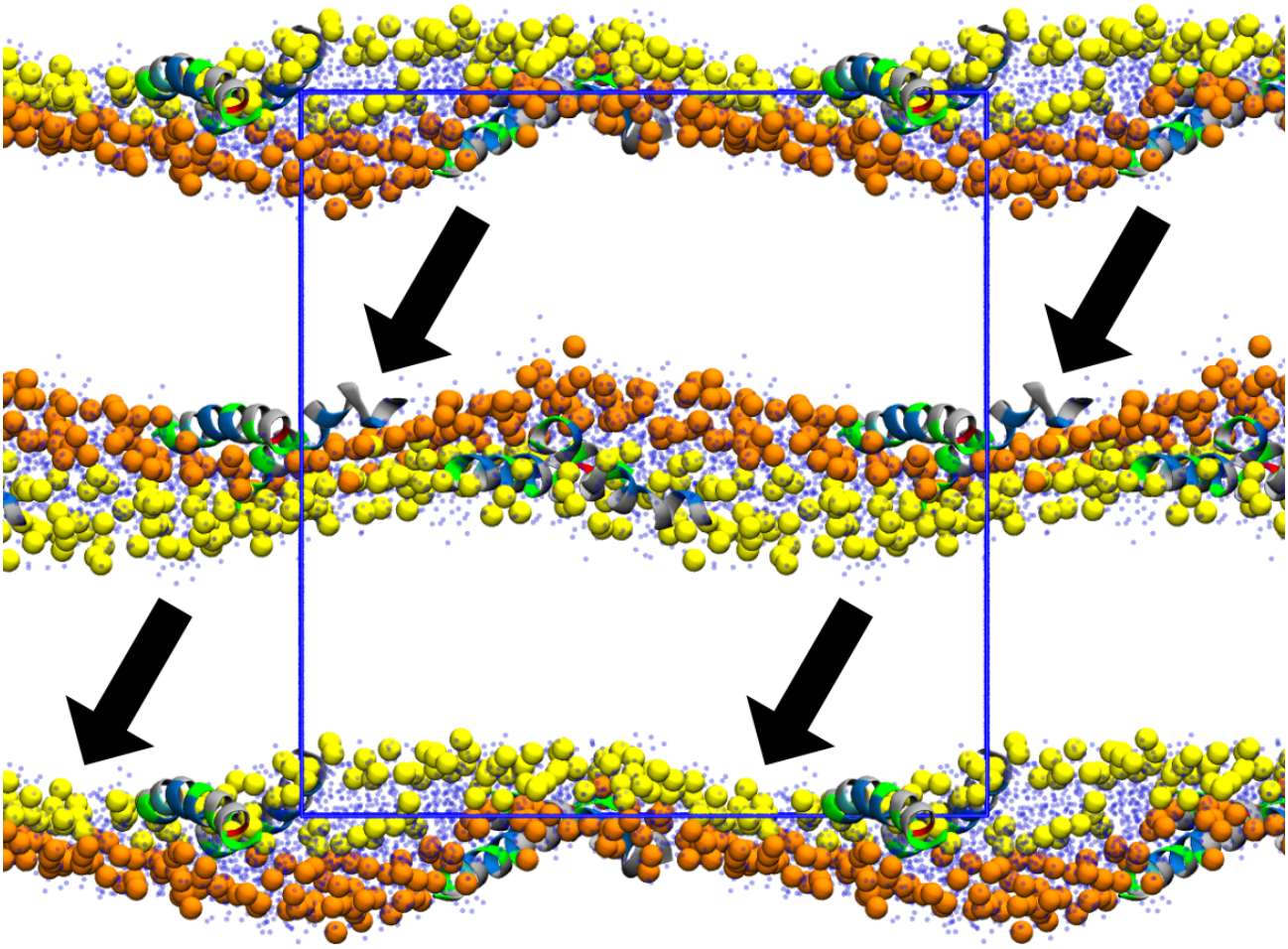

Figure S11: Initial configuration for an all-atom simulation of two lipid bilayers. Blue rectangle marks the simulation cell. Lipid phosphate atoms of first and second bilayers are shown as orange and yellow spheres, respectively. Lipid tails are not shown for clarity. The peptides' secondary structures are displayed in cartoon representation and colored by residue type. Nonpolar: gray, polar: green, acidic: red, and basic: blue. Water oxygens are shown as semi-transparent dark-blue dots.

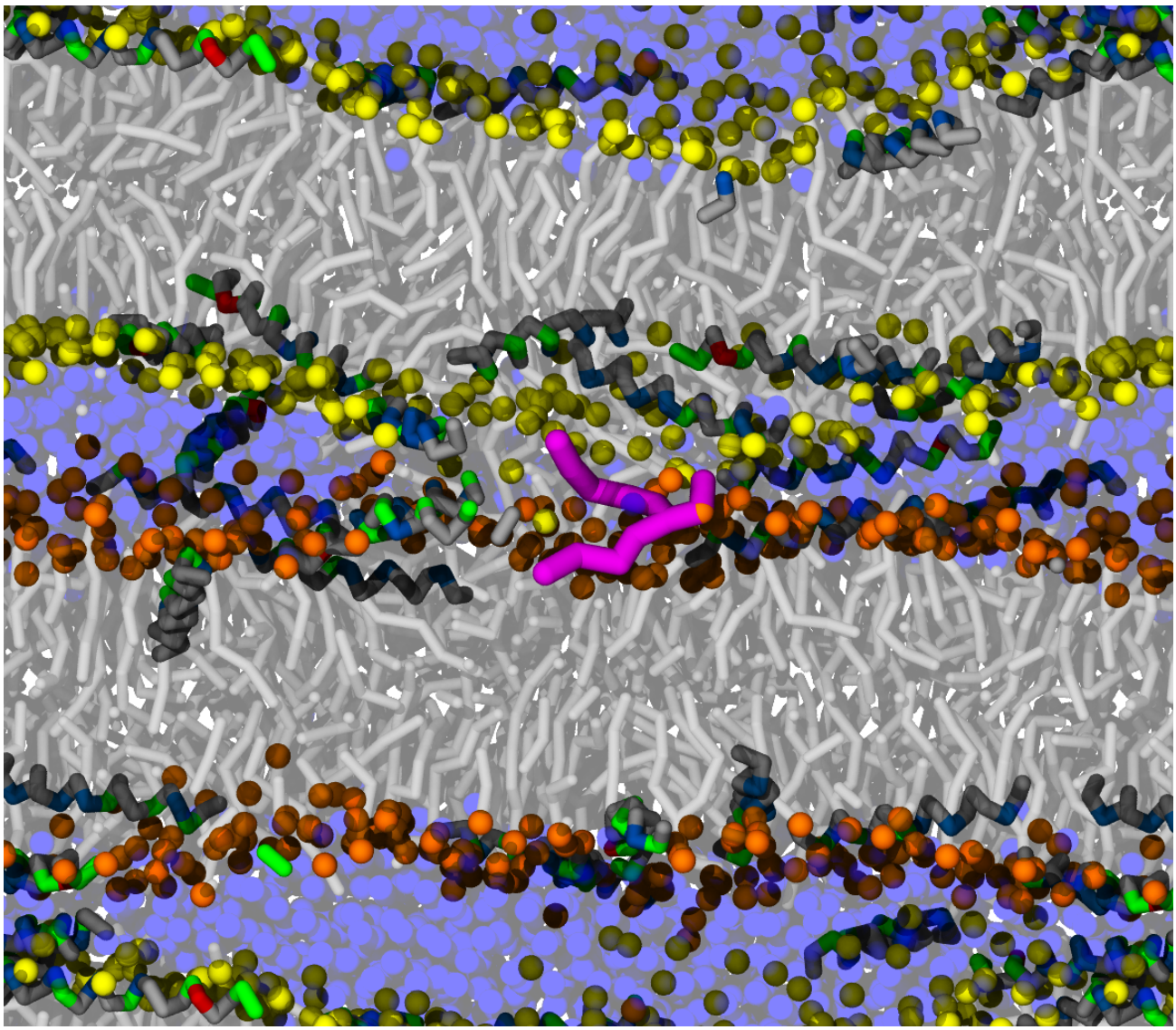

Figure S12: Simulation snapshot of two lipid bilayers connected with a fusion stalk and peptides at P/L = 1:21. Lipid phosphate atoms of first and second bilayers are shown as orange and yellow spheres, respectively. Lipids are shown as light-gray sticks. One lipid connecting both bilayers is highlighted by purple color. Nonpolar: gray, polar: green, acidic: red, and basic: blue. Water beads are shown as semi-transparent dark-blue spheres.

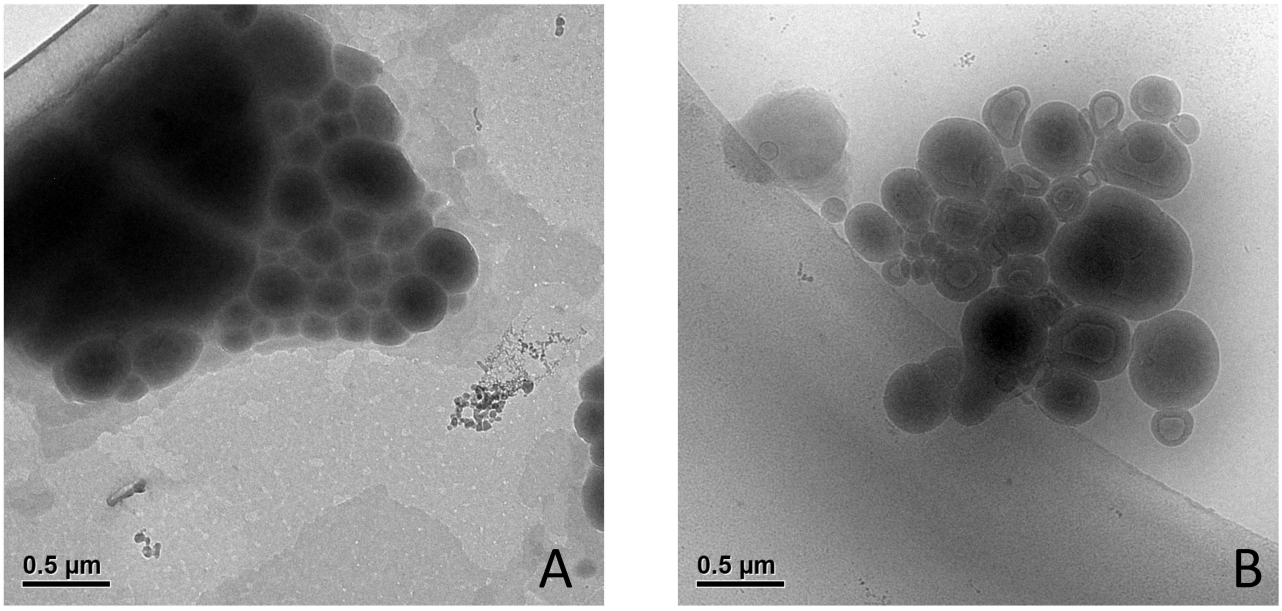

Figure S13: Cryo-TEM images of large unresolved aggregates found for POPE/POPG (3:1) in the presence of the equimolar peptide mixture (panel A) and the hybrid peptide (panel B).